Loughborough University

Electrocatalysis for Direct Alcohol Alkaline Fuel Cells

Ruirui ZHANG, B. Eng.

A thesis submitted in partial fulfillment of the requirements

for the award of Doctor of Philosophy of Loughborough University

School of Aeronautical, Automotive, Chemical and Materials Engineering

Loughborough University

September 2018

Acknowledgements

I would firstly like to express my appreciation to my supervisor, Prof. Wen-Feng Lin for his professional guidance and valuable support. It is an enjoyable and precious experience to working with you and learning from you.

Then, I would like to thank Prof. Lin's group members, Bao Liu, Chunlei Hou, Yafeng Chen, Sharleigh Talbot, Daniel Gayton, Alexandros Symillidis, Xiaoxian Xue and Jing Gu, I will always remember the time we spent together in lab. Special thanks to Dr. Dan Sun and Dr. Richao Zhang for their co-work in Ulster University.

I would also like to thank the staff in Queen's University, Belfast, where I finished my first-year research and the staff in Loughborough University, where I finished my whole project.

Finally, but most importantly, I would like to thank my parents Mr. Ming Zhang and Ms. Zhanyu Sun for their endless love, unrelenting support and help, and for this I am forever grateful.

Abstract

Due to the limited supply of fossil fuels and the increased concern for carbon emissions and global warming, fuel cells as a clean and highly efficient energy technology have been identified as a promising future alternative energy conversion solution. With advances being a liquid fuel and can be produced bio-renewably, ethanol has been proposed as a very attractive fuel for the direct ethanol fuel cells (DEFCs) which have currently garnered an increasing attention. A key challenge in the DEFCs is to find an efficient and cost-effective catalyst to oxidize ethanol at a low over-potential at relative low temperatures (below 90 ºC). In the direct ethanol fuel cell catalysis, Pd as a non-Pt catalyst, has been proposed as a promising catalyst for oxidizing ethanol under alkaline media, however, Pd alone is not sufficient and Pd-based catalysts are under developing to gain higher activity and stability for the DEFCs under alkaline media.

In this thesis, firstly the Pd electrocatalyst towards alcohol (methanol, ethanol butanol and glycerol) electrooxidation reaction in alkaline media at different temperatures (from 25 to 60 ºC) were studied for the direct alcohol fuel cells applications, then a series of Pd-based bimetallic electrocatalysts were developed to improve the activity and stability for ethanol electrooxidation reaction (EOR) in alkaline media under various conditions that a practical fuel cell would operate. Moreover, the kinetics of alcohol oxidation reaction on Pd and Pd-based electrocatalysts were explored from the activation energy calculated by Arrhenius plots using the data obtained from cyclic voltammetry (CV) and chronoamperometry (CA) studies at various temperatures and compared.

In comparison of the electrooxidation reactions of different alcohols, the positive peak current densities (J_p) at 30 ˚C follow such order: $J_{Glycerol} > J_{Butanol} > J_{Ethanol} > J_{Methanol}$, while the activation energies (Ea) follow the order of: $Ea_{Glycerol} < Ea_{Butanol} < Ea_{Methanol} < Ea_{Ethanol}$. These results implied that the reaction activities increased while the activation energy decreased with respect to increases in the length of the carbon chain

of the primary alcohols.

For ethanol electrooxidation reaction (EOR) in alkaline media, the catalytic reactivity of Pd is significantly enhanced by being decorated with a second metal (Pb, Ag, AuNPs, Sb). Activation energy (Ea) of X/Pd (X= Pb, Ag, AuNPs, Sb) at an optimal coverage of X is following the order: $Ea_{Sb(\theta=20\%)/Pd} < Ea_{Ag(\theta=37\%)/Pd} < Ea_{AuNPs(30nm)\ (\theta=45\%)/Pd} < Ea_{Pb(\theta=29\%)/Pd} < Ea_{AuNPs(3nm)\ (\theta=16\%)/Pd} < Ea_{bulk\ Pd}$, while oxidation peak current density at 30 ºC is following such order: $J_{Sb(\theta=20\%)/Pd} > J_{AuNPs(3nm)\ (\theta=16\%)/Pd} \approx J_{Ag(\theta=37\%)/Pd} > J_{Pb(\theta=29\%)/Pd} > J_{AuNPs(30nm)\ (\theta=45\%)/Pd} > Ja_{bulk\ Pd}$.

Among all these catalysts studied, $Sb_{(\theta=20\%)}/Pd$ and $Ag_{(\theta=37\%)}/Pd$ exhibit the highest reactivity, having the lowest Activation energy and highest peak current density.

Journal Publications

1. R. Zhang, D. Sun, R. R. Zhang, W. F. Lin, M. Macias-Montero, J. Patel, S. Askari, C. McDonald, D. Mariotti, P. Maguire, "Gold nanoparticle-polymer nanocomposites synthesized by room temperature atmospheric pressure plasma and their potential for fuel cell electrocatalytic application", Sci. Rep, 7, 46682, DOI: 10.1038/srep46682.

Conference Presentations

1. W. F. Lin, Y. Chen, R. Zhang, D. Gayton, A. Symillidis, "Electrocatalysis for Direct Alcohol Fuel Cells", UK Electrochemistry Meeting 2018, Lancaster, 16-18th September 2018, Abstract and Oral presentation.

2. W. F. Lin, R. Zhang, X. Lin, T. Sheng, S. G. Sun, "Understanding Methanol Electro-Oxidation Mechanisms on RuO_2(100) Surface at Atomic and Molecular Level by Combined Studies of in-situ FTIR Spectroscopy and DFT Atomistic Modelling", 68th Annual Meeting of the International Society of Electrochemistry, Providence, RI, USA, 27th August -2nd September 2017, Abstract -ise170957 and Oral presentation.

3. W. F. Lin, R. Zhang, X. Lin, P. Wang, H. Wang, T. Sheng, C. Hardacre, P. Hu, S. G. Sun, "Low Cost High Performance Nanocatalysts for Direct Ethanol Fuel Cell Application: Catalyst Development and Reaction Mechanism Studied by in-situ FTIR Spectroscopy and DFT Atomistic Modeling", 67th Annual Meeting of the International Society of Electrochemistry, The Hague, the Netherlands, 21-27 August 2016, Abstract -ise161003 and Oral presentation.

List of Symbols

ADAFC	Alkaline direct alcohol fuel cell	K	Temperature in Kelvin
AFC	Alkaline fuel cell	MCFC	Molten Carbonate fuel cell
CA	Chronoamperometry	MMO	Mercury/Mercuric Oxide reference electrode
CE	Counter electrode	MOR	Methanol oxidation reaction
CV	Cyclic voltammetry	n	Number of electrons transfered per mole of reactant
DAFC	Direct alcohol fuel cell	p	Pressure
DEFC	Direct ethanol fuel cell	PAFC	Phosphoric acid fuel cell
DMFC	Direct methanol fuel cell	PEMFC	Polymer electrolyte membrane fuel cell
E^0	Standard electrode potential	Q	Heat
E_a	Activation energy	R	Gas constant ($8.3145\ J\ K^{-1}\ mol^{-1}$)
E_o	Onset potential	RE	Reference electrode
E_p	Positive-going peak potential	RHE	Reversible hydrogen electrode
E_n	Negative-going peak potential	S	Entropy
ECSA	The electrochemical surface area	SHE	Standard hydrogen electrode
EOR	Ethanol oxidation reaction	SOFC	Solid oxide fuel cell
F	Faraday's constant (96.485 kC mol-1)	T	Thermodynamic temperature
f_l	*D*ecay rate to products	U	Internal energy

G	Gibbs free energy	V	Volume
GOR	Glycerol oxidation reaction	WE	Working electrode
H	Enthalpy	α	*T*ransfer coefficient
j_p	Positive-going peak current density	$\Delta G^{\ddagger}_1$	Activation barrier
j_n	Negative-going peak current density	η	Activation overvoltage

Contents

Chapter One

Introduction and Overview of Fuel Cell

1.1 Overview of fuel cell

Fuel cells, which efficiently and directly convert the chemical energy of a fuel (hydrogen, natural gas, methanol, ethanol, hydrocarbons, etc.) into electrical energy bypassing the intermediate energy loss are very promising power sources to reduce energy consumption and pollution. Among the most considered future alternative energy conversion systems are fuel cells[1]. However, fuel cell technology is not new. The principles of fuel cells were first discovered by Christian Friedrich Schonbein[2], a professor of a university while the invention of fuel cells was demonstrated by a British scientist William Grove in 1839. The following picture shows the first fuel cell developed by Grove (which Grove called the gas voltaic battery)[3].

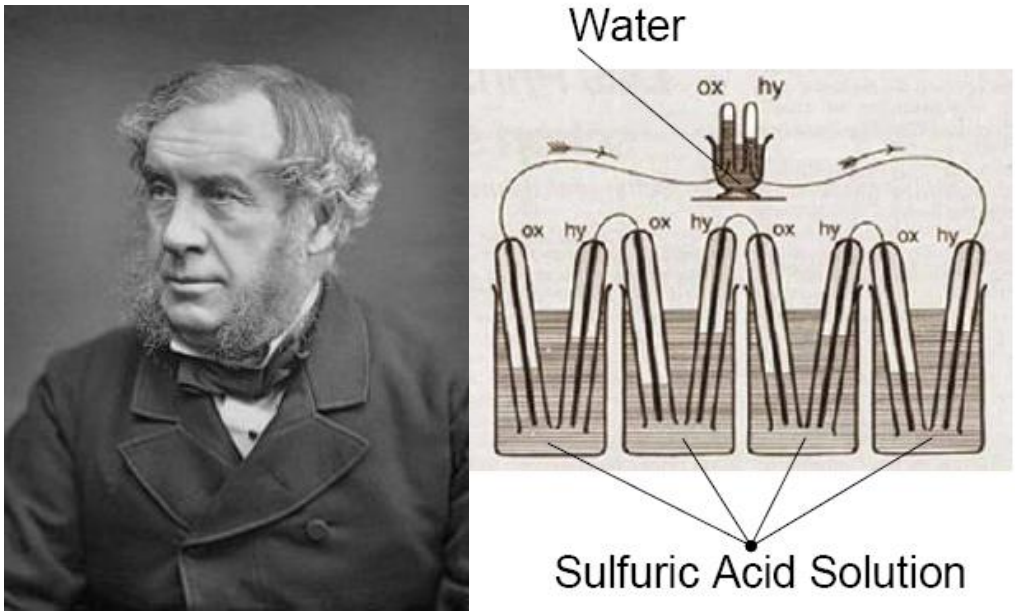

Figure 1.1 William Grove and he's 1839 gas voltaic battery diagram

On the whole, fuel cells operate like batteries, but do not stop functioning as long as fuel is supplied and can be recharged by refueling[4]. A fuel cell is generally composed of an anode electrode, a cathode electrode and membrane(electrolyte) which is showed in Figure 1.2.

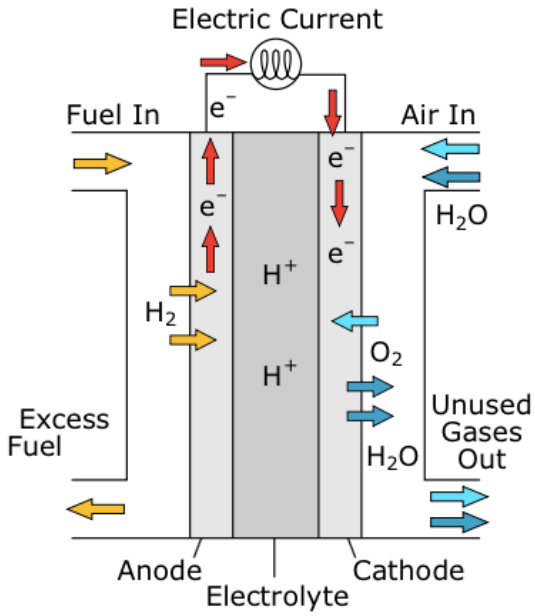

Figure 1.2 Basic fuel cell working concepts[5]

The fuel is oxidized at the anode(negative) electrode and only produce water and/or carbon dioxide which are rejected in the atmosphere, whereas the oxidant (oxygen from the air) is reduced at the cathode(positive) electrode. This whole process is not limited by the Carnot's theorem which means higher efficiencies are expected (40%-50% in electrical energy, 80%-85% in total energy (electricity + heat production) by dealing with high temperature of heat engine[3].

The thermal efficiency of the fuel cell can be defined as the percentage of useful electrical energy produced relative to the heat that would have been obtained through the combustion of the fuel (enthalpy of formation). In the ideal case, the maximum efficiency (or thermodynamic efficiency) of a fuel cell operating irreversibly can be expressed as the percentage ratio of Gibbs free energy over the enthalpy of formation, that is, Efficiency $\varepsilon = \frac{\Delta G}{\Delta H}$, where ΔG is change in Gibbs free energy and ΔH is the enthalpy of formation of the reaction. For the hydrogen/oxygen fuel cell the thermodynamic efficiency limit at the higher heating value (HHV) is equal to 83%[5].

In practice the efficiency of the fuel cell can be expressed in terms of the percentage ratio of operating cell voltage relative to the ideal cell voltage as ideal cell Efficiency = $V_{op}/V_{id} = 0.83$ where V_{op} is the actual voltage of the cell and V_{id} is the voltage obtained from Gibbs free energy in the ideal case. The 0.83 is from the thermodynamic limit (HHV).

In the non-ideal case, the actual operating voltage is less than the ideal voltage because of the irreversible losses associated with the fuel cell electrochemistry. There are three primary irreversible losses that result in the degradation of fuel cell performance and these are activation polarisation, ohmic polarisation, and concentration polarization[5]. Fig.1.3 illustrates the effects of the irreversible losses on cell voltage for a low temperature, hydrogen/oxygen fuel cell.

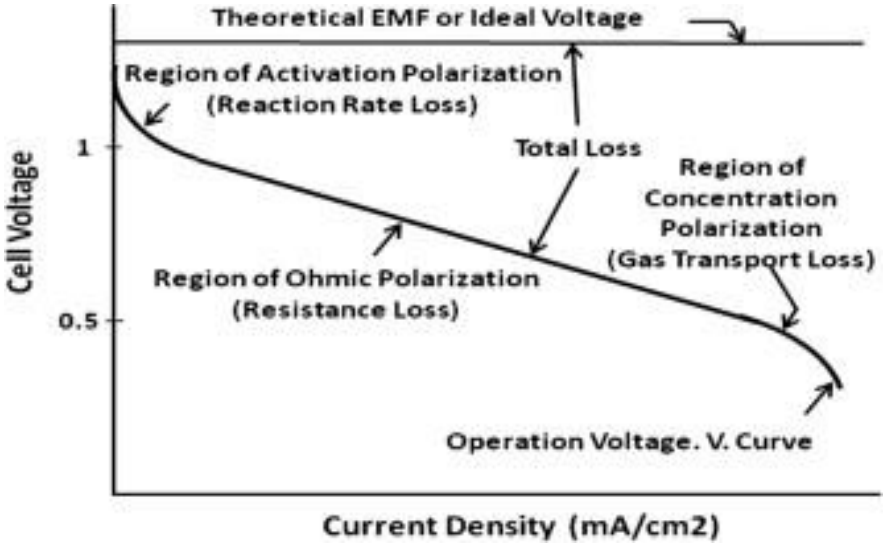

Figure 1.3 Illustration of actual performance of fuel cell

Activation polarisation is caused by limited reaction rates at the surface of the electrodes and is dominant at low current density and increases marginally with an increase in current density. Ohmic polarisation as the major loss of fuel cell voltage is caused by the resistance to the flow of ions in the electrolyte and to the flow of electrons through the electrode materials. This loss is directly proportional to the current density.

Efforts are made to reduce the polarisations, this can be done by improving the electrode structure, using highly conducting electrolyte and better electrocatalysts. Concentration polarisation is caused by a loss of concentration of the fuel or oxidant at the surface of the electrodes. The reason of concentration voltage drop at high current densities is the slow transportation of reactants to the reaction sites. These losses are present over the entire current density range but become prevalent at high limiting currents where it becomes difficult to provide enough reactant flow to the cell reaction sites.

1.2 Introduction to relevant electrochemistry and fuel cell electrocatalysis

1.2.1 The operation principle of a galvanic cell (fuel cell)

A galvanic cell (fuel cell) is composed of two electrodes (anode and cathode) and an electrolyte. The anode is the negative electrode which provides the place for an oxidation reaction, whereas the cathode is the positive electrode where the reduction reaction occurs. The electrolyte is used to separate the two electrodes and help the transportation of specific ions to form a circuit[6-7].

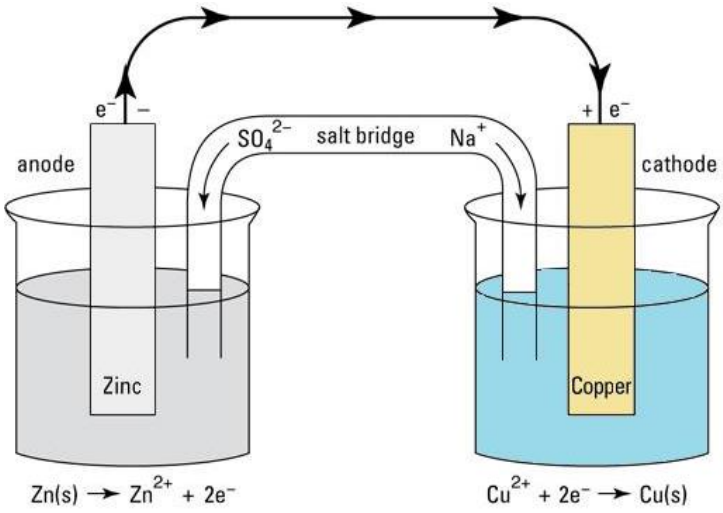

Figure 1.4 Operation mechanisms of Daniell cell

The operation principle of a fuel cell is similar to the battery. However, in a battery, the electrodes may be consumed as at least one of the electrodes is always made of solid metal which could be converted to other chemical compounds when the electricity is generated. An electromotive force could be generated by the reaction of chemicals present in the battery, so the energy produced by a battery is limited by the amount of solid metal that can be converted. The operation mechanisms of Daniell cell are exhibited in Figure 1.4.

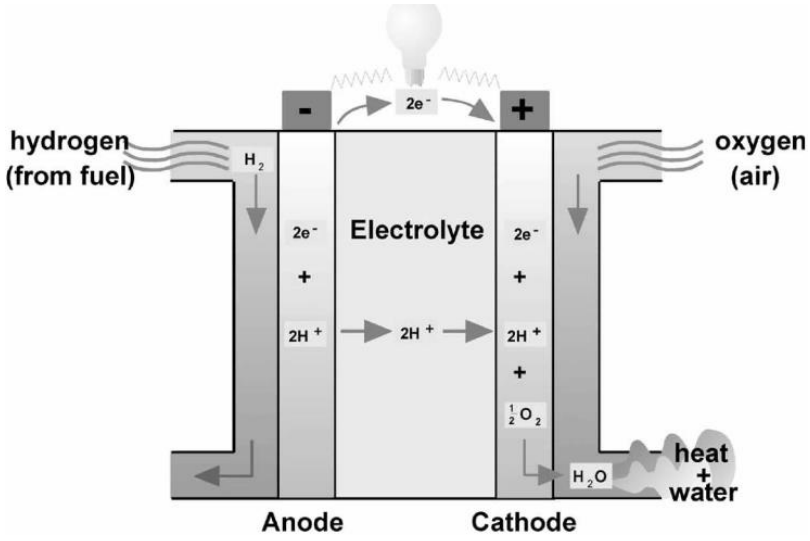

Figure 1.5 Schematic of a proton exchange membrane fuel cell operation

On the other hand, instead of solid metal, the electrodes which could not be consumed are used in the fuel cell. Fuel cells need to supply fuel and oxygen/air continuously and it can produce electricity as long as there is enough fuel and oxidant pumping through it[3]. The schematic of a proton exchange membrane fuel cell operation is presented in Figure 1.5.

1.2.2 Fuel cell thermodynamics

Thermodynamics is the study of heat and temperature and their relationship with energy and work. For fuel cells, thermodynamics can judge whether fuel cell reactions can react energetically spontaneously and there is thermodynamic limit in the performance of the real fuel cell.

Thermodynamics defines a series of variables, including internal energy (U), entropy (S), enthalpy (H) and Gibbs free energy (G). Internal energy is the total energy in a system which contained the energy of microscopic movement and interaction between

atom or molecule. Entropy can be regarded as a measurement of "disorder". Fuel's enthalpy reaction can provide the maximum heat energy which can be extracted from the fuel in a constant-pressure process (dp = 0). While ΔG indicates the spontaneity of a reaction. Several significant equations are as follows:

$$dU = dQ - dW \qquad (1.1)$$

$$dS = \frac{dQ_{rev}}{T} \qquad (1.2)$$

$$dH = TdS + Vdp \qquad (1.3)$$

$$dG = -SdT + Vdp \qquad (1.4)$$

Where Q is heat (J, J mol^{-1}), W is work (J, J mol^{-1}), p is pressure (Pa), V is the volume (m^3).

For electrochemical reactions, Nernst equation provides the relation between electrode potential (E) and the concentrations of reactants (C_O) and products (C_R) when the system is thermodynamically or electrochemically reversible.

$$O + ne \leftrightarrow R \qquad (1.5)$$

$$E = E^0 + \frac{RT}{nF} ln \frac{C_O}{C_R}$$

Where E^0 (V) is the standard potential. R is the molar gas constant (8.314 J K^{-1} mol^{-1}) n is the number of moles of electrons per mole of the reactant, F is faraday constant (the charge on a mole of electrons, which is approximately 96485 C mol^{-1}). T is temperature in K.

For fuel cells, there is a close relationship between Gibbs free energy and voltage.

|ΔG| = charge passed × reversible potential difference

$$|\Delta G| = nF|E| \qquad (1.6)$$

It is mentioned above that ΔG represents the spontaneity of a reaction. When the reaction is spontaneous, ΔG < 0.

$$\Delta G = -nFE_{rxn} \qquad (1.7)$$

$$\Delta G^0 = -nFE^0_{rxn} \qquad (1.8)$$

Where ΔG^0 is the standard Gibbs free energy, E^0_{rxn} is the standard emf.

1.2.3 Fuel cell reaction kinetics

Fuel cell reaction kinetics govern the mechanisms of fuel cell reactions. There are extreme differences between electrochemical reactions and chemical reactions. The main difference is that the electrochemical processes are heterogeneous due to the transfer of charge between an electrode and analyte. HOR is one of the examples showed in the Figure 1.6.

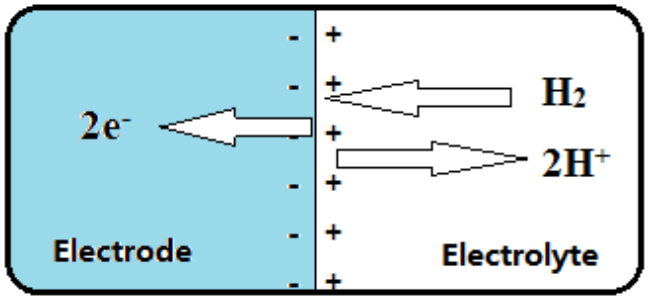

$$H_2 \rightleftharpoons 2H^+ + 2e^-$$

Figure 1.6 HOR only can occur at the interface between an electrolyte and an electrode

In a fuel cell system, the net current density for the reaction j is defined by Butler-Volmer equation：

$$j = j_0(e^{\frac{\overleftarrow{\alpha}F\eta}{RT}} - e^{-\frac{\overleftarrow{\alpha}F\eta}{RT}}) \qquad (1.9)$$

Where j_0 (mA cm^{-2}) is the exchange current density for the reaction (equilibrium), α is the transfer coefficient, η is activation overvoltage (V) and T (K) is the temperature.

According to Bulter-Volmer equation, increasing j_0 is the original method to improve kinetic performance.

The exchange current density for the reaction j_0 is defined as:

$$j_0 = nFc_R^* f_1 e^{-\frac{\Delta G_1^{\ddagger}}{RT}} \qquad (1.10)$$

Where c_R^*(mol L^{-1}) is reactant concentration, $\Delta G_1^{\ddagger}$ (J mol^{-1}) is the activation barrier, T (K) is the temperature and f_1 is the decay rate to products.

Based on Equation 1.10, there are several methods to improve fuel cells reaction kinetics, including increasing temperature, reactant concentration and reaction sites and decreasing activation barrier. The increasing thermal energy (temperature) is beneficial to reactant reaching their activated state. However, the current density may be on the decrease when the temperature is increasing at high overvoltage levels. With respect to reactant concentration, increasing the concentration will increase the current density as is apparent from Equation 1.10. Most fuel cells use air rather than oxygen which means about five times the reduction can occur at the cathode in the oxygen kinetics. In addition, due to mass transport limitations, the supplement cannot satisfy the consumption of the reactants. Consequently, decreasing reactant concentration will occur in high-current-density operation at electrodes.

Similarity, increasing the reaction sites will increase the current density j_0. j_0 is based on the projected geometric electrode area. Furthermore, a rough electrode surface can offer more reaction sites than a smooth electrode surface. A rougher electrode surface therefore will improve the performance of fuel cells. On the contrary, increasing the size of the activation barrier can decrease j_0. A small increase in the activation barrier can lead to a sharp decrease in current density. A catalytic electrode, which can change the free energy surface of the reaction can help lower the activation barrier, as shown in Figure 1.7. Compared with the absence of catalyst, the existing of catalyst lower the activation energy of the reaction without affect the energy of the reactants or products.

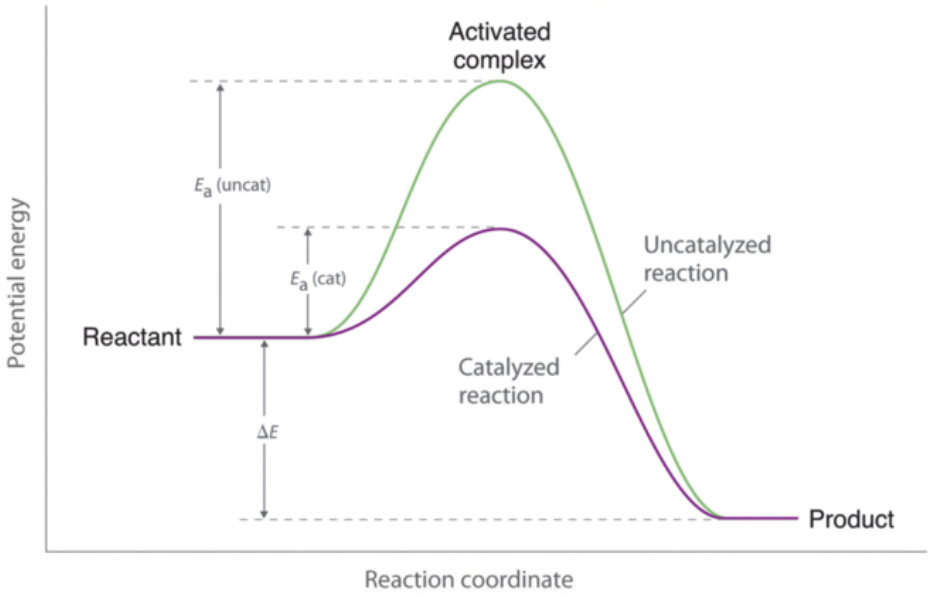

Figure 1.7 **Lowering the Activation Energy of a Reaction by a Catalyst.**

1.3 The types of fuel cells

To date, numerous types of fuel cells have already been made by researchers. There are five major types of fuel cells, classified by the electrolyte employed in the cell[8-9]: alkaline fuel cell (AFC), phosphoric acid fuel cell (PAFC), polymer electrolyte membrane fuel cell (PEMFC), molten carbonate fuel cell (MCFC) and solid-oxide fuel cell (SOFC). An exception to this classification is the DMFC (Direct methanol fuel cell) which is a fuel cell in which methanol is directly fed to the anode. The electrolyte of this cell is not determining for the class. An overview of the fuel cell types is given in Table 1.

Table 1.1 The properties of different fuel cells[5]

	AFC (Alkaline)	**DMFC** (Direct Methanol)	**PEMFC** (Polymer Electrolyte Membrane)	**PAFC** (Phosphoric Acid)	**MCFC** (Molten Carbonate)	**SOFC** (Solid Oxide)
Operating temperature (℃)	< 100	60-120	60-120	160-220	600-800	800-1000
Anode reaction	$H_2 + 2OH^- \rightarrow 2H_2O + 2e^-$	$CH_3OH + H_2O \rightarrow CO_2 + 6H^+ + 6e^-$	$H_2 \rightarrow 2H^+ + 2e^-$	$H_2 \rightarrow 2H^+ + 2e^-$	$H_2 + CO_3^{2-} \rightarrow H_2O + CO_2 + 2e^-$	$H_2 + O^{2-} \rightarrow H_2O + 2e^-$
Cathode reaction	$1/2O_2 + H_2O + 2e^- \rightarrow 2OH^-$	$3/2O_2 + 6H^+ + 6e^- \rightarrow 3H_2O$	$1/2O_2 + 2H^+ + 2e^- \rightarrow H_2O$	$1/2O_2 + 2H^+ + 2e^- \rightarrow H_2O$	$1/2O_2 + CO_2 + 2e^- \rightarrow CO_3^{2-}$	$1/2O_2 + 2e^- \rightarrow O^{2-}$
Application	Transportation, space, military, energy storage systems			Combined heat and power for decentralised stationary power systems	Combined heat and power for stationary decentralised systems and for transportation (trans, boats, etc)	
Realised Power	Small plants 5-150kW modular	Small plants 5kW	Small plants 5-150kW modular	Small-medium sized plants 50kW-11kW	Small power plants 100kW-2MW	Small power plants 100kW-250kW
Charge Carrier in the Electrolye	OH^-	H^+	H^+	H^+	CO_3^{2-}	O^{2-}

1.3.1 Alkaline fuel cells (AFCs)[5, 10-12]

The alkaline fuel cell operates between 50-250°C. The electrolyte in this fuel cell is KOH and can be either mobile or retained in a matrix material. Many catalysts can be used in this fuel cell, an attribute that provides development flexibility. The AFC has excellent performance on hydrogen and oxygen compared to other candidate fuel cells. The major disadvantage of this fuel cell is that it is very susceptible to CO_2 and CO poisoning and hence its use with reformed fuels and air is limited.

1.3.2 Direct methanol fuel cells (DMFCs)[13-16]

Direct alcohol fuel cells (DAFCs), in which alcohol is directly fed into the cells without the intermediate step of reforming the alcohol into hydrogen, operating at s at 50- 100°C. Direct methanol fuel cells (DMFCs) are proper examples of DAFCs, where diluted methanol in a water mixture is used. DMFCs' have high catalysts loadings and possess allow electrode kinetics but low overall efficiency.

1.3.3 Polymer electrolyte membrane fuel cells (PEMFCs)[17-19]

The polymer electrolyte membrane fuel cell operates at 50- 100°C. The electrolyte in this fuel cell is a solid ion exchange membrane used to conduct protons. Hardware corrosion and gas crossover are minimised as a result of the solid electrolyte and very high current densities as well as fast start times have been realised for this cell. However due to the low temperature operation, catalysts (mostly platinum) are needed to increase the rate of reaction. In addition, heat and water management issues are not easily over come in a practical system, and tolerance for CO is low.

1.3.4 Phosphoric acid fuel cells (PAFCs)[20-22]

The phosphoric acid fuel cell operates at 200°C with phosphoric acid (100%) used for the electrolyte. The matrix universally used to retain the acid is silicon carbide, and the catalyst is Platinum. The use of concentrated acid (100%) minimises the water vapour pressure so water management in the cell is not difficult. The cell is tolerant to CO_2 and the higher temperature operation is of benefit for co-generation applications. The main limitation of the PAFC is the lower efficiency realised in comparison with other fuel cells.

1.3.5 Molten carbonate fuel cells (MCFCs)[5,8]

The molten carbonate fuel cell operates at 600°C. The electrolyte in this fuel cell is usually a combination of alkali carbonates retained in a ceramic matrix. At the high temperature of operation, the alkali carbonates form a highly conductive molten salt, with carbonate ions providing ionic conduction. The high reaction rates remove the need for noble metal catalysts and gases such as natural gas can be internally reformed without the need for a separate unit. In addition, the cell can be made of commonly available sheet metals for less costly fabrication. One feature of the MCFC is the requirement of CO_2 at the cathode for efficient operation. The main disadvantage of the MCFC is the very corrosive electrolyte that is formed, which impacts on the fuel cell life, as does the high temperature operation.

1.3.6 Solid oxide fuel cells (SOFCs)[23-25]

A range of optimal operation temperature for solid oxide fuel cell is between 500-1000°C. Because of its high temperature operation, it is easy to accelerate reaction

rates without expensive catalysts. In addition, natural gas can be regenerated without fuel reforming. However, the high temperature also impedes the material selection and makes assemble process more difficult. A firm, porous-free metal oxide and oxygen ions can be utilized as SOFC electrolyte and charge carriers respectively. In order to maintain interior unsophistication, the electrolyte in solid oxide fuel cell is always under solid state. On the other hand, ceramic material used in cell can alleviate hardware corrosion, increase the flexibility of cell design, and is impassable to gas circulation between two electrodes. Unfortunately, the application of ceramic material in electrolyte results in a lower conductivity, which negatively affects the fuel cell function.

1.4 Direct ethanol fuel cells (DEFCs)

Direct ethanol fuel cells work through a simple oxidation reaction. The reaction can take place in two different types of environment; acidic or alkaline, both methods provide electrons through an oxidation reaction, only they use different mechanisms to achieve this.

1.4.1 Acid direct ethanol fuel cell

Acid based direct ethanol fuel cells use an oxidation reaction in relatively low pH values of around 5. It utilizes a proton exchange membrane (PEM) to allow hydrogen ions to move from the anode side to the cathode side through the electrolyte. The most commonly used PEM is Nafion® which is a copolymer of fluoro-3, 6-dioxo 4, 6-octane sulfonic acid and polytetra-fluorethylene (PTFE), which provides the support for the membrane structure[26]. The Nafion membrane allows the movement of cations (in

this case H^+) but prohibits the flow of anions (in this case e^-). The reactions that occur in an acid based DEFC are shown below:

Anodic half-cell reaction:

$$C_2H_5OH + 3H_2O \rightarrow 2CO_2 + 12H^+ + 12e^- \quad (1.11)$$

Cathodic half-cell reaction:

$$3O_2 + 12H^+ + 12e^- \rightarrow 6H_2O \quad (1.12)$$

Overall reaction:

$$C_2H_5OH + 3O_2 \rightarrow 2CO_2 + 3H_2O \quad (1.13)$$

1.4.2 Alkaline direct ethanol fuel cells

Alkaline based direct ethanol fuel cells use a high pH value to achieve oxidation (7-12pH). Instead of moving cations through the membrane, an anion exchange membrane (AEM) is utilized to allow the movement of only OH^- ions through. The anions move from the cathode side to the anode side, the opposite direction to the acid DEFC. The electrons still travel from the anode to the cathode though.

The reactions that occurs in an alkaline DEFC are as follows:

Anodic half-cell reaction:

$$C_2H_5OH + 12OH^- \rightarrow 2CO_2 + 9H_2O + 12e^- \quad (1.14)$$

Cathodic half-cell reaction:

$$3O_2 + 6H_2O + 12e^- \rightarrow 12OH^- \quad (1.15)$$

Overall reaction:

$$C_2H_5OH + 3O_2 \rightarrow 2CO_2 + 3H_2O \qquad (1.16)$$

The reaction kinetics of the alkaline oxidation reaction are known to be fairly slow, therefore a base is normally added to the ethanol fuel feed such as KOH or NaOH to increase the concentration of OH^- ions by dissociation:

$$12NaOH \rightarrow 12Na^+ + 12OH^- \qquad (1.17)$$

Hence, the actual overall reaction in the AEM DEFC is shown as Eq. 1.18, the main product of the reaction is acetic acid rather than CO_2.

$$C_2H_5OH + O_2 + OH^- \rightarrow CH_3COO^- + 2H_2O \qquad (1.18)$$

With an increase in OH^- ions comes an increase in pH, speeding up the ethanol oxidation reaction (EOR) kinetics but also increasing the efficiency of the AEM[27].

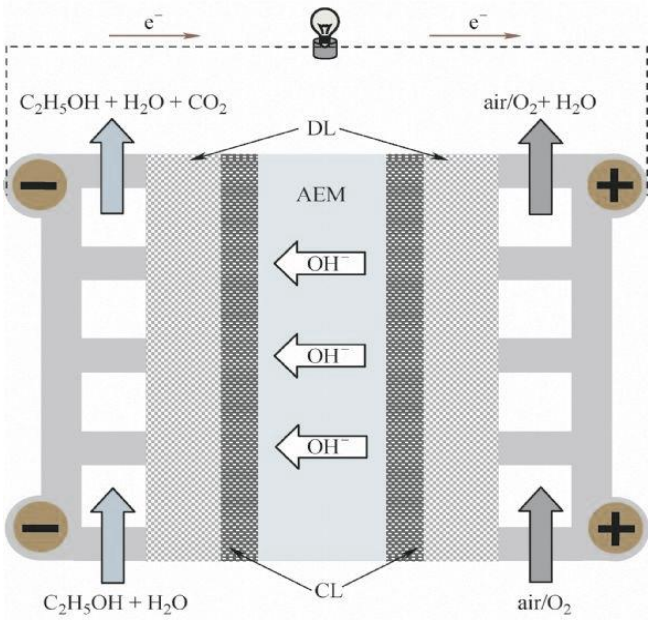

Figure 1.8 The structure of a liquid-feed alkaline membrane-based direct ethanol fuel cell[28].

Figure 1.8 exhibits a liquid-feed AEM DEFC equipment that contains a membrane electrode assembly (MEA) which is regarded as an integrated multi-layered structure, is composed sequentially of an anode diffusion layer (DL), an anode catalyst layer (CL), an AEM, a cathode catalyst layer (CL), and a cathode diffusion layer (DL). Both the anode CL and cathode CL are comprised of mixtures of catalysts and ionomer to provide triple-phase boundaries for the EOR and ORR. The DL is to provide support for the associated CL, to distribute the reactants over the CL and to conduct electricity to the current-collector, it is composed of two layers, a backing layer (BL)consist of carbon cloth or carbon paper, and a micro-porous layer (MPL) is made of a hydrophobic polymer and carbon powder.

On the anode, the ethanol solution is transported through the anode diffusion layer to the anode catalyst layer, where it is oxidized to form electrons, water, and CO_2 according to Eq. 1.14. The water, from the ethanol solution and that produced by EOR, diffuses through the membrane to the cathode catalyst layer, while the electrons travel through an external circuit to the cathode. On the cathode, the oxygen/air is transported through the cathode diffusion layer to the cathode catalyst layer, where the oxygen reacts with water from the anode to produce hydroxide ions according to Eq 1.15[28].

1.5 Catalysts development for DEFCs

Catalysts are required in both the cathode and the anode, so the EOR at the anode and the oxygen reduction reaction (ORR) at the cathode can occur as fast as possible. Since there are two different half-reactions occurring, a different material may be required for each catalyst to optimize its performance. Using catalysts in the electrodes reduces the energy consumed during the reaction by lowering the activation

energy and increasing the rate at which the reactions occur.

Many factors affect the catalyst performance such as particle distribution, functionalization of the carbon support, surface active area and catalytic activity[29]. Each metal being added will affect the catalysts behavior in different ways. For example, adding Ni to Pd weakens the intermediate bonds formed during the adsorption and desorption phase, reducing the amount the Pd catalyst gets poisoned by CO, therefore increasing the number of active sites available, and reducing the energy required for adsorption[30]. The co-catalyst can be alloyed with the base metal or it can be added as discrete drops onto the surface of the base metal.

The three main ways in which the performance of a catalyst is measured are activity, selectivity and stability[31]. Activity is a measure of how the catalyst affects the rate of reaction, influenced mainly by the rate of adsorption and desorption onto the surface of the catalyst. Selectivity is a measure of how well the catalyst can direct a reaction towards the desired products as opposed to by-products that may form. For ethanol oxidation, the desired reaction is full oxidation of ethanol to carbon dioxide and water. When partial oxidation occurs, which can result in the formation of acetic acid and acetaldehyde by-products, fewer electrons are passed across to the cathode. Therefore, optimizing the selectivity of the catalysts is vital to make sure full oxidation occurs, since you get a much larger number of electrons flowing through the circuit.

The chemical, mechanical and thermal stability of a catalyst all influence its lifespan. There is no value in having a catalyst that has high selectivity and high activity, if it will only last a few hours before decomposing. In commercial applications, efficiency of materials and energy are a major concern currently, therefore when choosing a catalyst selectivity is rated most highly, then stability, then activity.

1.5.1 Anode catalyst material

As stated previously, the anode is primarily responsible for the EOR. When deciding what material(s) to use the activity, selectivity and stability are the most important criteria to consider. The most prominent problems faced with designing an anode catalyst is difficulties in polarization of the catalyst and splitting the C-C bond in the ethanol, which, when not optimized, leads to partial oxidation to be favored by the catalyst[32]. The article 'Hydrogen production from ethanol reforming: Catalysts and reaction mechanism' stated that "Several metallic active phases mainly Ni, Co and noble metals such as Rh, Ru, Pt, Pd and Ir have been widely investigated considering that all these metals possess high C–C bond cleavage capacity, which is an indispensable function for ethanol conversion".

a. Platinum

The most common catalyst used for the anode is platinum, since it is the most effective monometallic catalyst for the anode identified to date, especially in an acid media. This is why almost all research on platinum catalysts has been carried out in acidic media with a proton exchange membrane direct ethanol fuel cell (Figure 1). While Pt is known to be the most effective monometallic catalyst for EOR, studies have shown that it has a selectivity of 0.5%-7.5%[33] in acid, which is not enough for commercial use in a DEFC and found to have low stability, as it is easily poisoned by intermediates generated during the EOR such as carbon monoxide. Kavanagh states in 'Origin of Low CO_2 Selectivity on Platinum in the Direct Ethanol Fuel Cell' – "1) the catalytic reactions occur on solid surfaces in the presence of a solvent, resulting in a system that is complex to understand at the molecular level; and 2) electrocatalysts operate at an applied potential (i.e. bearing charge), leading to more complications. Hence, it is extremely difficult to characterize the molecular-level surface processes by using experimental techniques, and it is also a huge computational challenge to realistically

model the system."[33]

When incomplete oxidation occurs, CO stays bonded to the surface of the anode, reducing the number of available sites for adsorption. Platinum displays low selectivity meaning it has difficulty with splitting the ethanol C-C bond[34], which is why it is sometimes combined with other metals to promote the electrocatalytic activity, selectivity and stability of the platinum, such as Ru, Pb, Sb, Rh, Mo, Os and Sn. A lot of research into platinum catalysts in DEFCs has come from previous research into DMFCs which has acted as a stepping stone for DEFC research as ethanol and methanol have similar qualities.

Many studies have investigated the effects of binary platinum-based catalysts on the EOR. Beyhan et al studied Pt/C and PtSn/C based catalysts for the oxidation of ethanol. He compared several different binary Pt-based and ternary PtSn-based catalysts. His findings concluded that the ternary catalysts PtSnCo/C and PtSnNi/C had a higher activity compared to PtSn/C, which is known to have the highest activity for a binary catalyst in acidic media[33], both ternary catalysts had lower onset potentials for ethanol electrooxidation and the peak current densities far exceeded that of PtSn/C. The addition of Ni or Co seems to promote C-C bond cleavage and helps remove adsorbed intermediates from the catalyst surface. It also improves the stability of the PtSn/C, which is known to be relatively weak. These results can be confirmed by testing in a DEFC, since PtSnCo/C and PtSnNi/C are known to have much higher performance and peak power density than Pt/C, PtSn/C and other tested ternary catalysts such as PtSnRh/C or PtSnPd/C[35].

A recent study examined the performance of a platinum-copper (PtCu/C) binary catalyst for ethanol oxidation in alkaline media. The report concluded that a PtCu/C catalyst had on average twice the current peak density and power density of a Pt/C catalyst. This rise in catalytic activity is due to the Cu promoting a higher availability of Pt active sites and the lower onset potential. Using single cell characterisation, the power density curves can be observed in 1M ethanol with PtCu/C was found to have a

maximum power density of 14.2 $mWcm^{-2}$ while Pt/C had a maximum of 7.1 $mWcm^{-2}$ as can be seen in Figure 1.9[36].

It is difficult to compare the performance of PtCu with other catalysts because no research has currently been done into comparing their performance under common conditions, even so these results prove promising for PtCu as a potentially useful catalyst in the future.

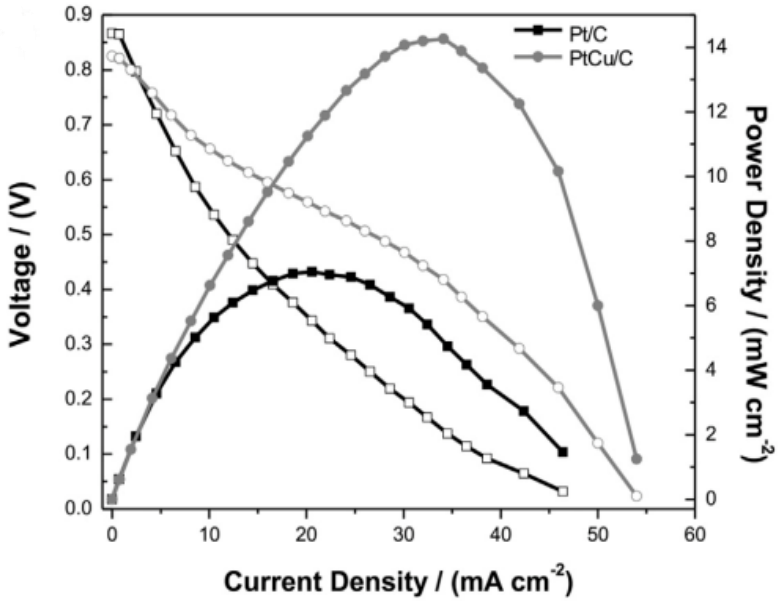

Figure 1.9 Polarization curves (filled points) and power density curves (hollow points) for the oxidation of ethanol on PtCu/C and Pt/C[36].

While platinum is a very good material for use as an anode catalyst with high performance relative to other monometallic catalysts and some very highly performing binary and ternary catalysts, it does have several drawbacks. The high price and limited availability of platinum is a big problem, if DEFCs were to become commercially viable with use in vehicles and such, the demand for platinum would far exceed the availability.

b. Palladium

Recent advances in alkaline direct alcohol fuel cells has allowed for the development of palladium, Pd, catalysts to become an alternative to the more commonly used platinum catalysts. Pt catalysts operate less effectively in alkaline than in acid. The use of palladium is favored over platinum because platinum is very expensive, rare, and platinum has a lower catalytic activity for ethanol oxidation in alkaline media. Palladium catalysts perform poorly in acid media the same as Pt struggles in alkaline fuel cells. Palladium studies are a relatively new topic therefore a lot of study has gone into looking at binary palladium catalysts while very few have currently looked into ternary catalysts.

Palladium suffers from similar drawbacks to platinum, such as being prone to carbon monoxide poisoning and loss of stability, reducing the long-term performance of the DEFC. This is due to the changes in morphology and size distribution of co-catalyst[37]. Palladium does have characteristics that make it a much more usable material though, because the difference in pH means a wider range metals are viable for use as a co-catalyst because a higher pH means a less corrosive environment[38], for example instead of using Ru which is an expensive metal but non-corrosive, Ni can be used which is much cheaper.

Just like Pt, research into binary and ternary Pd catalysts aim to identify characteristics that improve their activity, selectivity and stability as a catalyst for ethanol electro-oxidation. L. P. R. Moraes et al studied the performance of several Pd catalysts. Using cyclic voltammetry, his analysis showed a higher catalytic activity for the binary catalysts PdNi/C and PdSn/C, evidenced by the onset potential for ethanol oxidation when compared to Pd/C. PdNi/C and PdSn/C had a negative shift in the onset potential indicating a higher potential difference between the anode and the cathode, therefore a higher power output is achieved for the same current for these binary catalysts compared to Pd/C. For PdNi/C, the higher activity was due to hydrous oxide being present on the surface of the catalyst. Hydrous oxides are able to promote the

conversion of CO to CO_2 adsorbed on the surface of the metal[39], which releases the waste products, enabling the active site to stay active and perform further reactions and avoid poisoning. The higher performance of PdSn/C was due to the change in electronic structure of the Pd when alloyed with Sn, reducing the activation energy for the EOR. L. P. R. Moraes et al. also tested the power density of each binary catalyst in an ADEFC and found that the maximum power density achieved with PdNi/C was ~30 $mWcm^{-2}$, PdSn/C was ~16 $mWcm^{-2}$ and Pd/C was ~20 $mWcm^{-2}$ although the maximum power density very much depends on factors such as electrolyte membrane, fuel flow rate, fuel concentration and operating temperature[40].

Table 1.2 shows several different Pd-based binary and ternary catalysts supported by both non-vulcanised (C) and vulcanised carbon (C_F), PdNiSn/C is a very promising catalyst for the EOR. It has the most negative onset potential and the highest power density peak of all the palladium-based catalysts.

Table 1.2 The onset potential, current peak density, peak potential, specific resistance, open circuit voltage and maximum power density for the EOR on palladium-based catalysts[40].

CATALYST	E_{ONSET}(V)	I_{PEAK}(MA CM^{-2})	E_{PEAK}(V)	R(Ω CM^2)	OCV(MV)	P_{MAX}(MW CM^{-2})
PD/C	-0.45	6.54	-0.22	2.43	774	30.1
PD/C_F	-0.43	11.69	-0.20	2.24	779	38.4
PDSN/C	-0.39	7.12	-0.15	2.28	793	27.2
PDSN/C_F	-0.43	9.69	-0.17	1.81	751	28.6
PDNI/C	-0.41	0.96	-0.23	3.58	804	19.8
PDNI/C_F	-0.45	0.74	-0.22	2.16	774	19.4
PDNISN/C	-0.42	3.14	-0.21	2.99	807	27.1
PDNISN/C_F	-0.48	3.27	-0.27	1.88	858	38.8

One promising binary palladium-based catalysts in Niobium (Nb). There has been very promising research done on PdNb/C, showing that the current density peak for Pd_1Nb_1/C was 2.86 times that of Pd/C (45.5 $mAmg^{-1}$ and 15.9 $mAmg^{-1}$ respectively) using chronoamperometry[41]. Pd_1Nb_1/C also showed a more negative onset potential than Pd/C (-0.54 V and -0.5 V respectively). The niobium addition also showed reduced poisoning from carbon monoxide adsorption. The results suggested that Nb reduced poisoning "due to the bifunctional mechanism where Nb supplies oxygenated species to the poisoned sites on the Pd for CO oxidation". The next step would be to consider which ternary PdNb-based catalysts that could further improve the performance of alkaline direct ethanol fuel cells.

Gold nanoparticles (AuNP) have been studied recently due to their high activity as catalysts in several major industrial reactions[42]. AuNP have been found to be active in strong alkaline media and good at promoting the desorption of CO species, reducing poisoning on the catalyst. A recent study showed that PdAu was able to reach peak power density of 44 $mWcm^{-2}$ at 85 °C whereas Pd only produced peak power density of 25 $mWcm^{-2}$ at the same temperature[43] also confirmed by a study done in 2017 shown in Figure 1.10[44]. Another study found that PdNiAu/C catalyst had a peak power density three times larger than Pd/C[45].

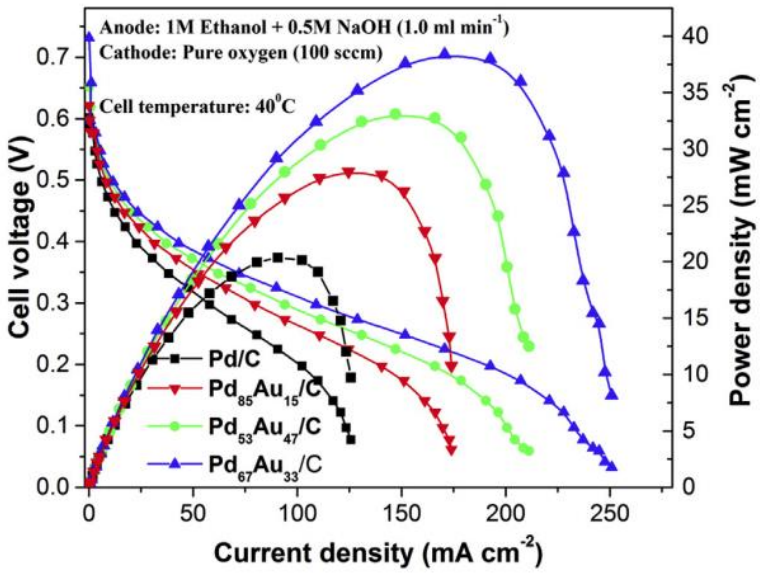

Figure 1.10 Polarisation curves and power density curves for PdAu/C catalysts of different composition[s][44].

Very recently, the use of silver as a co-catalyst in ethanol oxidation was studied. AgPd was deposited onto polyaniline/glassy carbon electrode (PANI/GCE) then compared to Pd/PANI/GCE, Pd/GCE, Ag/PANI/GCE and PANI/GCE to test its performance for EOR in alkaline media. The AgPd was then deposited on carbon filter cloth (CC) to test its performance in a DEFC. Figure 1.11 shows the results comparing AgPd deposited on PANI/GCE, it clearly shows AgPd on both GCE and PANI/GCE higher a higher current density than base Pd catalyst and a more negative onset potential, therefore making it a more effective catalyst for EOR.

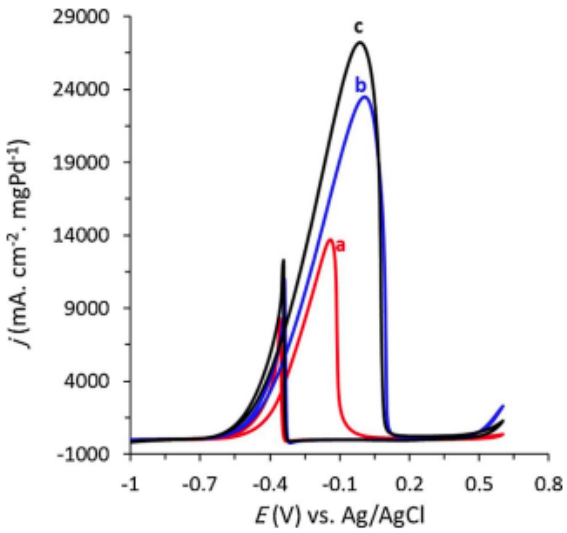

Figure 1.11 EOR in 1 M EtOH + 0.5 M NaOH on Pd/GCE (a), AgPd/GCE (b) and AgPd/PANI/GCE (c) Scan rate: 50 mVs^{-1}.

Figure 1.12 shows the results from AgPd being tested on CC for its effectiveness in a DEFC. It clearly shows the synergy of using Ag and PANI with a base Pd catalyst, with AgPd/PANI/CC having double the current density of base Pd catalyst. "Therefore, according to simplicity, easy and fast preparation of the proposed electrode can offer an idea method for the preparation of promising electrode for EOR in ethanol fuel cell."[46]

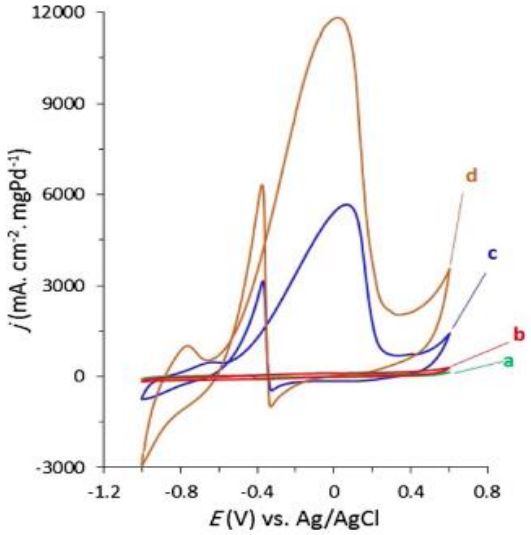

Figure 1.12 EOR CV in 1 M EtOH + 0.5 M NaOH on Pd/CC (a), AgPd/CC (b) and Pd/PANI/CC (c) and AgPd/PANI/CC (d) Scan rate: 50 mVs^{-1}.

c. Platinum vs Palladium

Platinum and palladium are both very effective catalysts for ethanol electro-oxidation. Palladium performs extremely poorly in acidic media while platinum has fairly low performance in alkaline media. Ma et al. compared the electro-oxidation of ethanol on Pt/C and Pd/C based catalysts in an alkaline media, varying the ethanol concentration, the alkaline concentration and the temperature. When comparing only the base catalysts, Pd/C showed higher activity compared to Pt/C for partial ethanol electro-oxidation, due to "the higher oxyphilic characteristics of the Pd/C and the relatively inert nature of the Pd/C on C–C bond cleavage". Tafel slopes were used to analyse both catalysts, the Tafel slope determines how much the overpotential needs to be raised to increase the rate of reaction by a factor of ten. Comparing Tafel slopes for both catalysts, the graphs can be split into two parts; at low overpotentials, both catalysts achieved 120 mV at all tested temperatures. At higher overpotentials, Pd/C was approximately 260mV on the Tafel slope whereas Pt/C was much higher, especially at higher temperatures. This experiment demonstrated that Pd/C has a much higher

activity for ethanol to acetate and has a higher resistance to poisoning than Pt/C. This shows that Pd is a suitable replacement for the more traditional Pt catalyst, with its greater performance in an alkaline medium[47].

d. Other viable catalysts

Few other metal catalysts compare to either platinum or palladium, very little research has been put into alternatives currently because of their low comparative performance. Chai et al. proposed an alternative that was platinum free, attempting to reduce the cost of the catalyst and drive down the price of fuel cells. He studied Ir_3Sn-CeO_2/C heterogeneous catalyst in acidic conditions for the EOR. As shown in Table 1.3, Ir_3Sn-CeO_2/C displayed higher catalytic activity and stability than commercial Pt/C, Ir/C and $IrSn_3$/C and while it doesn't compare to some of the more highly performing Pt-based binary and ternary catalysts, it still proves it to be a strong Pt free alternative[48].

Table 1.3 Comparison of electrocatalytic properties of Pt and Ir based catalysts with peak potential (E_P) and peak current (I_P)[48].

ELECTROCATALYST	ALCOHOL SOLUTION	E_P/V	I_P/MA MG^{-1}
IR_3SN-CEO_2/C	0.5 M H2SO4/0.5 M Ethanol	0.28(vs. Ag/AgCl)	24.65
IR_3SN/C	0.5 M H2SO4/0.5 M Ethanol	0.28(vs. Ag/AgCl)	16.49
IR/C	0.5 M H2SO4/0.5 M Ethanol	0.28(vs. Ag/AgCl)	11.22
PT/C	0.5 M H2SO4/0.5 M Ethanol	0.2(vs. Ag/AgCl)	18.5
$IR_{77}RU_{23}$/C	0.5 M H2SO4/0.5 M Ethanol	0.2(vs. Ag/AgCl)	72.0
$IR_{91}RU_9$/C	0.5 M H2SO4/0.5 M Ethanol	0.2(vs. Ag/AgCl)	31.7
$IR_{71}RU_{29}$/C	0.5 M H2SO4/0.5 M Ethanol	0.07(vs. Ag/AgCl)	130
PTSN-CEO_2/C	0.5 M H2SO4/0.5 M Ethanol	0.92(vs. RHE)	0.57(A mg^{-1})
PTSN/C	0.5 M H2SO4/0.5 M Ethanol	0.9(vs. RHE)	0.32(A mg^{-1})

1.5.2 Cathode catalyst material

Whilst the anode is primarily responsible for the EOR, the cathode is responsible for the oxygen reduction reaction (ORR). This is just as important as the EOR, if an anode with strong activity is paired with a cathode that reduces oxygen slowly, then it will reduce the performance of the fuel cell. As with the anode, the most popular catalysts are platinum for acid media and palladium for alkaline media. The selection of these metals is mainly due to their effectiveness in DMFCs, having high activity and good stability for the ORR and a lack of research into cathodes in a DEFC, even so, studies have shown Pt and Pd both exhibit average performance as a cathode catalyst[49-50].

Similar results have been seen when Sn and Ni were added to Pt. Beyhan et al. observed the activity of Pt-based catalysts and found that PtNi/C and PtSnNi/C had higher performance than the base catalyst. PtSn/C had a higher performance than both PtNi/C and PtSnNi/C, due to the optimal Sn oxides as an unalloyed state in PtSn/C[51].

PtNi/C however was found to have a lower performance than Pt/C for the ORR.

The study also showed that PtSn/C had a higher oxygen reactivity than the other tested catalysts, making it easier for the O-O bond to be broken.

a. Platinum

Pt has shown only average performance as a cathode for ORR. Similarly, to the EOR, adding co-catalysts can help increase the catalysts performance. Alloying Pd to Pt enhances the oxygen reduction abilities of the catalyst. In ethanol, PtPd was found to have a larger overpotential compared to base Pt catalyst and showing a higher resilience to ethanol crossover. The addition of the palladium was found to decrease the affinity for OH^- and CO species while increasing affinity for O_2 species[52]. It was also found that cobalt (Co) was able to promote the oxygen reduction performance of a Pt catalyst, although it did not display an increase in ethanol tolerance.

b. Palladium

Palladium has good activity and chemical stability for use as the cathode catalyst, which is why Pd-based electrocatalysts are a popular option for the ORR in acid based DEFCs. The most widely researched binary palladium-based catalysts are PdCo, PdTi, PdCu and PdNi and the most widely researched ternary palladium-based catalysts are PdCoAu, PdCoMo, PdCoCe and PdCoNi. Although new research has shown that Pt coated Pd catalysts (Pt-Pd/C) with coverages of Pt being almost monolayer have a high activity towards ORR. These results have huge implications towards how catalyst surfaces are designed and nano-engineered for oxygen reduction[53].

c. Platinum vs Palladium

Both metals perform well as base catalysts for the ORR. Styven Lankiang et al. studied the performance of Pt, Pd and Au (gold) based binary and ternary catalysts in O_2 saturated 0.1 M $HClO_4$. The palladium led to a decrease in ORR activity each time the ratio of PdPt was increased, although when gold was added to platinum the activity increased for ratios of up to 1:1. He concluded that catalysts based on Pd and Au were had lower activity towards ORR than Pt did in acid medium, because of the performance of the base catalysts in acid environments; Pt/C had a higher activity than both Pd/C and Au/C. Using data obtained from binary catalyst tests. It was determined that ternary catalysts $Pt_{70}Pd_{15}Au_{15}$/C and $Pt_{50}Pd_{25}Au_{25}$/C showed higher catalytic activity for the ORR and both had a higher stability than the base catalysts. The main cause of degradation of the catalyst was aggregation of particles on the surface, therefore hampering its performance. It was shown however that the Au segregated from the bulk to the nanoparticle surface during the aging test, which is good for stability but reduces the catalyst activity[54].

d. Other viable catalysts

An article recently studied the oxygen reduction capacity of a non-noble metal catalyst Fe-N-C. Its behavior was tested in alkaline conditions using cyclic voltammetry and rotating disk electrode, looking at its reduction capability, selectivity and activity towards hydrogen peroxide. In the single cell DEFC test, after optimisation of the catalyst ink, the peak power density recorded was 62 $mWcm^{-2}$ at low and mid-range currents[55], comparing to some of the most prominent non-noble metal catalysts. The results showed Fe-N-C is highly tolerant to ethanol, stable and has good selectivity for direct oxygen reduction to OH^- with $4e^-$. However, at high current densities, the DEFC test produced results showing steep decay occurring on the catalyst, seriously affecting the catalyst stability. Osmieri said this was due to “instability of the membrane

conductivity, the MEA fabrication procedure (absence of hot-pressing, poor compatibility between the membrane and the ionomer used for the catalyst ink preparation), mass transport issues (flooding of catalyst layer), and Ru electro-dissolution/ crossover." Figure 1.13 shows the reduction in both polarisation and power density during the short-term durability test performed in an alkaline DEFC. The performance of the catalyst did improve after a purge drying, although not as greatly as other non-noble metal catalysts, attributed to, but not exclusively, the irreversible deactivation of the Fe-N-C catalyst. Zhang et al. reported similar findings in his paper 'Highly active and stable non-noble metal catalyst for oxygen reduction reaction' in which he studied the performance of Fe_4N in alkaline solution and found that the highest performing catalyst showed similar onset potential to Pt/C in alkaline conditions[56].

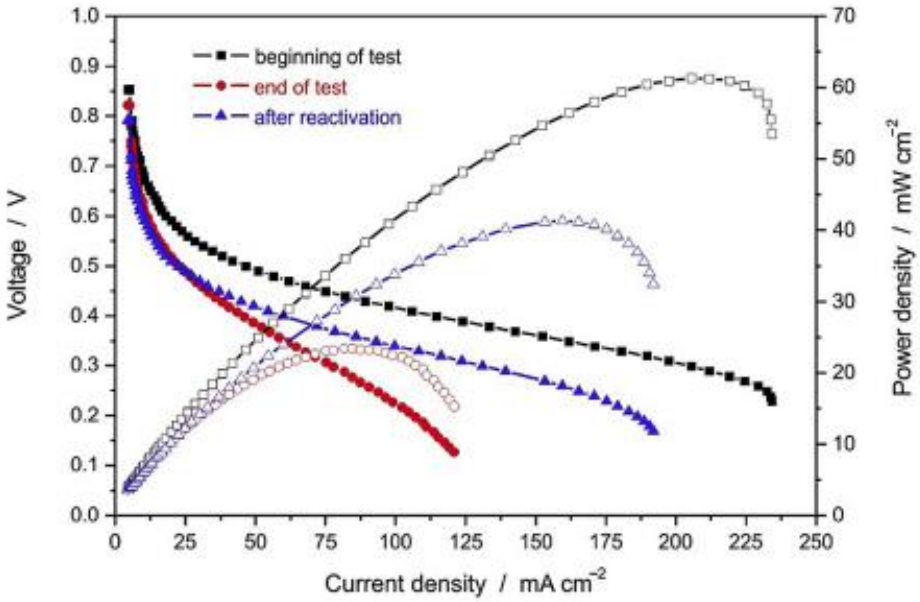

Figure 1.13 Polarisation (filled out points) and power density curves (hollow points) Short-term durability test in alkaline DEFC for Fe-N-C[55].

1.5.3 Challenges in catalyst development and the aim of the research

Platinum is currently the most common catalyst for ethanol oxidation, however this is an expensive and rare metal, and is therefore difficult to use in large scale fuel cell production. The aim is to develop a catalyst that operates with the performance of platinum but at a much lower cost. There are several promising candidates such as palladium and palladium-based catalysts, but they still need optimizing before they can be used commercially.

The most difficult part of ethanol oxidation is the cleavage of the C-C bond in the ethanol. If this bond is not broken, partial oxidation will occur, leading to the formation of acetic acid and aldehyde instead of carbon dioxide and water and fewer electrons being transferred. This is a major contributor to low performance in DEFCs and reduces the amount of energy that can be generated.

Catalysts in a DEFC are currently have fairly low stability and are very susceptible to poisoning of intermediates such as CO and other products of partial oxidation. These products can also cause the degradation of the catalyst. Therefore, to increase the longevity and the potential for commercial use, current catalysts must be developed to withstand such poisoning and degradation.

The aim of this thesis work is to develop cost-effective non-Pt catalysts for the direct ethanol fuel cell operating in alkaline media. A series of Pd-based catalysts are to be developed and tested for ethanol electrooxidation under various conditions that a practical fuel cell operates. The kinetic of ethanol oxidation over the improved catalysts so developed will be studied and compared to the bare Pd catalyst to understand the fundamental of reactivity improvement.

1.6 Reference

1. A. Brouzgou, F. Tzorbatzoglou, P. Tsiakaras, ***Direct Alcohol Fuel Cells: Challenges and Future Trends***, Energetics(IYCE), Proceedings of the 2011 3rd International Youth Conference on, 2011.

2. U. Bossel, ***The birth of the Fuel Cell***, 2000.

3. F. Vigier, S. Rousseau, C. Coutanceau, J. M. Leger, C. Lamy, ***Electrocatalysis for the Direct Alcohol Fuel Cell***, Top. Catal., 2006, 40, 111-121.

4. A. E. Lutz, R. S. Larson, J. O. Keller, ***Thermodynamic Comparison of Fuel Cells to the Carnot Cycle***, Int. J. Hydrog. Energy, 2002, 27, 1103-1111.

5. L. Carrette, K.A. Friedrich, U. Stimming, ***Fuel cells–Fundamentals and Applications***, Fuel Cells, 2001, 1, 5-3

6. M. Winter, R. J. Brodd, ***What Are Batteries, Fuel Cells, and Supercapacitors?*** Chem. Rev., 2004, 104, 4245-4270.

7. X. G. Li, ***Principles of Fuel Cells***, 2006.

8. B. C. H. Steele, A. Heinzel, ***Materials for Fuel-Cell Technologies***, Nature, 2001, 414, 345-352.

9. R. O'hayre, S. Cha, W. Colella and F. Prinz, ***Fuel Cell Fundamentals***, 2nd Edition, 2008.

10. K. Kordesch, V. Hacker, J. Gsellmann, M. Cifrain, G. Faleschini, P. Enzinger, R. Fankhauser, M. Ortner, M. Muhr, R. R. Aronson, ***Alkaline Fuel Cells Applications***, J. Power Source, 2000, 86, 162-165.

11. K. Matsuoka, Y. Iriyama, T. Abe, M. Matsuoka, Z. Ogumi, ***Electro-Oxidation of Methanol and Ethylene Glycol on Platinum in Alkaline Solution: Poisoning Effects***

and Product Analysis, Electrochimica Acta, 2005, 51, 1085-1090.

12. G. F. McLean, T. Niet, S. Prince-Richard, N. Djilali, ***An Assessment of Alkaline Fuel Cell Technology***, Int. J. Hydrog. Energy, 2002, 27, 507-526.

13. R. Dillon, S. Srinivasan, A. S. Arico, V. Antonucci, ***International Activities in DMFC R&D: Status of Technologies and Potential Applications***, J. Power Sources, 2004, 127, 112-126.

14. S. Wasmus, A. Kuver, ***Methanol Oxidation and Direct Methanol Fuel Cells: A Selective Review***, J. Electroanal. Chem., 1999, 461, 14-31.

15. E. Antolini, ***Catalysts for Direct Ethanol Fuel Cells***, J. Power Sources, 20007, 170, 1-12.

16. P. Kumar, K. Dutta, S. D. P. P. Kundu, ***An Overview of Unsolved Deficiencies of Direct Methanol Fuel Cell Technology: Factors and Parameters Affecting its Widespread Use***, Int. J. Energy Res., 2014, 38, 1367–1390.

17. Z. M. Wan, H. W. Chang, S. M. Shu, Y. X. Wang, H. L.n Tang, ***A Review on Cold Start of Proton Exchange Membrane Fuel Cells***, Energies, 2014, 7, 3179-3203.

18. R. Taherian, A ***Review of Composite and Metallic Bipolar Plates in Proton Exchange Membrane Fuel Cell: Materials, Fabrication, and Material Selection***, J. Power Sources, 2014, 265, 370-390.

19. Y. Wang, K. S. Chen, J. Mishler, S. C. Cho, X. C. Adroher, ***A Review of Polymer Electrolyte Membrane Fuel Cells: Technology, Applications, and Needs on Fundamental Research***, Appl. Energy, 2011, 88, 981-1007.

20. Th. Brenscheidt, K. Janowitz, H. J. Salge, H. Wendt, F. Brammer, ***Performance of ONSI PC25 PAFC Cogeneration Plant***, Int. J. Hydrogen Energy, 1998, 23, 53-56.

21. N. Sammes, R. Bove, K. Stahl, ***Phosphoric Acid Fuel Cells: Fundamentals and Applications***, Curr. Opin. Solid State Mater. Sci., 2004, 8, 372-378.

22. S. R. Narayanan, T. I. Valdez and W. Chun, ***Design and Operation of an Electrochemical Methanol Concentration Sensor for Direct Methanol Fuel Cell Systems***, Electrochem. Solid-State Lett., 2000, 3, 117-120.

23. W. Z. Zhu, S. C. Deevi, ***Development of Interconnect Materials for Solid Oxide Fuel Cells***, Mater. Sci. Eng., A, 348, 227-243.

24. T. Hibinoa, H. Tsunekawa, S. Tanimoto, Mi. Sano, ***Improvement of a Single-Chamber Solid-Oxide Fuel Cell and Evaluation of New Cell Designs***, J. Electrochem. Soc., 2000, 147, 1338-1343.

25. J. Patakangas, Y. Ma, Y. F. Jing, P. Lund, ***Review and Analysis of Characterization Methods and Ionic Conductivities for Low-Temperature Solid Oxide Fuel Cells (LT-SOFC)***, J. Power Sources, 2014, 263, 315-331.

26. S. Shamim, K. Sudhakar, B. Choudhary, J. Anwar, ***A Review on Recent Advances in Proton Exchange Membrane Fuel Cells: Materials, Technology and Applications***, Adv. Appl. Si. Res.,, 2015, 6, 89-100.

27. A. Liang, T. Zhao, ***An Alkaline Direct Ethanol Fuel Cell with a Cation Exchange Membrane***, Energy Environ. Sci., 2011, 4, 2213-2217.

28. T. S. Zhao, Y. S. Li, S. Y. Shen, ***Anion-exchange Membrane Direct Ethanol Fuel Cells: Status and Perspective***, Energy Power Eng. China, 2010, 4, 443–458.

29. B. R. Cuenya, ***Synthesis and Catalytic Properties of Metal Nanoparticles: Size, Dhape, Dupport, Composition, and Oxidation State Effects***, Thin Solid Films, 2010, 518, 3127-3150.

30. Y. Feng, D. Bin, B. Yan, Y. k. Du, T. Majima, We. Q. Zhou, ***Porous Bimetallic***

PdNi Catalyst with High Electrocatalytic Activity for Ethanol Electrooxidation, J. Colloid Interface Sci., 2017, 493, 190-197.

31. J. Hagen, ***Industrial Catalysis: A Practical Approach***, 2nd Edition, 2006, 1-13.

32. T. F. Hou, S. Y. Zhang, Y. D. Chen, D. Z. Wang, W. J. Cai, ***Hydrogen Production from Ethanol Reforming: Catalysts and Reaction Mechanism***, Renew. Sust. Energy Rev., 2015, 44, 132-148.

33. J. M. Jin, T. Sheng, X. Lin, R. Kavanagh, P. Hamer, P. J. Hu, C. Hardacre, A, M. Bonastre, J. Sharman, D. Thompsett, W. F. Lin, ***The origin of High Activity but Low CO_2 Selectivity on Binary PtSn in the Direct Ehanol Fuel Cell***, Phys. Chem. Chem. Phys., 2014,16, 9432-9440.

34. R. Kavanagh, X. M. Cao, W. F. Lin, C. Hardacre, P. J. Hu, ***Origin of Low CO_2 Selectivity on Platinum in the Direct Ethanol Fuel Cell***, Angew. Chem. Int. Ed. Engl., 2012, 51, 1572–1575.

35. S. Beyhan, C. Coutanceau, J. M. Leger, T. W. Napporn, F. Kadirgan, ***Promising Anode Candidates for Direct Ethanol Fuel Cell: Carbon Supported PtSn-based Trimetallic Catalysts Prepared by Bönnemann Method***, Int. J. Hydrogen Energy, 2013, 38, 6830-6841.

36. J. Maya-Cornejo, R. Carrera-Cerritos, D. Sebastián, V. Baglio, ***PtCu Catalyst for the Electro-Oxidation of Ethanol in an Alkaline Direct Alcohol Fuel Cell***, Int. J. Hydrogen Energy, 2017, 42, 27919-27928.

37. R. C. Cerritos, M. Guerra-Balcázar, R. F. Ramírez, J. Ledesma-García, L. G. Arriaga, ***Morphological Effect of Pd Catalyst on Ethanol Electro-Oxidation Reaction***, Materials, 2012, 5, 1689-1697.

38. Y. S. Li, T. S. Zhao, ***A High-Performance Integrated Electrode for Anion-Exchange Membrane Direct Ethanol Fuel Cells***, Int. J. Hydrogen Energy, 2011, 36,

7707-7713.

39. M. J. Lee, J. S. Kang, Y. S. Kang, D. Y. Chung, H. J. Shin, C. Y. Ahn, S. B. Park, M. J. Kim, S. J. Kim, K. S. Lee, Y. E. Sung, ***Understanding the Bifunctional Effect for Removal of CO Poisoning: Blend of a Platinum Nanocatalyst and Hydrous Ruthenium Oxide as a Model System***, ACS Catal., 2016, 6, 2398-2407.

40. L. P. R. Moraes, B. R. Matos, C. Radtke, E. I. Santiago, F. C. Fonseca, S. C. Amico, C. F. Malfatti, ***Synthesis and Performance of Palladium-Based Electrocatalysts in Alkaline Direct Ethanol Fuel Cell***, Int. J. Hydrogen Energy, 2015, 41, 6457-6468.

41. F. M. Souza, L. S. Parreira, P. Hammer, B. L. Batista, M. C. Santos, ***Niobium: A Promising Pd Co-Electrocatalyst for Ethanol Electrooxidation Reactions***, J. Solid State Electrochem., 2018, 22, 1495-1506.

42. R. Ciriminna, E. Falletta, C. D. Pina, J. H. Teles, M. Pagliaro, ***Industrial Applications of Gold Catalysis***, Angew. Chem. Int. Ed., 2016, 55, 14210–14217.

43. A. N. Geraldes, et al., ***Ethanol Electro-Oxidation in an Alkaline Medium Using Pd/C, Au/C and PdAu/C Electrocatalysts Prepared by Electron Beam Irradiation***, Electrochim. Acta, 2013, 111, 455-465.

44. A. Dutta, A. Mondal, P. Broekmann, J. Datta, ***Optimal level of Au nanoparticles on Pd nanostructures providing remarkable electro-catalysis in direct ethanol fuel cell***, J. Power Sources, 2017, 361, 276-284.

45. A. Dutta, D. Jayati, ***Outstanding Catalyst Performance of PdAuNi Nanoparticles for the Anodic Reaction in an Alkaline Direct Ethanol (with Anion-Exchange Membrane) Fuel Cell***, J. Phys. Chem., 2012, 116, 25677–25688.

46. Z. Nodehia, A. A. Rafatia, A. Ghaffarinejad, ***Palladium-Silver Polyaniline Composite as an Efficient Catalyst for Ethanol Oxidation***, Appl. Catal., A, 2018, 554, 24-34.

47. L. Ma, D. Chub, R. Chen, ***Comparison of Ethanol Electro-Oxidation on Pt/C and Pd/C Catalysts in Alkaline Media***, Int. J. Hydrogen Energy, 2012, 37, 11185-11194.

48. D. Chai, et al., ***Heterogeneous Ir_3Sn CeO_2/C as Alternative Pt-free Electrocatalysts for Ethanol Oxidation in Acidic Media***, Int. J. Hydrogen Energy, 2017, 42, 9775-9783.

49. A. M. Gómez–Marína, E. A. Ticianelli, ***A Reviewed Vision of the Oxygen Reduction Reaction Mechanism on Pt-based Catalysts***, Current Opinion in Electrochemistry, 2018, 9, 139-136.

50. H. Erikson, A. Sarapuu, J. Solla-Gullón, K. Tammeveski, ***Recent Progress in Oxygen Reduction Electrocatalysis on Pd-based Catalysts***, J. Electroanal. Chem., 2016, 780, 327-336.

51. S. Beyhan, N. E. Şahin, S. Pronier, J. M. Léger, F. Kadırgan, ***Comparison of Oxygen Reduction Reaction on Pt/C, Pt-Sn/C, Pt-Ni/C, and Pt-Sn-Ni/C Catalysts Prepared by Bönnemann Method: A Rotating Ring Disk Electrode Study***, Electrochim. Acta, 2015, 151, 565–573.

52. T. Lopes, E. Antolini, E. R. Gonzalez, ***Carbon Supported Pt–Pd Alloy as an Ethanol Tolerant Oxygen Reduction Electrocatalyst for Direct Ethanol Fuel Cells***, Int. J. Hydrogen Energy, 2008, 33, 5563–5570.

53. M. Y. Liao, W. P. Li, X. P. Xi, C. L. Luo, Y. X. Fu, S. L. Gui, Z. H. Mai, H. Yan, C. Jiang, ***Highly Active Pt Decorated Pd/C Nanocatalysts for Oxygen Reduction Reaction***, Int. J. Hydrogen Energy, 2017, 42, 24090-24098.

54. S. Lankiang, M. Chiwata, S. Baranton, H. Uchida, C. Coutanceau, ***Oxygen Reduction Reaction at Binary and Ternary Nanocatalysts Based on Pt, Pd and Au***, Electrochim. Acta, 2015, 182, 131-142.

55. L. Osmieri, R. Escudero-Cid, A. H. A. Monteverde Videla, P. Ocón, S. Specchia, ***Application of a Non-Noble Fe-N-C Catalyst for Oxygen Reduction Reaction in an Alkaline Direct Ethanol Fuel Cell***, Renewable Energy, 2018, 115, 226-237.

56. B. Zhang, et al., ***Highly Active and Stable Non Noble Metal Catalyst for Oxygen Reduction Reaction***, Int. J. Hydrogen Energy, 2017, 42, 10423-10434.

Chapter Two

Equipment and Experimental Techniques

This chapter describes the equipment and techniques used in this study. The procedure details and the electrocatalyst characterization results will be presented in following chapters.

2.1 Electrochemistry system

2.1.1 Water jacketed variable temperature three-electrode cell system

(a).

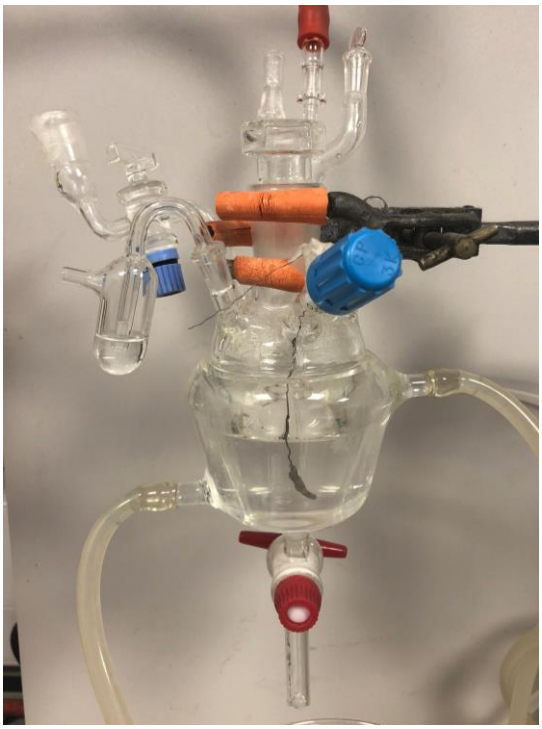

(b).

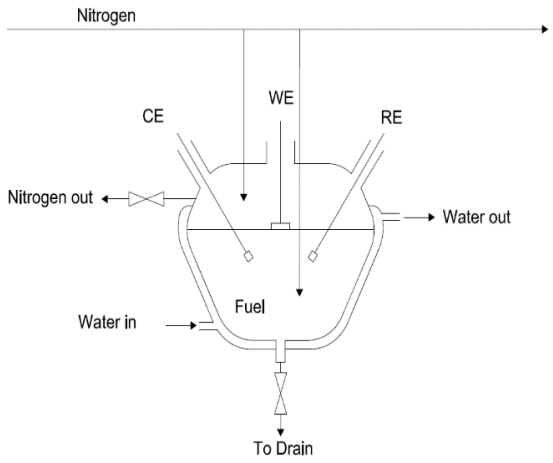

Figure 2.1. (a). Three-electrode cell in this research, (b). Three-electrode cell diagram

As displayed in Figure 2.1.a is one of the in-house designed three-electrode electrochemical cells with variable temperature water jacketed which was employed in the whole experiment. The entire system was constructed 3 sites, Site A was used for electrochemical deposition, Site B for acid test, and Site C for alcohol electrooxidation reactions.

As shown in Figure 2.1.b, the cell consists mainly of an inner and cover glass jacket compartment with several connections available for three electrodes, gas and circulating water. The working electrode (WE) is located in the middle of the cell. The counter electrode (CE) is a piece of Pt mesh. The reference electrode (RE) is housed in the salt bridge compartment of the cell maintaining a stable and fixed potential for the working electrode which allows the reference electrode to maintain a constant reference potential by remaining at room temperature even when the rest of the cell is heated at high temperature. An Ag/AgCl in H_2SO_4 (0.1M) was used as the reference electrode for acidic media and a Hg/HgO (in 1 M NaOH) reference electrode

for alkaline media. The system was deoxygenated via two nitrogen inlets, one over the surface of the electrolyte solution and one bubbled through the electrolyte solution beneath the surface and discharged into atmosphere through a valve. The cell was jacketed to allow regulate temperature by the external temperature controlled water bath (Grant GD 120 thermostatic water bath).

All the cells need to be cleaned regularly. Initially, cells were rinsed well with a solution of $K_2Cr_2O_7$ + 97% H_2SO_4 for 15 min and immersed in cleaning agent for 24 h then rinsed with distilled water 5 times to complete the deep clean. The whole cell was raised by ultrapure water each time before electrochemical experiments and cleaned by boiled water every other week.

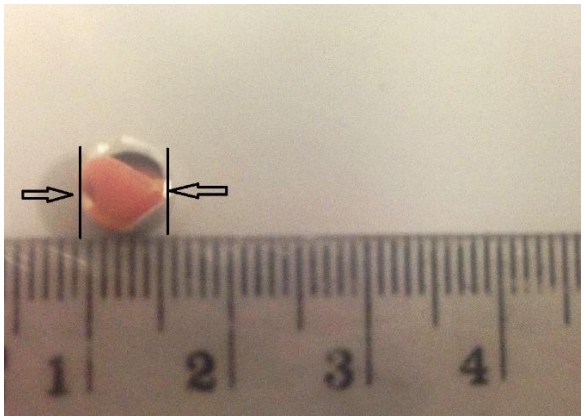

Figure 2.2 bulk Pd working electrode used in the research.

Shown in Figure 2.2.a is the working electrode used in the experiment. This 6.5 mm-diameter, 5mm-thick bulk Pd is connected by titanium wire and wrapped around by PTFE tape and parafilm to ensure that only the surface is contacted with the electrolyte solution during electrooxidation experiments in the three-electrode cell.

For the accuracy of experiments, the bulk Pd electrode was mechanically polished to a mirror-finish by using a range of alumina oxide powders of three different particle sizes

in sequence, e.g. 1, 0.3 and 0.05 μm, then rinsed thoroughly with ultrapure water and followed up with ultrasonic washing in ultrapure water for several times. Further polish was performed by cyclic voltammetry (CV) in 0.1 M sulfuric acid, with a scan rate of 50 mV/s, a potential step of 0.00244 V and a potential range from 0.15 V to 1.35 V (vs. RHE).

(a)

(b)

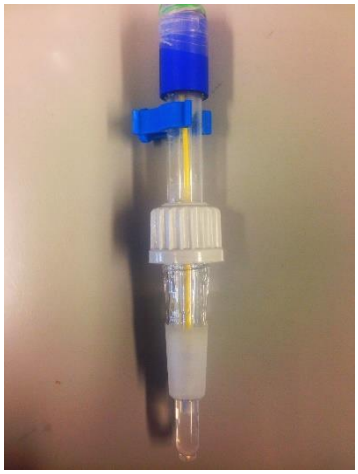

Figure 2.3 Reference electrodes (RE) used in the research, (a). Ag/AgCl electrode, (b). Hg/HgO electrode.

Ag/AgCl reference electrode shown in Figure 2.3.a is to support a stable potential as a standard for all other electrodes reaction in acid electrolyte. The electrode reaction is shown as:

$$AgCl(s) + e^- \rightarrow Ag(s) + Cl^- \qquad (1)$$

The electrode potential is related with the concentration of chloridion, thus RE is infused in saturated KCl to make it more advantageous.

Figure 2.3.b shows the Hg/HgO reference electrode which is used in alkaline media in this whole research. The electrode is kept in 1 M NaOH and the reaction is shown as:

$$HgO + H_2O + 2e^- \rightarrow Hg + 2OH^- \qquad (2)$$

In order to further compare data obtained from experiments, all voltages reference to Ag/AgCl and Hg/HgO were transferred to voltage reference to RHE using equation 3 and equation 4:

$$E(\text{vs. RHE}) = E(\text{vs. Ag/AgCl}) + 0.210V + 0.059V \times PH \qquad (3)$$

$$E(\text{vs. RHE}) = E(\text{vs. Hg/HgO}) + 0.140V + 0.059V \times PH \qquad (4)$$

Figure 2.4 Platinum counter electrode used in the research.

The counter electrode used in the research is a piece of Pt mesh connect by Pt wire displayed by Figure 2.4. In the three-electrode system, the counter electrode (CE) is involved to ascertain potential drop within the work electrode (WE) and reference electrode (RE) and also provides current if WE needs.

2.1.2 Potentiostat and function generator

Figure 2.6 Potentiostat in conjunction with a functional

The potentiostat is an electronic instrument required to control the voltage difference between the working and reference electrode in a three-electrode cell. It consists of an electric circuit which ensures that current only flows between the working electrode (WE) and counter electrode (CE) and control the potential of the working electrode (WE) relatively to the stable reference electrode (RE) where a constant fixed potential is applied.

The potentiostat (Metrohm Autolab PGSTA302N) in Figure 2.6 was employed in the electrochemical measurements. The maximum current is ± 2 A with a compliance voltage of ± 30 V and a bandwidth of 1 MHz. Autolab NOVA 1.8 software was used to record and analyze the output data[1].

2.1.3 Cyclic voltammetry[2-3]

Cyclic voltammetry (CV) is the most widely used potentiodynamic electrochemical measurement which worked by cycling the potential of a working electrode with a triangular potential waveform and measuring the current resulting from electrochemical reactions. Information on both the oxidation and reduction processed can be provided by cyclic voltammograms[4].

The potential of a working electrode is measured against the reference electrode which keeps a constant potential value. The potential of working electrode rises from a starting value E_1 to a final value E_2 then returns back to the starting potential at a constant potential sweep tare. The sweep rate applied can vary from a few millivolts to a hundred volts per second.

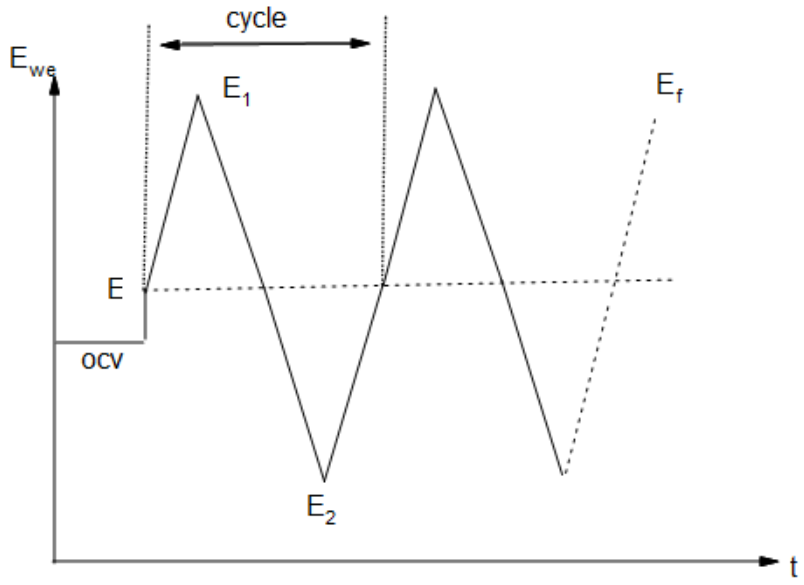

Figure 2.7 Cyclic voltammetry (CV) waveform

In a reversible system, the electron transfer is faster and other processes like diffusion can be ignored, thus the peak separation can be described as the Nernst equation:

$$\Delta E_p = \left|E_{pa} - E_{pc}\right| = 2.303\frac{RT}{nF} \qquad (3)$$

Where E_{pc} is cathodic peak potential (V), E_{pa} is anodic peak potential (V) and n is the number of electrons participating in the redox reaction.

Theoretically, for a reversible redox reaction at 25 °C with *n* electrons, ΔE_p is considered as 0.0592/*n*V. However, the value is difficult to attain because of such factors as cell resistance which lead to a slow electron transfer rate of $\Delta Ep > 0.0592/n$ V.

According to the Randles-Sevcik expression, the concentration is related to the peak and can be calculated at 25 ℃ using following equation:

$$i_p = 2.69 \times 10^5 n^{\frac{3}{2}} AcD^{\frac{1}{2}} v^{\frac{1}{2}} \qquad (4)$$

Where i_p is peak current (A), n is equal to the number of electrons gained in the reduction, D is diffusion coefficient ($cm^2\ s^{-1}$), v is the scan rate ($V\ s^{-1}$), A is the surface area of the working electrode (cm^2) and c is the concentration ($mol\ cm^{-3}$).

2.1.4 Chronoamperometry

Chronoamperometry is a typical electrochemical technique for the quantitative analysis of nucleation processes and stability performance by stepping the potential of the working electrode from an initial potential (no faradic reaction occurs) to a potential Ei (faradic reaction occurs) and measuring the resulting current[4].

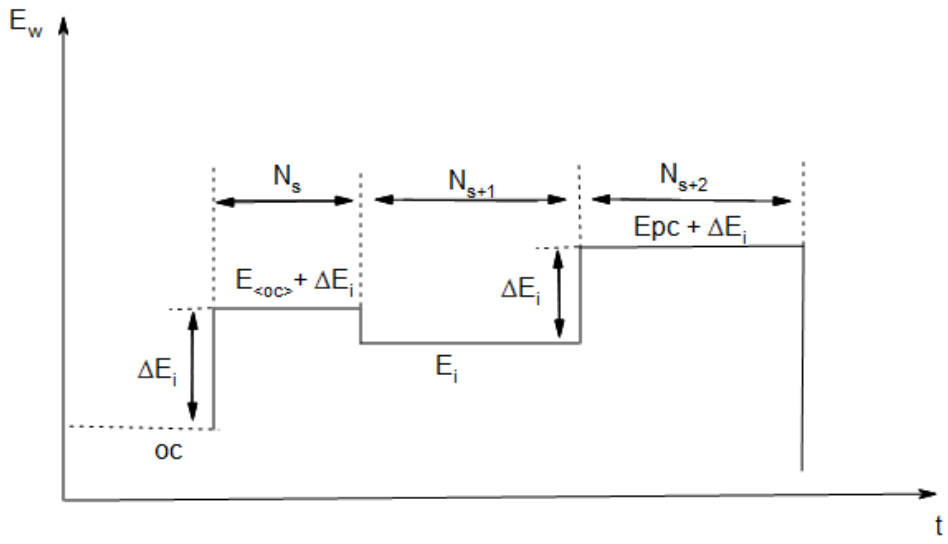

Figure 2.8 Stepping potential of chronoamperometry (CA)

For a planer electrode, according to the Cottrell equation[5], the relationship between the current i and time is given by:

$$i = \frac{nFAD^{\frac{1}{2}}C}{\pi^{\frac{1}{2}}t^{\frac{1}{2}}} \qquad (5)$$

Where n equals to the number of electrons transferred in the reaction, F is Faraday's constant, A is the electrode area(cm^2), D is the diffusion coefficient for electroactive species(cm^2/s) and C is concentration of electroactive species(mol/cm^3).

2.2 Reference

1. ***Instruments for Electrochemical Research Metrohm Autolab Application Notes***, 2012.

2. S. P. Kounaves, ***Voltammetric Techniques***.

3. A. J. Bard, L. R. Faulkner, ***Electrochemical Methods: Fundamentals and Applications***, 2nd ed., 2001.

4. R. O'Hayre, S. W. Cha, W. Colella, F. B. Prinz, ***Fuel Cell Fundamentals***, 2006.

5. C. Zoski, ***Handbook of Electrochemistry***, 2006.

Chapter Three

Mechanistic Study of bulk Pd for Alcohol Electrooxidation in Alkaline Media

3.1 Introduction

Direct alcohol fuel cells (DAFCs) have been identified as promising potential candidates to replace hydrogen fuel cells and overcome hydrogen specific restrictions [1]. Several advantages of DAFCs which use alcohols such as methanol, ethanol and other polyalcohols as fuels, have been identified. Most notably alcohols generally exhibit higher volumetric energy density, high power density output and low pollutant emissions, as well as easier storage and transport, however are hindered by uncertain reaction mechanism, slower oxidation kinetics, alcohol crossover, lower fuel utilization and efficiency and thermal management[2-4]. Therefore, increasing research efforts are being carried out to explore and develop the DAFCs with high activity.

Direct methanol fuel cells in acidic media are most common of alcohol fuel cells but are limited by their toxicity which can cause CO poisoning, and corrosion of carbon materials and cell hardware[5]. There is increasing interest into higher molecular weight alcohols due to their increased solubility, lower toxicity and higher boiling points, specific heats and capacity to be renewable as well as interest into their partial oxidation products[2,6]. Various studies indicate that ethanol may be the most promising fuel[1,7], as it can be produced in large volumes from biomass feedstocks[8], forestry and urban residues[9], and algae[10]; it is less toxic than methanol; and has a higher energy density[3]. Higher molecular weight alcohols and polyalcohols have also been investigated such as ethylene glycol, 1,2 propanediol which exhibit similar benefits over methanol[11].

Alkaline conditions have shown to yield favorable improvements for alcohol oxidation, compared to acidic conditions, due to the enhancement of electrochemical kinetics at low anode overpotentials. Acidic conditions are also unfavorable due to issues with durability of the fuel cell casing[12]. The development of alkaline anion exchange membranes has made a strong case in favor of alkaline based as opposed to acid based fuel cells due to the faster reaction kinetics as a result of electrolyte carbonation

minimisation[2,13-14]. Further advantages of the use of alkaline conditions include improved kinetics at the anode and cathode; reduced alcohol crossover; easier water management – preventing flooding; reduced risk of corrosion of materials including catalyst carbons; and reduced adsorption of spectator ions that might limit electrocatalysis[2]. This increase in performance has in turn increased the possibility to use less expensive and more abundant alternatives to platinum[13] such as Palladium which is considerably cheaper and 50 times more abundant.

The most commonly used electrocatalyst for alcohol fuel cells is currently platinum[13] which has restricted widespread use due to its high cost and limited world supply[15]. Platinum is also readily poisoned by carbon monoxide from reformate gas used as a hydrogen carrier in PEMFC and a byproduct of alcohol oxidation in DAFC[15]. Palladium has been identified as a superior alternative to Platinum due to its' higher activity, stability and tolerance to poisoning during the oxidation of ethanol in alkaline conditions[16-18].

In the present work, we compared the temperature effect and proposed the mechanism of bulk Pd towards alcohol (methanol, ethanol butanol and glycerol) electrooxidation reaction in alkaline media using cyclic voltammetry (CV) and chronoamperometry (CA). The kinetics and possible pathways of alcohol electrooxidation reaction are obtained from the Arrhenius plots.

3.2 Experimental

3.2.1 Chemicals

Sulphuric acid (95%~98%, puriss grade), sodium hydroxide (semiconductor grade, 99.99%), methanol (≥99.9%), ethanol (≥99.9%), butanol (≥99.9%), glycerol (≥99.9%). All chemicals were used as received without further purification. All water used to clean the electrode and prepare aqueous solutions was purified by thermoscientific Barnstead water System (18.2 MΩ•cm resistivity).

3.2.2 Electrochemical preparation and characterization

A home designed water-jacketed variable temperature three-electrode setup was used in the whole research under a N_2 atmosphere. The electrochemical setup includes a piece of Pt mesh as the counter electrode, an Ag/AgCl (in saturated KCl) reference electrode for acidic media or a Hg/HgO (in 1 M NaOH) reference electrode for alkaline media, a bulk Pd as the working electrode. The cell was thoroughly cleaned by a solution of hydrogen peroxide and sulphuric acid followed by rinsed with boiling water before use. Prior to the electrochemical measurements, all solutions were deoxygenated by bubbling through high purity nitrogen gas for 30 minutes. Bulk Pd, working electrode, was mechanically polished using a range of alumina powders of different particle sized, e.g., 1,0.3 and 0.05 μm. The working electrode was then connected with titanium wire and wrapped around with PTFE tape. It was then sonicated thoroughly with water in a bath-type ultrasonicator several times. A further cyclic voltammetry (CV) acid test using 0.1 M H_2SO_4 was used to ensure the surface was clean with a stable voltammograms.

An Autolab electrochemical work station (Potentiostat, Eco Chemie, Netherlands) was employed for the electro-deposition and electrochemical measurements.

Electrochemical data were recorded using Autolab NOVA software and further analysed using Excel.

3.2.3 Alcohol electrooxidation on bare bulk Pd

Efficiency of electrooxidation reaction of alcohol on the bare bulk Pd were studied in a solution of 0.1 M Alcohol (Methanol/ Ethanol/ Butanol/ Glycerol) + 0.1 M NaOH at at a range of temperatures (25, 30, 40, 50, 60 ˚C) employed by both cyclic voltammetry (CV) and chronoampromerty (CA). The electrochemical setup includes a piece of Pt mesh as the counter electrode, a Hg/HgO (in 1 M NaOH) as the reference electrode, a bulk Pd as the working electrode. Electrolyte solution was deaerated by bubbling ultrapure N_2 for 30 minutes before experiments. The potential range between 0.11 and1.11 V (*vs.* RHE) at a scan rate of 50 mV s^{-1} was used in the CV, whilst a fixed potential of 0.71 V(*vs.*RHE) was chosen for the CA as it is relevant to alkaline ethanol fuel cell. The current density of ethanol electrooxidation was normalized with the electrochemical surface area (ECSA) of bare bulk Pd.

3.3 Results and discussion

3.3.1 Electrochemical study of bulk Pd by cyclic voltammetry

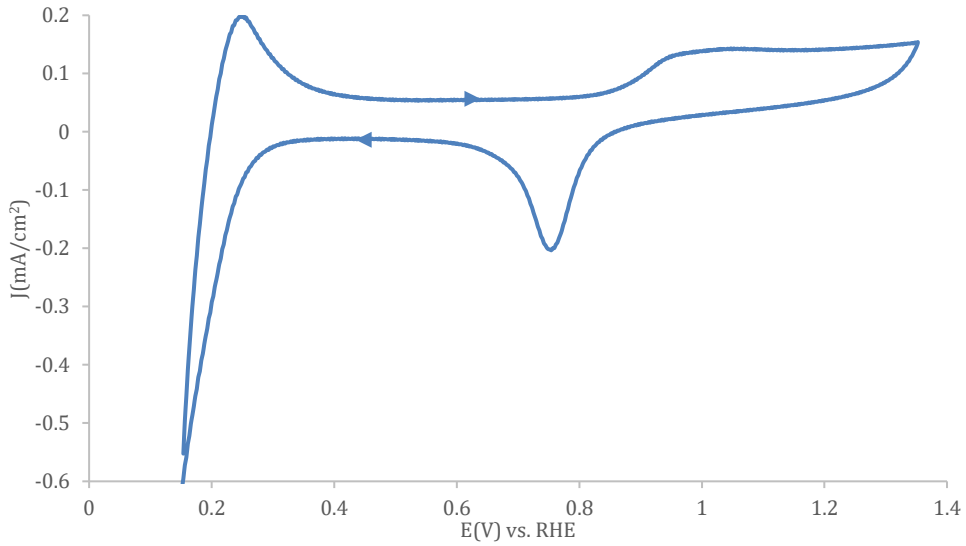

Figure 3.1 Cyclic voltammograms (CVs) of bulk Pd in 0.1 M H_2SO_4.
Scan rate: 50 mVs^{-1}.

As represented in Figure 3.1, the typical cyclic voltammograms (CVs) of bare Pd electrode in 0.1 M H_2SO_4 with potential range from 0.15 V to 1.35 V (*vs.* RHE) at a scan rate of 50 $mV \cdot s^{-1}$ at room temperature was studied to examine the affinity of hydrogen toward Pd catalyst[19]. A broaden peak in positive scan which can be observed from 0.15 V (*vs.* to 0.5 V (*vs.* RHE) is corresponding to the oxidation of the adsorbed hydrogen (H_{ad}) whilst a negative peak at 0.15 V (*vs.* RHE) is assigned to the oxidation of the absorbed of hydrogen (H_{ab}) on Pd surface[20-23]. A cathodic peak starts from 0.75 V (*vs.* RHE) has been attributed to the reduction of Pd oxides produced during the forward scan[19.24-25].

Additionally, the electrochemical active surface area (ECSA) of bulk Pd was determined by the integrated charge of hydrogen adsorption/ desorption region by adjusting the assumption of 212μC cm^{-2}. In order to contrast the electrooxidation performance of bulk Pd, the current is stabilized to electrochemical surface area (ECSA) current density (*J*).

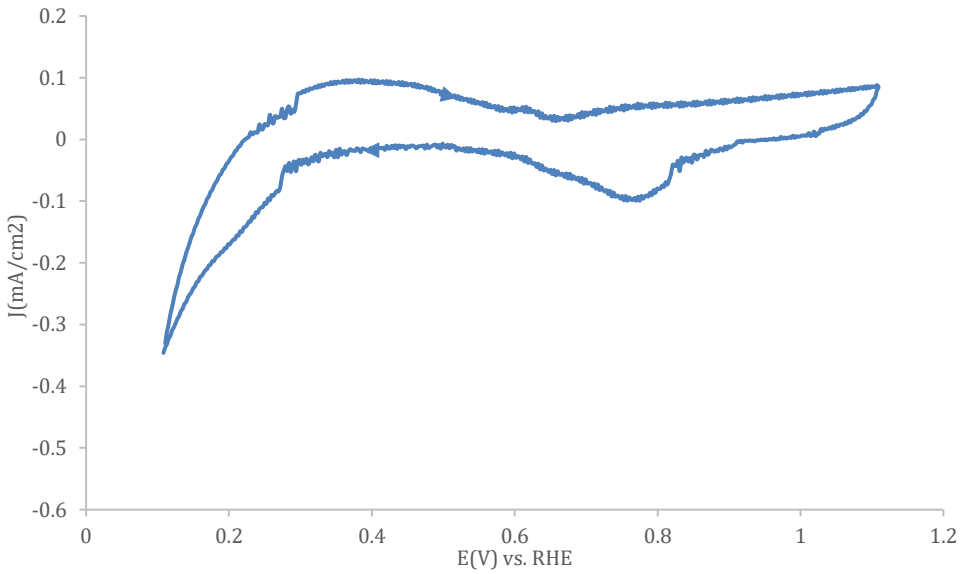

Figure 3.2 Cyclic voltammograms (CVs) obtained for bulk Pd in 0.1 M NaOH solution. Scan rate: 50mVs^{-1}

In order to further investigate the adsorption of hydroxyl species onto bulk Pd electrode, a typical CV profile in 0.1 M NaOH alkaline medium is presented in Figure 3.2. Compared to that in acidic medium (Figure 3.1), there are several noticeable changes such as a broader but less well-defined hydrogen adsorption/desorption current density peak, a significantly narrower double layer region, and a less significant but broader current density peak associated to surface oxygen-containing (e.g., hydroxyl) species formation/stripping processes.

3.3.2 Methanol electrooxidation reaction

Scheme 3.1 Schematic representation of the mechanism for methanol electrooxidation at Pd surface in alkaline media.

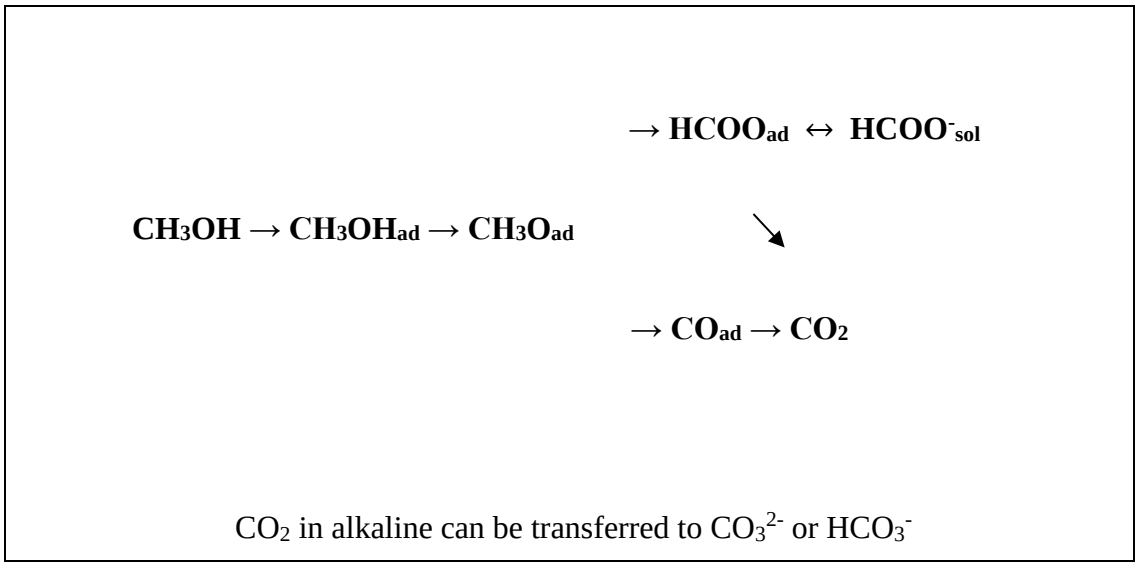

The dual-pathway mechanism for complete electrooxidation from methanol to CO_2 at the Pd surface has been put forward in Scheme 3.1[26], which involves interfacial formate and CO_{ads} as the intermediates. The cleavage of C-H bond is considered to be the rate-determining step for the dissociation of methanol. The formate ion is the other by-product of incomplete methanol oxidation. Some of the interfacial formate is electrooxidized to CO_2 at high potentials to a similar extent to the CO_{ads} species or diffuse into the solution as a product of partial electooxidation. CO_{ads} is obtained by the stepwise dehydrogenation of surface CH_3O and is electrooxidized to CO_2 at low potentials.

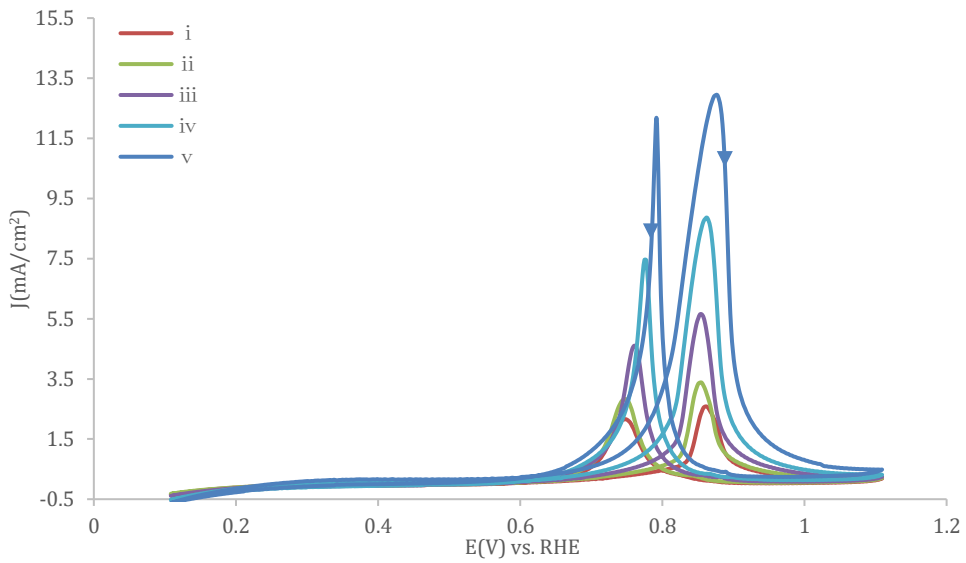

Figure 3.3 Cyclic voltammograms of bulk Pd electrode in 0.1 M Methanol + 0.1 M NaOH solution. Scan rate: 50 mV s^{-1}, from 25 to 60 ˚C, i：25 ˚C， ii：30 ˚C， iii：40 ˚C， iv：50 ˚C， v：60 ˚C.

Figure 3.3 displays the CVs of bulk Pd electrode for the methanol electrooxidation reaction in the solution of 0.1 M NaOH containing 0.1 M Methanol at temperatures 25, 30, 40, 50 and 60 ˚C with the scan rate of 50 mV s^{-1}. The methanol electrooxidation was characterized by two well-defined anodic peaks from the positive and negative direction scans. The peaks in the positive scans are associated to oxidation of adsorbed methanol while the peaks in the negative scans appear to be the removal of CO species adsorbed on Pd surface.

As obtained from Figure 3.3, the CV for the Methanol electrooxidation at 25 ˚C, obtained as i, gives rise to a current density peak of 2.580 mA/cm^{-2} in the forward scan. The onset potential for the current peak in the forward cycle occurs at 0.577 V (vs. RHE) and has a peak potential of 0.860 V (vs. RHE). The CV for the electrooxidation reaction at 30 ˚C is listed as ii in figure 3.3, the current peak density has a value of 3.376 mA/cm^2 which is about 1.3 times higher than the value of that at 25 ˚C. The onset peak potential maintains the same value of 0.577 V (vs. RHE) and the peak potential

left shifts to 0.853 V (vs. RHE). The CV for the electrooxidation reaction at 40 ˚C, shown in iii, has a current density peak in the forward scan with value 5.648 mA/cm^2. The onset potential occurs slight earlier than that at 30 ˚C with a value of 0.855 V (vs. RHE), however it is noticeable from the graph that the peak potential right shifts to a value of 0.855 V (vs. RHE). Line iv shows the CV for the electrooxidation at 50 ˚C. Although again the onset potential left shifts to 0.563 V (vs. RHE), the peak potential right shifts considerably to 0.863 V in comparison to 0.860 V at 40 ˚C. The peak current had a value of 8.865 cm/cm^2, which is over 3 times that of the value at 25 ˚C. The CV for electrooxidation at 60 ˚C is shown by Line v, the peak potential shifts further to 0.877 (vs. RHE) and the onset potential remains at a similar value to that at 50 ˚C (0.563 V (vs. RHE)), giving rise to a much wider peak. The peak current density in the forward scan at this temperature is 12.939 mA/cm^2, almost 5 times the value at 25 ˚C.

It is clear to see that the activities are improving with the increasing temperature on bulk Pd for methanol electrooxidation, probably due to the enhancement of methanol adsorption or dehydrogenation at high temperature[27]. The positive-going peak potentials are slightly more positive than the negative-going peak potentials due to the negligible CO_{ads} electrooxidation in the negative scan with reference to the positive scan.

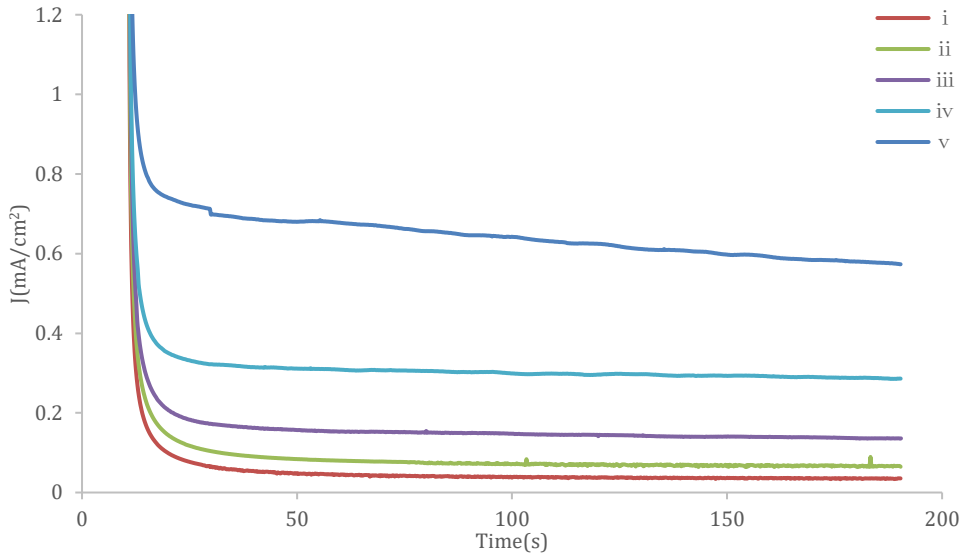

Figure 3.4 Chronoamperometric curves of bulk Pd electrode in 0.1 M Methanol + 0.1 M NaOH solution at the potential of 0.71 V vs. RHE from 25 to 60 ℃, i：25 ℃， ii：30 ℃， iii：40 ℃， iv：50 ℃， v：60 ℃.

In order to further assess the stability of ethanol electrooxidation and the poisoning condition on both bulk Pd electrode, Chronoamperometry was also carried out at a potential of 0.71 V (vs. RHE) for a period of 190 s in 0.1 M Methanol + 0.1 M NaOH and the results are presented in fig.3.4.

Prior to the current transients recorded at the study potential, the electrodes were initially kept at 1.01 V (*vs.* RHE) for 3 s to oxidize all the adsorbed intermediated and get the surface cleaned. Then, the electrodes were polarized at 0.11 V (*vs.* RHE) for 0.1s to reduce the oxides and adsorbed ethanol. Subsequently, constant potential tests were kept at 0.71 V (*vs.* RHE) for 190 s. The transient current curves of bulk Pd for methanol electrooxidation drop very rapid at the initial stage. According to Xu's previous work, the current decay is attributed to the poisoning effect by CO residues or to the formation of Pd-oxide[28]. Under all 5 temperatures, the current densities are kept relatively constant which indicates stability of the Pd catalyst towards methanol electrooxidation. Moreover, the data obtained from Figure 3.4 show that the

electrocatalytic activity of bulk Pd electrodes are getting higher with increasing temperature, which are consistent with the cyclic voltammogram data.

Table 3.1 List of onset potential, positive-going peak potential, positive-going peak current density, negative-going peak potential and negative-going peak current density obtained from Figure 3.3.

Methanol / Temp.	E_o / V (vs. RHE)	E_p / V (vs. RHE)	j_p /mA·cm^{-2}	E_n / V (vs.RHE)	j_n /mA·cm^{-2}
25 ˚C	0.577	0.860	2.580	0.748	2.162
30 ˚C	0.577	0.853	3.376	0.748	2.834
40 ˚C	0.572	0.855	5.648	0.760	4.599
50 ˚C	0.563	0.863	8.865	0.775	7.457
60 ˚C	0.563	0.877	12.939	0.792	12.174

In order to understand the electro-catalytic activity of bulk Pd for ethanol electrooxidation reaction, the onset potential (E_o), positive-going peak potential (E^p), positive-going peak current density (j_p), negative-going peak potential (E_n) and negative-going peak current density (j_n) obtained from Figure 3.3 are listed in Table 3.1. Basically, E_o getting negative shifted while peak current densities getting significantly improved with temperature increasing. The improvement in the onset potential indicates an enhancement of reaction kinetics due to the high index facets.

As the electroactive potential range for various alcohols are not identical, the peak current densities are obtained to plot profiles of the activation energy values calculated that are based on the Arrhenius equation seen below[29]:

$$\ln j = \ln A - \frac{E_a}{RT} \qquad (1)$$

Where, j is the corresponding peak current densities; R is gas constant, assuming 8.314 J K^{-1} mol^{-1}; T is temperature in K and Ea is the activation energy at relevant peak potential.

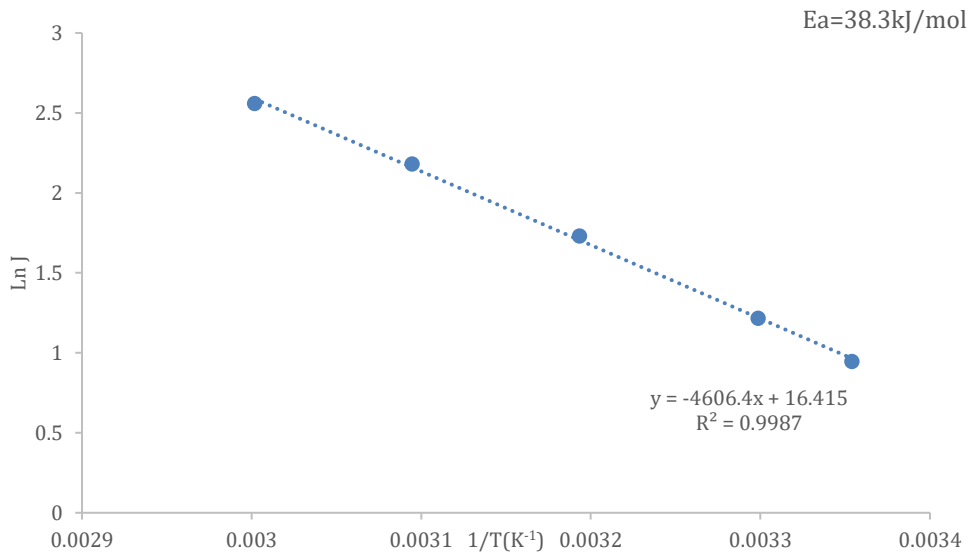

Figure 3.5 Arrhenius plots for Methanol electrooxidation on bulk Pd at peak potential.

Figure 3.5 shows an Arhenius plot for methanol electrooxidation on bulk Pd from peak current densities under different temperatures obtained from figure 3.3 which was used to calculate the activation energy of the electrooxidation reaction. It considers the current density peak on the anodic sweep against temperature. The R^2 value is 0.9987 which indicates a strong linear relationship between temperature and current peak density with gradient Ea/RT.

The activation energy (Ea) was therefore obtained graphically by taking the gradient and multiplying by R (8.314 kJ mol^{-1}) giving the value of 38.3 kJ/mol. On the basis

of the data above, some intuitive comments can be made regarding methanol electrooxidation on Pd surface. The predominant pathway of bulk Pd, formate ion is obtained by the dehydrogenation step of CH_3OH and is going to be oxidized to CO_2 at higher potentials.

3.3.3 Ethanol electrooxidation reaction

Scheme 3.2 Schematic diagram for ethanol electrooxidation on the Pd surface in alkaline media.

$$\rightarrow \quad CH_3COOH \qquad 4e^-$$

$$CH_3CH_2OH \rightarrow CH_3CHOH_{ads} \rightarrow CH_3CHO \rightarrow CH_3CO_{ads}$$

$$\rightarrow \quad CO_{ads} \rightarrow CO_2 \qquad 12e^-$$

(CO_2 in alkaline can be transferred to CO_3^{2-} or HCO_3^-)

It is accepted that ethanol tends to be oxidized to acetaldehyde and subsequently to acetic acid, transferring only 4 electrons in the process. However, acetic acid always marks a "dead end" in the mechanism, since its further oxidation is extremely difficult under ambient conditions. Alternatively, the carbon-carbon bond can be cleaved in ethanol or acetaldehyde, yielding the adsorbed single carbon species CO_{ads} and $CH_{x,ads}$.

These species can subsequently be oxidized to CO_2, liberating 12 electrons in total. Although this is the preferred pathway from a fuel cell application point of view, the single carbon adsorbates require a high over potential to be oxidized, thereby reducing the efficiency of the reaction[30].

According to Shen and Bian chini's work, the cleavage of C-C bona is favoured on the Pd in dilute NaOH to result in the complete oxidation of ethanol with the limited conversion of ethanol at the same time[31].

Based on the above consideration, it is suspected that C-C bond cleavage is preferred on Pd due to sufficient high index sites for EOR and liberating 12 electrons with high activity but reducing the efficiency and having a high barrier to overcome. To reduce the high barrier and increase the capability of free Pd sites to supply OH_{ads} species[32], the introduction of other transition metal such as Bi, Ag and Sn into the Pd surface, either by alloying or irreversible adsorption is a promising method[33-34].

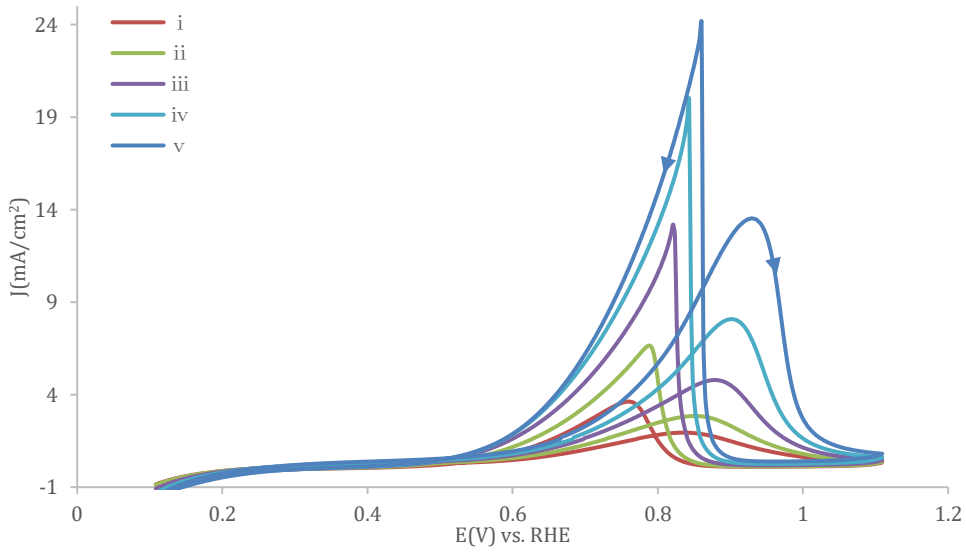

Figure 3.6 Cyclic voltammograms of bulk Pd electrode in 0.1 M Ethanol + 0.1 M NaOH solution. Scan rate: 50 mV·s^{-1}, from 25 to 60 ˚C, i：25 ˚C， ii：30 ˚C， iii：40 ˚C， iv：50 ˚C， v：60 ˚C.

Presented in Figure 3.6 is the cyclic voltammetry curves of ethanol electrooxidation reaction on the bulk Pd electrode in a solution of 0.1 M NaOH and 0.1 M EtOH at different temperatures of i: 25 ˚C, ii: 30 ˚C, iii: 40 ˚C, iv: 50 ˚C and v: 60 ˚C at a scan rate of 50mVs^{-1} from 0.11 V to 1.11 V(*vs.* RHE). The curves were recorded when stable responses were obtained. At each temperature, two well-defined peaks represented as positive-going peak and negative-going peak are corresponded to different electrochemical process occurring on the surface of working electrode. During forward scan, the positive-going peak is used for evaluating the catalytic activity as it is associated with the ethanol oxidation, whereas the peak in the backward scan mainly attributed to the further electrooxidation of carbonaceous species not completely oxidized in the forward scan[35-38].

At 25 ˚C, the ethanol oxidation reaction starts at 0.565(*vs.* RHE) and a forward current density peak centres at 0.833 (*vs.* RHE) with a value of 1.949 mA/cm^2 as a continues oxidation of ethanol. After the current density reaches the maximum value, it then starts to decline with a further increase in the potential. Previous studies suggested that the decrease in current density was related to the formation of the Pd(II) oxide layer on the surface of the electrode at higher potentials(Eqs.2 and Eqs.3) [39].

$$Pd - OH_{ads} + OH^- \leftrightarrow Pd - O + H_2O + e^- \qquad (2)$$

$$Pd - OH_{ads} + Pd - OH_{ads} \leftrightarrow Pd - O + H_2O \qquad (3)$$

The formation of the oxide layer can block the adsorption of the reactive species onto the Pd surface and lead to a decrease in the electrocatalytic activity, as a result, reducing the current density. As the positive-going sweep proceeds, more Pd (II) oxide covers the surface of the electrode. Consequently, the current density of the EOR is further decreased with the increase in the potential. When the potential is above 1.11 V (*vs.* RHE), the current density drops to 0.346 mA/cm^2, indicating that the EOR occurs on the fully developed Pd oxide layer is negligible. Fortunately, the decrease in the electrocatalytic activity can be recovered during the negative-going sweep, as

evidenced by the presence of backward peak at about 0.760 V (*vs*. RHE). This reactivation can be attributed to the reduction of the Pd (II) oxide (Qu.4), which is similar to the behaviour observed with the Pt-base catalyst[39-40].

$$Pd - O + H_2O + 2e^- \leftrightarrow Pd + 2OH^- \qquad (4)$$

At 30 ˚C, onset potential and positive peak potential are at around 0.565 V (*vs*. RHE) and 0.848 V (*vs*. RHE) which are similar to the values at 25 ˚C. The positive peak current density is 2.849 mA cm^{-2} which is about one and a half times higher than that at 25 ˚C showing an increase in catalytic activity. At 40 ˚C, the onset potential is minimal left shifts to 0.516 V (*vs*. RHE), and the peak current density has a value of 4.794 mA cm^{-2} at the potential of 0.877 V (*vs*. RHE). At 50 ˚C, the peak current density in the forward scan rises to 8.082 mA cm^{-2} with a peak potential of 0.902 V (*vs*. RHE) and the onset potential occurs earlier at 0.494 V (*vs*. RHE). The positive peak current density at 60 ˚C is around 7 times higher than that at 25 ˚C with a value of 13.526 mA cm^{-2} whilst the peak potential further right shifts to 0.929 V (*vs*. RHE) and the onset potential left shifts to 0.479 V (*vs*. RHE).

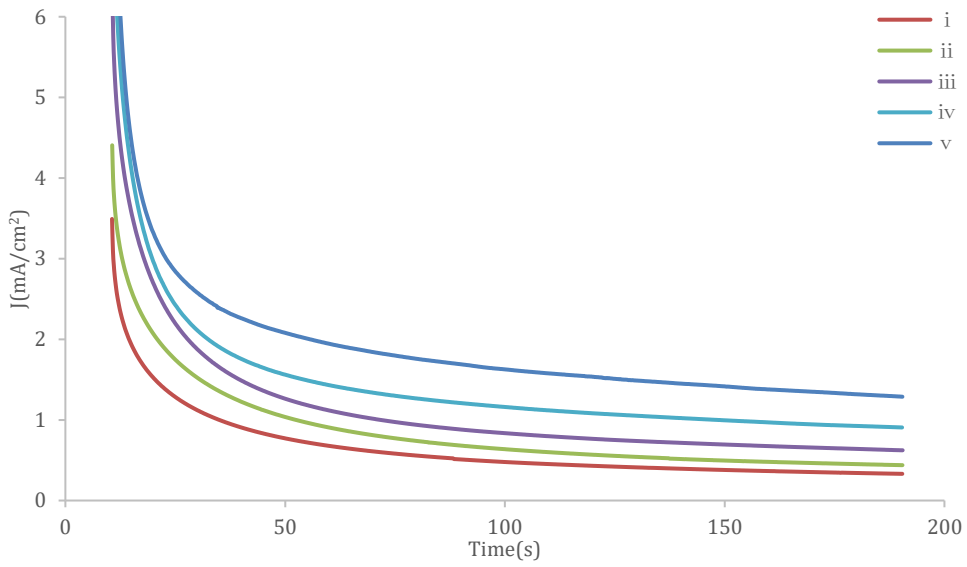

Figure 3.7 Chronoamperometric curves of bulk Pd electrode in 0.1 M Ethanol + 0.1 M NaOH solution at the potential of 0.71 V vs. RHE from 25 to 60 ℃, i：25 ℃， ii：30 ℃， iii：40 ℃， iv：50 ℃， v：60 ℃.

Chronoamperometry is also performed with the results displayed in Figure 3.7. Prior to the current transients recorded at the study potential, the electrodes were initially kept at 1.01 V (*vs.* RHE) for 3 s to oxidize all the adsorbed intermediated and get the surface cleaned. Then, the electrodes were polarized at 0.11 V (*vs.* RHE) for 0.1s to reduce the oxides and adsorbed ethanol. Subsequently, constant potential tests were kept at 0.71 V (*vs.* RHE) for 190 s. It is notable that at all temperatures the change in current densities are very gradual with time, showing relatively good stability. The records also show that the electrocatalytic activities of bulk Pd electrodes are getting higher with the temperature increasing, which is identical with the cyclic voltammogram data.

Table 3.2 List of onset potential, positive-going peak potential, positive-going peak current density, negative-going peak potential and negative-going peak current density obtained from Figure 3.6.

Ethanol / Temp.	E_o / V (vs. RHE)	E_p / V (vs. RHE)	j_p /mA·cm^{-2}	E_n / V (vs.RHE)	j_n /mA·cm^{-2}
25 ˚C	0.545	0.833	1.949	0.760	3.630
30 ˚C	0.545	0.848	2.849	0.787	6.643
40 ˚C	0.516	0.877	4.794	0.821	13.195
50 ˚C	0.494	0.902	8.082	0.843	19.933
60 ˚C	0.479	0.929	13.526	0.860	24.115

The onset potential (E_o), positive-going peak potential (E_p), positive-going peak current density (j_p), negative-going peak potential (E_n) and negative-going peak current density (j_n) obtained from Figure 3.6 are listed in Table 3.2. As observed, the onset potentials are left shifting from 0.545 V (*vs*. RHE) to 0.479 V(*vs*. RHE) ollowing such order: $E_{o,\ 25^{\circ}C} = E_{o,\ 30^{\circ}C} > E_{o,\ 40\ ^{\circ}C} > E_{o,\ 50\ ^{\circ}C} > E_{o,\ 60\ ^{\circ}C}$. Moreover, forward peak current densities are increasing from 1.949 mA/cm^2 to 13.526 mA/cm^2 with the elevated temperatures from 25 ˚C to 60 ˚C, suggesting that the adsorption of the OH^- species on Pd surface is facilitated at higher temperatures.

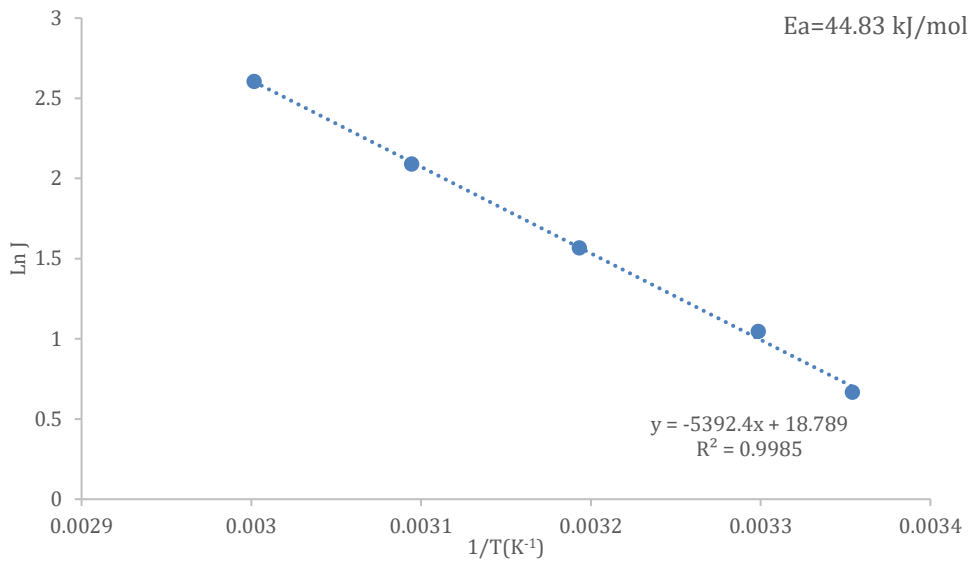

Figure 3.8 Arrhenius plots for Ethanol electrooxidation on bulk Pd at peak potential.

The Arhenius plot for the ethanol electrooxidation reactions at different temperatures is displayed in Figure 3.8. The R^2 value was 0.9985 which still shows strong linearity between temperature and current. The activation energy was calculated in the same way as for the methanol electrooxidation and was found to be 44.83 kJ/mol.

3.3.4 Butanol electrooxidation reaction

***Scheme 3.3 Proposed reaction mechanism for 1-Butanol oxidation on a Pt electrode*[41].**

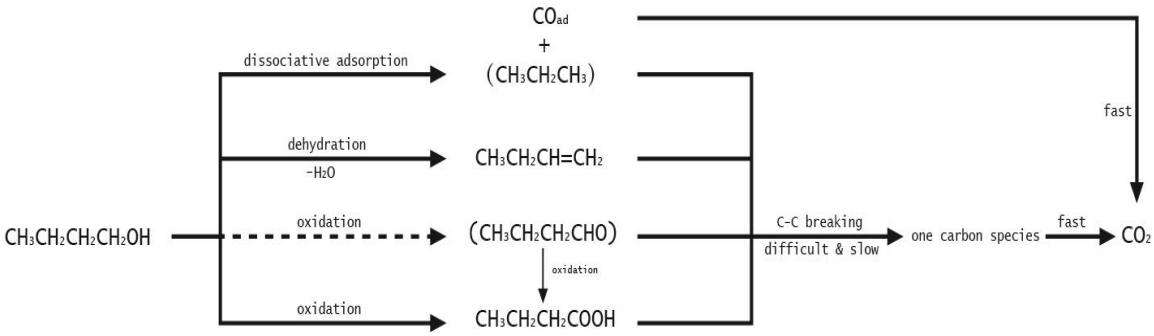

From previous mechanistic studies of alcohol oxidation reactions, the proton removal from the αC-H bond is the first step in the oxidation reaction of alcohol[42-44], this occurs at a low potential, leading to the dissociative adsorption of the alcohol molecule on Pd. Scheme 3.3 shows a Proposed reaction mechanism for 1-Butanol oxidation on a Pt electrode. 1-Butanol can dissociate into CO and $CH_3CH_2CH_3$, and CO is the main poisoning intermediate determined by in situ FTIRS. 1-Butanol can be also dehydrated into $CH_3CH{=}CH_2$ in acid solutions. The direct oxidation of 1-Butanol to butyric acid (or via $CH_3CH_2CH_2CHO$) is the principal pathway of oxidation. Except CO, the breaking process of the C-C bond of all other intermediates may take place and produce one carbon species at higher potentials. Nevertheless, the rate of the C-C breaking process is very slow. Once the one carbon species is formed, it can be oxidized rapidly into CO_2.

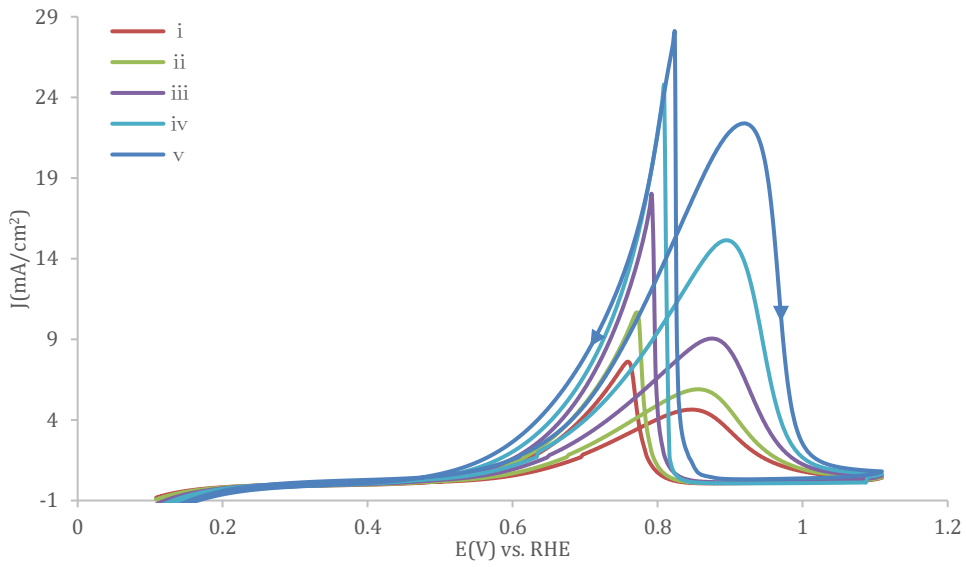

Figure 3.9 Cyclic voltammograms of bulk Pd electrode in 0.1 M Butanol + 0.1 M NaOH solution. Scan rate: 50 mV s^{-1}, from 25 to 60 ˚C, i：25 ˚C， ii：30 ˚C， iii：40 ˚C， iv：50 ˚C， v：60 ˚C.

Figure 3.9 shows the cyclic voltammetry curves of bulk Pd electrode towards butanol electrooxidation reaction in 0.1 M Butanol + 0.1 M NaOH solution. Exhibited by line i is the CVs at 25 ˚C, it can be seen that the onset potential appears at 0.504 V (*vs.* RHE). The forward anodic peak at 0.846 V (*vs.* RHE) in the forward scan is well assigned to the oxidation freshly chemisorbed species coming from butanol adsorption while another peak at 0.758 V (*vs.* RHE) in the backword scan is derived from the incompletely oxidized carbonaceous species generated from the forward scan. Specially, at high potentials, when OH_{ads} is not entirely consumed, excessive OH_{ads} begins to behave as a poisoning species, blocking the surface and thus, the total activity of the reaction decreases to lower values. In addition, the extreme sharp negative-going peaks demonstrate significant oxide coverage on the Pd catalyst surfaces forming PdO.

The current densities for butanol oxidation which obtained at peak potential in the forward sweep raised from 4.640 mA/cm^2 to 22.386 mA/cm^2 as the temperature increased from 25 to 60 ˚C, approximately 5 times superior. In the meantime, the peak potentials are shifted to the higher potential with respect to the higher temperature. Moreover, the activities are improving with the temperature increasing on bulk Pd for butanol electrooxidation.

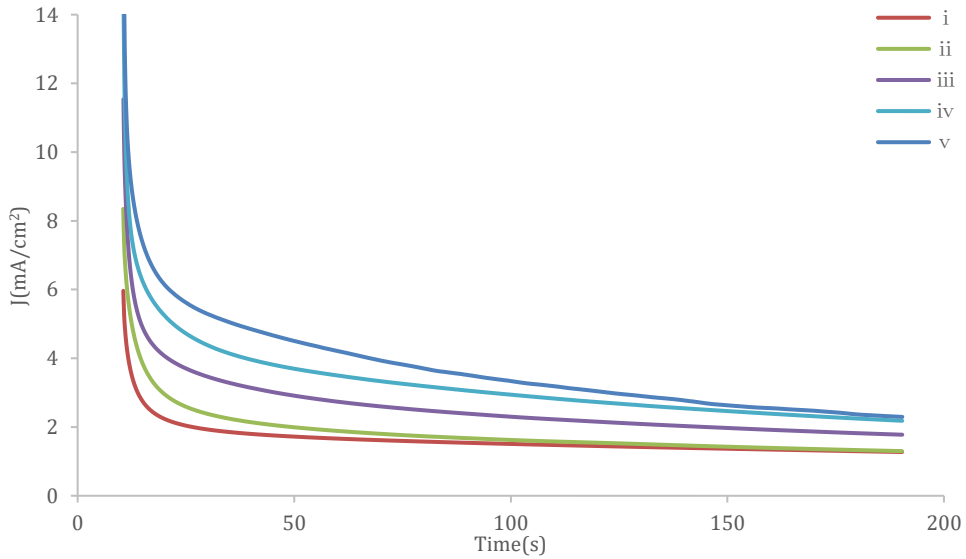

Figure 3.10 Chronoamperometric curves of bulk Pd electrode in 0.1 M Butanol + 0.1 M NaOH solution at the potential of 0.71 V vs. RHE from 25 to 60 ˚C, i：25 ˚C， ii：30 ˚C， iii：40 ˚C， iv：50 ˚C， v：60 ˚C.

Further evaluating the electrocatalytic activity and stability of bulk Pd electrode under continuous operating potentials, the chronoamperometric experiments were carried out in the solution of 0.1 M Butanol + 0.1 M NaOH at the potential of 0.71 V (*vs.* RHE) for 190 s. It can be clearly seen from Figure 3.10, the current densities decay rapidly during the first few seconds due to the poisoning effect of intermediates such as dimethyl methane on the catalyst surface. Then, the currents reach a relatively

constant value after 190 s. The electrocatalytic activity of bulk Pd is increasing as the temperature increases, which is consistent with the results from cyclic voltammograms.

Table 3.3 List of onset potential, positive-going peak potential, positive-going peak current density, negative-going peak potential and negative-going peak current density obtained from Figure 4.3.b

Butanol / Temp.	E_o / V (vs. RHE)	E_p / V (vs. RHE)	j_p /mA·cm^{-2}	E_n / V (vs.RHE)	j_n /mA·cm^{-2}
25 ˚C	0.504	0.846	4.640	0.758	7.597
30 ˚C	0.504	0.858	5.900	0.772	10.644
40 ˚C	0.494	0.875	9.048	0.792	17.946
50 ˚C	0.484	0.897	15.138	0.809	24.707
60 ˚C	0.477	0.921	22.386	0.824	28.042

In order to explore the electro-catalytic activity of bulk Pd towards BOR, the onset potential (E_o), positive-going peak potential (E_p), positive-going peak current density (j_p), negative-going peak potential (E_n) and negative-going peak current density (j_n) obtained from Figure 3.9 are listed in Table 3.3. On Pd surface, more facile OH_{ads} processed at higher temperature as evidenced by the onset potential (E_o) shifting negative from 0.504 V (*vs.* RHE) to 0477 V (*vs.* RHE) with the elevated temperatures from 25 ˚C to 60 ˚C, leading to a faster reaction rate and kinetics. Conversely, considerable peak potential shifts to a higher potential with respect to the higher temperature meaning the electroactive potential range is getting broader.

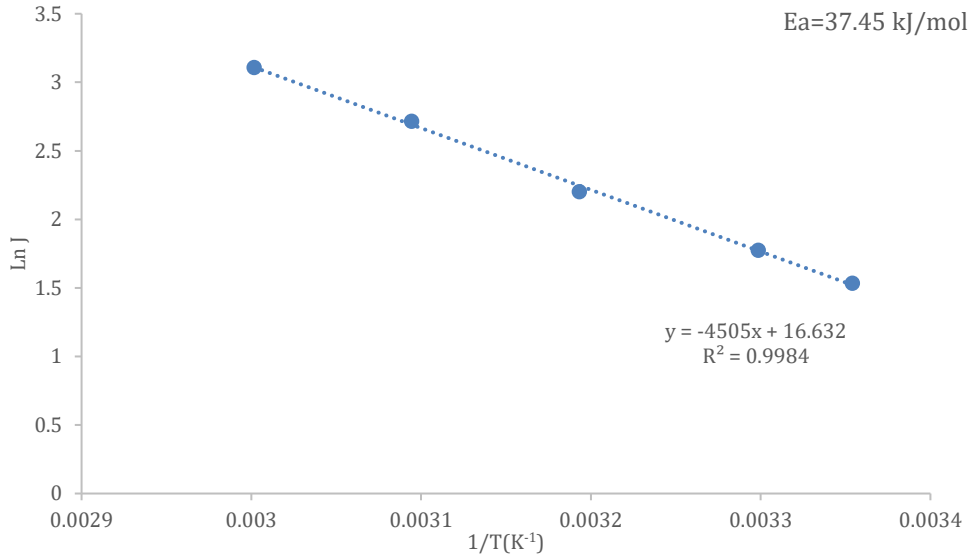

Figure 3.11 Arrhenius plots for Butanol electrooxidation on bulk Pd at peak potential.

Figure 3.11 displays the Arrhenius plots for butanol electrooxidation on bulk Pd on the resulting peak current densities during the positive scans. The R^2 value is found to be 0.9984, shows reliable linearity between temperature and current density. The Ea value of bulk Pd towards BOR is 37.45 kJ/mol which is much lower than that towards EOR of 44.83 kJ/mol.

3.3.5 Glycerol electrooxidation reaction

Scheme 3.4. Oxygenated products from the oxidation of glycerol[45]

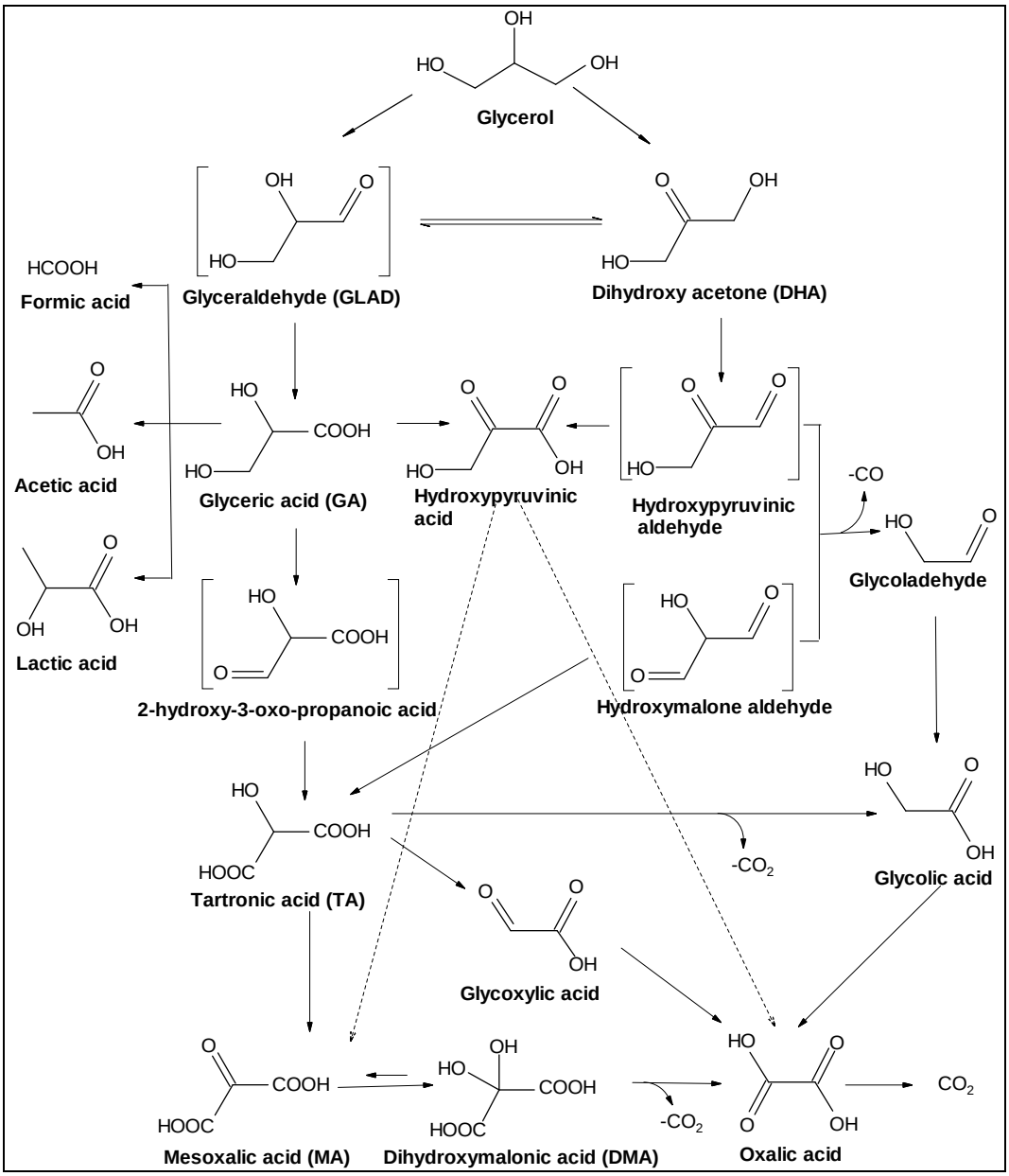

Scheme 3.4 shows the possible intermediated produces in the process of glycerol oxidation. In the structure of glycerol molecule, there are two typical hydroxyl groups as a function of different positions (two primary hydroxyl groups and one secondary hydroxyl group) and the hydroxyl groups are easily oxidized when treated with

appropriate catalysts. However, as for different hydroxyl groups, the oxidation selectivity would be distinct for the various condition and catalysts. Consequently, the oxidation of glycerol can produce a series of value-added oxygenates, including glyceric acid (GLA), tartronic acid (TS), mesoxaic acid (MOS) and glycolic acid.

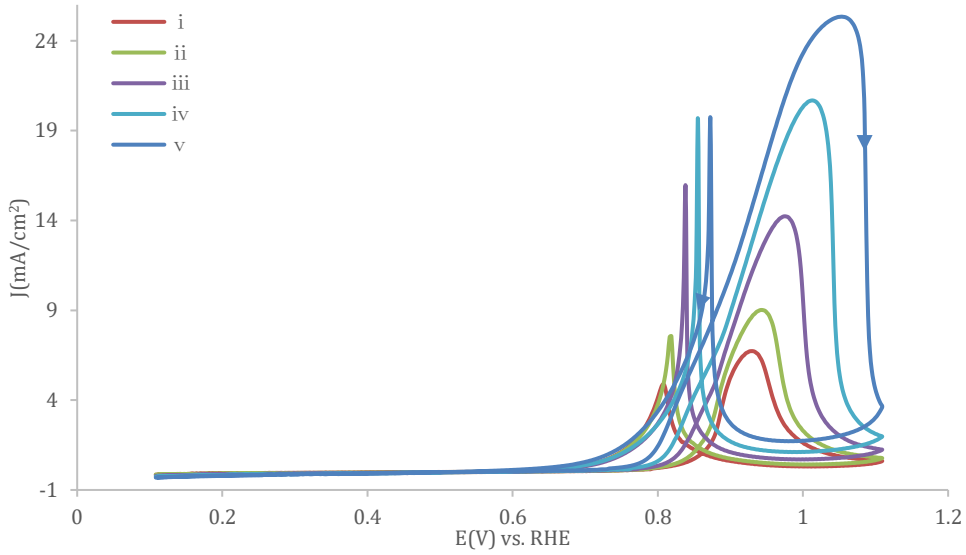

Figure 3.12 Cyclic voltammograms of bulk Pd electrode in 0.1 M Glycerol + 0.1 M NaOH solution. Scan rate: 50 mV s^{-1}, from 25 to 60 ˚C, ***i：25*** ˚C， ***ii：30*** ˚C， ***iii：40*** ˚C， ***iv：50*** ˚C， ***v：60*** ˚C.

CVs for GOR in the solution of 0.1 M Glycerol + 0.1 M NaOH on bare bulk Pd catalysts from 25 to 60 ˚C from 0.11 to 1.11 V (*vs.* RHE) are displayed in Figure 3.12. At 25 ºC, the onset potential occurs at 0.733 V (*vs.* RHE). Afterwards, the positive current density exhibits a significant growth and reaches a peak of 6.725 mA/cm^2 at 0.929 V (*vs.* RHE). Thereafter, overoxidation of the palladium surface decrease the current density to 0.60 mA/cm^2 at 1.11V (*vs.* RHE). During the reverse scan, the oxidation products of glycerol increases slowly. However, it presents a sharp oxidation peak at 0.807 V (*vs.* RHE), which indicates a pronounced increase of CO and CO_2[46-47]. The

CV for the electrooxidation reaction at 30 ˚C is shown by ii. The onset potential starts at 0.731 V (*vs.* RHE) which is almost the same with that at 25 ˚C. The forward scan current density has a value of 9.017 mA/cm^2, almost 1.4 times higher than that at 25 ˚C with the E_p of 0.943 V (*vs.* RHE). At 40 ˚C, The CV for the electrooxidation reaction has a current density peak in the forward scan with value 14.231 mA/cm^2. The onset potential left shifts to 0.723 V (*vs.* RHE) while the peak potential continues to right shift to 0.975 V (*vs.* RHE). The CV for electrooxidation at 50 ˚C is exhibited by line iv, the onset potential remains at a similar value to that at 40 ˚C (0.721V (*vs.* RHE) and a significant increase of forward peak current density occurs at 1.012 V (*vs.* RHE) with the value of 20.674 mA/cm^2, which is over 3 times higher than that of 25 ˚C. The CV for electrooxidation at 60 ˚C is shown by line v. The peak potential shifts further to 1.053 V (*vs.* RHE) but the onset potential left shifts to 0.715 V (*vs.* RHE) giving rise to a much wider peak. Moreover, the peak current density in the forward scan at this temperature is 25.343 mA/cm^2, almost 4 times than the value at 25 ˚C.

In the light of the above, significant influence of temperature on the catalytic activity is seen clearly from these data. The current densities for glycerol oxidation which obtained at peak potential in the forward sweep raised from 6.725 mA/cm^2 to 25.343 mA/cm^2 as the temperature increased from 25 to 60 ˚C. In the meantime, the positive-going current peaks turn to plateau's with the temperature increasing, indicating the electroactive potential range getting broader. The onset potential moved to a more negative direction at 60 ˚C compared to that potential at 25 ˚C. Thereafter, there is a slight decrease during a long period as the adsorbed glycerol molecules block the electrode surface and the glycerol oxidation reaction occur over the first minutes[48-49].

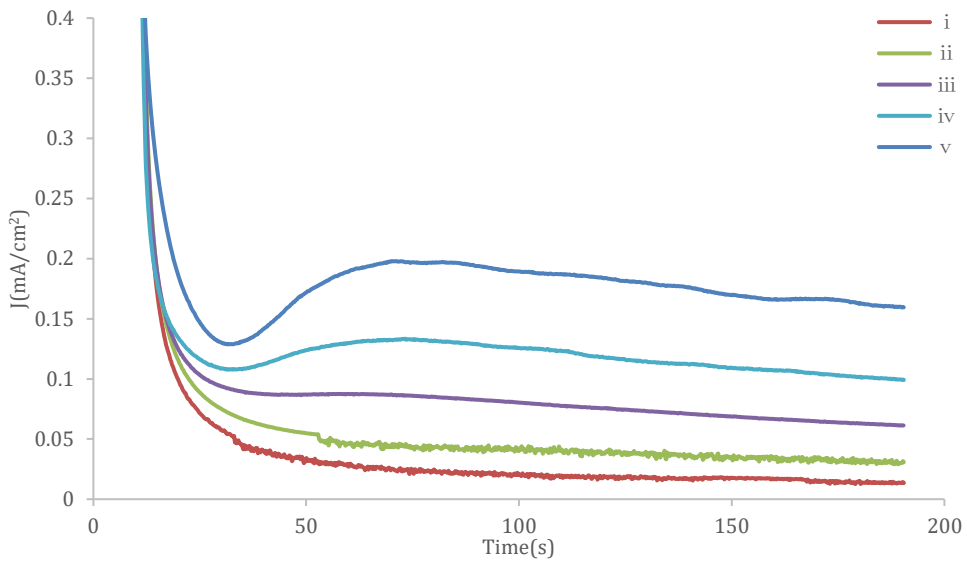

Figure 3.13 Chronoamperometric curves of bulk Pd electrode in 0.1 M Glycerol + 0.1 M NaOH solution at the potential of 0.71 V vs. RHE from 25 to 60 ˚C, i：25 ˚C， ii：30 ˚C， iii：40 ˚C， iv：50 ˚C， v：60 ˚C.

CAs for GOR in the solution of 0.1 M Glycerol + 0.1 M NaOH over bulk Pd at 0.71 V (vs. RHE) from 25 to 60 ˚C are presented in Figure 3.13. Prior to the current transients recorded at the study potential, the electrodes were initially kept at 1.01 V (*vs.* RHE) for 3 s to oxidize all the adsorbed intermediated and get the surface cleaned. Then, the electrodes were polarized at 0.11 V (*vs.* RHE) for 0.1s to reduce the oxides and adsorbed ethanol. Subsequently, constant potential tests were kept at 0.71 V (*vs.* RHE) for 190 s. Under each temperature, the initial decay in current density is attributed to the strong adsorption of reaction intermediates to the surface of the electrode, which results in poisoning and therefore reduces GOR. Afterwards, it can be seen that current densities at 50 ˚C and 60 ˚C show an increase within the first 33 s to 73 s. After this period, the current densities show a slow decrease over the time indicating a fairly high stability. Meanwhile, the rest of the curves show a sharp current density decrease. More specifically, the decrease of current densities are related to the formation of intermediates on the electrode surface[50-51]. In the end, as the current

density reaches a steady state, carbonaceous intermediate poisoning and GOR reaches relative equilibrium. It is worth noting that CA curves for GOR on bulk Pd are progressively improved with increasing temperature which is identical with the cyclic voltammogram data.

Table 3. List of onset potential, positive-going peak potential, positive-going peak current density, negative-going peak potential and negative-going peak current density obtained from Figure 4.3.b

Glycerol / Temp.	Eo / V (vs. RHE)	E_p / V (vs. RHE)	j_p /mA·cm^{-2}	E_n / V (vs.RHE)	j_n /mA·cm^{-2}
25 ˚C	0.733	0.929	6.725	0.807	4.860
30 ˚C	0.731	0.943	9.017	0.819	7.550
40 ˚C	0.724	0.975	14.231	0.838	15.881
50 ˚C	0.721	1.012	20.674	0.8585	19.665
60 ˚C	0.715	1.053	25.343	0.872	19.680

As listed in Table 3.3 are the relative onset potential (E_o), positive-going peak potential (E_p), positive-going peak current density (j_p), negative-going peak potential (E_n) and negative-going peak current density (j_n) obtained from Figure 3.9. The onset potential (E_o) of glycerol electrooxidation is shifting negative from 0.733 V(*vs.* RHE) to 0.715 V(*vs.* RHE) whilst the positive going peak current density (j_p) is increasing from 6.725 mA/cm^2 to 25.343 mA/cm^2 with the elevated temperature from 25 ˚C to 60 ˚C, leading to a faster reaction rate and kinetics and indicating that GOR on Pd surfaces is a highly active process.

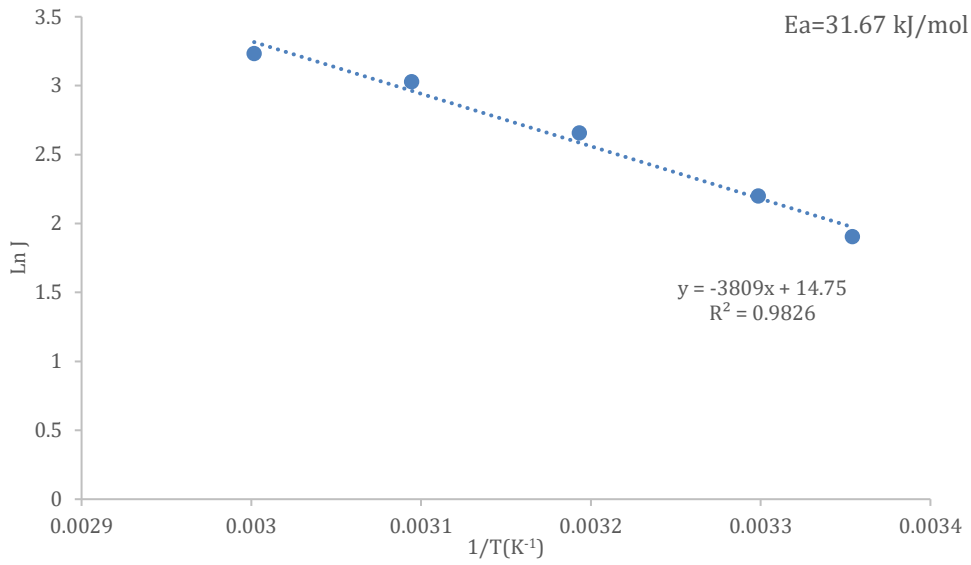

Figure 3.14 Arrhenius plots for Glycerol electrooxidation on bulk Pd at peak potential.

The Arhenius plot for the Glycerol electrooxidation reactions at different temperatures is displayed in Figure 3.14. The R^2 value is found to be 0.9826, shows strong linearity between temperature and current density. The activation energy was calculated in the same way as for the methanol electrooxidation and was found to be 31.67 kJ/mol.

3.4 Conclusions

In this work, the electrochemical behaviour of the bulk Pd electrode was studied for different alcohols (methanol, ethanol butanol and glycerol) in alkaline medium using cyclic voltammetry and chronoamperometry at 25 ˚C, 30 ˚C, 40 ˚C, 50 ˚C and 60 ˚C, respectively. The activation energy of alcohol electrooxidation reaction with bulk Pd was obtained by utilising Arrhenius plots which correlated anodic sweep peak current density with cell temperature. On the basis of comparison of the electrochemical characteristics obtained from CVs and CAs and activation energy, we can reach the following conclusion:

1. For all the alcohol electrooxidation reactions, the catalyst actives and kinetic were facilitated at higher temperatures evidenced by the following fact. The onset potentials are getting lower and positive peak current densities are increasing with the elevated temperature. Particularly, the positive peak current density of Methanol achieved 5 times superior with the temperature increase from 25 ˚C to 60 ˚C, while it achieved 6.9 times for Ethanol, 4.8 times for Butanol and 3.8 times for Glycerol. In the meantime, the peak potentials are shifted to the higher potential with respect to the higher temperature.

2. In comparison of the different alcohols, the positive peak current densities (J_p) at 30 ˚C are following such order: $J_{Glycerol} > J_{Butanol} > J_{Ethanol} > J_{Methanol}$ while the activation energy (Ea) are following order: $Ea_{Glycerol} < Ea_{Butanol} < Ea_{Methanol} < Ea_{Ethanol}$. This result implied that the reaction activities increased while the activation energy decreased with respect to increases in the length of the carbon chain of the primary alcohols.

3.5 Reference

1. E. Antolini, ***Catalysts for Direct Ethanol Fuel Cells***, J. Power Sources, 2007, 170, 1-12.
2. C. Bianchini, P. K. Shen, ***Palladium-based Electrocatalysts for Alcohol Oxidation in Half Cells and in Direct Alcohol Fuel Cells***, Chem. Rev., 2009, 109, 4183-4206.
3. L. Yang, S. Kinoshita, T. Yamada, S. Kanda, H. Kitagawa, M. Tokunaga, T. Ishimoto, T. Ogura, R. Nagumo, A. Miyamoto, M. Koyama, ***A Metal–Organic Framework as an Electrocatalyst for Ethanol Oxidation***, Angewandte Chemie, 2010, 122, 5476-5479.
4. S. Q. Song, Y. Wang, P. Tsiakaras, P.K. Shen, ***Direct Alcohol Fuel Cells: A Novel Non-Platinum and Alcohol Inert ORR Electrocatalyst***, Appl. Catal., B, 2008, 78, 381-387.
5. K. I. Ozoemena, ***Nanostructured Platinum-free Electrocatalysts in Alkaline Direct Alcohol Fuel Cells: Catalyst Design, Principles and Applications***, RSC Adv., 2016, 6, 89523-89550.
6. D. J. Chadderdon, L. Xin, J. Qi, B. Brady, J. A. Miller, K. Sun, M. J. Janik, W. Z. Li, ***Selective Oxidation of 1,2-Propanediol in Alkaline Anion-Exchange Membrane Electrocatalytic Flow Reactors: Experimental and DFT Investigations***, ACS Catal., 2015, 5, 6926-6936.
7. K. Kordesch, G. Simader, ***Fuel Cells and their Applications***, 1st ed., VCH, 1996.
8. R. Luque, C. Lin, K. Wilson, J. Clark, ***Handbook of Biofuels Production: Processes and Technologies***, 2nd ed., Woodhead Publishing, 2016.
9. S. Kim, B. E. Dale, ***Global Potential Bioethanol Production from Wasted Crops and Crop Residues***, Biomass Bioenergy, 2004, 26, 361-375.
10. L. Brennan, P. Owende, ***Biofuels from Microalgae—A Review of Technologies for Production, Processing, and Extractions of Biofuels and Co-products***, Renew Sust. Energ. Rev., 2010, 14, 557-577.

11. A. Lenarda, M. Bellini, A. Marchionni, H. A. Miller, T. Montini, M. Melchionna , F. Vizza, M. Prato, P. Fornasiero, ***Nanostructured Carbon Supported Pd-ceria as Anode Catalysts for Anion Exchange Membrane Fuel Cells Fed with Polyalcohols***, Inorganica Chimica Acta, 2017, 470, 213-220.

12. H. Pramanik, S. Basu, ***Modeling and Experimental Validation of Overpotentials of a Direct Ethanol Fuel Cell***, Chem. Eng. Process.. 2010, 49, 634-641.

13. E. Antolini, E. R. Gonzalez, ***Alkaline Direct Alcohol Fuel Cell***s, J. Power Sources, 2010, 195, 3431-3450.

14. P. Wang, X. Lin, B. Yang, J. M. Jin, C. Hardacre, N. F. Yu, S. G. Sun, W. F. Lin, ***Activity Enhancement of Tetrahexahedral Pd Nanocrystals by Bi Decoration towards Ethanol Electrooxidation in Alkaline Media***, Electrochim. Acta, 2015, 162, 290-299.

15. E. Antolini, ***Palladium in Fuel Cell Catalysis***, Energy Environ. Sci., 2009, 2, 915-931.

16. C. W. Xu, L. Q. Chen, P. K. Shen, Y. L. Liu, ***Methanol and Ethanol Electrooxidation on Pt and Pd Supported on Carbon Microspheres in Alkaline Media***, Electrochem. Commun., 2007, 9, 997-1001.

17. L. Ma, D. Chu, R. R. Chen, ***Comparison of Ethanol Electro-Oxidation on Pt / C and Pd / C Catalysts in Alkaline Media***, Int. J. Hydrogen Energy., 2012, 37, 11185-11194.

18. V. Bambagioni, C. Bianchini, A. Marchionni, J. Filippi, F. Vizza, J. Teddy, P. Serp, M. Zhiani, ***Pd and Pt–Ru Anode Electrocatalysts Supported on Multi-Walled Carbon Nanotubes and their use in Passive and Active Direct Alcohol Fuel Cells with an Anion-Exchange Membrane (Alcohol = Methanol , Ethanol , Glycerol)***, J. Power Sources, 2009, 190, 241-251.

19. A. Safavi, H. Kazemi, S. Momeni, M. Tohidi, P. K. Mehrin, ***Facile Electrocatalytic Oxidation of Ethanol Using Ag/Pd Nanoalloys Modified Carbon Ionic Liquid Electrode***, Int. J. Hydrogen Energy, 2013, 38, 3380-3386.

20. S. T. Nguyen, H. M. Law, H. T. Nguyen, N. Kristian, S. Y. Wang, S. H. Chan, X. Wang, ***Enhancement Effect of Ag for Pd/C towards the Ethanol Electro-Oxidation in Alkaline Media***, Appl. Catal., B, 2009, 91, 507–515.

21. J. S. Wang, C. H. Liu, A. Lushington, N. C. Cheng, M. N. Banis, A. Riese, X. L. Sun, ***Pd on carbon nanotubes-supported Ag for formate oxidation: The effect of Ag on anti-poisoning performance***, Electrochim. Acta, 2016, 210, 285–292.

22. G. L. Li, L. H. Jiang, Q. Jiang, S. L. Wang, G. Q. Sun, ***Preparation and Characterization of PdxAgy/C Electrocatalysts for Ethanol Electrooxidation Reaction in Alkaline Media***, Electrochim. Acta, 2011, 56, 7703–7711.

23. R. K. Pandey, V. Lakshminarayanan, ***Electro-Oxidation of Formic Acid, Methanol, and Ethanol on Electrodeposited Pd-Polyaniline Nanofiber Films in Acidic and Alkaline Medium***, J. Phys. Chem., 2009, 113, 21596-21603.

24. X. Teng, ***Anodic Catalyst Design for Ethanol Oxidation Fuel Cell***. Available online: http://www.formatex.info/energymaterialsbook/book/473-484.pdf

25. H. P. Liang, N. S. Lawerence, T. G. J. Jones, C. E. Banks, C. Ducati, ***Nanoscale Tunable Proton/Hydrogen Sensing: Evidence for Surface-Adsorbed Hydrogen Atom on Architectured Palladium Nanoparticles***, J. Am. Chem. Soc. 2007, 129, 6068-6069.

26. Y. Y. Yang, J. Ren, H. X. Zhang, Z. Y. Zhou, S. G. Sun, W. B. Cai, ***Infrared Spectroelectrochemical Study of Dissociation and Oxidation of Methanol at a Palladium Electrode in Alkaline Solution***, Langmuir, 2013, 29, 1709-1716.

27. A. V. Tripkovic, K. D. PopoviA, B. N. Grgur, B. Blizanac, P. N. Ross, N. M. Markovic, ***Methanol Electrooxidation on Supported Pt and PtRu Catalysts in Acid and Alkaline Solutions***, Electrochim. Acta, 2002, 47, 3707-3714.

28. J. Lu, S. Lu, D. Wang, M. Yang, Z. Liu, C. Xu, S. P. Jiang, ***Nano-Structured PdxPt1-x/Ti Anodes Prepared by Electrodeposition for Alcohol Electrooxidation***, Electrochim. Acta, 2009, 54, 5486-5491.

29. J. L. Cohen, D. J. Volpe, H. D. Abruna, ***Electrochemical Determination of Activation Energies for Methanol Oxidation on Polycrystalline Platinum in Acidic and Alkaline Electrolytes***, Phys. Chem. Chem. Phys., 2007, 9, 49-77.

30. W. Zhou, M. Li, L. Zhang, S. H. Chan, ***Supported PtAu Catalysts with Different Nano-Structures for Ethanol Electrooxidation***, Electrochim. Acta, 2014, 123, 233-239.

31. Q. S. Chen, Z. Y. Zhou, F. J. Vidal-Iglesias, J. Solla-Gullon, J. M. Feliu, S. G. Sun, ***Significantly Enhancing Catalytic Activity of Tetrahexahedral Pt Nanocrystals by Bi Adatom Decoration***, J. Am. Chem. Soc., 2011, 133, 12930-12933.

32. S. T. Nguyen, Y. H. Yang, X. Wang, ***Ethanol Electro-Oxidation Activity of Nbdoped-TiO2 Supported PdAg Catalysts in Alkaline Media***, Appl. Catal. B-Environ., 2012, 113, 261-270.

33. S. T. Nguyen, H. M. Law, H. T. Nguyen, N. Kristian, S. Y. Wang, S. H. Chan, X. Wang, ***Enhancement Effect of Ag for Pd/C Towards the Ethanol Electro-Oxidation in Alkaline Media***, Appl. Catal. B-Environ., 2009, 91, 507-515.

34. W. Du, K. E. Mackenzie, D. F. Milano, N. A. Deskins, D. Su, X. Teng, ***Palladium-Tin Alloyed Catalysts for the Ethanol Oxidation Reaction in an Alkaline Medium***, ACS Catal., 2012, 2, 287-297.

35. H. L. Yang, S. U. Kang, H. Zou, J. Jin, J. T. Ma, S. W. Li, ***Polydopamine-functionalized Multi-walled Carbon Nanotubes-supported Palladium-lead Bimetallic Alloy Nanoparticles as Highly Efficient and Robust Catalysts for Ethanol Oxidation***, RSC Adv., 2016, 6, 90462-90464.

36. M. C. Morin, C. Lamy, J. M. Leger, J. L.Vasquez, A. Aldaz, ***Structural Effects in Electrocatalysis – Oxidation of Ethanol on Platinum Single- Crystal Electrodes: Effect of PH***, J. Electroanal. Chem., 1990, 283, 287-302.

37. J. C. Huang, Z. L. Liu, C. B. He, L. M. Gan, ***Synthesis of PtRu Nanoparticles From the Hydrosilylation Reaction and Application as Catalyst for Direct Methanol Fuel Cell***, J. Phys. Chem. B, 2005, 109, 16644-16649.

38. H. Na, L. Zhang, H. Qiu, T. Wu, M. Chen, N. Yang, L. Li, F. Xing, J. Gao, ***A Two Step Method to Synthesize Palladium-copper Nanoparticles on Reduced Graphene Oxide and their Extremely High Electrocatalytic Activity for the Electrooxidation of Methanol and Ethanol***, J. Power Sources, 2015, 288, 160–167.

39. Z. X. Liang, T. S. Zhao, J. B. Xu, L. D. Zhu, ***Mechanism Study of the Ethanol Oxidation Reaction on Palladium in Alkaline Media***, Electrochim. Acta, 2009, 54, 2203-2208.

40. M. Grden, A. Czerwinski, ***EQCM Studies on Pd–Ni Alloy Oxidation in Basic Solutio***, J. Solid State Electrochem. 2008, 12, 375-385.

41. N. H. Li, S. G. Sun, ***In Situ FTIR Spectroscopic Studies of the Electrooxidation of C_4 Alcohol on a Platinum Electrode in Acid Solutions Part I. Reaction Mechanism of 1-Butanol Oxidation***, J. Electroanal. Chem., 1997, 436, 65-72.

42. D. Takky, B. Beden, J. M. Leger, C. Lamy, ***Evidence for the Effect of Molecular Structure on the Electrochemical Reactivity of Alcohols: Part II. Electrocatalytic Oxidation of the Butanol Isomers on Platinum in Alkaline Medium***, J. Electroanal. Chem. Interfacial Electrochem., 1985, 193, 159−173.

43. M. Y. Zhu, G. Q. Sun, Q. Xin, ***Effect of Alloying Degree in PtSn Catalyst on the Catalytic behavior for Ethanol Electro-Oxidation***, Electrochim. Acta, 2009, 54, 1511−1518.

44. B. Habibi, E. Dadashpour, ***Electrooxidation of 2-Propanol and 2-Butanol on the Pt−Ni Alloy Nanoparticles in Acidic Media***, Electrochim. Acta, 2013, 88 , 157−164.

45. B. Katryniok, H. Kimura, E. Skrzynska, J. S. Girardon, P. Fongarland, M. Capron, R. Ducoulombier, N. Mimura, S. Paul, F. Dumeignil, ***Selective Catalytic Oxidation of Glycerol: Perspectives for High Value Chemicals***, Green Chem., 2011, 13, 1960-1979.

46. X. H. Xia, H. D. Liess, T. Iwasita, ***Early Stages in the Oxidation of Ethanol at Low Index Single Crystal Platinum Electrodes***, J. Electroanal. Chem., 1997, 437, 233-240.

47. J. M. Jin, T. Sheng, X. Lin, R. Kavanagh, P. Hamer, P. J. Hu, C. Hardacre, A. M. Bonastre, J. Sharman, D. Thompsett, W. F. Lin, ***The Origin of High Activity but Low CO_2 Selectivity on Binary PtSn in the Direct Ethanol Fuel Cell***, Phys. Chem. Chem. Phys., 2014, 16, 9432-9440.

48. J. Ribeiro, D. M. dos Anjos, J. M. Leger, F. Hahn, P. Olivi, A. R. de Andrade, G. Tremiliosi-Filho, K. B. Kokoh, ***Effect of W on PtSn/C Catalysts for Ethanol Electrooxidation***, J. Appl. Electrochem., 2008, 38, 653-662.

49. J. Rossmeisl, G. S. Karlberg, T. Jaramillo, J. K. Norskov, ***Steady State Oxygen Reduction and Cyclic Voltammetry***, Faraday Discuss., 2008, 140, 379-397.

50. H. Rostami, A. Omrani, A. AliRostami, ***On the Role of Electrodeposited Nanostructured Pd–Co Alloy on Au for the Electrocatalytic Oxidation of Glycerol in Alkaline Media***, Int. J. Hydrogen Energy, 2015, 40, 9444-9451.

51. M. Zhiani, H. Rostami, S. Majidi, K. Karami, ***Bis (Dibenzylidene Acetone) Palladium (0) Catalyst for Glycerol Oxidation in Half Cell and in Alkaline Direct Glycerol Fuel Cell***, Int. J. Hydrogen Energy, 2013, 38, 5435-5441.

Chapter Four

Activity Enhancement of Bulk Pd with Pb Decorated towards Ethanol Electrooxidation in Alkaline Media

4.1 Introduction

The development of direct alcohol fuel cells (DAFCs) has attracted considerable attention for portable applications due to its high efficiency, low emission and low toxicity for decades[1-6]. As a potential candidate of fuel, ethanol can be easily produced from renewable sources using a fermentation process[7]. It is also environmental-friendly compared to other liquid fuels such as methanol and formic acid[2]. More specifically, ethanol is non-toxic and has high gravimetric and volumetric energy density as it can transfer 12 electrons per molecule in the condition of fully electro-oxidized to CO_2 theoretically[8]. However the C-C bond cleavage is difficult to be implemented at low temperature[9-10]. Previous researched have been devoted to electrochemical oxidation of ethanol in alkaline medium rather than in acid atmosphere for the faster oxidation kinetics[11-12]. Moreover, intermediates such as CH_3COH and CHCO will prevent further adsorption and electrooxidation of ethanol, leading to a decrease in the catalyst efficiency[13]. These drawbacks have become a bottleneck in the commercialization of DEFCs. Consequently, high activity anode catalysts with high durability are extremely desired[14-16].

In alkaline media, Pd is considered more attractive than Pt for ethanol electrooxidation reaction(EOR) on the basis of the following reasons: Pd is more sufficient than Pt on the earth; Pd gives the higher electrocatalytic activity and less poisoning effect compared to Pt for EOR in alkaline medium. Therefore, Pd and Pd based catalysts for EOR in alkaline media has great potential for the application of DAFCs[17-22]. However, the Pd catalyst has some drawbacks. Especially, Pd is easily oxidized compared with Pt. Thus, one of the disadvantages of Pd as an anodic catalyst is its instability[23]. Previous research reported some efforts to improve the performance of Pd by combining Pd with other metals, such as Pd-Pt, Pd-Au[24], Pd-Ag[18], Pd-Sn[25]. The right combination of metals is important for producing the desirable effect[23].

It was reported that Pb in Pt-based catalysts can promote their tolerance towards CO-like specie poisoning by weakening the bond energy of Pt-CO or enhancing electrooxidation of CO-like species[26]. These promoting effects are defined as the electronic effect, the geometric effect and the bifunctional mechanism[26,27], which may also occur on Pd-based catalysts.

Based on the above considerations, we have managed to organize and compose Pb-decorated Pd and analyzed their electrocatalysts activity and durability in the direction of ethanol oxidation reaction (EOR) in alkaline circumstances at diversified temperatures and under half-cell conditions. It has showed, compared with conventional Pd, Pb-Pd catalyst displays considerably greater catalytic activity with a certain Pb coverage range. Moreover, by calculating activation energy using Arrhenius equation, the general kinetics data of EOR for Pb-trimmed bulk Pd and original bulk Pd have been acquired.

4.2 Experimental

4.2.1 Chemicals

Sulphuric acid (95%~98%, puriss grade), absolute ethanol, sodium hydroxide (semiconductor grade, 99.99%), lead chloride (99.999%). All chemicals were used as received without further purification. Water was purified in a thermoscientific Barnstead water System (18.2 MΩ•cm resistivity) and was used for the preparation of all aqueous solutions.

4.2.2 Electrochemical preparation and characterization

A water-jacketed variable temperature three-electrode setup was used to evaluate the efficiency of the PbPd catalyst towards the oxidation of ethanol in a alkaline media under a N_2 atmosphere. The electrochemical setup includes a piece of Pd mesh as the counter electrode, an Ag/AgCl (in saturated KCl) reference electrode for acidic media or a Hg/HgO (in 1 M NaOH) reference electrode for alkaline media, a bulk Pd / PbPd as working electrode. The cell was thoroughly cleaned by a solution of hydrogen peroxide and sulphuric acid followed by rinsed with boiling water before use. Prior to the electrochemical measurements, all solutions were deoxygenated by bubbling through high purity nitrogen gas for 30 minutes. Bulk Pd, working electrode, was mechanically polished successively using a range of alumina powders of different particle sized, e.g., 1,0.3 and 0.05 μm. It was then sonicated thoroughly with water in a bath-type ultrasonicator several times.

An Autolab electrochemical work station (Potentiostat, Eco Chemie, Netherlands) was employed for the electro-deposition and electrochemical measurements. Electrochemical data were recorded using Autolab NOVA software and further analysed using Excel.

4.2.3 Pb-decorated on bulk Pd

Pd supported Pb-Pd was prepared by electrochemical approach using $PdCl_2$. Before deposition, the bulk Pd was electrochemically cleaned and characterized in 0.1 M H_2SO_4 electrolyte solution by continuous potential cycling with a potential range of -0.15 to 1.35 V (*vs.* RHE) with a scan rate of 50 mV s^{-1} until the stable cyclic voltammograms were obtained. Lead atoms were then decorated by using cyclic voltammetry (CV) in a Pb^{2+}-containing solution (~10^{-5} M of Pb^{2+} ions, prepared from $PbCl_2$ dissolved in 0.1 M H_2SO_4) over a potential range of 0.05 to 0.75 V (*vs.* RHE) with a scan rate of 20 mV s^{-1}. The upper potential limit dropped down to 0.75 V (*vs.* RHE) to avoid strong oxygen adsorption occurring. Different Pb coverages were obtained by varying the potential cycling numbers in the CV. After the Pb-decoration, the electrode was rinsed gently with ultra pure water and transferred to a second cell with 0.1 M H_2SO_4 for electrochemical characterization employing CV. The practical coverage of Pb was evaluated using CV with the potential range of 0.15 to 0.75 V (*vs.* RHE) at a scan rate of 50 mV s^{-1}.

4.2.4 Ethanol electrooxidation on bare and Pb –decorated bulk Pd

Efficiency of electrooxidation reaction of ethanol on the bare and Pb-decoration bulk Pd were studied in a solution of 0.1 M Ethanol + 0.1 M NaOH at different temperatures employed by both cyclic voltammetry (CV) and chronoampromerty (CA). Electrolyte solution was deaerated by bubbling ultrapure N_2 for 30 minutes before experiments. The potential range between 0.11 and 1.11 V (*vs.* RHE) at a scan rate of 50 mV s^{-1} was used in the CV, whilst a fixed potential of 0.71 V (*vs.* RHE) was chosen for the CA as it is relevant to alkaline ethanol fuel cell. The current density of ethanol electrooxidation was normalized with the electrochemical surface area (ECSA) of bare bulk Pd.

4.3 Results and discussion

4.3.1 Electrochemical study of bulk Pd by cyclic voltammetry

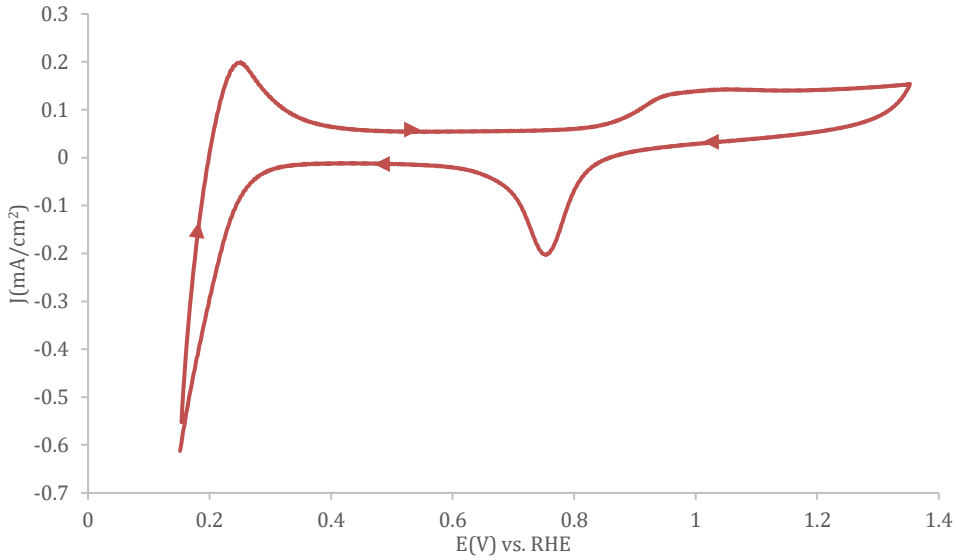

Figure 4.1 Cyclic voltammograms (CVs) obtained for bulk Pd in 0.1 M H_2SO_4 solution. Scan rate: 50 mVs^{-1} .

The cyclic voltammetric measurement of bulk Pd electrode was examined in 0.1M H_2SO_4 solution with a scan rate of 50 mVs^{-1} from 0.15 V to 1.35 V (*vs*. RHE) as shown in Figure 4.1. It can be seen that, on bulk Pd electrode, not only the adsorption and desorption of hydrogen, but also the hydrogen absorption can be noted, which follows the results reported formerly[28-29]. More specifically, the initial cathodic and anodic current peaks between 0.20 V and 0.45 V (*vs*. RHE) were associated with the hydrogen adsorption-desorption processes. Subsequently, a sharp peak of hydroxyl and oxygen species adsorption begins with 0.80 V (*vs*. RHE) and a small shoulder arises at around 1.05 V (*vs*. RHE). Lastly, a Pd oxide reduction peak shows up between 0.95 V to 0.6 V (*vs*. RHE) with the corresponding cathodic peak at around 0.75 V (*vs*. RHE)[30]. Additionally, the electrochemical active surface area (ECSA) of bulk Pd was

determined by the integrated charge of hydrogen adsorption/ desorption region by adjusting the assumption of 212 μC cm^{-2}. In order to compare the electrooxidation performance of bulk Pd, the current is normalized to electrochemical surface area (ECSA) current density (*J*).

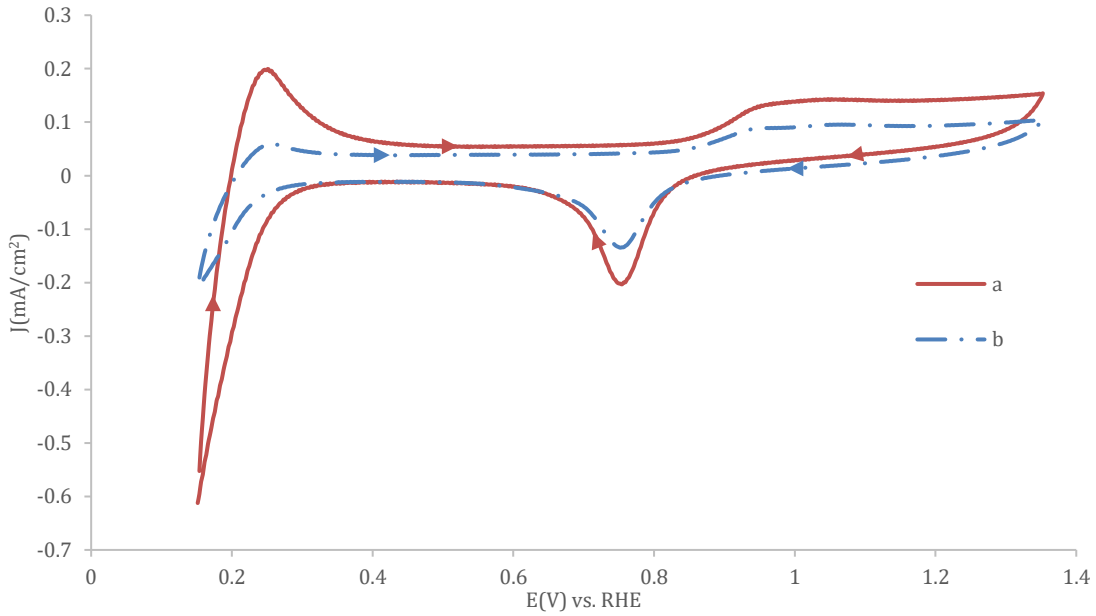

Figure 4.2 Cyclic voltammograms (CVs) obtained for a. bulk Pd and b. Pb-Pd (θ_{Pb} = 0.46) in 0.1 M H_2SO_4 solution. Scan rate: 50 mVs^{-1}.

Presented in Figure 4.2 are the cyclic voltammograms of the bulk Pd electrode and Pb-Pd electrode in 0.1 M H_2SO_4 operated from 0.15 V to 1.35 V (*vs*. RHE) at a scan rate of 50 mVs^{-1}. It can be observed that the hydrogen adsorption and desorption peaks of bulk Pd electrodes between 0.20 V to 0.45 V (*vs*. RHE) at a peak of 0.20mA·cm^{-2} while it's between 0.20 V to 0.33 V (*vs*. RHE) at a peak of 0.075 mA·cm^{-2} of Pb-Pd electrode, so the electrochemical surface area (ECSA) as well as the coverage of Pb can be evaluated. The formation waves and stripping peaks for Pb-Pd oxide on Pb-Pd

electrode are much more distinct than those on bulk Pd, indicating the presence of hydroxide adsorption as well as he high index facets on Pb-Pd electrode.

The total charge passed during hydrogen adsorption (Q_H)/desorption region between -0.30 V to 0.45 V (*vs*. RHE), after accounting for the double layer capacity, is used to determine the ECSA, dividing the proven assumption of 212 μC cm^{-2} for Pd surface[30].

The evaluation of Pb coverage (θ_{Pb}) can be equated with the blockage of hydrogen adsorption. Therefore, θ_{Pb} can be defined as:

$$\theta_{Pb} = 1 - \theta_H = 1 - \frac{Q_H^{Pb}}{Q_H^{bare}} \qquad (1)$$

Here Q_H^{Pb} is the charge for hydrogen adsorption on the Pb-Pd electrode while Q_H^{bare} is the charge for hydrogen adsorption on bare Pd.

It can be seen that the presence of Pb results in inhibited hydrogen adsorption and desorption processes on bulk Pd. The hydrogen adsorption/desorption peak at around 0.20 V (*vs*. RHE) disappears while that at 0.29 V (*vs*. RHE) remains noticeable, indicating Pb adatom being present preferentially on the stepped sites of the bulk Pd surface. It was found that Pb adatom on bulk Pd surfaces tend to diffuse and reach a position of a minimum energy[31]. The overall rate of Pb decoration is not only solution diffusion but also surface diffusion controlled, which has to facilitate the decoration of stepped surfaces. Once Pb adatom is deposited on terrace, it moves over the surface until it reaches a stepped sit where the energy level for adsorption is lower than that on terrace, Pb cannot move and is trapped on the stepped sit.

4.3.2 Ethanol electrooxidation reaction (EOR)

(a).

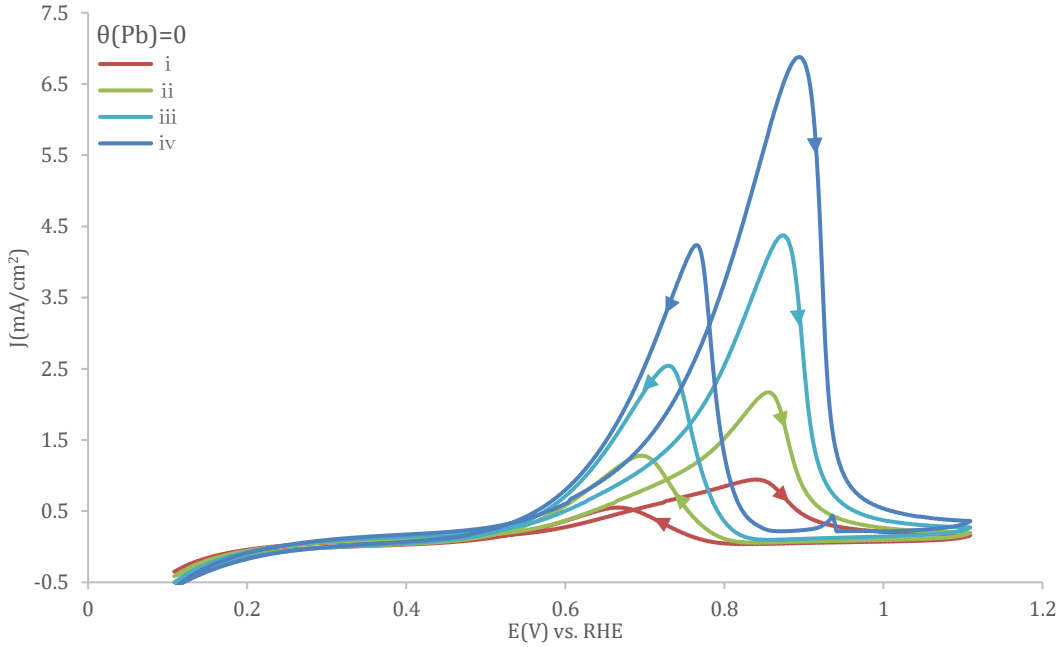

(b).

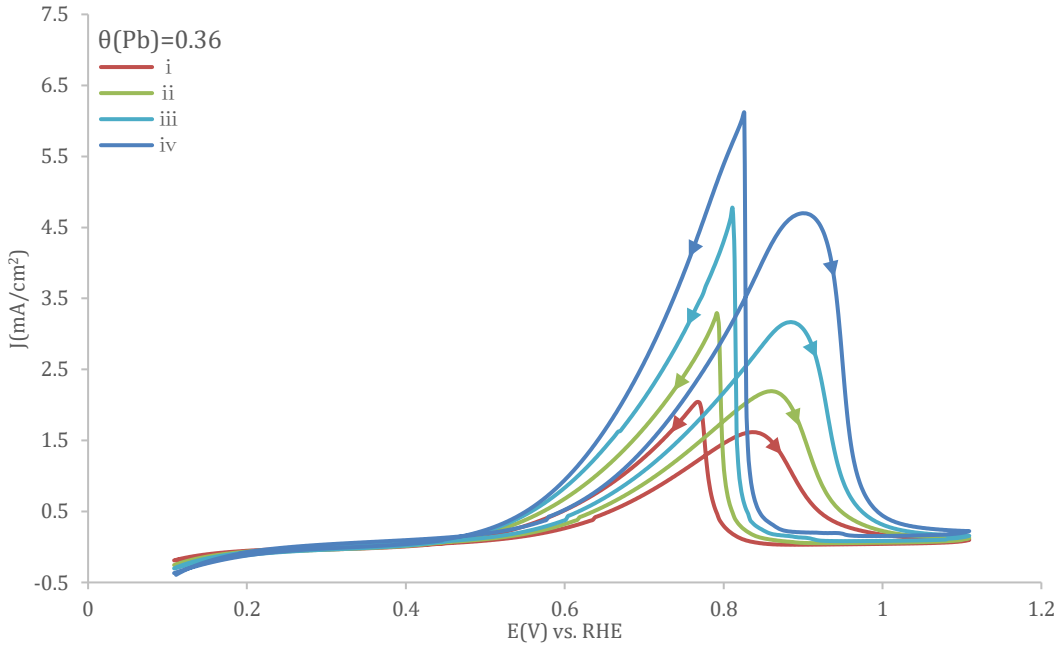

Figure 4.3. Cyclic voltammograms of (a). bulk Pd, (b). Pb-Pd (θ_{Pb} = 0.36) in 0.1 M Ethanol + 0.1 M NaOH solution at different temperatures: i. T = 25 ˚C, ii. T = 30˚C, iii. T = 40 ˚C, iv. T = 50 ˚C. Scan rate: 50 mVs^{-1}.

Presented in Figure 4.3.a and Figure. 4.3.b are the cyclic voltammetry curves of ethanol electrooxidation reaction on the bulk Pd electrode and Pb-Pd (θ_{Pb} =0.36) electrode in a solution of 0.1M NaOH and 0.1M EtOH at different temperatures of 30 ˚C, 40 ˚C, 50 ˚C and 60 ˚C at a scan rate of 50 mVs^{-1} from 0.11 V to 1.11 V (*vs*. RHE). The curves were recorded when stable responses were obtained. Two well-defined peaks observed on the figure represent as positive-going peak and negative-going peak are corresponded to different electrochemical process occurring on the surface of working electrode. During forward scan, the positive-going peaks are always used for evaluating the catalytic activity as they are associated with the ethanol oxidation, whereas the peaks in the backward scan mainly attributed to the further electrooxidation of carbonaceous species not completely oxidized in the forward scan[19, 32-34]. As seen from Fig. 4.3.a, at 30 ˚C, the ethanol oxidation reaction starts at 0.513 V (*vs.* RHE) and a forward current density peak cantered at 0.838 V (*vs.* RHE) with a value of 0.95 mA/cm^2 as a continues oxidation of ethanol. After the current density reaches the maximum value, it then starts to decline with a further increase in the potential. Precious studies suggested that the decrease in current density was related to the formation of the Pd (II) oxide layer on the surface of the electrode at higher potentials (Eqs.3 and Eqs.4)[35].

$$Pd - OH_{ads} + OH^- \leftrightarrow Pd - O + H_2O + e^- \qquad (2)$$

$$Pd - OH_{ads} + Pd - OH_{ads} \leftrightarrow Pd - O + H_2O \qquad (3)$$

The formation of the oxide layer can block the adsorption of the reactive species onto the Pd surface and lead to a decrease in the electrocatalytic activity, as a result, reducing

the current density. As the positive-going sweep proceeds, more Pd (II) oxide covers the surface of the electrode. Consequently, the current density of the EOR is further decreased with the increase in the potential. When the potential is above 1.11 V (*vs.* RHE), the current density drops to 0.01 mA/cm^2, indicating that the EOR occurs on the fully developed Pd oxide layer is negligible. Fortunately, the decrease in the electrocatalytic activity can be recovered during the negative-going sweep, as evidenced by the presence of backward peak at about 0.67 V (*vs.* RHE). This reactivation can be attributed to the reduction of the Pd (II) oxide, which is similar to the behaviour observed with the Pt-base catalyst[35-36].

$$Pd - O + H_2O + 2e^- \leftrightarrow Pd + 2OH^- \qquad (4)$$

The temperature effect of EOR on working electrode was investigated from CVs under different temperatures, the onset potentials are left shifting from 0.513 V (*vs*. RHE) to 0.486 V (*vs*. RHE) and forward peak current densities are increasing from 0.945 mA/cm^2 to 6.877 mA/cm^2 with the elevated temperatures from 30 ˚C to 60 ˚C, suggesting that the adsorption of the OH^- species on Pd surface is facilitated at higher temperatures. Notably, the peak current density of bulk Pd at 60 ˚C is 7.3 times superior to that at 30 ˚C. It appears that the catalyst surfaces get self activated with the more adsorbed OH^- species even at low potentials with the increasing temperatures[37-38].

In Figure 4.3.b, the temperature effect of EOR on Pb-Pd (θ_{Pb} =0.36) electrode follows the same routine of that on bulk Pd electrode. The onset potentials at 30 ˚C, 40 ˚C, 50 ˚C and 60 ˚C are following such order: $E_{o,\,30^\circ C} > E_{o,\,40^\circ C} > E_{o,\,50^\circ C} > E_{o,\,60^\circ C}$. Maximum current density at 30 ˚C is 1.617 mA/cm^2 while it is 4.70 mA /cm^2 at 60 ˚C which means the oxidation peaks are getting higher with the increasing of temperature during the forward scan. Meanwhile, compared with peak current density of EOR occurring on the bulk Pd, a larger peak current density of EOR occurring on the Pb-Pd (θ_{Pb} =0.36) is observed under same temperature, showing a better electrocatalytic performance of Pb-Pd (θ_{Pb} =0.36) electrode. Additionally, as corresponding Arrhenius plots shown in

Figure 4.11, the linear relationships between log J_p and 1/t of Pb-Pd (θ_{Pb} =0.36) maintains the same compared to that of bulk Pd, suggests that the reaction mechanism are consistent, as discussed later.

(a).

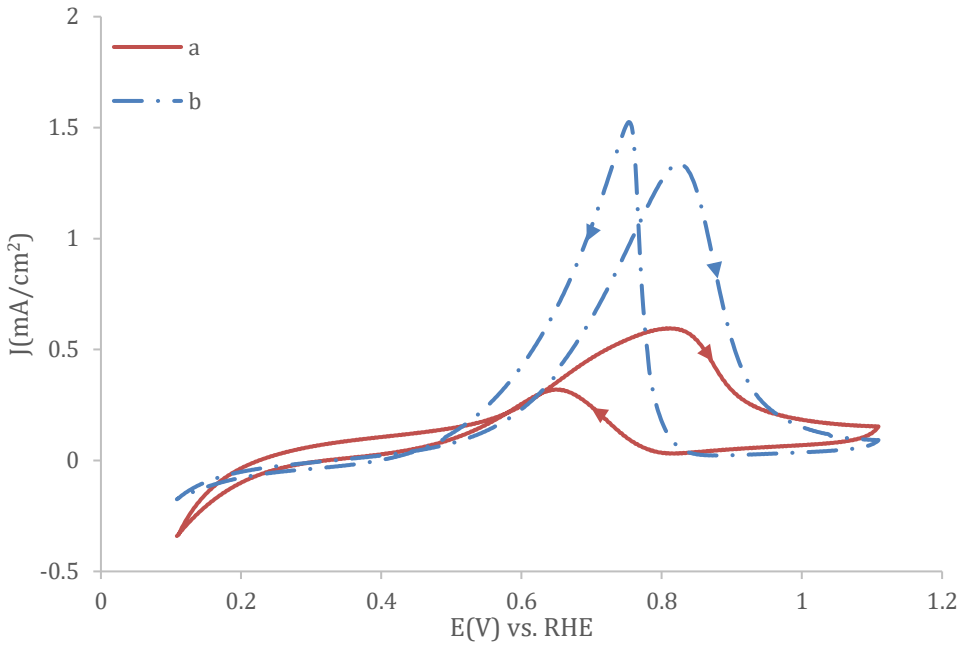

(b).

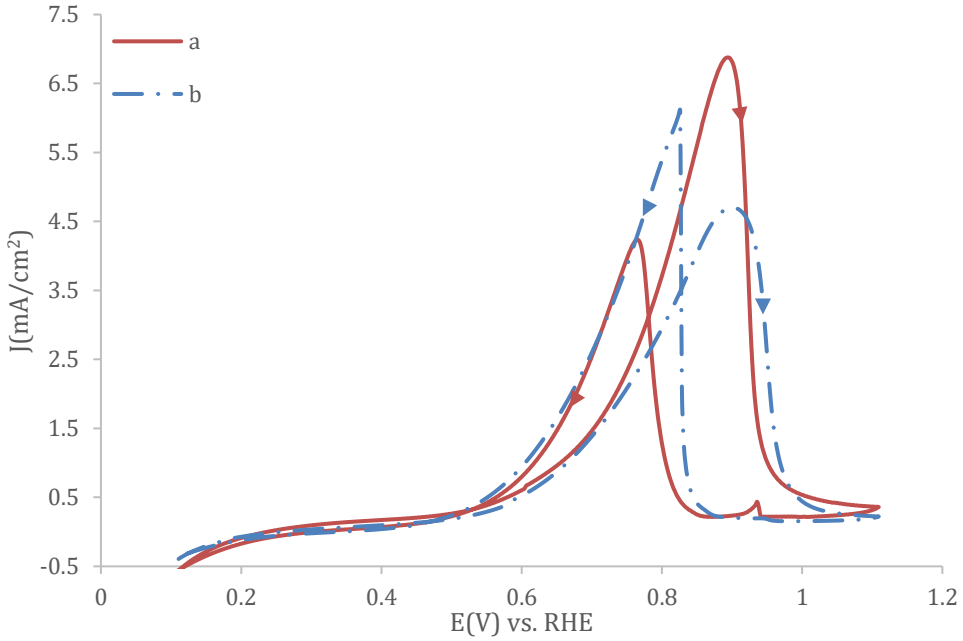

Figure 4.4. Cyclic voltammograms of (a). bulk Pd and Pb-Pd (θ_{Pb} = 0.36) at 25 ˚C, (b). bulk Pd and Pb-Pd (θ_{Pb} = 0.36) at 60 ˚C in 0.1 M Ethanol+ 0.1 M NaOH solution. Scan rate: 50mVs^{-1}. a. $\theta_{Pb} = 0$, b. $\theta_{Pb} = 0.36$.

In order to further investigate the impact of addition of Pb, CV curves of EOR on bulk Pd and Pb-decorated Pd at 25 ˚C and 60 ˚C are presented in Figure 4.4.a and 4.4.b. Under each temperature, the Pb-Pd (θ_{Pb} = 0.36) electrode is obviously a better catalyst compared to bulk Pd because it shows a bigger ethanol reaction peak current density of 1.337 mA/cm^2 at 25 ˚C and 4.700 mA/cm^2 at 60 ˚C, respectively. This result suggests that adding Pb could promote the Pd catalytic activity in ethanol oxidation. Therefore, a further investigating of optimal Pb coverage is indispensable.

(a).

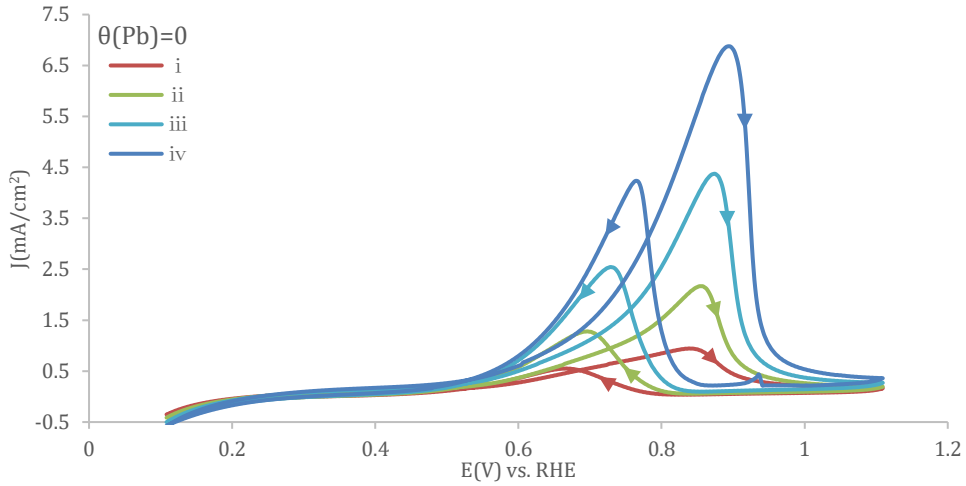
θ(Pb)=0
i
ii
iii
iv
J(mA/cm²)
E(V) vs. RHE

(b).

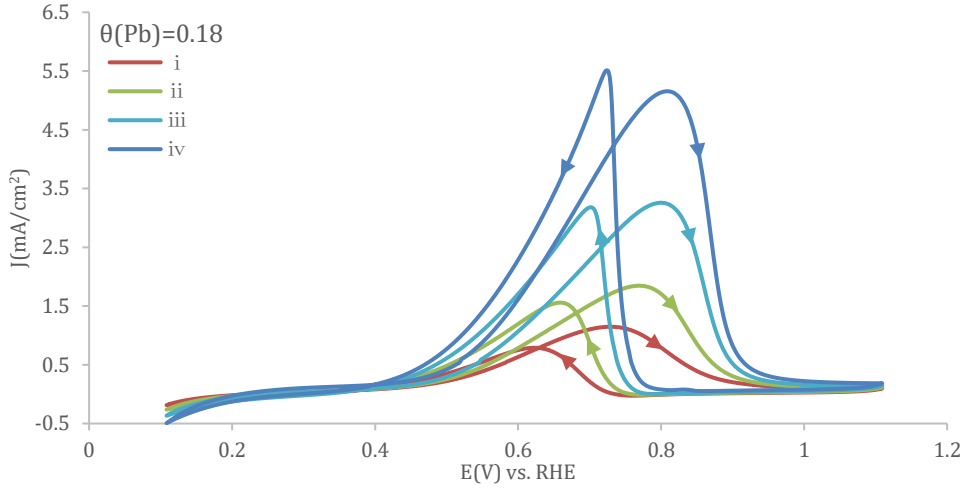
θ(Pb)=0.18
i
ii
iii
iv
J(mA/cm²)
E(V) vs. RHE

(c).

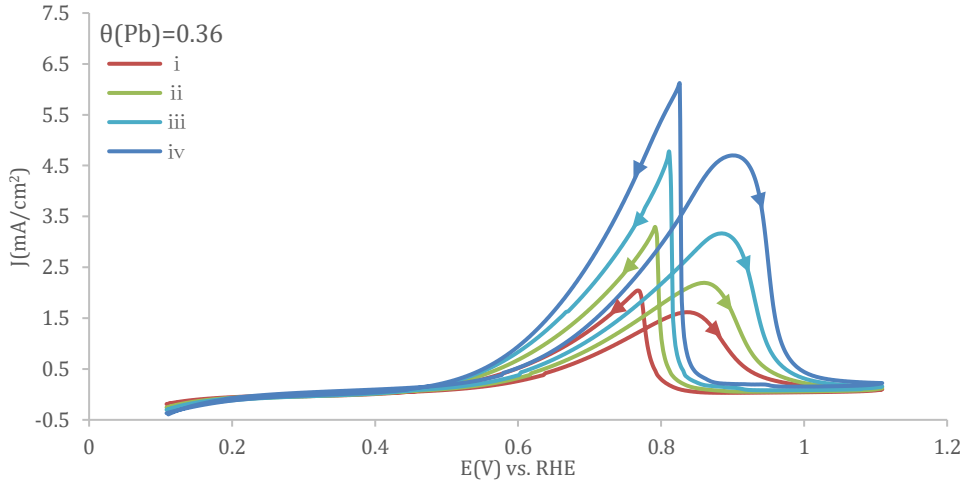
θ(Pb)=0.36
i
ii
iii
iv
J(mA/cm²)
E(V) vs. RHE

(d).

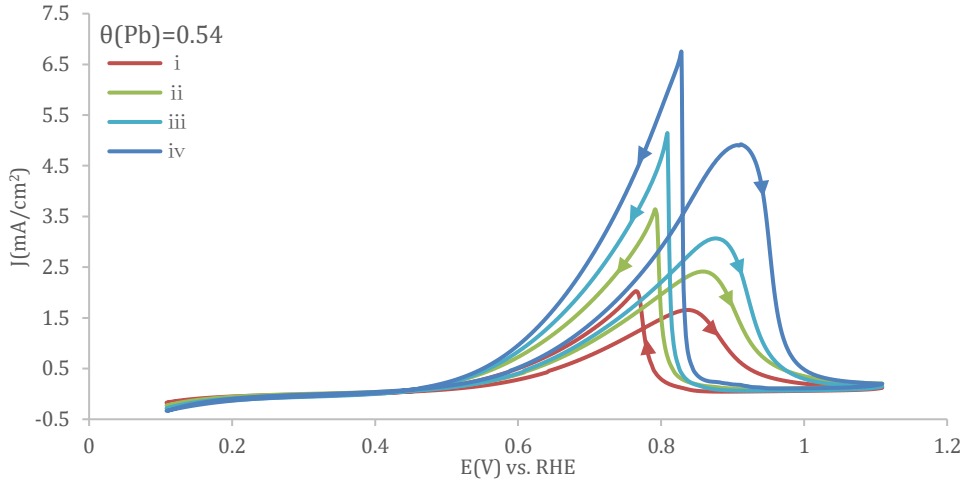

(e).

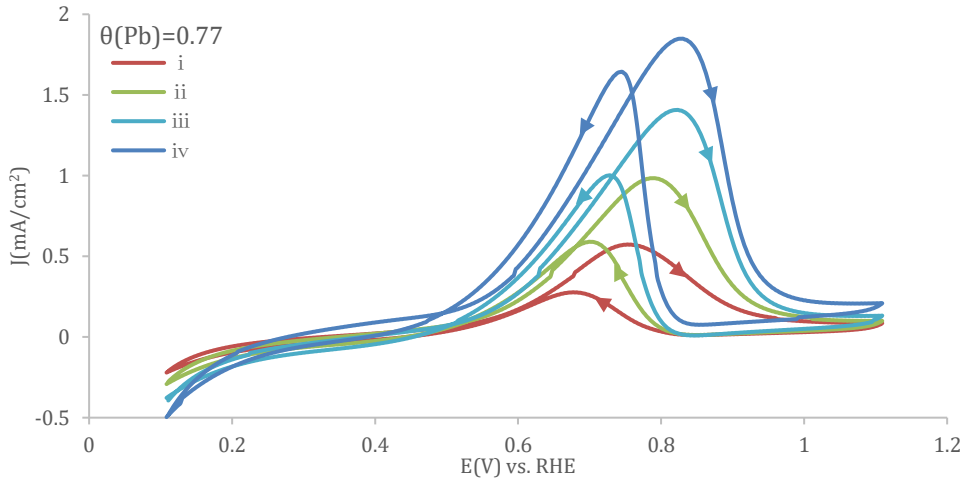

Figure 4.5 Cyclic voltammograms of bulk Pd with various Pb coverages: (a). $\theta_{Pb} = 0$, (b). $\theta_{Pb} = 0.18$, (c). $\theta_{Pb} = 0.36$, (d). $\theta_{Pb} = 0.54$, (e). $\theta_{Pb} = 0.77$ toward ethanol electrooxidation at different temperatures: i. T = 25 ˚C, ii. T =30 ˚C, iii. T =40 ˚C, iv. T =50 ˚C. in 0.1 M Ethanol + 0.1 M NaOH solution. Scan rate: 50mVs^{-1}.

Figure 4.5 displays the CVs of ethanol electrooxidation on bulk Pd with various Pb coverage ($\theta_{Pb} = 0, 0.18, 0.36, 0.54, 0.77$) under different temperatures (30, 40, 50, 60 ˚C) in 0.1M Ethanol+ 0.1M NaOH solution. For all the catalysts studies, remarkable enhancement in the EOR activities were observed with the increase of temperature from

30 ˚C to 60 ˚C, the onset potential shifted earlier/negatively and current density increased markedly at the elevated temperature, suggesting that formation of active surface oxidants and the kinetic of EOR were facilitated at higher temperatures[24].

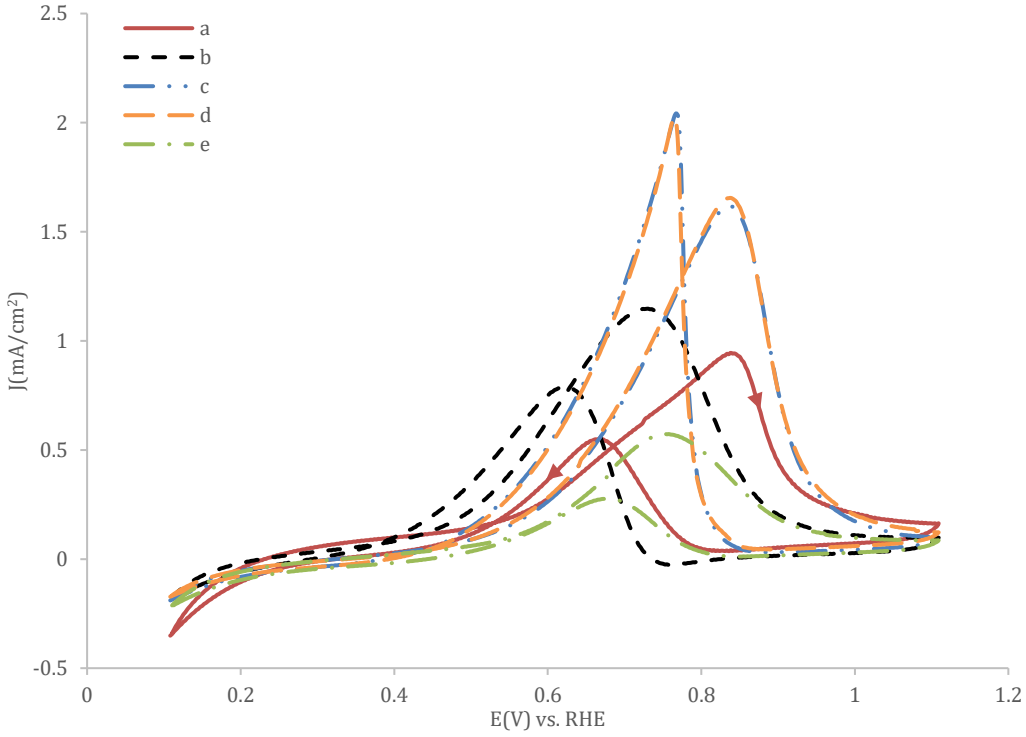

Figure 4.6 Cyclic voltammograms of Pb-Pd electrodes with different Pb coverages: (a). θ_{Pb} =0, (b). $\theta_{Pb} = 0.18$, (c). $\theta_{Pb} = 0.36$, (d). $\theta_{Pb} = 0.54$, (e). $\theta_{Pb} = 0.77$ toward ethanol electrooxidation in 0.1 M Ethanol + 0.1 M NaOH solution at 30 ˚C. Scan rate: 50 mVs^{-1}.

Figure 4.6 exhibits the cyclic voltammograms of Pb-Pd electrodes with different Pb coverages in 0.1 M Ethanol+ 0.1 M NaOH solution at 30˚C and it is obviously showing that Pb contributes a lot in the whole process. Pb-Pd (θ_{Pb} =0.54) catalyst exhibits a maximum positive peak current density of 1.655 mA/cm^2 whilst the peak current density of Pb-Pd (θ_{Pb} =0.36) catalyst achieves almost a same value of 1.617 mA/cm^2.

Moreover, the onset potential on the Pb-Pd (θ_{Pb} =0.54) catalyst and Pb-Pd (θ_{Pb} =0.36) catalyst at 30 ˚C are 0.408 V (*vs.* RHE) and 0.425 V (*vs.* RHE) respectively, more negative than that of bulk Pd. As is well known, the negative shift of onset potential indicates the significant enhancement in kinetics of the EOR[19]. Thus, the catalyst activity for ethanol electrooxidation achieves the best with Pb coverage at approximately 40%. However, Pb-Pd electrode facilitates the anodic oxidation under most coverage except 77%. This result suggests that adding Pb could promote the Pd catalytic activity in ethanol oxidation; but excessive Pb may begin to block the Pd active sites, leading to the decrease of total reaction.

(a).

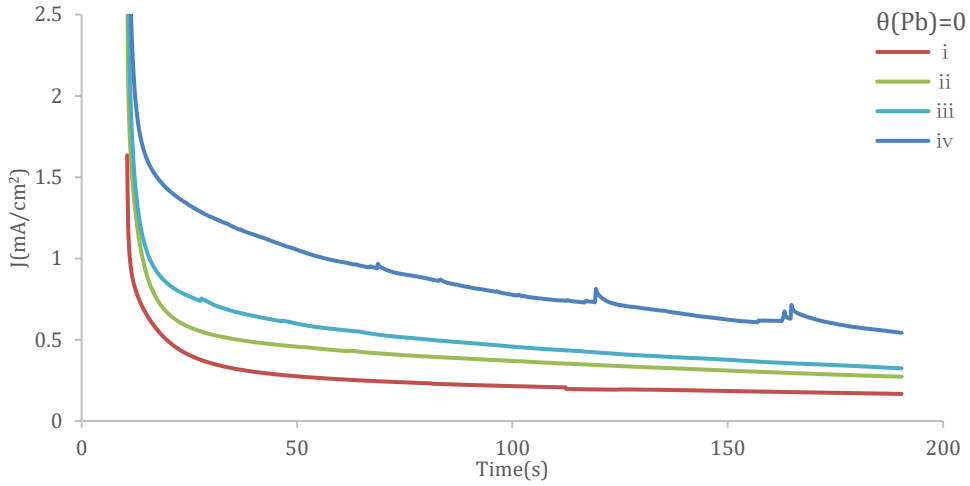
θ(Pb)=0
i
ii
iii
iv
J(mA/cm²)
Time(s)
0
0.5
1
1.5
2
2.5
0
50
100
150
200

(b).

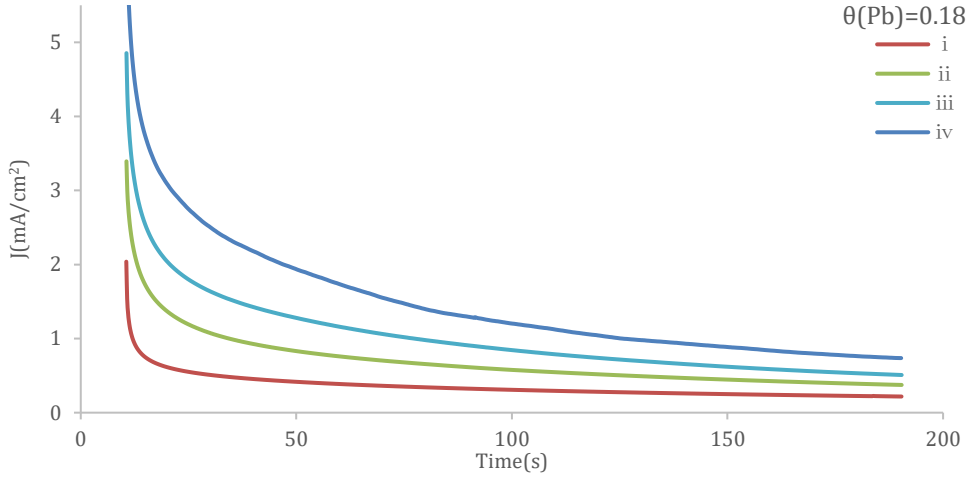
θ(Pb)=0.18
i
ii
iii
iv
J(mA/cm²)
Time(s)
0
1
2
3
4
5
0
50
100
150
200

(c).

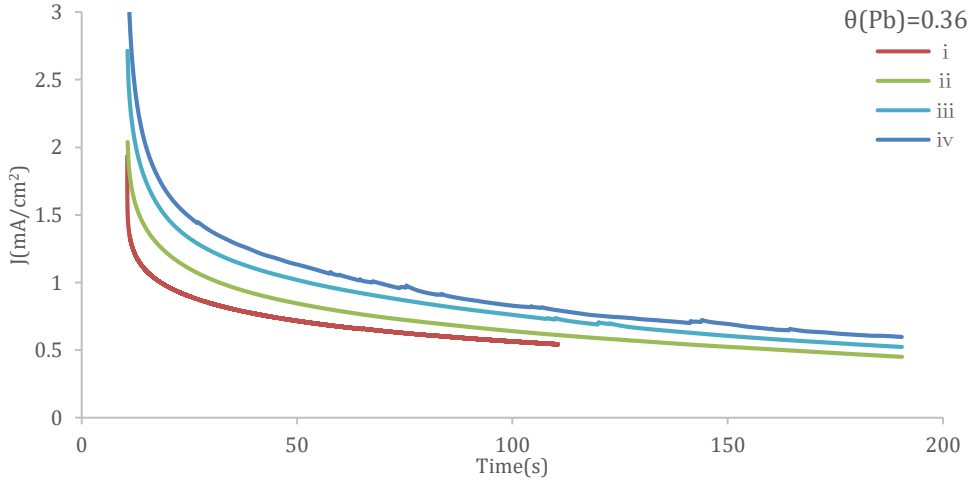
θ(Pb)=0.36
i
ii
iii
iv
J(mA/cm²)
Time(s)
0
0.5
1
1.5
2
2.5
3
0
50
100
150
200

(d).

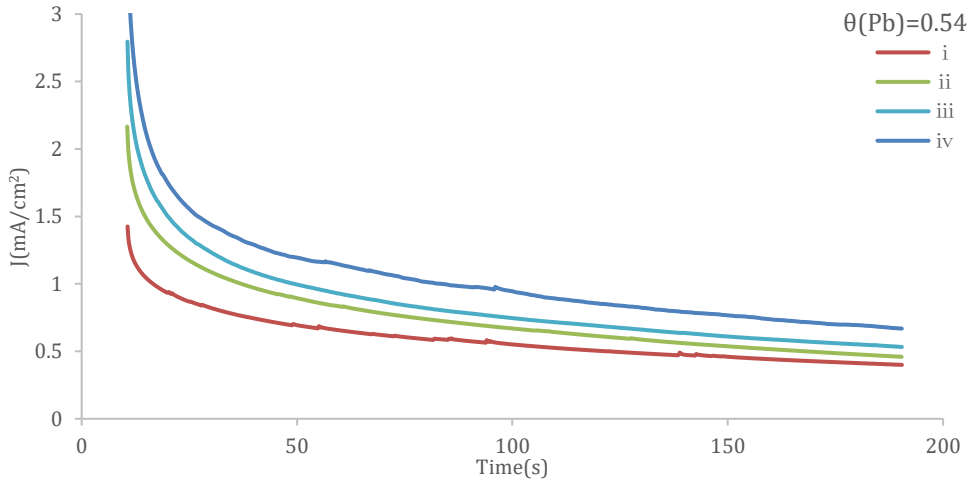

(e).

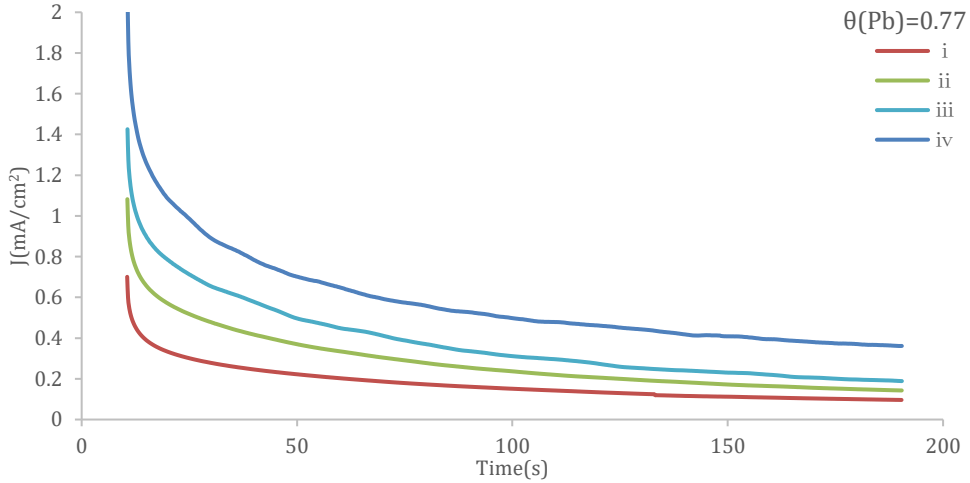

Figure 4.7 Chronoamperometric curves of bulk Pd and Pb-decorated Pd electrodes: (a). bulk Pd, (b). $\theta_{Pb} = 0.18$, (c). $\theta_{Pb} = 0.36$, (d). $\theta_{Pb} = 0.54$, (e). $\theta_{Pb} = 0.77$ in 0.1 M Ethanol + 0.1 M NaOH solution at the potential of 0.71 V (vs. RHE) under different temperatures: $i.\ T = 25\ ^{\circ}C$, $ii.\ T = 30\ ^{\circ}C$, $iii.\ T = 40\ ^{\circ}C$, $iv.\ T = 50\ ^{\circ}C$. Scan rate: 50 mVs^{-1}.

In order to further investigate the steady-state performance of ethanol electrooxidation and the poisoning condition on Pb-Pd electrode, Figure 4.7.(a), (b), (c), (d), (e) display the representative CAs of ethanol electrooxidation on bulk Pd without and with various Pb coverages ($\theta_{Pb} = 0, 0.18, 0.36, 0.54, 0.77$) under different temperatures (30, 40, 50,

60 ˚C) at a potential of 0.71 V (*vs.* RHE) for a period of 190 s in 0.1M EtOH + 0.1M NaOH solution presented. Prior to the current transients recorded at the study potential, the electrodes were initially kept at 1.01 V (*vs.* RHE) for 3 s to oxidize all the adsorbed intermediated and get the surface cleaned. Then, the electrodes were polarized at 0.11 V (*vs.* RHE) for 0.1s to reduce the oxides and adsorbed ethanol. Subsequently, constant potential tests were kept at 0.71 V (*vs.* RHE) for 190 s.

In all the transient curves, the current densities of all catalysts fall quickly at the stage of 0 – 20 s, which are ascribed to the deactivation of Pd surface by chemisorbed carbonaceous species, and then decrease slowly after that stage, finally tend to be relatively steady. Initially, the active surface sites are free from any adsorbed species. Ethanol would then be adsorbed during the oxidation process and accumulate intermediates such as CH_3CHO and CO-like species, which poison the active sites of the catalyst. Meanwhile, the liberation of the adsorbed species provides the new active sites for ethanol to continue EOR[39]. The data acquired shows that the electrocatalytic activity of both bulk Pd electrode and Pb-decorated Pd electrodes improve progressively with increasing temperature.

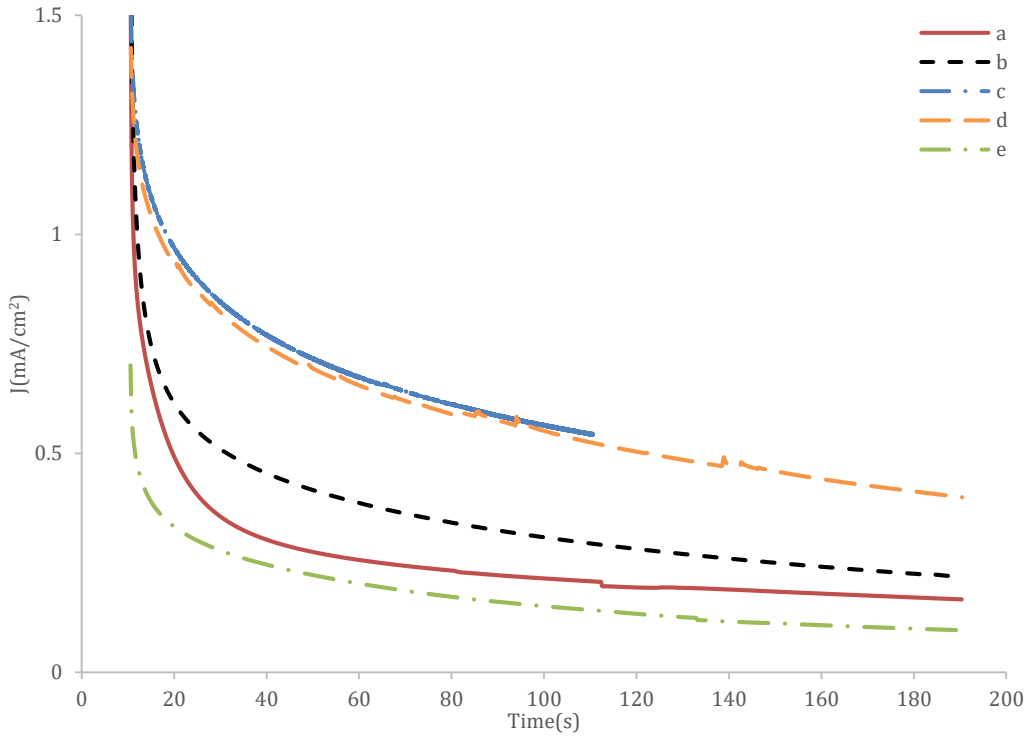

Figure 4.8 Chronoamperometric curves of Pb-Pd electrodes with different Pb coverages: a. θ_{Pb} =0, b. $\theta_{Pb} = 0.18$, c. $\theta_{Pb} = 0.36$, d. $\theta_{Pb} = 0.54$, e. $\theta_{Pb} = 0.77$ in 0.1 M Ethanol + 0.1 M NaOH solution at the potential of 0.71 V (vs. RHE) at 30 ˚C. Scan rate: 50 mVs^{-1}.

Figure 4.8 shows chomoamperometric curves of as-prepared Pb-Pd electro-catalysts with different Pb coverage in 0.1M Ethanol + 0.1M NaOH solution at the potential of 0.71 V (*vs*. RHE) at 30 ˚C. According to the current transient curves, the current densities decay dramatically at the initial stage and decay gradually achieving a pseudo steady state. It can be seen that current densities of Pb-Pd (θ_{Pb} =0.36) as well as Pb-Pd (θ_{Pb} =0.54) keeps highest in the first 100 s among all catalysts with that of bulk Pd has the bottommost activity indicating the better tolerance towards poisonous species and catalytic durability of the catalyst. However, Pb-Pd (θ_{Pb} =0.77) exhibits the lowest current density in the end, which is possibly due to the instability of superabundant Pb loaded.

In general, the chronoamperometry data are consistent with the cyclic voltammogram data and Pb-decorated Pb catalyst particularly with Pb coverage of 36% and 54% show better activities and stabilities compared to the bulk Pd catalyst.

Table 4.1.(a) List of onset potential (E_o), positive-going peak potentiall (E_p), positive-going peak current density (J_o), negative-going peak potential (E_n) and negative-going peak current density (J_n) obtained from Figure 4.5.a

Bulk Pd / Temp.	E_o / V (*vs*. RHE)	E_p / V (*vs*. RHE)	J_p /mA·cm^{-2}	E_n / V (*vs*. RHE)	J_n /mA·cm^{-2}
25 ˚C	0.521	0.811	0.596	0.655	0.320
30 ˚C	0.513	0.838	0.945	0.667	0.552
40 ˚C	0.501	0.853	2.167	0.696	1.280
50 ˚C	0.494	0.875	4.374	0.728	2.543
60 ˚C	0.486	0.894	6.877	0.765	4.236

Table 4.1.(b) List of onset potential (E_o), positive-going peak potential (E_p), positive-going peak current density (J_p), negative-going peak potential (E_n) and negative-going peak current density (J_n) obtained from Figure 4.5.c

θ_{Pb}=0.36 / Temp.	E_o / V (*vs*. RHE)	E_p / V (*vs*. RHE)	J_p /mA·cm^{-2}	E_n / V (*vs*. RHE)	J_n/ mA·cm^{-2}
25 ˚C	0.437	0.825	1.337	0.755	1.525
30 ˚C	0.425	0.838	1.617	0.469	2.043
40 ˚C	0.425	0.862	2.194	0.794	3.289
50 ˚C	0.422	0.886	3.167	0.813	4.765
60 ˚C	0.421	0.901	4.700	0.828	6.114

In order to understand the electro-catalytic of Pb-Pd electrode for ethanol electrooxidation reaction, the onset potential (E_o), positive-going peak potential (E_p),

positive-going peak current density (J_p), negative-going peak potential (E_n) and negative-going current density (J_n) which obtained from Figure 4.5 are listed in Table 4.1. As observed from Figure 4.5 and Figure A.1., E_o gets negative shifted whilst E_p gets positive shifted with the temperature ascending. The E_o of ethanol electrooxidation obtained on bulk Pd at 25 ˚C is 0.52 V (*vs.* RHE) while E_o of ethanol electrooxidation obtained on Pb-Pd (θ_{Pb} =0.36) at 25 ˚C is 0.437 V (*vs.* RHE), more negative than that of the bulk Pd and this tends to apply for all temperatures.

As the electroactive potential range for various alcohols are not identical, the peak current densities are obtained to plot profiles of the activation energy values calculated that are based on the Arrhenius equation seen below[40]:

$$\ln j = lnA - \frac{E_a}{RT} \qquad (5)$$

Where, j is the corresponding peak current densities. R is the gas constant, assuming 8.314 J K^{-1} mol^{-1}. T is the thermodynamic temperature (K) and E_a is the apparent activation energy at relevant peak potential.

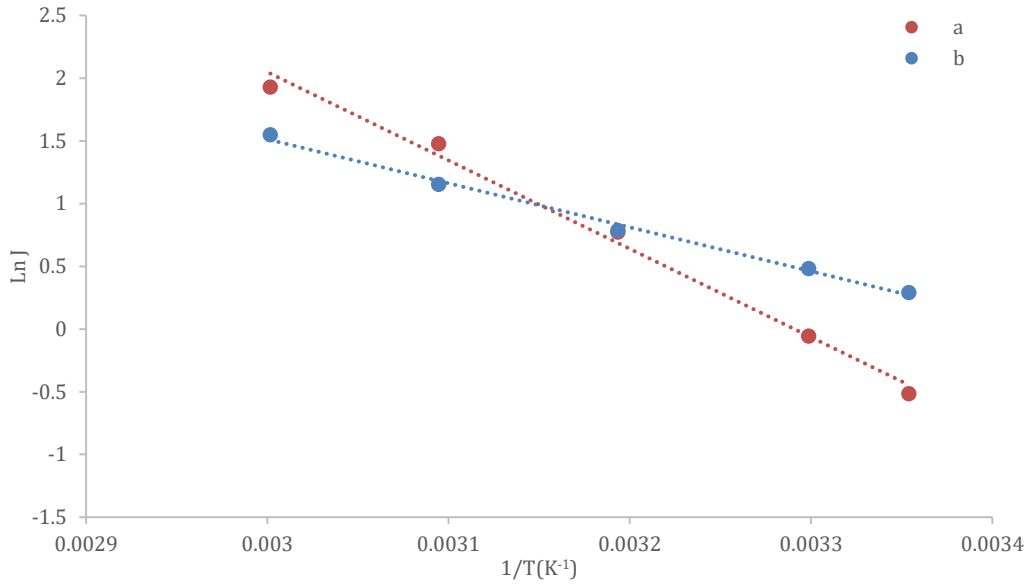

Figure 4.9 Arrhenius plots for ethanol electrooxidation on a. bulk Pd and b. Pb-Pd (θ_{Pb} = 0.36) at peak potential.

Presented in Figure 4.9 are the Arrhenius plots for ethanol electrooxidation on bulk Pd and Pb-Pd (θ_{Pb} =0.36) in the resulting peak current densities on the anodic sweep obtained from Figure 4.5 and Figure A.4.1. From these plots, the EOR activation energy value was calculated based on Arrhenius equation as appointed before. The linear relationship between log J and 1/t suggests that the reaction mechanism is not changed with different catalyst. Compared with the E_a value of bulk Pd (58.57 kJ/mol), the E_a value of Pb-Pd (θ_{Pb} =0.36) is relatively lower with a value of 29.181 kJ/mol. As is accepted widely, the electrooxidation of ethanol consists of a dual pathway mechanism[41], under this circumstance, lower E_a means a higher intrinsic activity.

4.3.3 Activation energies

(a).

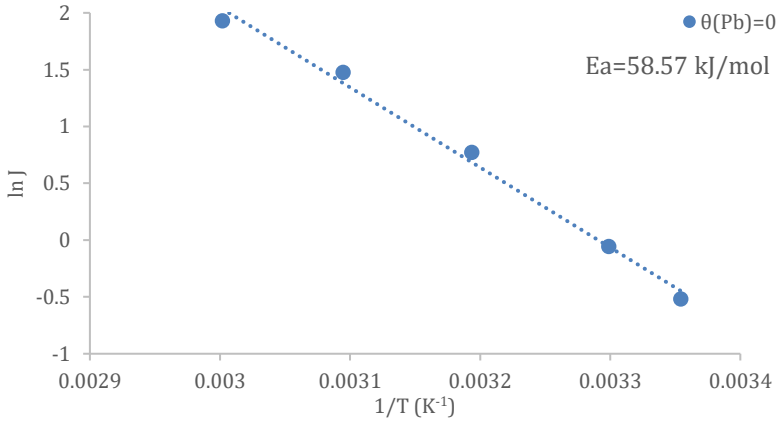

(b).

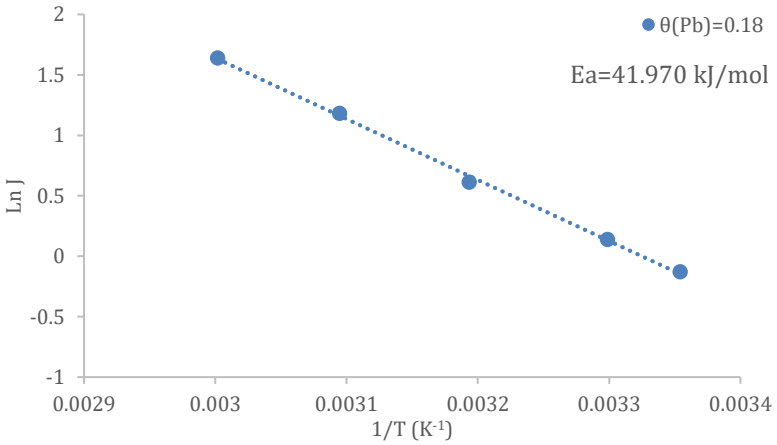

(c).

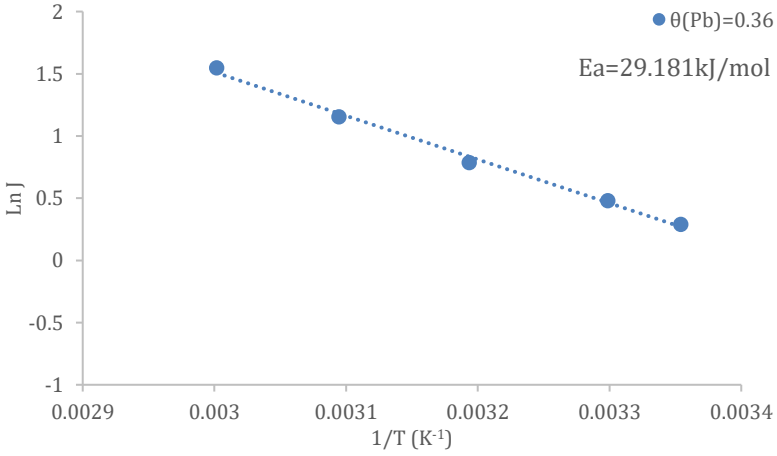

(d).

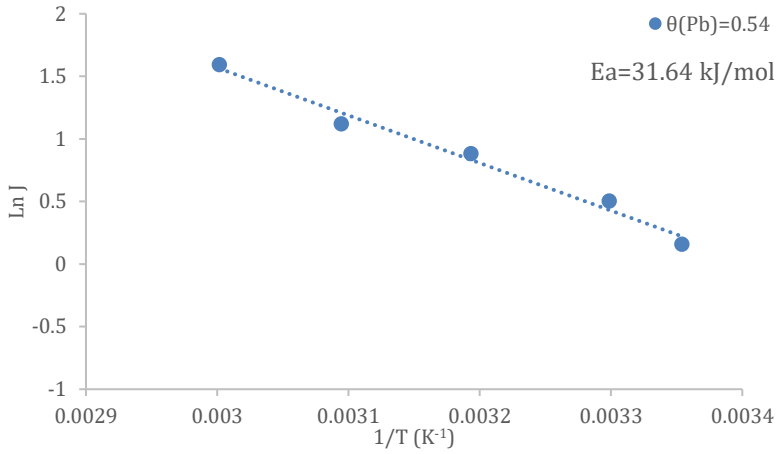

(e).

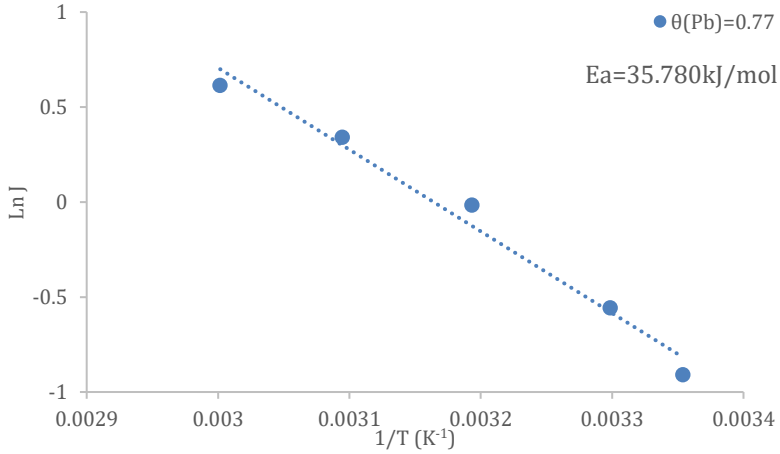

Figure 4.10 Arrhenius plots of the ethanol electrooxidation reaction (EOR) on the Pd with various Pb coverages: (a). $\theta_{Pb} = 0$, (b). $\theta_{Pb} = 0.09$, (c). $\theta_{Pb} = 0.36$, (d). $\theta_{Pb} = 0.54$, (e). $\theta_{Pb} = 0.77$, the data were obtained from current densities at peak potential on the anodic sweep for EOR at different temperatures in 0.1 M Ethanol + 0.1 M NaOH solution;

The Arrhenius plots for EOR on the Pd with various Pb coverages are displayed in Figure 4.10. The records were based on peak current density on the anodic sweep for EOR at each temperature obtained from Figure 4.5. From these plots, the EOR activation energy value was calculated based on Arrhenius equation. The lowest value of 29.18 kJ/mol for the EOR on Pb-Pd (θ_{Pb} = 0.36) is obtained as against the highest value of 58.57 kJ/mol on Pb-Pd (θ_{Pb} = 0). The activation energy values for Pb-Pd (θ_{Pb}

= 0), Pb-Pd (θ_{Pb} = 0.09), Pb-Pd (θ_{Pb} = 0.18), Pb-Pd (θ_{Pb} = 0.25), Pb-Pd (θ_{Pb} = 0.36), Pb-Pd (θ_{Pb} = 0.46), Pb-Pd (θ_{Pb} = 0.54), Pb-Pd (θ_{Pb} = 0.77) are 58.57, 50.339, 41.970, 29.181, 33.046, 31.64, 35.780 kJ/mol, respectively. The lower Ea means a higher intrinsic activity for the catalyst, as the effect of catalyst surface area has been excluded. Pb-Pd (θ_{Pb} = 0.36) achieved the best among all the catalysts, which is consistent with the above observation.

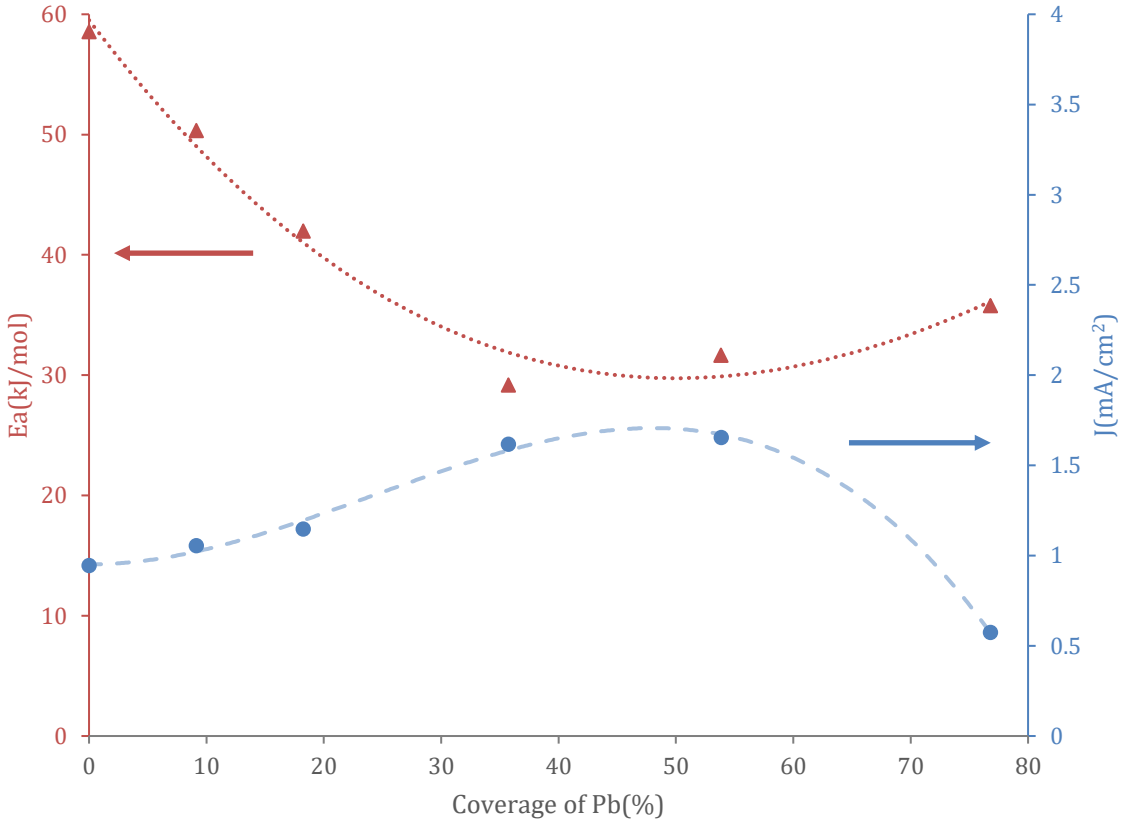

Figure 4.11 Plots of the peak current density and activation energy obtained for EOR on Pb-decorated Pd as a function of typical Pb-coverages. Activation energies were calculated from the Arrhenius plots in Figure 4.10 and the Arrhenius equation whilst peak current densities were only referred to CVs of EOR at 30 ˚C.

The activation energy for the EOR along with the peak current density obtained from CVs at 30 ˚C on Pb-decorated Pd as a function of Pb coverage is shown in Figure 4.11. It can be obtained that E_a starts with a highest value of 58.57 kJ/mol with the Pd coverage of zero whilst the current density is in a lower station. Followed by a decreasing tendency, a minimum value of *Ea* is exhibited with 29.181 kJ/mol at Pb-Pd (θ_{Pb} =0.36) while an optimum current density is achieved between 1.617 mA·cm^{-2} ($\theta_{Pb} = 0.36$) and 1.655 mA·cm^{-2} ($\theta_{Pb} = 0.54$) after an increasing from 0.609 mA·cm^{-2} ($\theta_{Pb} = 0$). Further increase/decrease of electro-catalytic/current density activity are achieved by higher Pb coverage on the bulk Pd. With a higher Pb coverage, e.g., 0.77, the peak current density dropped to a bottom value (0.57 mA·cm^{-2}) whilst the corresponding activation energy increased to 35.78 kJ/mol. The lower E_a indicates a higher intrinsic activity for the catalyst, as the effect of catalyst surface area has been excluded[42].

4.4 Conclusions

Based on comparison of the electrooxidation of ethanol on bulk Pd electrode and various coverages of Pb-decorated Pd electrodes in alkaline media, significantly higher activity of a Pb-Pd bimetallic catalyst compared to the pure Pd has been clearly demonstrated. The reactivity of the catalysts towards ethanol electrooxidation reaction (EOR) was studied at various temperatures and under other conditions that practical fuel cells operate using cyclic voltammetry (CV) and chronoamperometry (CA). For all catalysts, increasing temperature from 25 ˚C to 60 ˚C enhance the reactivity commendable. Pb-Pd (θ_{Pb} = 0.36) catalyst displayed almost the highest peak current density of 1.617 mA·cm^{-2} at 30 ˚C, which is roughly 3 times higher than that of bulk Pd (0.609 mA·cm^{-2}). Moreover, relevant activity enhancements, up to 3 times, were observed for the Pb-Pd (θ_{Pb} = 0.36) with corresponding activation energy being reduced significantly.

4.5 Reference

1. E. Antolini, E. R. Gonzales, ***Alkaline direct alcohol fuel cells***, J. Power Sources, 2010, 195, 3241-3450.

2. C. Lamy, E. M. Belgsir, J. M. Leger, ***Electrocatalytic oxidation of aliphatic alcohols: Application to the direct alcohol fuel cell (DAFC)***, J. Appl. Electrochem., 2001, 31, 799–809.

3. C. Bianchini, P. K. Shen, ***Palladium-Based Electrocatalysts for Alcohol Oxidation in Half Cells and in Direct Alcohol Fuel Cells***, Chem. Rev., 2009, 109, 4183–4206.

4. F. Vigier, C. Coutanceau, A. Perrard, E. M. Belgsir, C. Lamy, ***Development of anode catalysts for a direct ethanol fuel cell***, J. Appl. Electrochem., 2004, 34, 439-446.

5. K. Matsuoka, M. Inaba, Y. Iriyama, T. Abe, Z. Ogumi, M. Matsuoka, ***Anodic Oxidation of Polyhydric Alcohols on a Pt Electrode in Alkaline Solution***, Fuel Cells, 2002, 2, 35-39.

6. Y. H. Xue, L. Zhsng, W. J. Zhou, S. H. Chan, ***Pd Nanoparticles Supported on PDDA-functionalized Carbon Black with Enhanced ORR Activity in Alkaline Medium***, Int. J. Hydrogen Energy, 2014,39, 8449-8456.

7. F. P. Hu, C. L. Chen, Z. Y. Wang, G. Y. Wei, P. K. Shen, ***Mechanistic study of ethanol oxidation on Pd-NiO/C electrocatalyst,*** Electrochim. Acta, 2006, 52, 1087-1091.

8. R. Kavanagh, X. M. Cao, W. F. Lin, C. Hardacre, P. Hu, ***Origin of low CO_2 selectivity on platinum in the direct ethanol fuel cells***, Angew. Chem. Int. Ed., 2012, 51, 1572–1575.

9. A. Kowal, M. Li, M. Shao, K. Sasaki, M. B. Vukmirovic, J. Zhang, N. S. Marinkovic, P. Liu, A. I. Frenkel, R. R. Adzic, ***Ternary Pt/Rh/SnO Electrocatalysts for Oxidizingethanol to CO_2***, Nat. Mater., 2009, 8, 325-330.

10. Z. Y. Zhou, Q. Wang, J. L. Lin, N. Tian, S. G. Sun, ***In situ FTIR Spectroscopic Studies of Electrooxidation of Ethanol on Pd Electrode in Alkaline Media***, Electrochim. Acta, 2010, 55, 7995-7999.

11. M. K. Jeon, J. S. Cooper, P. J. McGinn, ***Methanol Electro-oxidation by a Ternary Pt-Ru-Cu Catalyst Identified by a Combinatorial Approach***, J. Power Sources, 2008,185, 913-916.

12. L. Jiang, A. Hsu, D. Chu, R. Chen, ***Ethanol Electro-oxidation on Pt/C and PtSn/C Catalysts in Alkaline and Acid Ssolutions***, Int. J. Hydrogen Energy, 2010, 35, 365-372.

13. P. Wu, Y. Y. Huang, L. Q. Zho, Y. B. Wang, Y. K. Bu, J. N. Yao, ***Nitrogen-doped Graphene Supported Highly Dispersed Palladium-Lead Nanoparticles for Synergetic Enhancement of Ethanol Electrooxidation in Alkaline Medium***, Electrochim. Acta, 2015, 152, 68–74.

14. S. Q. Song, P. Tsiakaras, ***Recent Progress in Direct Ethanol Proton Exchange Membrane Fuel Cells (DE-PEMFCs)***, Appl. Catal. B: Environ., 2006, 63, 187-193.

15. M. Winter, R. J. Brodd, ***What Are Batteries, Fuel Cells, and Supercapacitors?*** Chem. Rev., 2004, 104, 4245-4270.

16. C. Lamy, S. Rousseau, E. M. Belgsir, C. Coutanceau, J. M. Léger, ***Recent Progress in the Direct Ethanol Fuel Cell: Development of New Platinum-Tin Electrocatalysts***, Electrochim. Acta, 2004, 49, 3901-3908.

17. Y. Y. Huang, Y. L. Guo, Y. B. Wang, J. N. Yao, ***Synthesis and Performance of a Novel PdCuPb/C Nanocatalyst for Ethanol Electrooxidation in Alkaline Medium***, Int. J. Hydrogen Energy, 2014, 39, 4274-4281.

18. S. T. Nguyen, H. M. Law, A. T. Nguyen, N. Kristian, S. Wang, S. H. Chan, X. Wang, ***Enhancement Effect of Ag for Pd/C Towards the Ethanol Electro-oxidation in Alkaline Media***, Appl. Catal., B: Environmental, 2009, 91, 507-515.

19. H. L. Yang, S. U. Kang, H. Zou, J. Jin, J. T. Ma, S. W. Li, ***Polydopamine-functionalized Multi-walled Carbon Nanotubes-supported Palladium-lead Bimetallic Alloy Nanoparticles as Highly Efficient and Robust Catalysts for Ethanol Oxidation***, RSC Adv., 2016, 6, 90462-90464.

20. C. W. Xu, L. Q. Cheng, P. K. Shen, Y. L. Liu, ***Methanol and Ethanol Electrooxidation on Pt and Pd Supported on Carbon Microspheres in Alkaline Media***, Electrochem. Commun., 2007, 9, 997–1001.

21. C. W. Xu, P. K. Shen, Y. L. Liu, ***Ethanol Electrooxidation on Pt/C and Pd/C Catalysts Promoted with Oxide***, J. Power Sources, 2007, 164, 527–531.

22. X. Yu, G. Peter. ***Novel Pd–Pb/C Bimetallic Catalysts for Direct Formic Acid Fuel Cells***, J. Power Sources, 2009, 192, 279-284.

23. K. Persson, A. Ersson, K. Jansson, N. Iverlund, S. Jaras, ***Influence of co-metals on Bimetallic Palladium Catalysts for Methane Combustion***. J. Catal., 2005, 231, 139.

24. S. S. Mahapatra, A. Dutta, J. Datta, ***Temperature Effect on the Electrode Kinetics of Ethanol Oxidation on Pd Modified Pt Electrodes and the Estimation of Intermediates Formed in Alkali Medium***, Electrochim, Acta, 2010, 55, 9097-9104.

25. A. Sadiki, P. Vo, S.Z. Hu, T. S. Copenhaver, L. Scudiero, S. Ha, J. L. Haan, ***Increase Electrochemical Oxidation Rate of Alcohols in Alkaline Media on***

Palladium Surfaces Electrochemically Modified by Antimony, Lead, and Tin, Electrochim, Acta, 2014, 139, 302-307.

26. D. J. Chen, Z. Y. Zhou, Q. Wang, D. M. Xiang, N. Tian, S. G. Sun, ***A non-intermetallic PtPb/C Catalyst of Hollow Structure with High Activity and Stability for Electrooxidation of Formic Acid***, Chem. Commun., 2010, 46, 4252-4254.

27. Y. Y. Huang, J. D. Cai, M. Y. Liu, Y. L. Guo, ***Fabrication of a Novel PtPbBi/C Catalyst for Ethanol Electro-oxidation in Alkaline Medium***, Electrochim, Acta, 2012, 83, 1-6.

28. P. M. Rigano, C. Mayer, T. Chierchie, ***Structural Investigation of the Initial Stages of Copper Electrodeposition on Polycrystalline and Single Crystal Palladium Electrodes***, Electrochim. Acta, 1990, 45, 1189-1194.

29. A. N. Correia, L. H. Mascaro, S. A. S. Machado, L. A. Avaca, ***Active Surface Area Determination of Pd- Si Alloys by H-adsorption***, Electrochim. Acta, 1997, 42, 493-495.

30. N. Tian, Z. Y. Zhou, N. F. Yu, L. Y. Wang, S. G. Sun, ***Direct Electrodeposition of Tetrahexahedral Pd Nanocrystals with High-Index Facets and High Catalytic Activity for Ethanol Electrooxidation***, J. Am. Chem. Soc., 2010, 132, 7580-7581.

31. E. Herrero, V. Climent, J. M. Feliu, ***On the Different Adsorption Behaviour of Bismuth, Sulphur, Selenium and Tellurium on a Pt(775) Stepped Surface***, Electrochem. Commum., 2000, 2, 636-640.

32. M. C. Morin, C. Lamy, J. M. Leger, J. L. Vasquez, A. Aldaz, ***Structural Effects in Electrocatalysis – Oxidation of Ethanol on Platinum Single- Crystal Electrodes: Effect of PH***, J. Electroanal. Chem., 1990, 283, 287-302.

33. J. C. Huang, Z. L. Liu, C. B. He, L. M. Gan, ***Synthesis of PtRu Nanoparticles From the Hydrosilylation Reaction and Application as Catalyst for Direct Methanol Fuel Cell***, J. Phys. Chem. B, 2005, 109, 16644-16649.

34. H. Na, L. Zhang, H. Qiu, T. Wu, M. Chen, N. Yang, L. Li, F. Xing, J. Gao, ***A Two Step Method to Synthesize Palladium-copper Nanoparticles on Reduced Graphene Oxide and their Extremely High Electrocatalytic Activity for the Electrooxidation of Methanol and Ethanol***, J. Power Sources, 2015, 288, 160–167.

35. Z. X. Liang, T. S. Zhao, J. B. Xu, L. D. Zhu, ***Mechanism Study of the Ethanol Oxidation Reaction on Palladium in Alkaline Media***, Electrochim. Acta, 2009, 54, 2203-2208.

36. M. Grden, A. Czerwinski, ***EQCM Studies on Pd–Ni Alloy Oxidation in Basic Solutio***, J. Solid State Electrochem. 2008, 12, 375-385.

37. S. S. Mahapatra, A. Dutta, J. Datta, ***Temperature Effect on the Electrode Kinetics of Ethanol Oxidation on Pd Modified Pt Electrodes and the Estimation of Intermediates Formed in Alkali Medium***, Electrochim. Acta, 2010, 55, 9097-9104.

38. Y. Kang, W. Wang, Y. L. Pu, J. M. Li, D. Chai, Z. Q. Lei, ***An Effective Pd-NiO_x-P Composite Catalyst for Electrooxidation: Co-existed Phosphorus and Nickel Oxide to Enhance Performance of Pd***, Chem. Eng. J., 2017, 308, 419-427.

39. Y. Ma, H. Li, H. Wang, X. Mao, V. Linkov, S. Ji, O. U. Gcilitshana, R. Wang, ***Evolution of the Electrocatalytic Activity of Carbon-supported Amorphous Platinum-ruthenium-nickel-phosphorous nanoparticles for Methanol Oxidation***, J. Power Sources, 2014, 268, 498-507.

40. J. L. Cohen, D. J. Volpe, H. D. Abruna, ***Electrochemical Determination of Activation Energies for Methanol Oxidation on Polycrystalline Platinum in Acidic and Alkaline Electrolytes***, Phys. Chem. Chem. Phys., 2007, 9, 49-77.

41. S. C. S. Lai, M. T. M. Koper, ***Ethanol Electro-oxidation on Platinum in Alkaline Media***, Phys. Chem. Chem. Phys., 2009, 11, 10446-10456.

42. S. T. Nguyen, H. M. Law, H. T. Nguyen, N. Kristian, S. Y. Wang, S. H. Chan, X. Wang, ***Enhancement Effect of Ag for Pd/C Towards the Ethanol Electro-oxidation in Alkaline Media***, Appl. Catal. B-Environ., 2009, 91, 507-515.

Chapter Five

Preparation and Structure and Reactivity Studies of Au-Pd Nanoparticles-polymer Nanocomposites towards Ethanol Electrooxidation in Alkaline Media

5.1 Introduction

Direct ethanol fuel cells (DEFCs) have attracted increasing interest as it come with advantages in many facets such as low-toxicity, high power density, remarkable renewability, superior stability and other features. Despite the fact that the surface electrochemical reactions are still unclear, such fuel cells have been used to generate power for practical applications[1-6]. Moreover, DEFCs functioning in alkaline conditions can significantly enhance the electrochemical kinetics at low anodic over potential and reduce the risk of corrosion of materials for high durability[7-8]. However, the direct ethanol fuel cells have some drawback[9-11], e.g. the slow-moving anodic kinetics of ethanol electrooxidation, the high cost of Pt catalysts and accumulation of poisonous intermediates which prevent the development of the practical DEFCs[12-14]. More specifically, Platinum (Pt) is currently regarded as the best catalyst for the electrochemical oxidation of alcohols, but the intermediate products in the process of ethanol oxidation, especially carbon monoxide (CO), a major intermediate of ethanol oxidation, can deactivate and poison the Pt catalyst due to the strong binding of Pt–CO, resulting in the catalyst poisoning and quick declining in catalyst performances. In addition, the price of the Pt metal is very high (the current price of Pt is \$50 g^{-1}) [15]. Therefore, more research studies were required to investigate the highly efficient anti-poisoning low-cost electrocatalysts with superior electrocatalytic activity[16-18].

Compared with platinum, palladium is more abundant in nature, less expensive (the current price of Pd is \$20 g^{-1})[15] and has much higher catalytic activity for EOR in alkaline medium[7,19]. However, numerous studies revealed that when using pure Pd as the anode catalyst for EOR, catalyst poisoning by CO always remained a challenging issue that was hard to resolve. To further improve the catalysts activity and reduce the dose of noble metal, Pd-based catalysts have been broadly explored and deeply investigated. In recent years, incorporation of a second metal into Pd to make bimetallic catalysts, such as PdRh[20], PdSn[21], PdCu[22], and PdAu[23, 24] has become a widely employed approach to improve the catalytic performance of Pd catalyst for EOR

while at the same time to further reduce the cost of Pd. Among the various bimetallic Pd-based catalysts, the PdAu bimetallic catalyst has attracted particular attention because Au can efficiently catalyze many reactions, including the oxidation of CO and the partial oxidation of hydrocarbons with high efficiencies but also can stabilize the neighboring metal catalyst through its unique electron-withdrawing effect on neighboring metal atoms[24-31].

Concerning the behavior of the alloyed metals, controversial results regarding increased stability of metals in alloyed nanoparticles compared to the pure metals are reported[32-36]. In general, the activity and stability of catalyst depends on its structure, size, dispersion, and other factors, all of which are affected by the method of preparation[27,37-39]. Owing to its unique highly open configuration, the nanoparticles structure could impart remarkable advantageous structural and electronic features for the electrocatalysis of liquid fuel, which therefore are expected to promote the electrocatalytic activity and durability of the nanoparticles[40].

On one hand, gold-based nanoparticles (1-5 nm) have recently emerged as highly active catalysts for many important catalytic reactions[41]. A major factor for their catalytic activity is related to the size- and composition-dependent properties of nanoparticles[42]. It is found that AuNPs as the base catalyst in ethanol oxidation is inert in acidic environment but active in high pH (alkaline) medium. In addition, nanoscale gold has been shown to produce surface oxygenated species such as gold (III) oxide, adsorbed gold hydroxide or gold (III) hydroxide which are highly active for the removal of adsorbed CO (reduced poisoning), especially in alkaline media.

On the other hand, conductive polymers have been increasingly used as fuel cell catalyst support due to their electrical conductivity, large surface areas and stability. The incorporation of metal nanoparticles into polymer matrix can effectively increase the specific surface area of these materials hence improve the catalytic efficiency. Poly (3,4-ethylenedioxy thiophene) polystyrene sulfonate (PEDOT:PSS), a π-conjugated conducting polymer is of particular interest due to its high conductivity,

high visible light transmissivity, excellent stability, and very good film-forming properties. The benefits of incorporating noble metal NPs, into conducting polymers and PEDOT: PSS in particular, have been recognized over the last decade[43-46]. These nanocomposites are of great interest as they combine the properties of low-dimensional organic conductors with a high specific surface area[47]. Incorporation of highly dispersed metal NPs into conductive polymers maximizes the area for the oxidation and reduction reactions and makes low loading of catalyst possible for fuel cell applications[48].

In this work, a benign one-step synthesis approach based on room temperature DC plasma-liquid interaction was demonstrated for the fabrication of AuNPs/PEDOT: PSS nanocomposites and the prepared nanocomposites were subsequently characterized by transmission electron microscopy (TEM). Furthermore, AuNPs/PEDOT:PSS-Pd catalysts were also prepared and further investigated under an practical alkaline fuel cell operation condition using cyclic voltammetry (CV) and chronoamperometry (CA) for its potential application as electrocatalysts.

5.2 Experimental

5.2.1 Chemicals

Sulfuric acid (95%~98%, purist grade), absolute ethanol (≥99.9%), sodium hydroxide (semiconductor grade, 99.99%). PEDOT: PSS (1.3wt % dispersion in H_2O) and $HAuCl_4 \cdot 3H_2O$ salt were purchased from Sigma-Aldrich. All chemicals were used as received without further purification. Water was purified in a thermos scientific Barnstead water System (18.2 MΩ•cm resistivity) and was used for the preparation of all aqueous solutions.

5.2.2 Sample preparation

$HAuCl_4$ aqueous solutions (50 mL) were prepared with different concentrations (2 µM, 20 µM and 200 µM) by dissolving the appropriate amount of $HAuCl_4 \cdot 3H_2O$ in distilled water. PEDOT:PSS solutions (10 mL) were sonicated for 30 mins and then filtered through a 0.2 µm pore size Millipore nylon filter (Sigma-Aldrich) to remove the precipitates. Then 80µL of the filtered PEDOT:PSS solution was added to each one of the $HAuCl_4$ aqueous solutions at different concentrations and magnetically stirred for one hour before plasma processing.

5.2.3 Microplasma synthesis of AuNPs in PEDOT:PSS/aqueous solutions

Figure 5.1. shows the micro plasma set-up used for the in-situ synthesis of AuNPs. A room temperature atmospheric pressure direct-current (DC) plasma was initiated between a stainless steel capillary (0.25mm inner diameter, 0.5mm outer diameter) and

the surface of the $HAuCl_4$/PEDOT:PSS aqueous solution to synthesize the AuNPs. The gas flow through the stainless-steel capillary (100% He) was held constant at 25 sccm. The detailed experimental set up can be also found elsewhere. The distance between the capillary and the plasma-liquid interface was initially adjusted to 0.9 mm. A carbon rod was used as a counter electrode and kept at a distance of ~2 cm from the metal capillary, as shown in Figure 5.1, Micro plasma processing was carried out for different time intervals (i.e., 2, 5, 10, 20 mins) on different samples at a constant current of 5 mA. The initial voltage was 2 kV and this was progressively reduced to 0.8 kV to maintain the current constant.

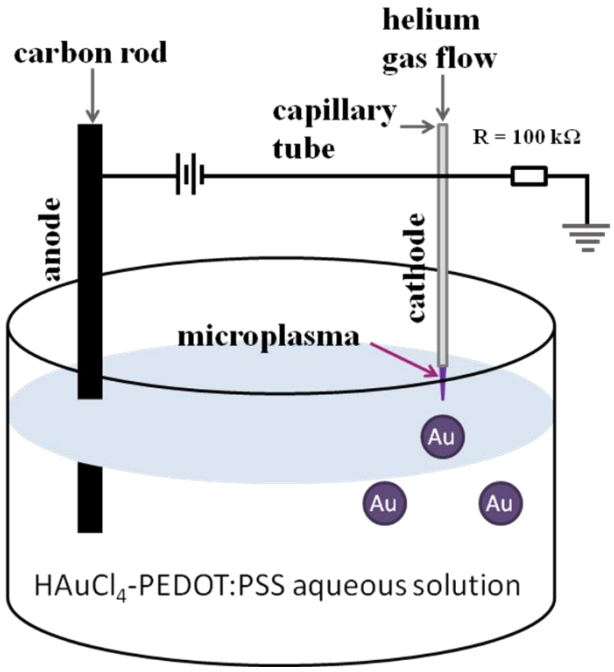

Figure 5.1. Schematic of the atmospheric pressure microplasma system.

5.2.4 Materials characterization

Transmission electron microscopy (TEM) was performed on a JEOL JEM-2100F to analyse the size and size distribution of AuNPs.

5.2.5 Electrochemical preparation and characterization

All electrolyte solutions were deoxygenated using high purity nitrogen unless otherwise stated. A home designed and built, three-electrode electrochemical fuel cell with a temperature-controlled water jacketed was used, which includes a piece of Pt mesh as the counter electrode, a Ag/AgCl (in saturated KCl) reference electrode for acidic media or a Hg/HgO (in 1 M NaOH) reference electrode for alkaline media and a bulk Pd as working electrode. The cell was thoroughly cleaned before using: it was initially immersed in a solution of hydrogen peroxide and sulfuric acid for 20 minutes. Then immersed in boiling water and rinsed with hot water several times. Prior to the electrochemical measurements, a bulk bare Pd (ø = 7.5 mm) electrode was mechanically polished delicately to a mirror-finish to remove surface contaminants by using a range of alumina oxide powders of three different particle sizes in sequence, e.g. 1, 0.3 and 0.05μm. It was then rinsed thoroughly with ultra pure water and followed up with ultrasonic washing in ultra pure water for several times.

The bare Pd electrode was further cleaned and investigated via cyclic voltammetry (CV) in a solution of 0.1 M H_2SO_4 with a potential range of 0. 15V to 1.35V(*vs.* RHE). An Autolab electrochemical workstation was employed for the electrochemical measurements and electro-deposition. Electrochemical data were recorded using Autolab NOVA software. The scan rate of 50 mVs^{-1} was used in cyclic voltammetry unless otherwise stated.

5.2.6 AuNPs-decorated on bulk Pd

After a successively polished of bare Pd, it was then deposited with different samples as the working electrode. Two of the AuNPs/PEDOT:PSS nanocomposite samples (obtained from 2 μM $HAuCl_4$ precursor, plasma treatment 2 min in 0.1M H_2SO_4 solution and 200 μM $HAuCl_4$ precursor, plasma treatment 2 min in 0.1M H_2SO_4 were

selected). These composite samples were dropped on to the polished bulk Pd electrode directly and allowed to keep for few minutes for different AuNPs/PEDOT:PSS coverages.

After the AuNPs/PEDOT:PSS-decoration, the electrode was rinsed with water and transferred to another cell containing a solution of 0.1 M H_2SO_4 for the potentiostatic decoration of AuNPs employing CV. The coverage of AuNPs/PEDOT:PSS was controlled by the dwell time from 30 s to 120 s and was evaluated using CV with the potential cycling range between 0.15 V and 0.75 V (*vs.* RHE) at a scan rate of 50 mV s^{-1}.

5.2.7 Ethanol electrooxidation on bare and AuNPs/PEDOT:PSS-decorated bulk Pd

Electroocidation of ethanol on the bare and AuNPs/PEDOT:PSS-decoration bulk Pd were characterized in a mixed solution of 0.1 M Ethanol and 0.1 M NaOH at 25 ^oC, 30 ^oC, 40 ^oC , 50 ^oC and 60 ^oC, respectively. Both cyclic voltammetry (CV) and chronoamperometry (CA) were employed. The catalyst activity towards the EOR in alkaline media was performed via CV at a scan rate of 50 $mV \cdot s^{-1}$ within the potential sweeping range from 0.11 V to 1.11 V (*vs.* RHE). Whilst for CA test, the initial potential was kept at 1.01 V(*vs.* RHE) for 3 s to oxidize all the adsorbed intermediated, followed by the potential of 0.11 V (*vs.* RHE) for 0.1 s to reduce the oxides as well as adsorbed ethanol, and finally stabled at a fixed potential of 0.71 V (*vs.* RHE) for 190 s which is relevant to alkaline ethanol fuel cell. It is noted that the current density of ethanol electrooxidation was normalized with the electrochemical surface area (ECSA) of bare bulk Pd.

5.3 Results and discussion

5.3.1 Materials characterization

Figure 5.2 shows the AuNP/PEDOT: PSS colloids obtained from various $HAuCl_4$/PEDOT:PSS solutions after 5 min plasma treatment. The colour change of the colloids indicates that the formation of AuNPs has taken place (confirmed also by TEM, see Figure 5.3.). Increasing the initial concentration of $HAuCl_4$, the colour becomes more intense with the sample containing 2 µM $HAuCl_4$showing negligible colour change and the sample containing 200 µM $HAuCl_4$ showing the most significant colour change.

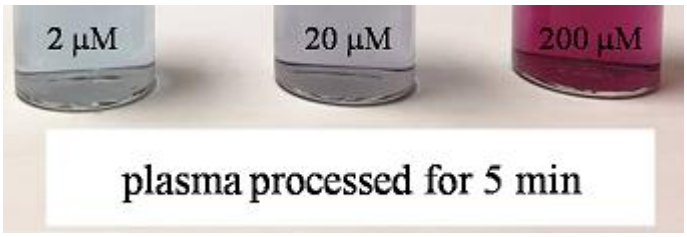

Figure 5.2. Colloidal gold nanoparticles (AuNPs) in poly(3,4-ethylenedioxythiophene) polystyrene sulfonate (PEDOT:PSS) aqueous solutions after synthesis by plasma processing.

Corresponding TEM images are shown in Figure 5.3. where both low and high magnification images confirm the formation of AuNPs at all three different concentrations. AuNPs produced with the lowest concentration (2 µM $HAuCl_4$, Figure 5.3.a and 5.3.d) are fairly uniform in size and being mostly spherical where the diameter of the NPs ranges from 2.3 nm to 6.9 nm and with an average of 4.1 nm. For higher molar concentration of $HAuCl_4$ (20 µM, Figure 5.3.b and 5.3.e), the NPs are still spherical with a diameter within the range 4.9-10.7 nm and an average of 7.5 nm. For

200 µM precursor concentration a large part of the AuNPs still remained spherical, however other shapes are emerging (hexagonal, pentagonal, triangular and rod shapes), see Figure 5.3.c and 5.3.f. Although the diameter is more difficult to evaluate in this case, an average size of the spherical particles was estimated to be ~35 nm.

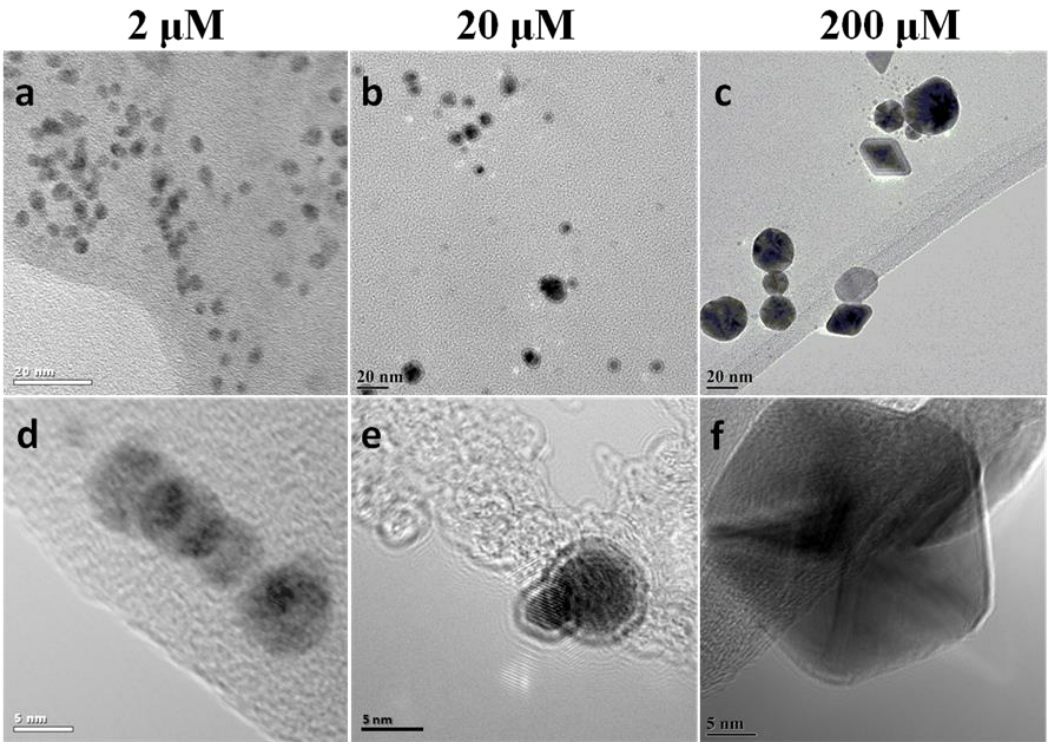

Figure 5.3. Low (top) and high (bottom) magnification transmission electron microscope images of Au/PEDOT:PSS nanocomposites synthesized from different gold salt precursor concentrations (plasma treatment time 5 min)

It is also found that for low gold salt precursor concentration, the resulting AuNPs appear to be uniformly dispersed/incorporated into a polymer matrix (Fig 5.3.d). With increasing precursor concentration, a distinct AuNP/polymer core-shell structure is produced (Fig 5.3.e). At even higher precursor concentration (200 µM, Fig 5.3.f), the core-shell structure becomes less visible. The reduction of the shell thickness could

be a consequence of the increasing AuNPs to PEDOT:PSS concentration ratio, considering that the amount of polymer was constant (80μL in 50mL water). With increasing size and number of AuNPs, the average amount of polymer encapsulating each NP is reduced.

5.3.2 Electrochemical study of AuNPs/PEDOT:PSS-Pd by cyclic voltammetry

(a).

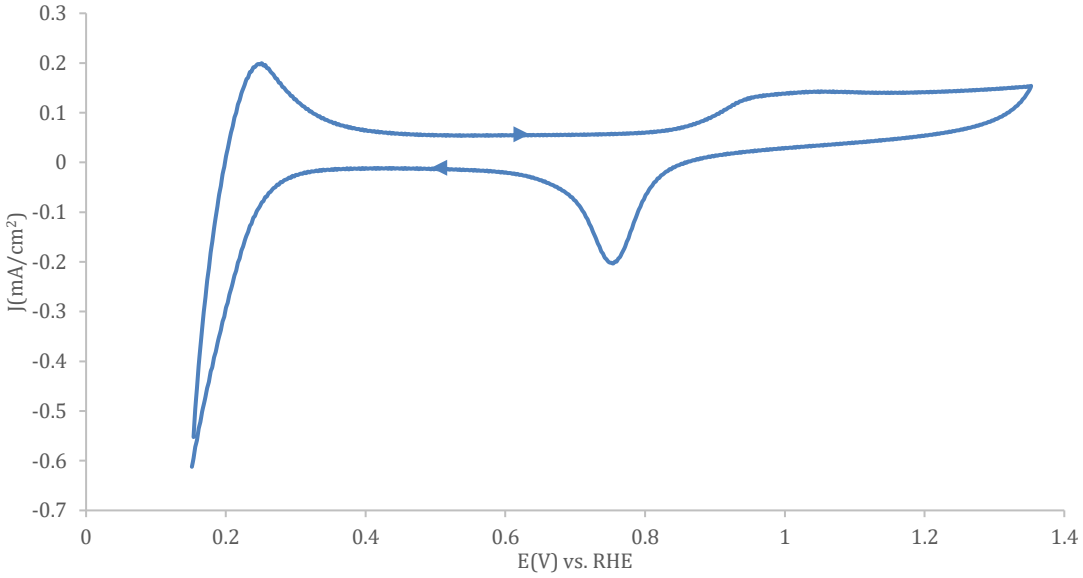

(b).

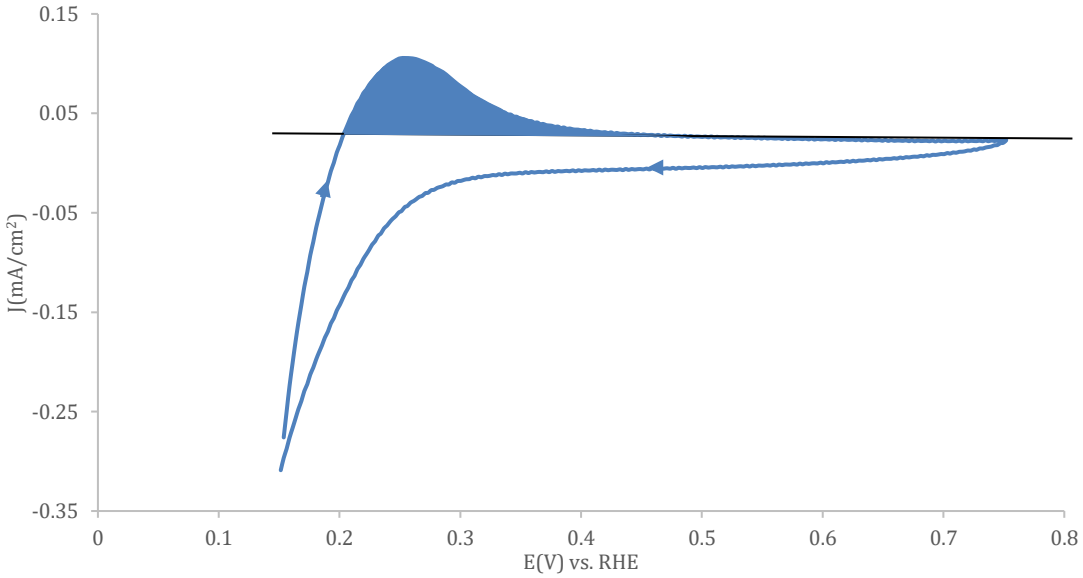

Figure 5.4. Cyclic voltammograms (CVs) obtained for (a). bulk Pd, (b). Au ($\theta_{Au,\ 3nm}$=0.16)/PEDOT:PSS-Pd in 0.1 M H_2SO_4 solution at room temperature. Scan rate: 50 mVs^{-1}.

Cyclic voltammetry (CV) is one of the most commonly used techniques in fuel cell electrocatalyst characterization. The cyclic voltammetry measurement of bulk Pd electrode was examined in 0.1 M H_2SO_4 solution with a scan rate of 50 mVs^{-1} from 0.15 V to 1.35 V (*vs*. RHE) as shown in Figure 5.4.a. It can be seen that, on bulk Pd electrode, not only the adsorption and desorption of hydrogen, but also the hydrogen absorption can be noted, which follows the results reported formerly[43-44]. More specifically, the initial cathodic and anodic current peaks between 0.2 V and 0.45 V (*vs*. RHE) were associated with the hydrogen adsorption-desorption processes. Subsequently, a peak of hydroxyl and oxygen species adsorption begins with 0.75 V (*vs*. RHE) and a small shoulder arises at around 1.05 V (*vs*. RHE). Lastly, a Pd oxide reduction peak shows up between 0.9 V to 0.6 V (*vs*. RHE) with the corresponding cathodic peak at around 0.7 V (*vs*. RHE)[45]. Additionally, the electrochemical active surface area (ECSA) of as-prepared electrodes was determined by the integrated charge of hydrogen adsorption/ desorption region by adjusting the assumption of 212 $\mu C \cdot cm^{-2}$. In order to contrast the electrooxidation performance of as-prepared electrodes, the current is stabilized to electrochemical surface area (ECSA) current density (*j*).

Presented in Figure 5.4.b is the cyclic voltammograms of AuNPs-Pd electrode in 0.1M H_2SO_4 operated from 0.15 V to 0.75 V (*vs*. RHE) at a scan rate of 50 $mV \cdot s^{-1}$. For the potentiostatic deposition of AuNPs on Pd under a certain condition, the amount of AuNPs depends on the deposition time. By running the deposition time, AuNPs-Pd catalysts with different AuNPs loading amounts can be fabricated. Small amounts of AuNPs can be expected from the short deposition time and the low concentration. Pd surface has a strong property to adsorb hydrogen at lower potentials, but the applied potential is in a potential region where the adsorption of a slight amount of hydrogen takes place on the Pd surface, so a 100% current efficiency can be used for the AuNPs/PEDOT:PSS deposition, and the AuNPs loading amounts are obtained from the above charges[49].

It can be observed from the figure that the hydrogen adsorption and desorption peak of AuNPs/PEDOT:PSS-Pd ($\theta_{Au,\,3nm}$=0.16) electrode is between 0.2 V to 0.45 V (*vs*. RHE) with a peak of 0.1 mA·cm^{-2}, so the coverage of Au_{3nm}/PEDOT:PSS can be evaluated.

The evaluation of AuNPs/PEDOT:PSS coverage (θ_{Au}) can be equated with the blockage of hydrogen adsorption. Therefore, θ_{Au} can be defined as:

$$\theta_{Au} = 1 - \theta_H = 1 - \frac{Q_H^{Au}}{Q_H^{bare}} \qquad (1)$$

Here Q_H^{Au} is the charge for hydrogen adsorption on the AuNPs/PEDOT:PSS-Pd electrode while Q_H^{bare} is the charge for hydrogen adsorption on bare Pd.

5.3.3 Ethanol electrooxidation reaction (EOR)

It has been discussed in previous article that Au can act as potential electro-catalyst for CO oxidation in alkaline medium since it can readily activate water forming Au–OH_{ads} at comparatively low potential by the following reaction[50-52].

$$CO_{ads} + Au{-}OH_{ads} \rightarrow Au{-}CO{-}OH \rightarrow Au{-}COOH \rightarrow Au + CO_2 + H_2O \qquad (2)$$

It may be recognized that Pd acts as primary active sites for catalyzing the dehydrogenation of ethanol and CO-like intermediate species could be oxidized by the surface oxide of Au to produce CO_2 or other products, subsequently releasing the active sites. Moreover, Pd having less ionization potential (8.34) than Au (9.225) may acquire δ^+ charge by transferring electron to the Au sites and weaken the oxygen bound to the surface thus making the composite matrix of optimal formulation, responsible for promoting the dissociative adsorption of ethanol, as shown in Scheme 1.

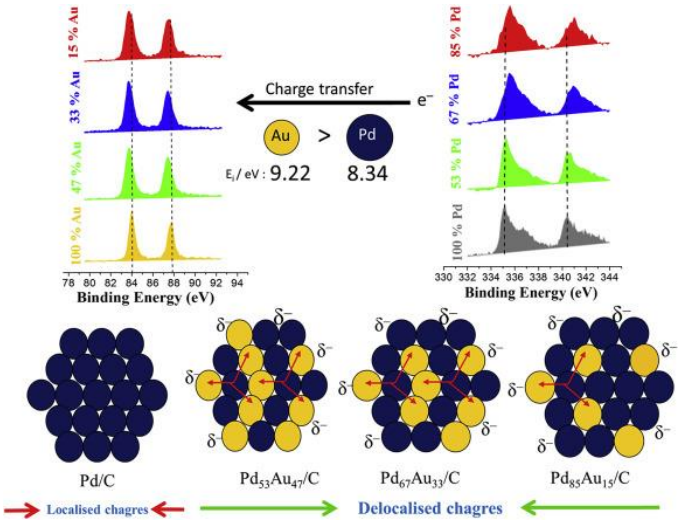

Scheme 1. Schematic representation of the charge distribution on different composition of PdAu/C catalysts.

(a).

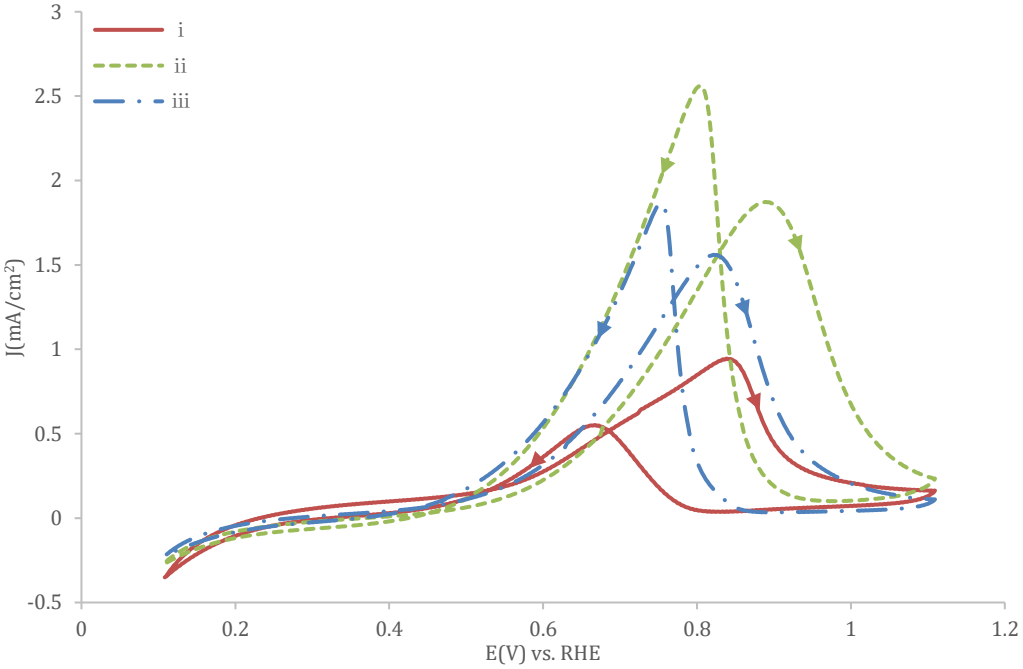

(b).

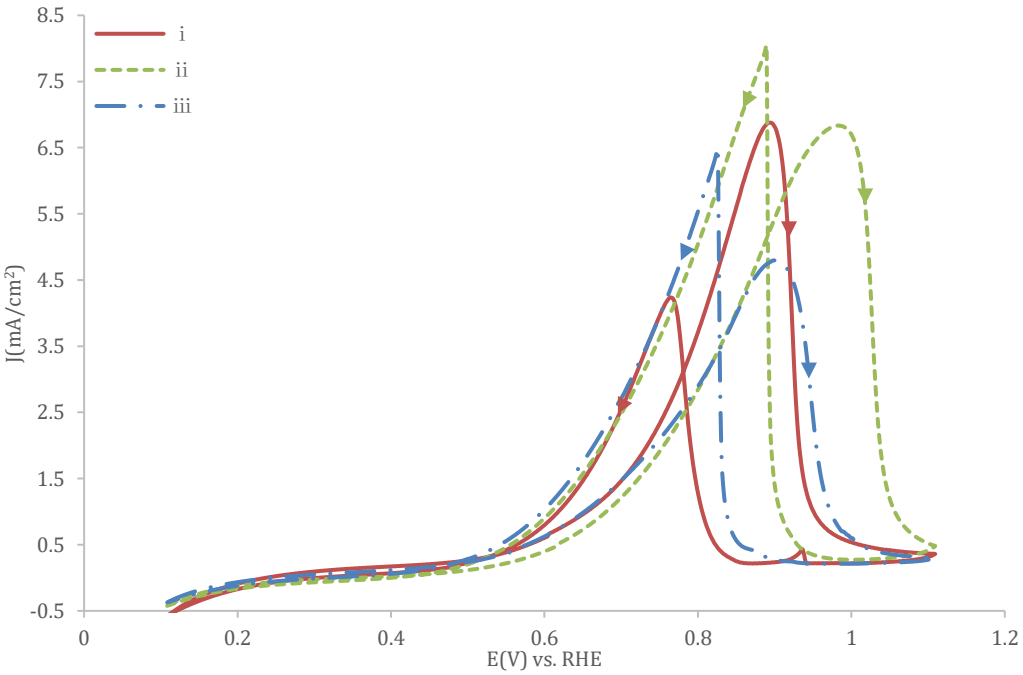

Figure 5.5. Cyclic voltammograms of i. bulk Pd, ii. AuNPs/PEDOT:PSS-Pd ($\theta_{Au,\ 3nm}$ = 0.27), iii. AuNPs/PEDOT: PSS-Pd ($\theta_{Au,\ 30nm}$ = 0.25) at (a). 30 ˚C, (b). 60 ˚C in 0.1 M Ethanol + 0.1 M NaOH solution. Scan rate: 50 mVs^{-1}.

For further studying the catalytic performances, typical cyclic voltammogram (CV) curves of ethanol electrooxidation on the as-prepared electrodes in a mix solution of 0.1 M Ethanol and 0.1 M NaOH were performed at 30 ˚C and 60 ˚C with a sweep rate of 50 mV s^{-1} and a potential range from 0.11 V to 1.11 V(vs. RHE), which are shown in Figure 5.5a and b, respectively. Two AuNPs/PEDOT:PSS nanocomposites samples, namely Au_{3nm}/PEDOT:PSS-Pd (from 2μM precursor, 2 min plasma treatment, average AuNP diameter 3nm) and Au_{30nm}/PEDOT:PSS-Pd (from 200 μM precursor, 2 min plasma treatment, average AuNP diameter 30 nm, were selected. A bulk Pd electrode is also employed as a reference for comparison.

Under the alkaline type direct ethanol fuel cell operation conditions, the oxidation current peak in the anodic scan can be used to evaluate the catalytic activity, as it is owing to the direct electrooxidation of ethanol and the newly chemisorbed species coming from ethanol dissociation. For the negative scan, the reversed peak is corresponding to the removal of poisonous species, which are incompletely oxidized in the forward scan. In order to compare the electrooxidation performance of different catalysts, the current is normalized to electrochemical surface area (ECSA) current density (j). Here, the peak current density and onset potential for the forward scan are the two essential limitations to estimating the virtual electrocatalytic performances of the electro-catalyst.

From Figure 5.5a, similar ethanol oxidation behaviours are observed on AuNPs-Pd and bulk Pd indicate that the reaction mechanisms show no significant difference. However, it is worth noting that the AuNPs/PEDOT:PSS modified Pd catalysts show much higher catalytic activity toward ethanol electrooxidation compared with that of pure Pd at 30˚C. In particular, the forward peak current density of AuNPs/PEDOT:PSS-Pd ($\theta_{Au,\,3nm}$=0.27) and AuNPs/PEDOT:PSS-Pd ($\theta_{Au,\,30nm}$=0.25) maintain about 2.0 and 1.5 times higher than that of the bulk Pd (0.95 mA cm^{-2}) with values of 1.87 mA·cm^{-2} and 1.56 mA·cm^{-2}, respectively. In the reverse scan, the current density peaks for AuNPs/PEDOT:PSS-Pd ($\theta_{Au,3nm}$=0.27) and

AuNPs/PEDOT:PSS-Pd ($\theta_{Au,\ 30nm}$=0.25) show even greater enhancement with reference to bulk Pd. Furthermore, it can be observed that the electrooxidation of ethanol on AuNPs/PEDOT:PSS-Pd ($\theta_{Au,\ 3nm}$=0.27) start earlier than that of AuNPs/PEDOT:PSS-Pd ($\theta_{Au,\ 30nm}$=0.25), both are more negative than the onset potential of pure Pd catalyst. The negative shift of onset potential indicates that the kinetics of the EOR is significantly enhanced and ethanol is more easily oxidized by AuNPs/PEDOT:PSS-Pd catalyst.

From Figure 5.5b, at 60˚C, however, only the reverse current density peak of AuNPs/PEDOT:PSS-Pd ($\theta_{Au,\ 3nm}$=0.27) electrode and AuNPs/PEDOT:PSS-Pd ($\theta_{Au,\ 30nm}$=0.25) electrode are higher than that of bulk Pd electrode. For the positive scan, AuNPs/PEDOT:PSS-Pd ($\theta_{Au,\ 3nm}$=0.27) exhibits a similar peak current density whilst the peak current density of AuNPs/PEDOT:PSS-Pd ($\theta_{Au,\ 3nm}$=0.27) is much lower than that of bulk Pd. All above evidence suggests the nanocomposites electrocatalyst is much more sensitive under lower temperature (i.e. 30 ˚C).

(a).

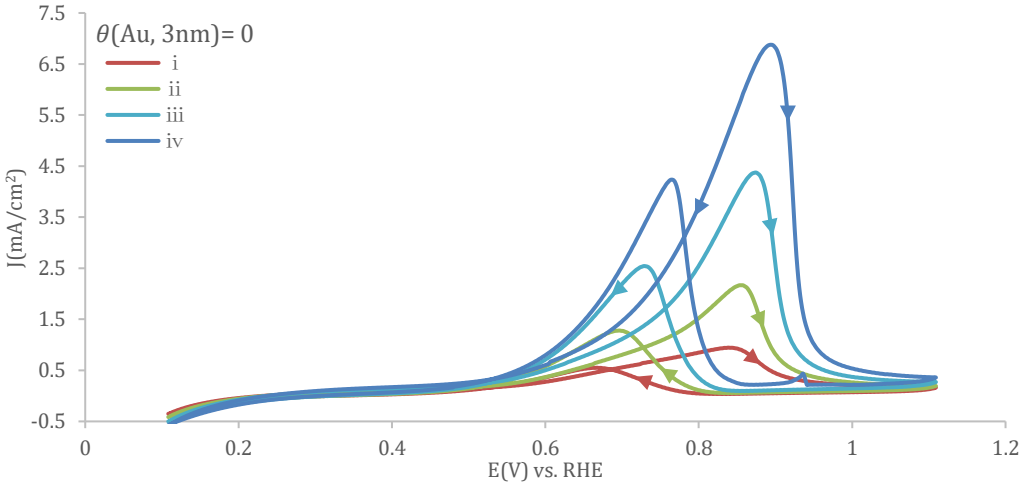
θ(Au, 3nm)= 0
i
ii
iii
iv
J(mA/cm²)
E(V) vs. RHE

(b).

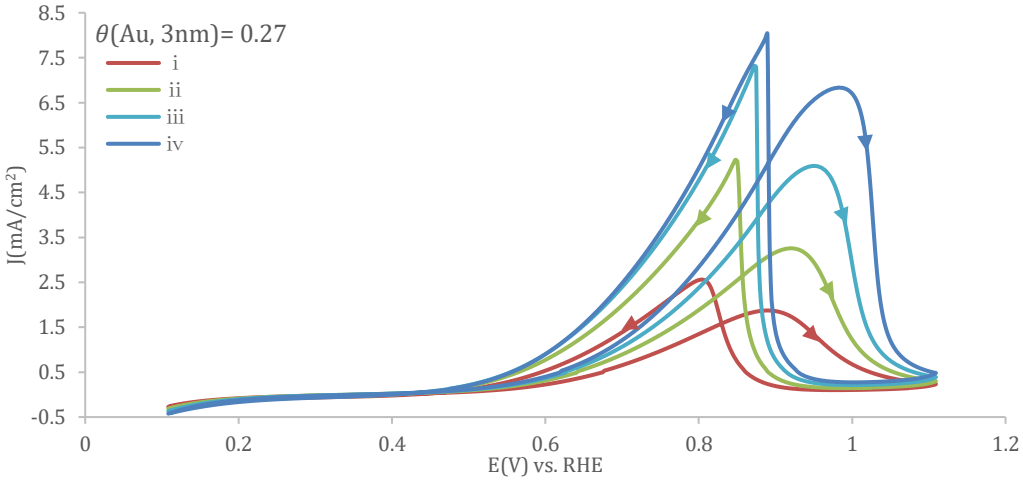
θ(Au, 3nm)= 0.27
i
ii
iii
iv
J(mA/cm²)
E(V) vs. RHE

(c).

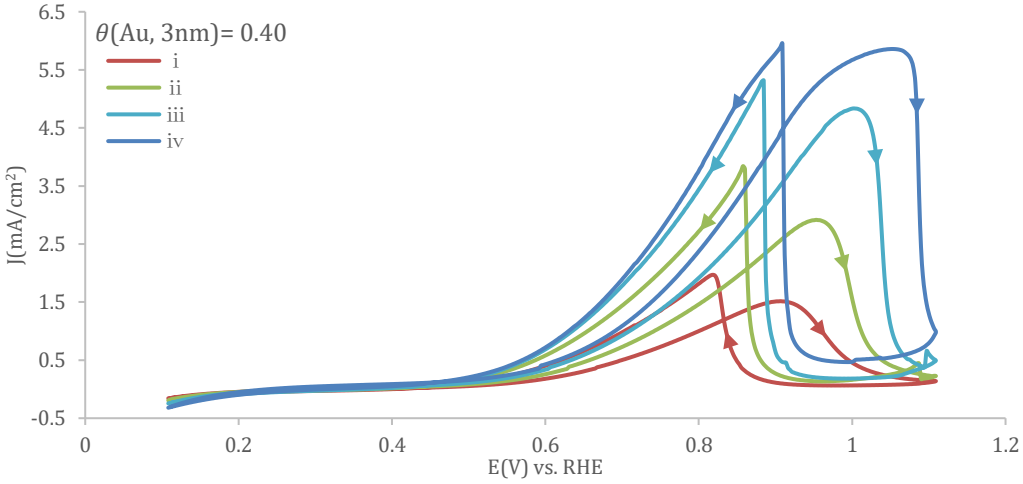
θ(Au, 3nm)= 0.40
i
ii
iii
iv
J(mA/cm²)
E(V) vs. RHE

(d).

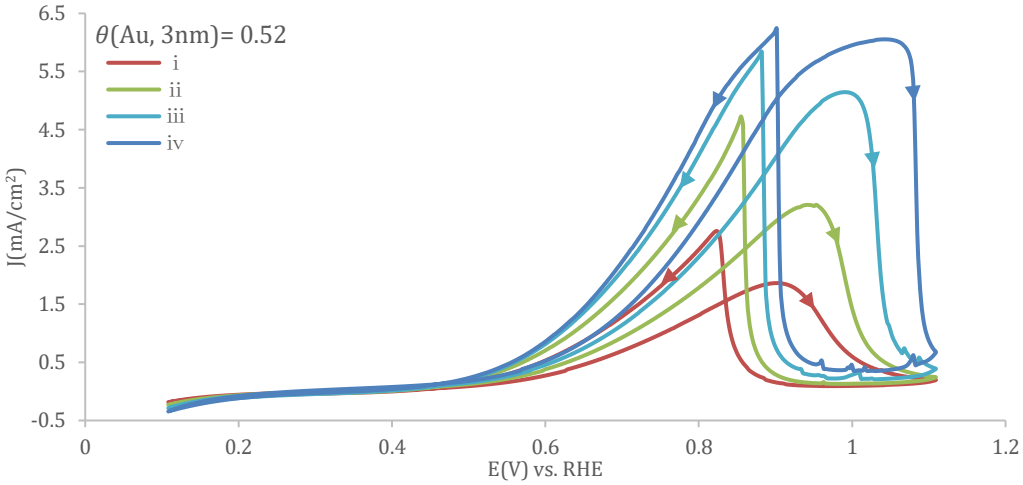

Figure 5.6. Cyclic voltammograms of (a). bulk Pd, (b). AuNPs/PEDOT:PSS-Pd ($\theta_{Au,\ 3nm}$ = 0.27), (c). AuNPs/PEDOT:PSS-Pd($\theta_{Au,\ 3nm}$ = 0.40), (d). AuNPs/PEDOT:PSS-Pd($\theta_{Au,\ 3nm}$ = 0.52) in 0.1 M Ethanol + 0.1 M NaOH solution at different temperatures: i. T = 30 ˚C, ii. T = 40 ˚C, iii. T = 50 ˚C, iv. T = 60 ˚C. Scan rate: 50 mVs^{-1}.

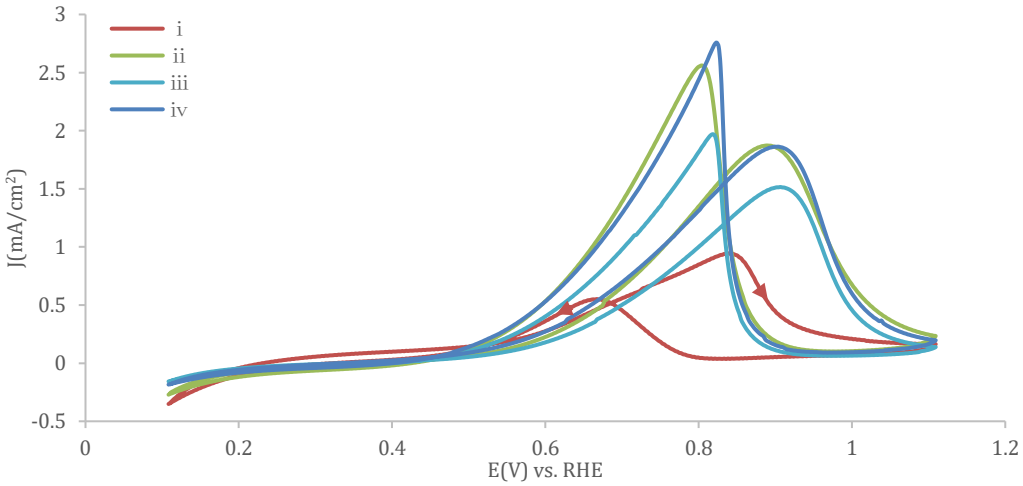

Figure 5.7. Cyclic voltammograms of Au_{3nm}/PEDOT:PSS-Pd with different Au_{3nm} coverages: i. $\theta_{Au,\ 3nm}$ = 0, ii. $\theta_{Au,\ 3nm}$ = 0.27, iii. $\theta_{Au,\ 3nm}$ = 0.40, iv. $\theta_{Au,\ 3nm}$ = 0.52 in 0.1 M Ethanol + 0.1 M NaOH solution from 30 ˚C. Scan rate: 50 mVs^{-1}.

Figure 5.6 demonstrates the representative CVs of ethanol electrooxidation on bulk Pd with various AuNPs/PEDOT:PSS-coverages ($\theta_{Au,3nm}$ = 0, 0.27, 0.40, 0.52) at different temperature (25, 30, 40, 50˚C) in 0.1 M Ethanol + 0.1 M NaOH solution. For all the catalysts studied, remarkable enhancement in the EOR activity was observed with the increase of temperature from 25 to 60˚C, the onset potential shifted earlier/negatively, and current density increase markedly at the elevated temperatures, suggesting that formation of active surface oxidants and the kinetic of EOR were facilitated at higher temperatures. More specifically, at low temperature dissociative adsorption of ethanol may be restricted, but the chemisorption process of ethanol become increasingly favoured on Au sites with temperature rise as has been reported for the case of methanol[53-54].

Figure 5.7 exhibits the cyclic voltammograms of different Au_{3nm}/PEDOT:PSS-Pd coverages in 0.1 M Ethanol+ 0.1 M NaOH solution at 30˚C and it shows that Au_{3nm}/PEDOT:PSS contributes a lot in the whole process. The anodic peak potential for Au_{3nm}/PEDOT:PSS-Pd electrode, both in the forward as well as reverse sweeps are shifted towards more positive value which is an indicative of the formation of pre-electrode layer that requires more over potential for charge transfer reaction, particularly when there is comparatively less amount of OH^- on the electrode surface[55-58]. Meanwhile, the outstanding performance of $Au_{3nm,\ \theta=0.16}$/PEDOT:PSS-Pd in the electro-catalytic activity is observed when compared between the catalysts with a maximum positive peak current density, which is almost 3 times higher than that of bulk Pd. The peak current density of $Au_{3nm,\ \theta=0.27}$/PEDOT:PSS-Pd, $Au_{3nm,\ \theta=0.52}$/PEDOT:PSS-Pd and $Au_{3nm,\ \theta=0.63}$/PEDOT:PSS-Pd are 2 times higher than that of bulk Pd, even the $Au_{3nm,\ \theta=0.40}$/PEDOT:PSS-Pd is 1.5 times higher than that of bulk Pd. It is seen that Au_{3nm}/PEDOT:PSS-Pd catalyst obviously facilitates the anodic oxidation.

(a).

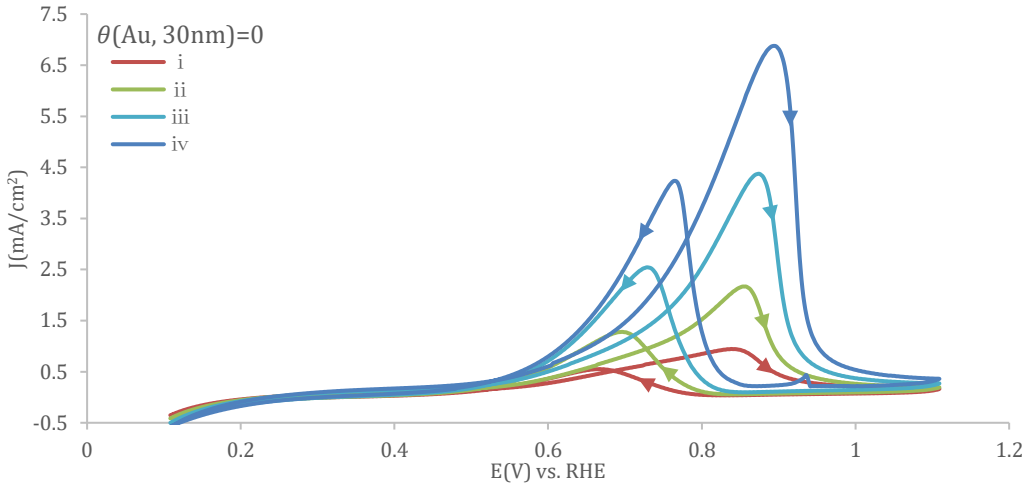
θ(Au, 30nm)=0
i
ii
iii
iv
J(mA/cm²)
E(V) vs. RHE

(b).

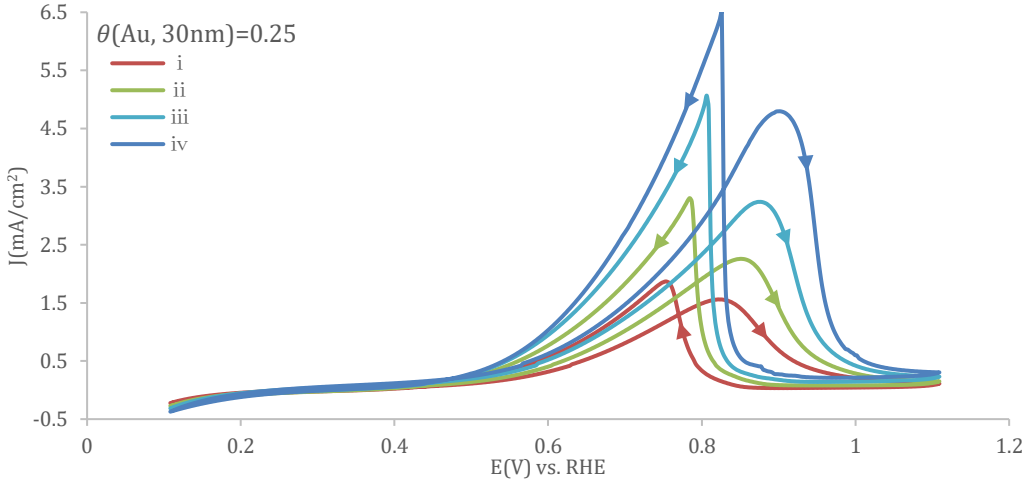
θ(Au, 30nm)=0.25
i
ii
iii
iv
J(mA/cm²)
E(V) vs. RHE

(c).

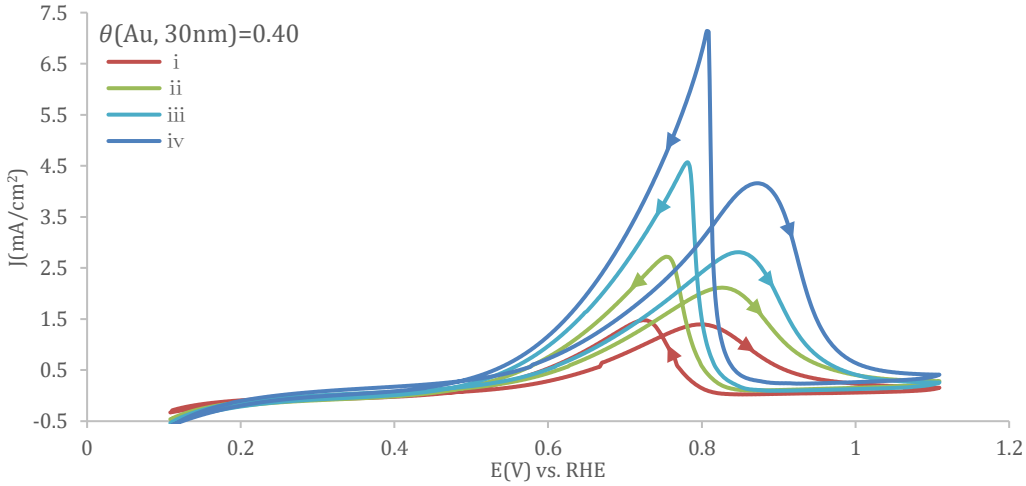
θ(Au, 30nm)=0.40
i
ii
iii
iv
J(mA/cm²)
E(V) vs. RHE

(d).

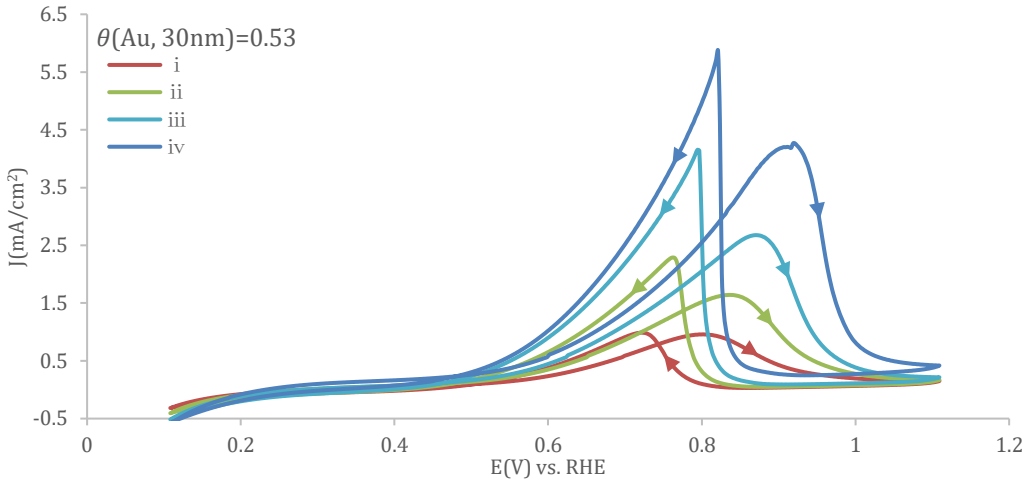

Figure 5.8. Cyclic voltammograms of (a). bulk Pd, (b). Au_{30nm}/PEDOT:PSS-Pd ($\theta_{Au,30nm}$ = 0.25), (c). Au_{30nm}/PEDOT:PSS-Pd ($\theta_{Au,30nm}$ = 0.40), (d). Au_{30nm}/PEDOT:PSS-Pd ($\theta_{Au,30nm}$ = 0.53) in 0.1 M Ethanol+ 0.1 M NaOH solution at different temperatures: i. T = 30 ˚C, ii. T = 40 ˚C, iii. T = 50 ˚C, iv. T = 60 ˚C. Scan rate: 50 mVs^{-1}.

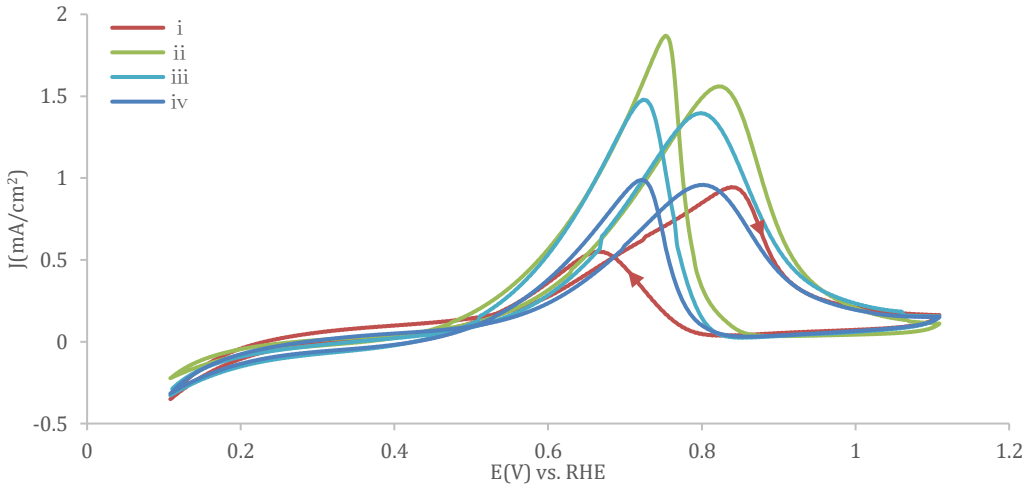

Figure 5.9. Cyclic voltammograms of Au_{30nm}/PEDOT: PSS-Pd with different Au_{3nm}/PEDOT:PSS-coverages: i. $\theta_{Au,\ 30nm}$ = 0, ii. $\theta_{Au,\ 30nm}$ = 0.25, iii. $\theta_{Au,\ 30nm}$ = 0.40, iv. $\theta_{Au,\ 30nm}$ = 0.53 in 0.1 M Ethanol + 0.1 M NaOH solution from 30 ˚C. Scan rate: 50 mVs^{-1}.

Figure 5.8 presents the representative cyclic volammograms of ethanol electrooxidation on bulk Pd with various Au_{30nm}/PEDOT:PSS coverages ($\theta_{Au,30nm}$ = 0, 0.25, 0.40, 0.53) at different temperatures (30, 40, 50, 60 ˚C) in 0.1 M Ethanol + 0.1 M NaOH solution with a scan rate of 50 mV s^{-1}. In Figure 5.8.a.b.c.d, the potential window was set from 0.11 V to 1.11 V (*vs.* RHE). The peak potential shifts positive with elevated temperature attributing to the enhanced turnover rate of ethanol adsorption and subsequent enhanced surface oxide consumption. When the temperature increases, the onset potential shifted earlier/negatively whilst the peak current density is increasing. For all the catalysts studied, remarkable enhancement in the EOR activity was observed with the increase of temperature from 25 ˚C to 60 ˚C.

Displayed in Figure 5.9 is the the cyclic voltammograms of different Au_{30nm}/PEDOT:PSS-Pd coverages in 0.1 M Ethanol + 0.1 M NaOH solution at 30 ˚C from 0.11 V to 0.11 V (*vs.* RHE). It can be seen that the peak current density of Au_{30nm}-Pd ($\theta_{Au,30nm}$=0.25) is the highest in around 1.5 mA·cm^{-2} which is 1.5 times higher than that of bulk Pd. The minimum peak current density in all Au_{30nm}/PEDOT:PSS-Pd electrodes is 0.9 mA·cm^{-2} when $\theta_{Au,30nm}$=0.53, which is the same as that of bulk Pd. In general, Au_{30nm}/PEDOT:PSS contributes a lot in the whole process.

At last, through the comparison of Figure 5.7 and Figure 5.9, both Au_{3nm}/PEDOT:PSS and Au_{30nm}/PEDOT:PSS have obviously contributions to the ethanol electrooxidation reaction whilst, Au_{3nm}/PEDOT:PSS shows a better property to facilitate the EOR with the maximum peak current density. It is obvious that the activity of AuNPs/PEDOT:PSS-modified Pd catalyst is related to the Au loading mass. Noticeably, a small or a large amount of Au leads to a considerable decrease in the EOR, but a suitable Au loading mass is desirable to achieve high activity for catalyst.

(a).

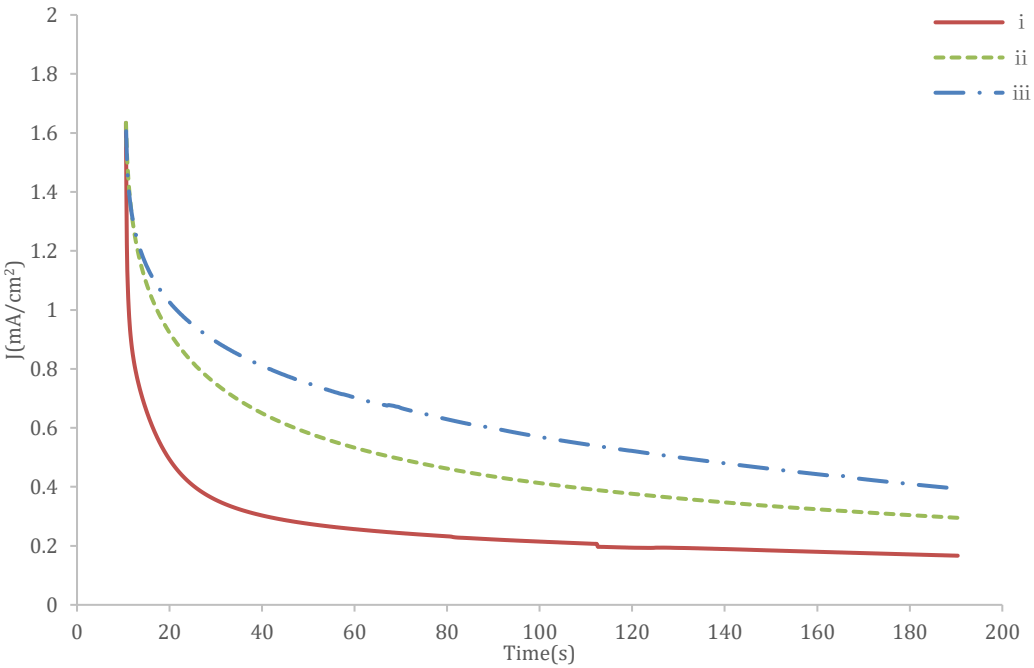
2
1.8
1.6
1.4
1.2
1
0.8
0.6
0.4
0.2
0
J(mA/cm²)
0
20
40
60
80
100
120
140
160
180
200
Time(s)
i
ii
iii

(b).

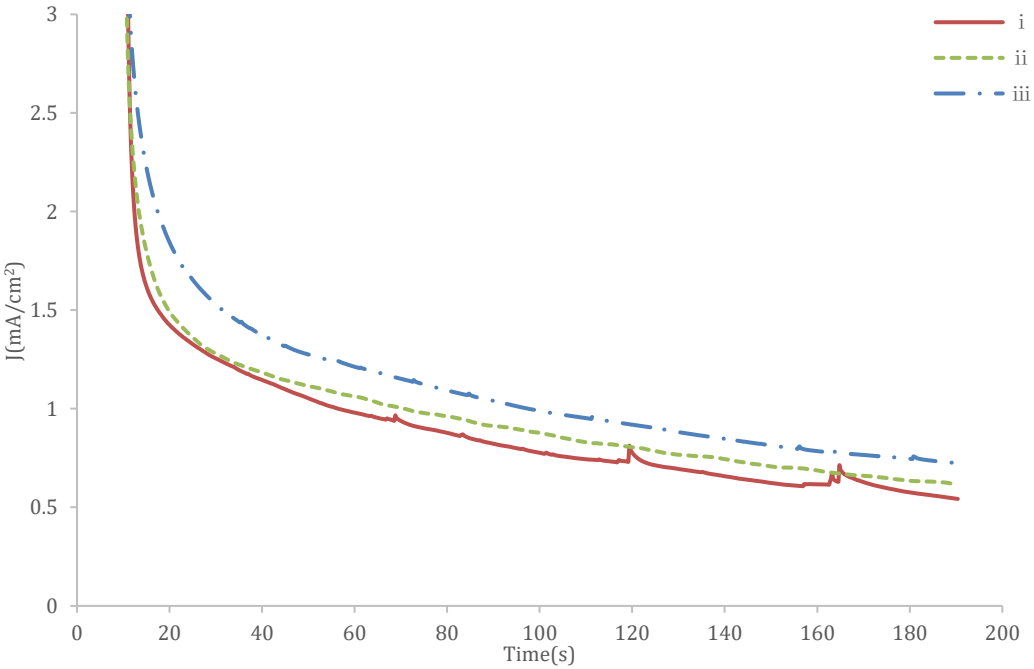
3
2.5
2
1.5
1
0.5
0
J(mA/cm²)
0
20
40
60
80
100
120
140
160
180
200
Time(s)
i
ii
iii

Figure 5.10. Chronoamperograms of i. bulk Pd, ii. AuNPs/PEDOT:PSS-Pd ($\theta_{Au,\ 3nm}$ = 0.27), iii. AuNPs/PEDOT:PSS-Pd ($\theta_{Au,\ 30nm}$ = 0.25) at (a). 30 ˚C, (b). 60 ˚C in 0.1 M Ethanol + 0.1 M NaOH solution. Scan rate: 50 mVs^{-1}.

In order to further investigate the steady-state performance of ethanol electrooxidation and the poisoning condition on all samples, representative chronoamperometric curves (CAs) of ethanol electrooxidation are plotted in Fig 5.10. Prior to the current transients recorded at the study potential, the electrodes were initially kept at 1.01 V (*vs.* RHE) for 3 s to oxidize all the adsorbed intermediated and get the surface cleaned. Subsequently, the electrodes were polarized at 0.11 V (*vs.* RHE) for 0.1 s to reduce the oxides and adsorbed ethanol. And then, keep the voltage at 0.71 V (*vs.* RHE) for 190 s.

In all the transient curves, the current densities decayed rapidly in the first few seconds before stabilization, which can be attributed to the poisoning of catalyst surface actives sites by CO-like species. More specifically, before the catalytic reaction, the electrocatalyst active sites are accessible for the adsorption of ethanol molecules. Afterward, the adsorption of new ethanol molecules would depend on the liberated active sites occupied by the chemisorbed CO-like intermediate carbonaceous species generated in ethanol oxidation process, eventually affecting the catalysis efficienc[49, 59].

As it can be seen in Figure 5.10.a and b, at 30 ˚C, the current density decay on the AuNPs/PEDOT:PSS-Pd ($\theta_{Au,\ 3nm}$ = 0.27) and AuNPs/PEDOT:PSS-Pd ($\theta_{Au,\ 30nm}$ = 0.25) electrodes were apparently slower than that on bulk Pd electrode, whilst all of three electrodes show a comparable stability at 60 ˚C, indicating the superior durability of AuNPs/PEDOT:PSS-decorated Pd in especial under lower temperatures.

(a).

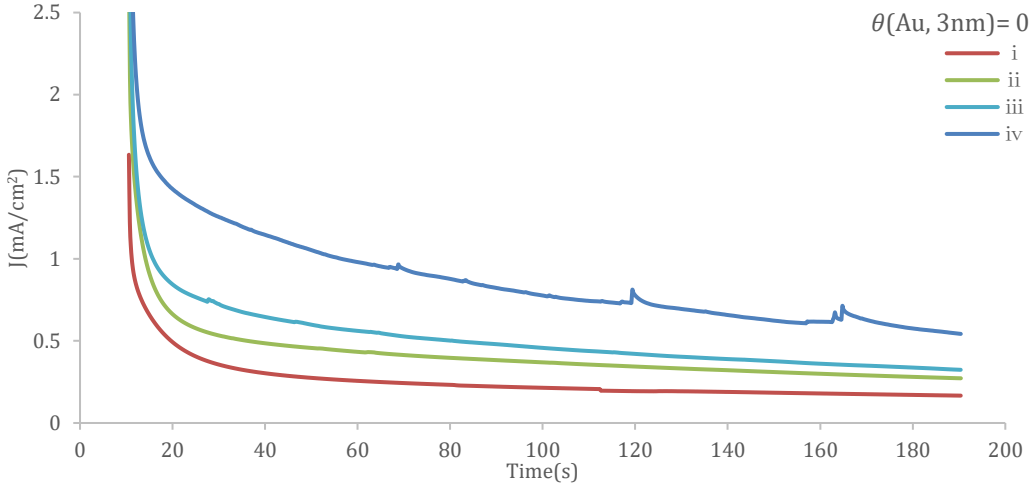
θ(Au, 3nm)= 0
i
ii
iii
iv
J(mA/cm²)
Time(s)
0
0.5
1
1.5
2
2.5
0
20
40
60
80
100
120
140
160
180
200

(b).

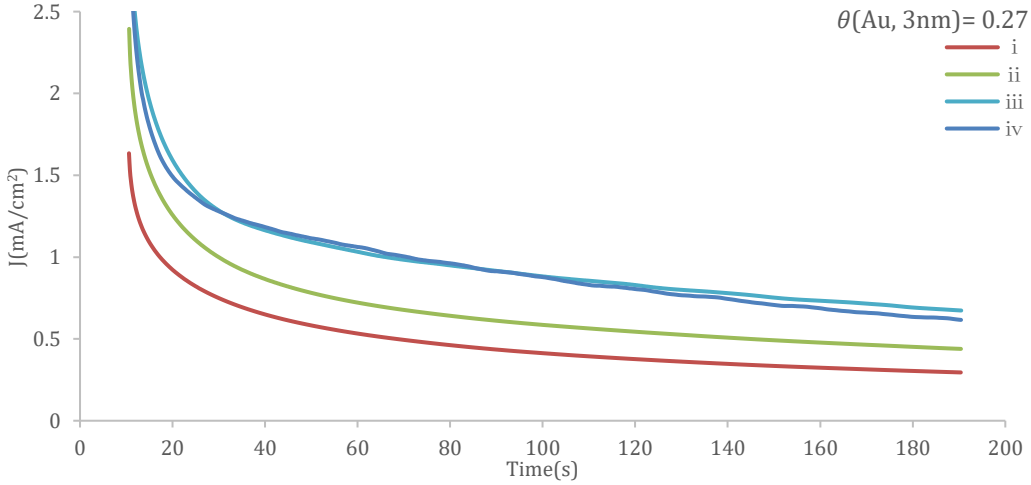
θ(Au, 3nm)= 0.27
i
ii
iii
iv
J(mA/cm²)
Time(s)
0
0.5
1
1.5
2
2.5
0
20
40
60
80
100
120
140
160
180
200

(c).

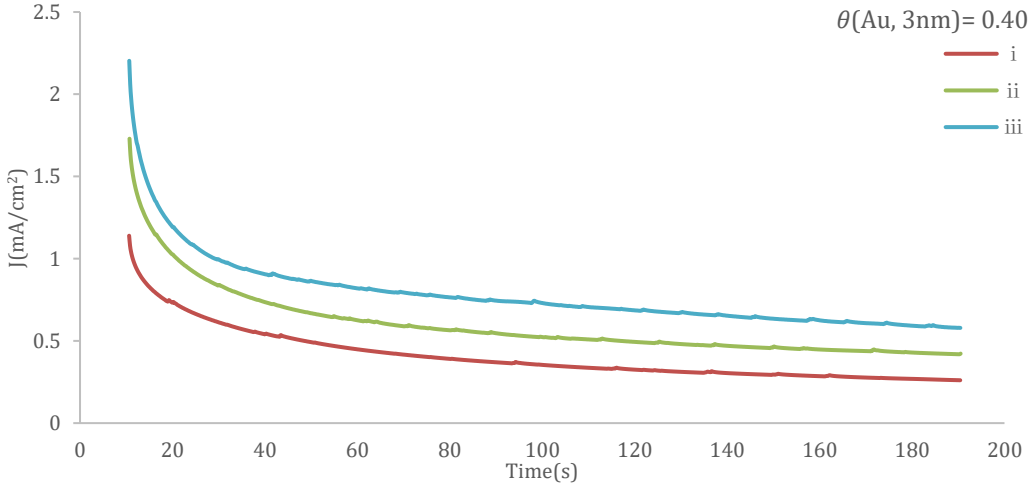
θ(Au, 3nm)= 0.40
i
ii
iii
J(mA/cm²)
Time(s)
0
0.5
1
1.5
2
2.5
0
20
40
60
80
100
120
140
160
180
200

(d).

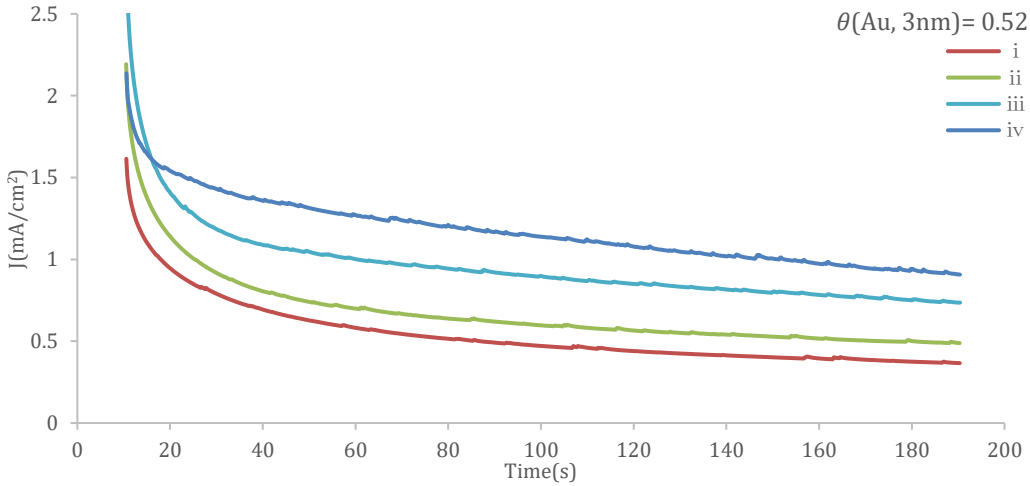

Figure 5.11. Chronoamperometric curves of (a). bulk Pd, (b). AuNPs/PEDOT:PSS-Pd ($\theta_{Au,\ 3nm}$ = 0.27), (c). AuNPs/PEDOT:PSS-Pd ($\theta_{Au,\ 3nm}$ = 0.40), (d). AuNPs/PEDOT:PSS-Pd ($\theta_{Au,\ 3nm}$ = 0.52) in 0.1 M Ethanol + 0.1 M NaOH solution at different temperatures: i. T = 30 ˚C, ii. T = 40 ˚C, iii. T = 50 ˚C, iv. T = 60 ˚C. Scan rate: 50 mVs^{-1}.

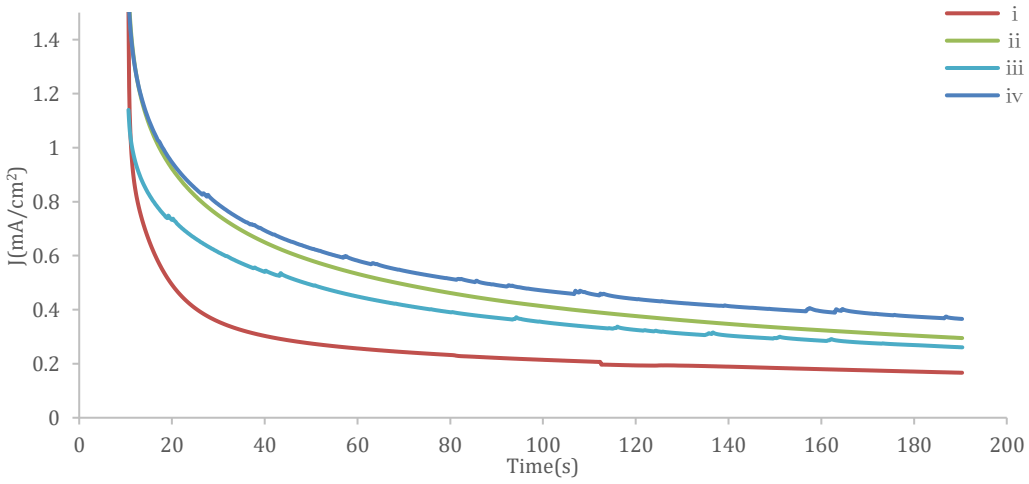

Figure 5.12. Chronoamperometric curves of ethanol electrooxidation on bulk Pd with various Au$_{3nm}$/PEDOT:PSS coverages: i. $\theta_{Au,\ 3nm}$ = 0, ii. $\theta_{Au,\ 3nm}$ = 0.27, iii. $\theta_{Au,\ 3nm}$ = 0.40, iv. $\theta_{Au,\ 3nm}$ = 0.52 in 0.1 M EtOH + 0.1 M NaOH solution under 30 ˚C. Scan rate: 50 mV·s^{-1}.

Figure 5.11. a, b, c, d display the representative CAs of ethanol electrooxidation on bulk Pd with various Au_{3nm}/PEDOT:PSS coverages ($\theta_{Au,3nm}$ = 0, 0.27, 0.40, 0.52) under different temperatures (30˚C, 40 ˚C, 50 ˚C, 60 ˚C) at a potential of 0.71 V (*vs.* RHE) for a period of 190 s in 0.1 M EtOH + 0.1 M NaOH solution presented with a scan rate of 50 $mV \cdot s^{-1}$.

Prior to the current transients recorded at the study potential, the electrodes were initially kept at 1.01 V (*vs.* RHE) for 3 s to oxidize all the adsorbed intermediated and get the surface cleaned. Subsequently, the electrodes were polarized at 0.11 V (*vs.* RHE) for 0.1 s to reduce the oxides and adsorbed ethanol. And then, keep the voltage at 0.71 V (*vs.* RHE) for 190 s.

In all the transient curves, the current densities drop sharply during the starting stage, which are ascribed to the double layer charging and the deactivation of electrodes surface by chemisorbed carbonaceous species and after 30s, they become apparently lower to a steady state till the end[60-61]. For making a clear explanation, before the catalytic reaction, the electrochemical active sites are accessible for the adsorption of ethanol molecules. Afterward, the adsorption of new ethanol molecules would depend on the liberated active sites occupied by the CO-like intermediate species generated in ethanol oxidation process, eventually affecting the catalysis efficiency[59, 62-63]. Science the decrease in the steady state current density is due to the poisoning of the electrode surface by intermediate species, it indicated that the poisoning species are hardly formed and/or adsorbed on the as-prepared electrodes surfaces at higher temperatures in comparison with that at lower temperatures[64].

As observed from figure 5.12, the current density decayed rapidly over time in the initial stage, while the $Au_{3nm,\ \theta=0.52}$/PEDOT:PSS-Pd electrode showed the slowest current density decay and retained the highest current density during the whole process. In addition, both of $Au_{3nm,\ \theta=0.27}$/PEDOT:PSS-Pd and $Au_{3nm,\ \theta=0.40}$/PEDOT:PSS-Pd also displayed the greatly enhanced current densities that are much higher than that of bulk

Pd, indicating the superior durability of Au_{3nm}/PEDOT:PSS-decorated AuPd catalysts which further confirmed their excellent electrocatalytic performances.

(a).

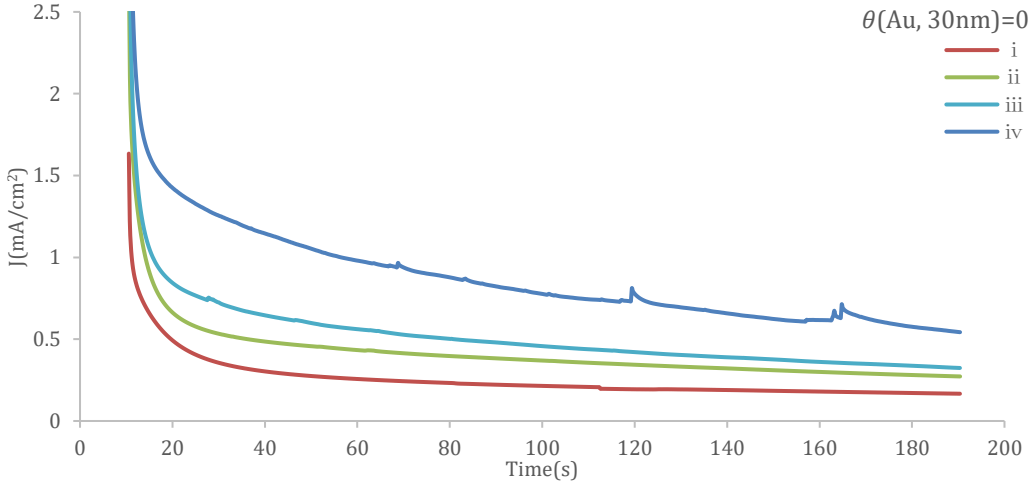
θ(Au, 30nm)=0
i
ii
iii
iv
J(mA/cm²)
Time(s)

(b).

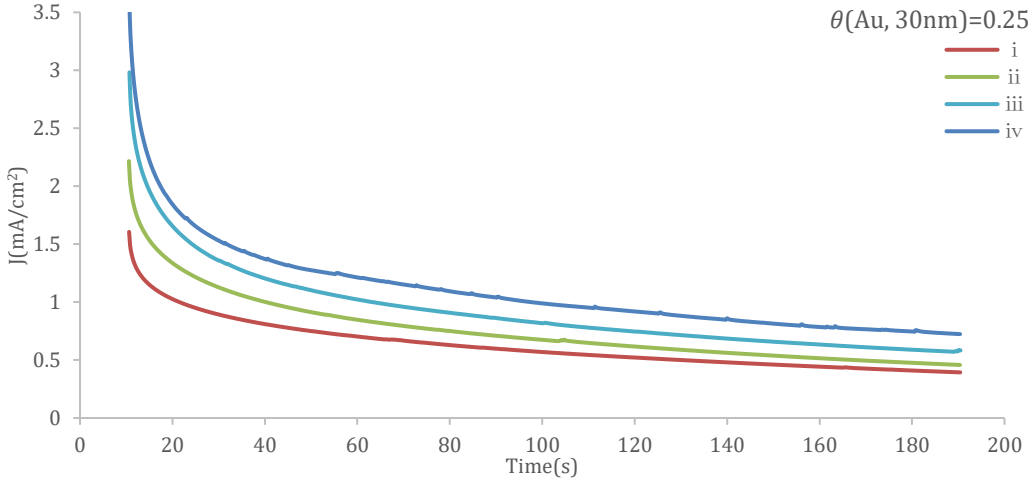
θ(Au, 30nm)=0.25
i
ii
iii
iv
J(mA/cm²)
Time(s)

(c).

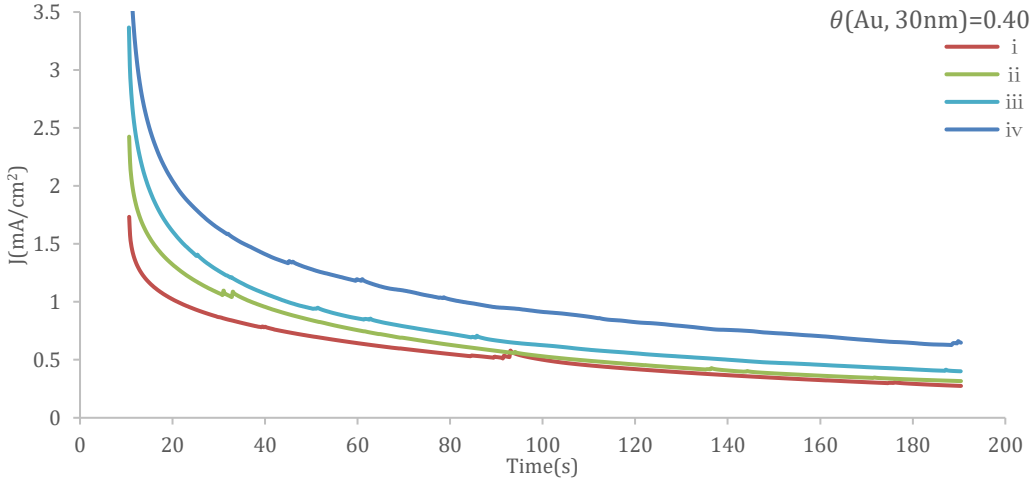
θ(Au, 30nm)=0.40
i
ii
iii
iv
J(mA/cm²)
Time(s)

(d).

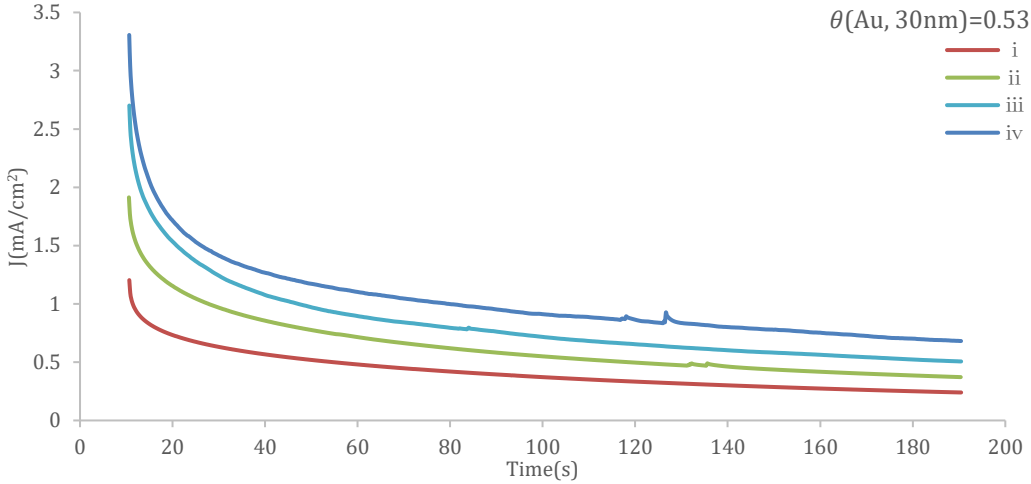

Figure 5.13. Chronoamperometric curves of (a). bulk Pd, (b). Au_{30nm}/PEDOT:PSS-Pd ($\theta_{Au,\ 30nm}$ = 0.25), (c). Au_{30nm}/PEDOT:PSS-Pd ($\theta_{Au,\ 30nm}$ = 0.40), (d). Au_{30nm}/PEDOT:PSS-Pd ($\theta_{Au,\ 30nm}$ = 0.53) in 0.1 M Ethanol + 0.1 M NaOH solution at different temperatures: i. T = 30 ˚C, ii. T = 40 ˚C, iii. T = 50 ˚C, iv. T = 60 ˚C. Scan rate: 50mVs^{-1}.

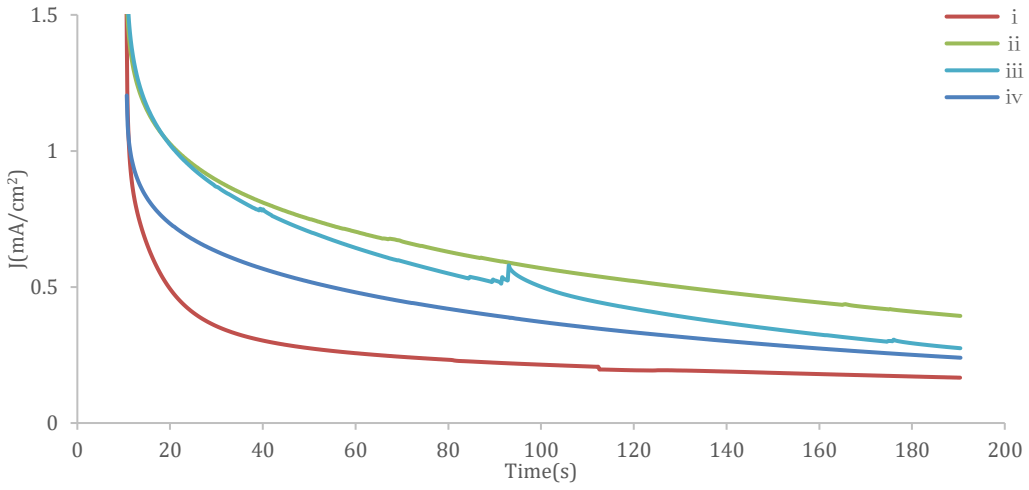

Figure 5.14 Chronoamperometric curves of ethanol electrooxidation on bulk Pd with various Au_{30nm} coverages: i. $\theta_{Au,\ 30nm}$ = 0, ii. $\theta_{Au,\ 30nm}$ = 0.25, iii. $\theta_{Au,\ 30nm}$ = 0.40, iv. $\theta_{Au,\ 30nm}$ =0.53 in 0.1 M EtOH + 0.1 M NaOH solution under 30 ˚C. Scan rate: 50 mV·s^{-1}.

Prior to the current transients recorded at the study potential, the electrodes were initially kept at 1.01 V (*vs.* RHE) for 3 s to oxidize all the adsorbed intermediated and get the surface cleaned. Subsequently, the electrodes were polarized at 0.11 V (*vs.* RHE) for 0.1 s to reduce the oxides and adsorbed ethanol. And then, keep the voltage at 0.71 V (*vs.* RHE) for 190 s.

As shown in figure 5.13, following the same result of Au_{3nm}/PEDOT:PSS-Pd electrodes, the current densities of Au_{30nm}/PEDOT:PSS-Pd drop quickly during the first few seconds in all the transient curves, which are ascribed to the double layer charging and the deactivation of Pd surface by chemisorbed carbonaceous species and then they tend to be relatively steady[60, 61, 65-66]. The current densities on all Au_{30nm}/PEDOT:PSS-Pd electrodes are increasing as the temperature increases, which is consistent with the results from cyclic voltammograms. Noticeably, until the end of the experiment, all electrodes maintain the highest steady-state current density at 60 ˚C.

Figure 5.14 shows the CV curves of AuNPs/PEDOT:PSS-Pd with different Au_{30nm}/PEDOT:PSS coverages in 0.1M NaOH containing 0.1M ethanol at 30 ˚C. In all the transient curves, the current densities drop sharply during the starting stage and gradually decrease as the process continuous operating conditions. Moreover, the long-term stability of the Au_{30nm}/PEDOT:PSS-Pd ($\theta_{Au,\ 30nm}$=0.25) towards EOR is superior to that of the others catalysts, which obeys the following order: Au_{30nm}/PEDOT:PSS-Pd ($\theta_{Au,\ 30nm}$=0.25) > Au_{30nm}/PEDOT:PSS-Pd ($\theta_{Au,\ 30nm}$=0.40) > Au_{30nm}/PEDOT:PSS-Pd ($\theta_{Au,\ 30nm}$=0.53) > Au_{30nm}/PEDOT:PSS-Pd ($\theta_{Au,\ 30nm}$=0).

Based on the above data acquired and analysis, the electrocatalytic activity of bulk Pd electrode and Au_{3nm}/PEDOT:PSS-decorated Pd as well as Au_{30nm}/PEDOT:PSS-decorated Pd electrode improve progressively with increasing temperature and are consistent with the cyclic voltammetry data. Both Au_{3nm}-decorated Pd and Au_{30nm}/PEDOT:PSS-decorated Pd show better activities and stabilities compared to the bulk Pd catalyst which are in agreement with CV results, further confirm that the

presence of AuNPs is beneficial for the removal of adsorbed poisoning species during the electrooxidation of ethanol.

Table 5.1.a List of onset potential, positive-going peak potential, positive-going peak current density, negative-going peak potential and negative-going peak current density obtained from Figure 5.6.a and A.5.1.a.

Bulk Pd / Temp.	E_o / V (*vs*.RHE)	E_p / V (*vs*.RHE)	J_p /mA·cm^{-2}	E_n / V (*vs*.RHE)	J_n /mA·cm^{-2}
25 ˚C	0.521	0.811	0.596	0.655	0.320
30 ˚C	0.513	0.838	0.945	0.667	0.552
40 ˚C	0.501	0.853	2.167	0.696	1.280
50 ˚C	0.494	0.875	4.374	0.728	2.543
60 ˚C	0.488	0.899	4.429	0.767	2.731

Table 5.1.b List of onset potential, positive-going peak potential, positive-going peak current density, negative-going peak potential and negative-going peak current density obtained from Figure 5.6.c and A.5.1.c.

$\theta_{Au,3nm} = 0.27$ / Temp.	E_o / V (*vs*.RHE)	E_p / V (*vs*.RHE)	j_p / mA·cm^{-2}	E_n / V (*vs*.RHE)	j_n /mA·cm^{-2}
25 ˚C	0.469	0.877	1.323	0.775	1.540
30 ˚C	0.472	0.889	1.843	0.804	2. 562
40 ˚C	0.474	0.898	3.257	0. 848	5. 229
50 ˚C	0.478	0.866	5.090	0. 872	7.321
60 ˚C	0.501	0.836	6.8350	0.891	8.0352

Table 5.1.c List of onset potential, positive-going peak potential, positive-going peak current density, negative-going peak potential and negative-going peak current density obtained from Figure 5.7.b and A.5.6.b.

$\theta_{Au,30nm} = 0.25$ Temp.	E_o / V (*vs*.RHE)	E_p / V (*vs*.RHE)	j_p /mA·cm^{-2}	E_n / V (*vs*.RHE)	j_n /mA·cm^{-2}
25 ˚C	0.430	0.801	1.149	0.931	1.341
30 ˚C	0.433	0.821	1.560	0.753	1. 869
40 ˚C	0.438	0.850	2.258	0. 784	3. 302
50 ˚C	0.452	0.877	3.238	0. 806	5.065
60 ˚C	0.469	0.903	4.7969	0.828	6.5001

To understand the electro-catalytic of AuNPs/PEDOT:PSS-decorated Pd electrodes for ethanol electrooxidation reaction, the onset potential (E_o), positive-going peak potential (E_p), positive-going peak current density (j_p), negative-going peak potential (E_n) and negative-going peak current density (j_n) obtained from Figure 5.6 and Figure 5.8 are listed in Table 5.1. Here, the onset potential (E_o) and peak current density(j_p) during the forward scan are the two important parameters to evaluate for a comparative account of the electrocatalytic performances.

The E_o of ethanol electrooxidation obtained on Au_{3nm}/PEDOT:PSS-Pd ($\theta_{Au,3nm}$=0.27) at 25 ˚C is 0.469 mV (vs. RHE) which is higher than that of Au_{30nm}/PEDOT:PSS-Pd ($\theta_{Au,30nm}$=0.25) with the value of 0.430 mV (vs. RHE) but they are both more negative than the bulk Pd with the value of 0.521 mV (vs. RHE) and this tends to apply for all temperatures. Basically, for bulk Pd electrode, E_o get negative shifted whilst Ep get positive shifted with the temperature ascending. For AuNPs decorated Pd electrodes, E_o get positive shifted whilst Ep get negative shifted with the temperature ascending.

The j_p of ethanol electrooxidation obtained on Au_{3nm}/PEDOT:PSS-Pd ($\theta_{Au,3nm}$=0.27) at 25 ˚C is 1.323 mA·cm^{-2} while the j_p obtained on Au_{30nm}/PEDOT:PSS-Pd ($\theta_{Au,30nm}$=0.25) at 25 ˚C is 1.149 mA·cm^{-2}, both are about 2 times higher than that of the bulk Pd of 0.596 mA·cm^{-2} and this regular applies from 25 ˚C to 60 ˚C suggesting the AuNPs/PEDOT: PSS addition in particular amounts in Pd is effective in promoting the catalytic activity towards ethanol oxidation.

As the electroactive potential range for alcohols on different catalysts are not identical, the peak current densities are obtained to plot profiles of the activation energy values calculated that are based on the Arrhenius equation seen below[47]:

$$\ln j = lnA - \frac{Ea}{RT} \qquad (3)$$

Where, T presented for the temperature (K), J presented for the forward peak current density (mA/cm^2), Ea presented for the EOR activation energy at peak potential on the anodic sweep (kJ/mol), R presented for universal gas constant (8.314 kJ/mol/K) and A presented for the prefactor.

5.3.4 Activation energies

(a).

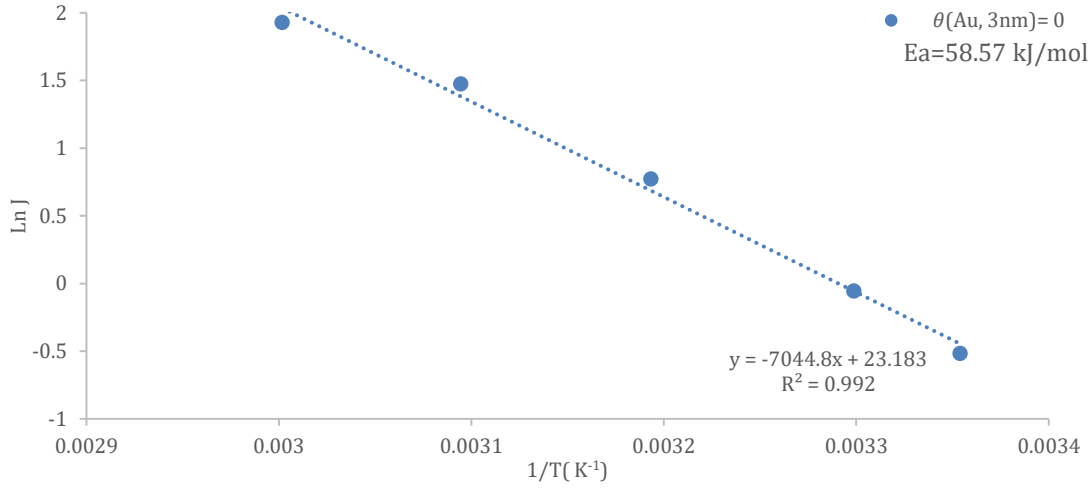

(b).

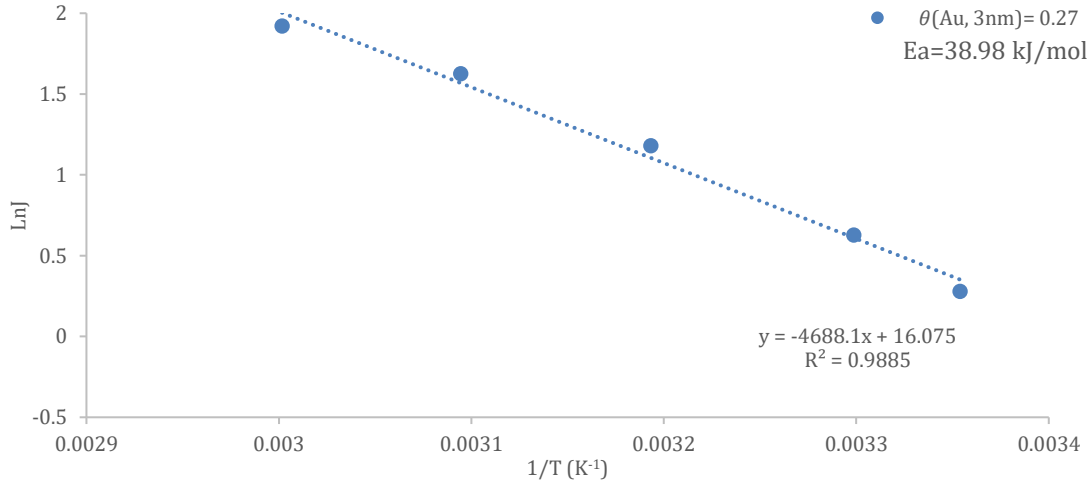

(c).

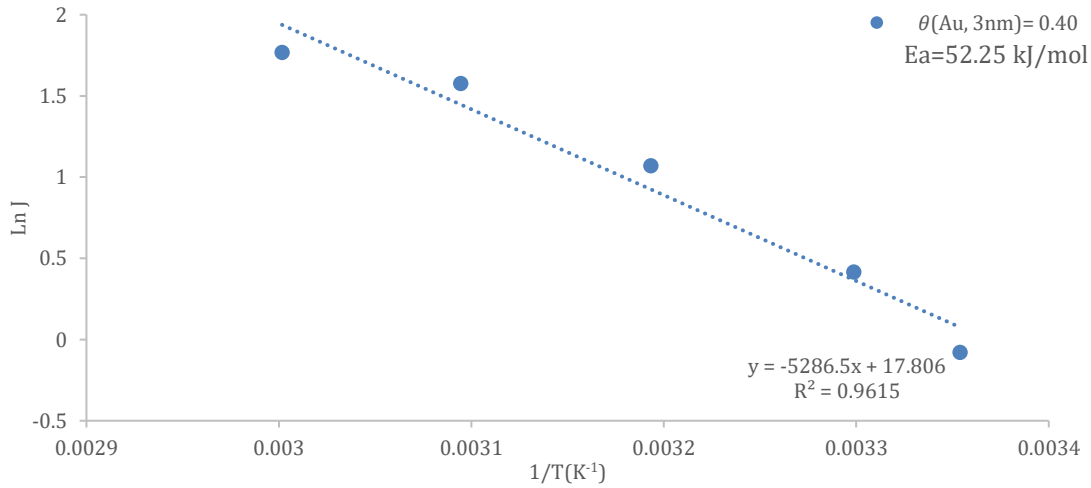

(d).

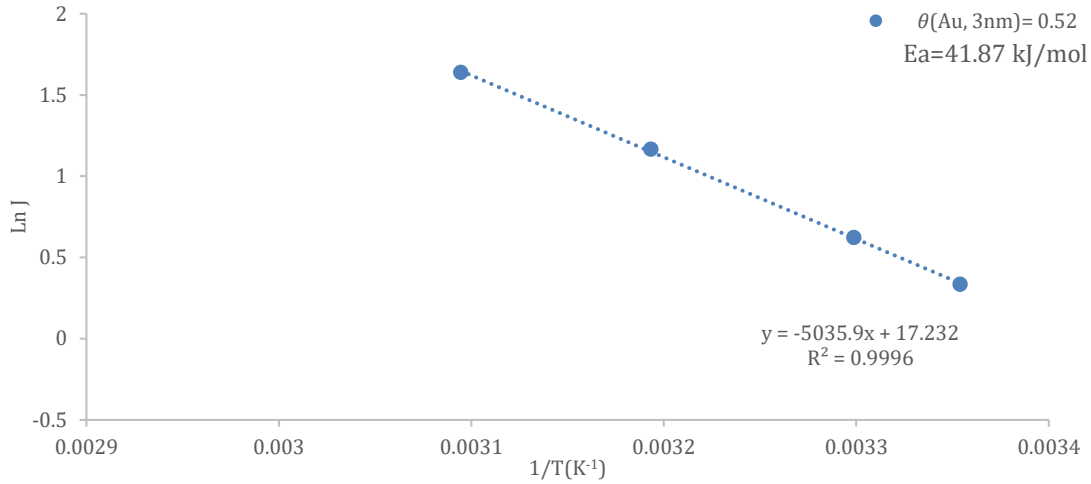

Figure 5.15. Arrhenius plots of the ethanol electrooxidation reaction (EOR) on the Pd with Au_{3nm}/PEDOT:PSS coverages: (a). $\theta_{Au,3nm}$ = 0, (b). $\theta_{Au,3nm}$ = 0.27, (c). $\theta_{Au,3nm}$ = 0.40, (d). $\theta_{Au,3nm}$ = 0.52, the data were obtained from current densities at peak potential on the anodic sweep for EOR at different temperatures in 0.1 M Ethanol + 0.1 M NaOH solution.

(a).

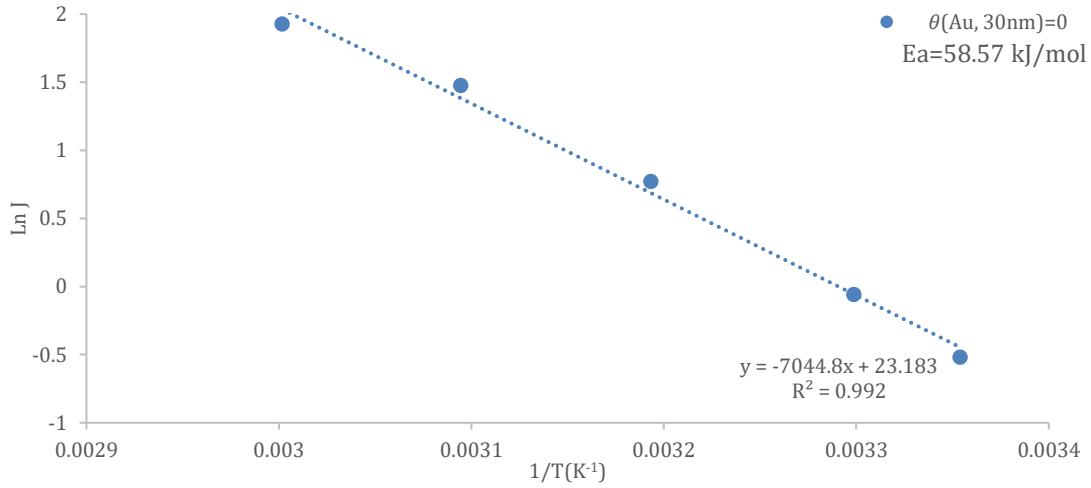
θ(Au, 30nm)=0
Ea=58.57 kJ/mol
y = -7044.8x + 23.183
R² = 0.992
Ln J
1/T(K⁻¹)
2
1.5
1
0.5
0
-0.5
-1
0.0029
0.003
0.0031
0.0032
0.0033
0.0034

(b).

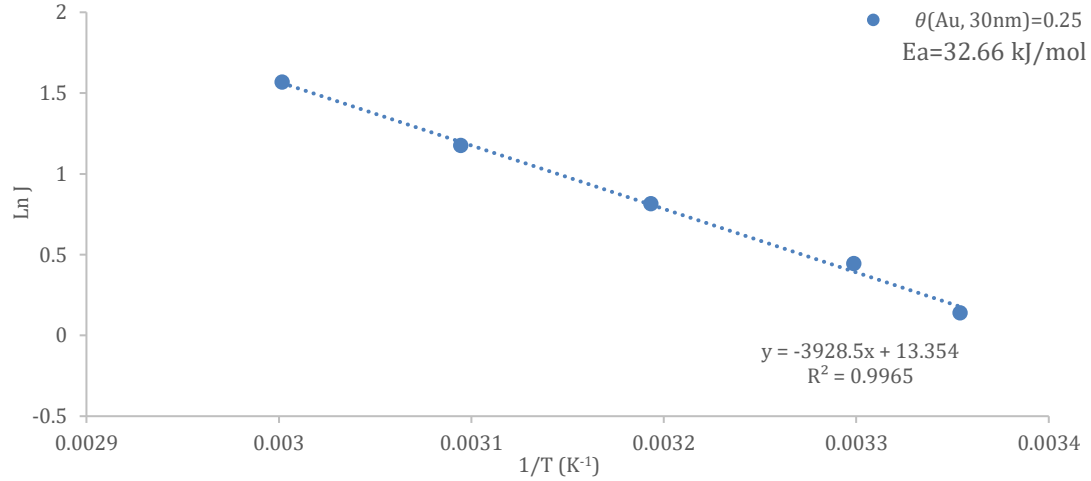
θ(Au, 30nm)=0.25
Ea=32.66 kJ/mol
y = -3928.5x + 13.354
R² = 0.9965
Ln J
1/T (K⁻¹)
2
1.5
1
0.5
0
-0.5
0.0029
0.003
0.0031
0.0032
0.0033
0.0034

(c).

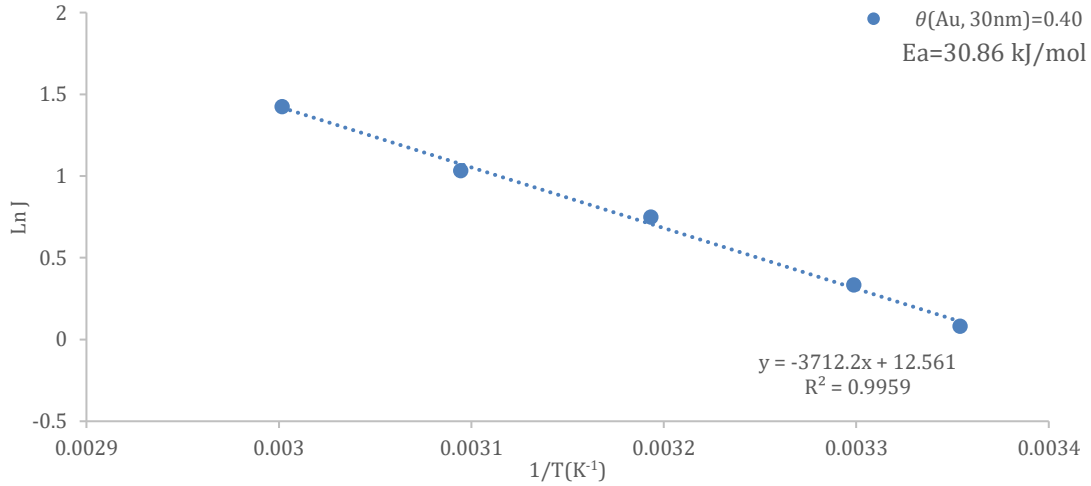
θ(Au, 30nm)=0.40
Ea=30.86 kJ/mol
y = -3712.2x + 12.561
R² = 0.9959
Ln J
1/T(K⁻¹)
2
1.5
1
0.5
0
-0.5
0.0029
0.003
0.0031
0.0032
0.0033
0.0034

(d).

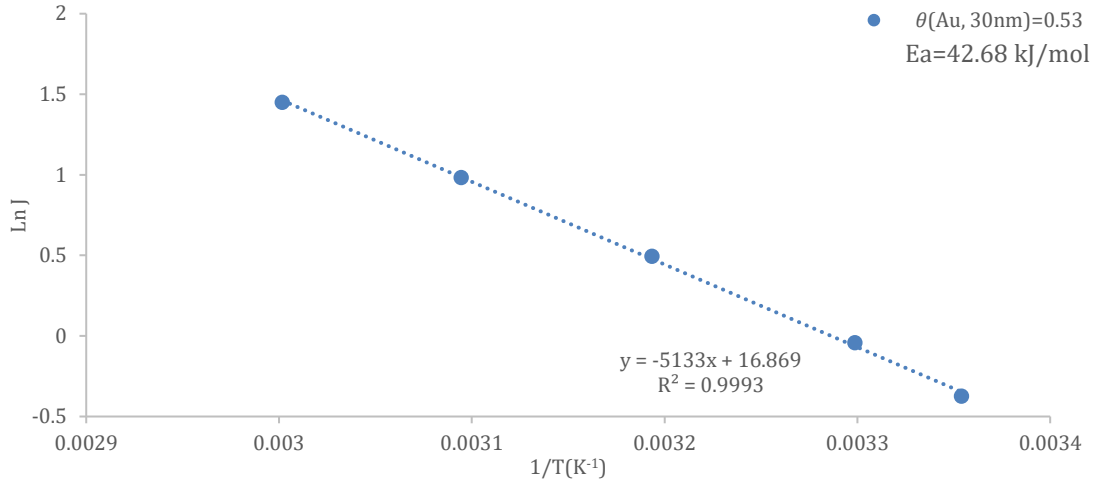

Figure 5.16. Arrhenius plots of the ethanol electrooxidation reaction (EOR) on the Pd with Au_{30nm}/PEDOT:PSS coverages: (a). $\theta_{Au,\ 30nm}$ = 0, (b). $\theta_{Au,\ 30nm}$ = 0.25, (c). $\theta_{Au,\ 30nm}$ = 0.40, (d). $\theta_{Au,\ 30nm}$ = 0.53, the data were obtained from current densities at peak potential on the anodic sweep for EOR at different temperatures in 0.1 M Ethanol + 0.1 M NaOH solution.

Figure 5.15 and Figure 5.16 show the Arrhenius plots for the current densities on EOR on the Pd electrodes with various Au_{3nm}/PEDOT:PSS and Au_{30nm}/PEDOT:PSS coverages. The records obtained from Figure 5.6. and Figure 5.8. show current densities at peak potential on the anodic sweep for EOR at each temperature. From these plots, the EOR activation energy value was calculated based on Equation 3 as appointed before.

The Ea for EOR on Au_{3nm}/PEDOT: PSS-Pd are found to be in the order: Au_{3nm}/PEDOT:PSS-Pd ($\theta_{Au,\ 3nm}$ = 0.27) < Au_{3nm}/PEDOT:PSS-Pd ($\theta_{Au,\ 3nm}$ =0 .52) < Au_{3nm}/PEDOT:PSS-Pd ($\theta_{Au,\ 3nm}$ = 0.40) < Au_{3nm}/PEDOT:PSS-Pd ($\theta_{Au,\ 3nm}$ = 0) and the Ea for EOR on Au_{30nm}/PEDOT:PSS-Pd are increased in the following order: Au_{30nm}/PEDOT:PSS-Pd ($\theta_{Au,\ 30nm}$ = 0.25) < Au_{30nm}/PEDOT:PSS-Pd ($\theta_{Au,\ 30nm}$ = 0.40) < Au_{30nm}/PEDOT:PSS-Pd ($\theta_{Au,\ 30nm}$ = 0.53) < Au_{30nm}/PEDOT:PSS-Pd ($\theta_{Au,\ 30nm}$ = 0). More specifically, The E_a value of bulk Pd is found to be 58.57 kJ/mol and for the

catalyst of Au_{3nm}/PEDOT:PSS-Pd ($\theta_{Au,3nm}$ = 0.27) the value was reduced to 38.98 kJ/mol while for Au_{30nm}/PEDOT:PSS-Pd ($\theta_{Au,3nm}$ = 0.25) the value was reduced to 32.66 kJ/mol.

It should be noted that the E_a determination may also be took at onset potential, but the maximum current observed at peak potential is considered as a more appropriate representative of the overall EOR, and the analysis of E_a obtained at peak potential is adopted here to facilitate the comparison of E_a values with the overall EOR processes on the bare and AuNPs-decorated Pd electrodes.

(a).

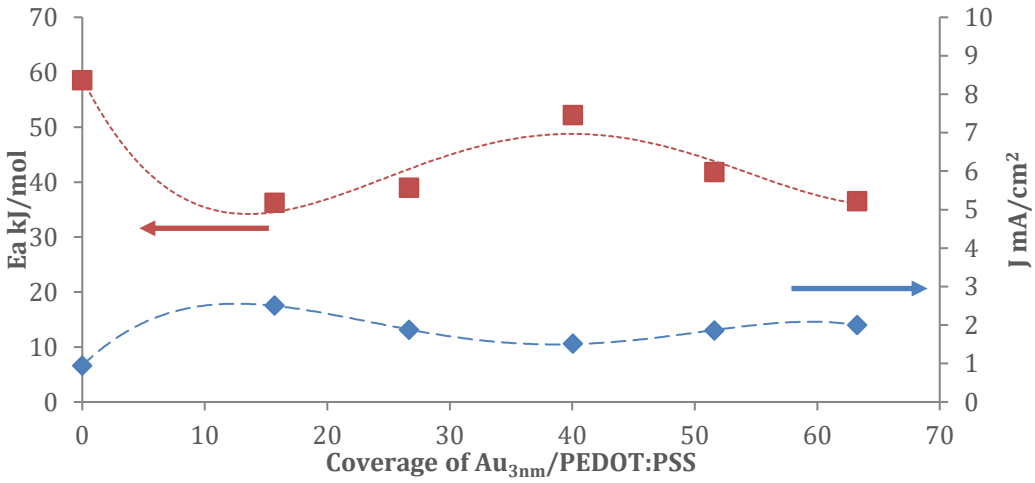

(b).

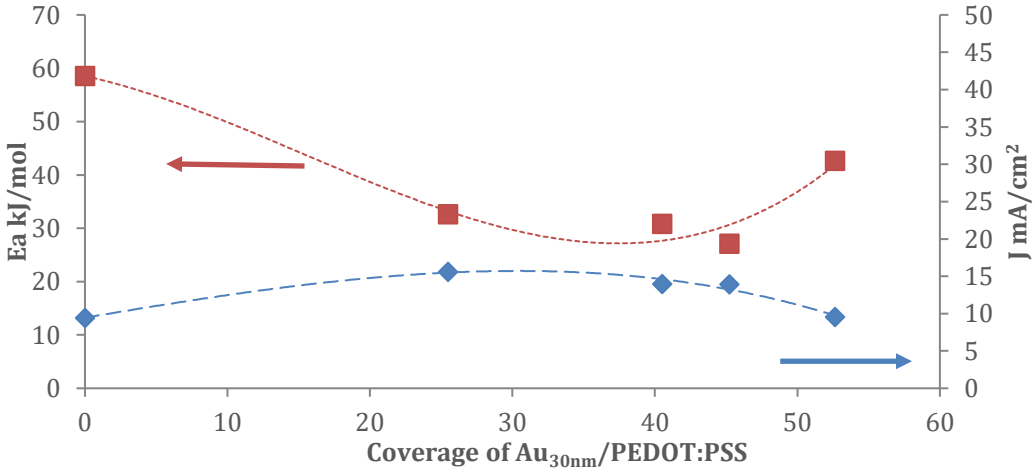

Figure 5.17 Activation energy and peak current density plots obtained at the peak poetntials for ethanol oxidation reaction (EOR) on (a). Au_{3nm}/PEDOT:PSS-Pd and (b). Au_{30nm}/PEDOT:PSS-Pd.

Figure 5.17. shows activation energy and peak current density plots obtained at the peak potentials for ethanol oxidation reaction (EOR) on Au_{3nm}/PEDOT:PSS-Pd and Au_{30nm}/PEDOT:PSS-Pd. Activation energies were calculated from Arrhenius as motioned previous and peak current densities were ferreted from CVs of EOR at 30 ˚C.

For Au_{3nm}/PEDOT:PSS-Pd, the highest Ea is achieved at zero AuNPs/PEDOT:PSS coverage then decreases to a minimum value at Au_{3nm}/PEDOT:PSS-Pd ($\theta_{Au,\ 3nm}$ = 0.16) before it increases to a higher value again. The Ea of Au_{30nm}/PEDOT:PSS-Pd shows a decreasing trend until the minimum is reached at Au_{30nm}/PEDOT:PSS-Pd ($\theta_{Au,\ 30nm}$ = 0.40) and increases again. Despite the different tendency shown in the Ea plots, the two curves corresponding to different electrocatalysts cross at 20% and 50% coverage, sectioning the plot into three distinct regions. In each region, a lower Ea indicates a higher intrinsic activity for the catalyst, as the effect of catalyst surface area has been excluded. Therefore, at lower coverage (<20%) Au_{3nm}/PEDOT:PSS-Pd is preferred, however, at coverage range of 20% to 50%, Au_{30nm}/PEDOT:PSS-Pd is better for its lower activation energy in this region[55].

The above results indicate that depending on the nanocomposite structures and the size of the AuNPs therein, the AuNP/PEDOT:PSS nanocomposites can be used as efficient electrocatalysts for the enhancement of the oxidation and/or the reduction kinetics of the ethanol fuel.

5.4 Conclusions

In this work, a benign one-step synthesis process for AuNPs-PEDOT:PSS nanocomposites and their applications in alkaline type direct ethanol fuel cells has been successfully demonstrated. Results show that by controlling the precursor / polymer concentration ratio and the plasma processing conditions, nanocomposites with wide range of structures/properties can be obtained. When characterizing selected nanocomposite films as direct ethanol fuel cell electrocatalysts under alkaline conditions, significant enhancement in EOR activity have been achieved hence suggesting the AuNP/PEDOT:PSS nanocomposite can serve as a promising candidate for a new class of Pt-free fuel cell catalysts. More importantly, this simple, rapid and environmentally friendly approach may be expanded to the synthesis of a much greater range of metal NPs/polymer nanocomposites with controlled structure/properties, providing enhanced functionality in various applications.

5.5 References

1. Y. Qiu, J. Huo, F. Jia, B.H. Shanksa, W.Z. Li, ***N-and S-doped Mesoporous Carbon as Metal-free Cathode Catalysts for Direct Biorenewable Alcohol Fuel Cells***, J. Mater. Chem. A, 2016, 4, 83-95.
2. L. An, T.S. Zhao, Y.S. Li, ***Carbon-neutral Sustainable Energy Technology: Direct Ethanol Fuel Cells***, Renew. Sust. Energ. Rev.,2015, 50, 1462-1468.
3. C. A. Martins, O. A. Ibrahim, P. Pei, E. Kjeang, ***Towards a Fuel-flexible Direct Alcohol Microfluidic Fuel Cell with Flow-through Porous Electrodes: Assessment of Methanol, Ethylene Glycol and Glycerol Fuels***, Electrochim. Acta, 2018, 271, 537-543.
4. L. M. Luo, R. H. Zhang, J. J. Du, F. Yang, H. M. Liu, Y. Yang, X. W. Zhou, ***Studies on the Synthesis and Electrocatalytic Properties of Hollow PdAu Nanocatalysts***, Int. J. Hydrogen Energy, 2017, 42, 16139-16148.
5. Y. Wen, F. F. Ren, T. C. Bai, H, Xua, Y. K. Du, ***Facile Construction of Trimetallic PtAuRu Nanostructures with Highly Porous Features and Perpendicular Pore Channels as Enhanced Formic Acid Catalysts***, Colloids Surf. A,2018, 537, 418-424.
6. J. Chang, L. Feng, K. Jiang, H. Xue, W. B. Cai, C. Liu, W. Xing, ***Pt–CoP/C as an Alternative PtRu/C Catalyst for Direct Methanol Fuel Cells***, J. Mater. Chem. A, 2016, 4, 18607-18613.
7. C. Bianchini, P. K. Shen, ***Palladium-based Electrocatalysts for Alcohol Oxidation in Half Cells and in Direct Alcohol Fuel Cells***, Chem. Rev., 2009, 109, 4183-4206.
8. R. Yue, H. Wang, D. Bin, J. Xu, Y. Du, W. Lu, J. Guo, ***Facile One-pot Synthesis of Pd-PEDOT/graphene Nanocomposites with Hierarchical Structure and High Electrocatalytic Performance for Ethanol Oxidation***, J. Mater. Chem. A, 2015, 3, 1077-1088.

9. R. Dillon, S. Srinivasan, A. Arico, V. Antonucci, ***International Activities in DMFC R&D: Status of Technologies and Potential Applications***, J. Power Sources, 2004, 127, 112-126.
10. H. R. Corti, E. R. Gonzalez, ***Direct Alcohol Fuel Cells: Materials, Performance, Durability and Applications***, Springer Science & Business Media, 2014, 1-32.
11. M. Z. F. Kamarudin, S. K. Kamarudin, M. S. Masdar, W. R. W. Daud, ***Review: Direct Ethanol Fuel Cells***, Int. J. Hydrog. Energy, 2013, 38, 9438-9453.
12. B. C. Ong, S. K. Kamarudin, S. Basri, ***Direct Liquid Fuell Cells: A Review***, Int. J. Hydrogen Energy, 2017, 42, 1014210157.
13. Y. J. Wang, D. P. Wilkinson, J. Zhang, ***Noncarbon Support Materials for Polymer Electrolyte Membrane Fuel Cell Electrocatalysts***, Chem. Rev., 2011, 111, 7625-7651.
14. K. Wu, X. Mao, Y. Liang, Y. Chen, Y. Tang, Y. Zhou, J. Lin, C. Ma, T. Lu, ***Multiwalled Carbon Nanotubes Supported Palladium-Phosphorus Nanoparticles for Ethanol Electrooxidation in Alkaline Solution***, J. Power Sources, 2012, 219, 258-262.
15. X. G. Wang, B. Tang, X. B. Huang, Y. Ma, Z, H. Zhang, ***High Activity of Novel Nanoporous Pd–Au Catalyst for Methanol Electro-Oxidation in Alkaline Media***, J. Alloys Compd., 2013, 565, 120-126.
16. F. Wang, J. S. Qiao, J. Wang, H. T. Wu, X. Y. Yue, Z. H. Wang, W. Sun, K. N. Sun, ***Reduced Graphene Oxide Supported Ni@Au@Pd Core@Bishell Nanoparticles as Highly Active Electrocatalysts for Ethanol Oxidation Reactions and Alkaline Direct Bioethanol Fuel Cells Applications***, Electrochim. Acta, 218, 271, 1-9.
17. Q. F. Yi, Q. H. Chen, Z. Yang, ***A Novel Membrane-less Direct Alcohol Fuel Cell***, J Power Sources 2015, 298, 171–176.
18. E. Lee, I. S. Park, A. Manthiram, ***Synthesis and Characterization of Pt−Sn−Pd/C Catalysts for Ethanol Electro-Oxidation Reaction***, J. Phys. Chem. C, 2010, 114, 10634–10640.

19. Y. W. Lee, M. J. Kim, Y. Kim, S. W. Kang, J. H. Lee, S. W. Han, ***Synthesis and Electrocatalytic Activity of Au–Pd Alloy Nanodendrites For Ethanol Oxidation***. J. Phys. Chem. C, 2010, 114, 7689–7693.

20. B. T. Sneed, C. H. Kuo, C. N. Brodsky, C. K. Tsung, ***Iodide-Mediated Control of Rhodium Epitaxial Growth on Well-Defined Noble Metal Nanocrystals: Synthesis, Characterization, and Structure-Dependent Catalytic Properties***, J. Am. Chem. Soc., 2012, 134, 18417–18426.

21. Q. G. He, W. Chen, S. Mukerjee, S. W. Che, F. Laufek, ***Carbon-supported PdM (M=Au and Sn) Nanocatalysts for the Electrooxidation of Ethanol in High pH Media***, J. Power Sources, 2009, 187, 298–304.

22. L. S. Jou, J. K. Chang, T. J. Twhang, I. W. Sun, ***Electrodeposition of Palladium-Copper Films from 1-ethyl-3-methylimidazolium Chloride-tetrafluoroborate Ionic Liquid on Indium Tin Oxide Electrodes***, J. Electrochem. Soc., 2009, 156, 193–197.

23. C. Hsu, C. W. Huang, Y. W. Hao, F. Q. Liu, ***Au/Pd Coreeshell Nanoparticles for Enhanced Electrocatalytic Activity and Durability***, Electrochem. Commun., 2012, 23, 133–136.

24. Y. H. Qin, Y. F. Li, R. L. Lv, T. L. Wang, W. G. Wang, C. W. Wang, ***Pd-Au/C Catalysts with Different Alloying Degrees for Ethanol Oxidation in Alkaline Media***, Electrochim Acta, 2014, 144, 50–55.

25. G. Del-Giudice, A. Y. Tesio, P. S. Cappellari, R. E. Palacios, G. A. Planes, ***Evolution of Adsorbed CO on Pt and Pt/Au Surface***, Electrochim. Acta, 2018, 270, 48-53.

26. C. H. Liu, X. L. Cai, J. S. Wang, J. Liu, A. Riese, Z. D. Chen, X. L. Sun, S. D. Wang, ***One-step Synthesis of AuPd Alloy Nanoparticles on Graphene as a Stable Catalyst for Ethanol Electro-Oxidation***, Int. J. Hydrogen Energy, 2016, 41, 13476-13484.

27. G. J. Zhang, Y. E. Wang, X. Wang, Y. Chen, Y. M. Zhou, Y. W. Tang, L. D. Lu, J. C. Bao, T. H. Lu, ***Preparation of Pd–Au/C Catalysts with Different Alloying***

Degree and their Electrocatalytic Performance for Formic Acid Oxidation, Appl. Catal. B: Environ, 2011, 102, 614–619.

28. H. Xu, J. Wang, B. Yan, K. Zhang, S. Li, C. Wang, Y. Shiraishi, Y. Du, P. Yang, ***Hollow AuxAg/Au Core/shell Nanospheres as Efficient Catalysts for Electrooxidation of Liquid Fuels***, Nanoscale, 2017, 9, 12996-13003.
29. C. H. Cui, J. W. Yu, H. H. Li, M. R. Gao, H. W. Liang, S. H. Yu, ***Remarkable Enhancement of Electrocatalytic Activity by Tuning the Interface of Pd–Au Bimetallic Nanoparticle Tubes***, ACS Nano, 2011, 5, 211-4218.
30. F. L. Cheng, X. C. Dai, H. Wang, S. P. Jiang, M. Zhang, C. W. Xu, ***Synergistic Effect of Pd–Au Bimetallic Surfaces in Au-covered Pd Nanowires Studied for Ethanol Oxidation***, Electrochim. Acta, 2010, 55, 2295-2298.
31. Y. Y. Feng, Z. H. Liu, Y. Xu, P. Wang, W. H. Wang, D. S. Kong, ***Highly Active PdAu Alloy Catalysts for Ethanol Electro-Oxidation***, J. Power Sources, 2013, 232, 99-105.
32. V. R. Stamenkovic, B. S. Mun, M. Arenz, K. J. J. Mayrhofer, C. A. Lucas, G. F. Wang, P. N. Ross, N. M. Markovic, ***Trends in Electrocatalysis on Extended and Nanoscale Pt-bimetallic Alloy Surfaces***, Nat. Mater., 2007, 6, 241–247.
33. G. E. Ramirez-Caballero, Y. G. Ma, R. Callejas-Tovar and P. B. Balbuena, ***Surface Segregation and Stability of Core–Shell Alloy Catalysts for Oxygen Reduction in Acid Medium***, Phys. Chem. Chem. Phys., 2010, 12, 2209–2218.
34. K. Sasaki, H. Naohara, Y. Cai, Y. M. Choi, P. Liu, M. B. Vukmirovic, J. X. Wang, R. R. Adzic, Angew. ***Core-Protected Platinum Monolayer Shell High-Stability Electrocatalysts for Fuel-Cell Cathodes***, Chem., Int. Ed., 2010, 49, 8602–8607.
35. K. Sasaki, H. Naohara, Y. M. Choi, Y. Cai, W. F. Chen, P. Liu, R. R. Adzic, ***Highly Stable Pt Monolayer on PdAu Nanoparticle Electrocatalysts for the Oxygen Reduction Reaction***, Nat. Commun., 2012, 3, 1115.

36. J. Greeley, J. K. Norskov, ***Electrochemical Dissolution of Surface Alloys in Acids: Thermodynamic Trends from First-Principles Calculations***, Electrochim. Acta, 2007, 52, 5829–5836.

37. D. Zhao, B. Q. Xu, ***Enhancement of Pt Utilization in Electrocatalysts by using Gold Nanoparticles***, Angew. Chem. Int. Ed., 2006, 45, 4955–4959.

38. M. Harada, K. Asakura, Y. Ueki, N. Toshima, ***Structural Analysis of Polymer-Protected Palladium/Rhodium Bimetallic Clusters using EXAFS Spectroscopy***, J. Phys. Chem., 1993, 97, 10742–10749.

39. Y. Chen, Y. W. Tang, C. P. Liu, W. Xing, T. H. Lu, ***Room Temperature Preparation of Carbon Supported Pt–Ru Catalysts***, J. Power Sources, 2006, 161, 470–473.

40. S. Z. Hu, F. Munoz, J. Noborikawa, J. Haan, L. Scudiero and S. Ha, ***Carbon Supported Pd-based Bimetallic and Trimetallic Catalyst for Formic Acid Electrochemical Oxidation***, Appl. Catal., B, 2016, 180, 758–765.

41. B. Hvolbæk, T. V. W. Janssens, B. S. Clausen, H. Falsig, C. H. Christensen, J. K. Nørskov, ***Catalytic Activity of Au Nanoparticles***, Nanotoday, 2007, 2, 14-18.

42. M. M. Maye, J. Luo, L. Han, N. Kariuki, Z. Rab, N. Khan, H. R. Naslund , C. J. Zhong, ***Gold and Alloy Nanoparticle Catalysts in Fuel Cell Reaction***, Div. Fuel Chem. 2004, 49, 938-939.

43. S. S. Kumar, C. S. Kumar, J. Mathiyarasu, K. L. Phani, ***Stabilized Gold Nanoparticles by Reduction using 3,4-ethylenedioxythiophene-polystyrenesulfonate in Aqueous Solutions: Nanocomposite Formation, Stability, and Application in Catalysis***, Langmuir 2007, 23, 3401–3408.

44. D. J. Kang, H. Kang, K. H. Kim, B. J. Kim, ***Nanosphere Templated Continuous PEDOT:PSS Films With Low Percolation Threshold for Application in Efficient Polymer Solar Cells***, ACS Nano, 2012, 6, 7902–7909.

45. J. L. Wu, F. C. Chen, Y. S. Hsiao, F. C. Chien, P. L. Chen, C. H. Kuo, M. H. Huang, C. S. Hsu, ***Surface Plasmonic Effects of Metallic Nanoparticles on the***

Performance of Polymer Bulk Heterojunction Solar Cells, ACS Nano, 2011, 5, 959–967.

46. N. Toshima, N. Jiravanichanun, ***Improvement of Thermoelectric Properties of PEDOT/PSS Films by Addition of Gold Nanoparticles: Enhancement of Seebeck Coefficient***, J. Electron. Mater., 2013, 42, 1882–1887.
47. M. Mumtaz, B. Ouvrard, L. Maillaud, C. Labrugere, E. Cloutet, H. Cramail, M. H. Delville, ***Hybrid PEDOT–Metal Nanoparticles–New Substitutes for PEDOT:PSS in Electrochromic Layers–towards Improved Performance***, Eur. J. Inorg. Chem., 2012, 5360–5370.
48. E. Antolini, E. R. Gonzalez, ***Polymer Supports for Low-Temperature Fuel Cell Catalysts***, Appl. Catal. A., 2009, 365, 1–19.
49. C. Jin, C. C. Wan, R. L. Dong, ***Electrocatalytic Activity Enhancement of Pd Nanoparticles Supported on Reduced Graphene Oxide by Surface Modification with Au***, J. Electrochem. Soc., 2017, 164, H696-H700.
50. K. A. Assiongbon, D. Roy, ***Electro-oxidation of Methanol on Gold in Alkaline Media: Adsorption Characteristics of Reaction Intermediates Studied Using Time Resolved Electro-chemical Impedance and Surface Plasmon Resonance Techniques***, Surf. Sci., 2005, 594, 99-119.
51. Z. Wu, S. H. Zhou, H. G. Zhu, S. Dai, S. H. Overbury, ***Oxygen-assisted Reduction of Au Species on Au/SiO_2 Catalyst in room Temperature CO Oxidation***, Chem. Commun.,2008, 3308-3310.
52. F. L. Cheng, X. C. Dai, H. Wang, S. P. Jiang, M. Zhang, C. W. Xu, ***Synergistic Effect of Pd–Au Bimetallic Surfaces in Au-covered Pd Nanowires Studied for Ethanol Oxidation***, Electrochim. Acta, 2010, 55, 2295-2298.
53. D. Kardash, C. Korzeniewski, N. Markovic, ***Effects of Thermal Activation on the Oxidation Pathways of Methanol at Bulk Pt–Ru Alloy Electrodes***, J. Electroanal. Chem., 2001, 500, 518-523.

54. H. A. Gasteiger, N. Marković, P. N. Ross, E. J. Cairns, ***Temperature-Dependent Methanol Electro-Oxidation on Well-Characterized Pt-Ru Alloys***, J. Electrochem. Soc., 1994, 141, 1795-1803.

55. A. Dutta, A. Mondal, P. Broekmann, J. Datta, ***Optimal Level of Au Nanoparticles on Pd Nanostructures Providing Remarkable Electro-Catalysis in Direct Ethanol Fuel Cell***, J. Power Sources, 2017, 361, 276-284.

56. J. Datta, A. Dutta, S. Mukherjee, ***The Beneficial Role of the Cometals Pd and Au in the Carbon-Supported PtPdAu Catalyst Toward Promoting Ethanol Oxidation Kinetics in Alkaline Fuel Cells: Temperature Effect and Reaction Mechanism***, J. Phys. Chem. C, 2011, 115, 15324-15334.

57. L. W. H. Leung, M. J. Weaver, ***Real-time FTIR Spectroscopy as a Quantitative Kinetic Probe of Competing Electrooxidation Pathways of Small Organic Molecules***, J. Phys. Chem., 1988, 92, 4019-4022.

58. T. Iwasita, ***Electrocatalysis of Methanol Oxidation***, Electrochim. Acta, 2002, 47, 3663-3674.

59. Q. L. Wang, R. Fang, L. L. He, J. J. Feng, J. h. Yuana, A. J. Wang, ***Bimetallic PdAu Alloyed Nanowires: Rapid Synthesis via Oriented Attachment Growth and Their High Electrocatalytic Activity for Methanol Oxidation Reaction***, J. Alloys Compd., 2016, 684, 379-388.

60. H. L. Yang, Z. N. Yu, S. W. Li, Q. L. Zhang, J. Jin, J. T. Ma, ***Ultrafine Palladium-Gold-Phosphorus Ternary Alloyed Nanoparticles Anchored on Ionic Liquids-Noncovalently Functionalized Carbon Nanotubes with Excellent Electrocatalytic Property for Ethanol Oxidation Reaction in Alkaline Media***, J. Catal., 2017, 353, 256-264.

61. F. A. Ksar, L. Ramos, B. Keita, L. Nadjo, P. Beaunier, H. Remita, ***Bimetallic Palladium−Gold Nanostructures: Application in Ethanol Oxidation***, Chem. Mater., 2009, 21, 3677-3683.

62. Sh. Y. Chen, H. Xu, B. Yan, S. M. Li, J. T. Dai, C. Q. Wang, Y. Shiraishi, Y. K. Du, ***Highly Active Electrooxidation of Ethylene Glycol enabled by Pinecone-like Pd–Au–Ag Nanocatalysts***, J. Taiwan Inst. Chem. Eng., 2018, 83, 64-73.

63. H. Xu, P. P. Song, B. Yan, J. Wang, F. Gao, Y. P. Zhang, Y. K. Du, ***Superior ethylene glycol electrocatalysis enabled by Au-decorated PdRu nanopopcorns***, J. Electroanal. Chem., 2018, 814, 31-37.

64. B. Rezaei, E. Havakeshian, A. A. Ensafi, ***Electrocatalytic Activity of Bimetallic PdAu Nanostructure Supported on Nanoporous Stainless Steel Surface using Galvanic Replacement Reaction Toward the Glycerol Oxidation in Alkaline Media***, J. Electroanal. Chem., 2016, 782, 108-116.

65. Y. Yang, L. Jin, B. Liu, P. Kerns, J. He, ***Direct Growth of Ultrasmall Bimetallic AuPd Nanoparticles Supported on Nitrided Carbon Towards Ethanol Electrooxidation***, Electrochim. Acta, 2016, 782, 108-116.

66. N. Li, W. Y. Xia, C. W. Xu, S. Chen, ***Pt/C and Pd/C Catalysts Promoted by Au for Glycerol and CO Electrooxidation in Alkaline Medium***, J. Energy Institute, 2017, 90, 725-733.

Chapter Six

High Electrochemical Performance of Ag-Pd Bimetallic Catalyst for the Ethanol Electrooxidation in Alkaline Media

6.1 Introduction

In recent years, renewable energy has drawn worldwide attentions due to the dwindling supplies of fossil fuels and environmental pollutions. Direct ethanol fuel cells (DEFCs), as one of the most promising clean energy solutions, are attracting increasing interests for its capability of replacing traditional fossil fuels by directly converting the chemical energy of ethanol to electricity with high energy density and almost zero emission[1-9].

Ethanol has its own unique advantage as a reliable fuel candidate over hydrogen, methanol and formic acid, for its less toxicity, safer transportation/storage, exceptionally high energy density and the sustainable production of large quantities from biomass[10-16]. The high energy density of ethanol originates from the complete oxidation of ethanol to CO_2 ($C_2H_5OH + 3H_2O \rightarrow 2CO_2 + 12H^+ + 12e^-$), yielding 12 electrons (as opposed to six electrons from methanol and two form hydrogen).

At present, acidic proton exchange membranes (PEMs) are widely employed in direct ethanol fuel cells (DEFCs). However, compared with PEMs, alkaline fuel cells (AFCs) exhibit a higher kinetics of ethanol oxidation reaction. In addition, the abundance of adsorbed hydroxyl groups (*OH) on the catalyst surface in alkaline media leads to the poisoning effect of carbonyl species being weak compared to that in acidic systems. Meanwhile, the less corrosive nature of alkaline electrolyte increases the possibility of using low-cost and Pt-free electrocatalysts[17-22].

Since fuel cell devices normally operate under strongly acetic/basic environment, which leads to the corrosion of the electrode materials[23], the usage of novel metals like Pt is indispensable. This brings on another problem: the worldwide Pt reserve volume is extremely low, and they are too expensive to bring high-performance DEFCs into service commercially. To this end, scientists have established several approaches to overcome these challenges. Firstly, Pd was discovered as a more prospective DEFC catalyst alternative to replace high-cost Pt, which exhibits similar catalytic reactivity

and is higher reserved on Earth (200 times) with lower material price[24-25]. Moreover, Pd is considered as the more active catalyst for the EOR in alkaline media than Pt among several pure metals[26]. However, alone Pd catalyst cannot meet the commercialization requirement and its catalytic reactivity still needs to be enhanced. Combing Pd with other metal to form bimetallic catalysts has been reported as a powerful approach to significantly improve the catalytic activity and facilitate C-C bond cleavage process to increase poisoning intermediates tolerance. On the other hand, combing Pd with less expensive metal will decrease the cost of catalyst [27-30]. In these regard, great efforts have been made on Pd-based catalyst, such as Pd-Bi[31], Pd-Co [32], Pd-Pb [33], Pd-Au [34], Pd-Cu [35], Pd-Ni [36], Pd-Ir [37], Pd-Ru [38], Pd-Sn [39] and Pd-Ag[40].

Accordingly, Norskov's d-band center theory[41] proposed that the reaction rate can be remarkably influenced by alloying metals with smaller lattice constants on initial metal for its shift up of d-band center, such as silver, leading to the enhancement of adsorption ability and catalytic activity of catalyst[42-44]. Reports show that Ag, as a cheaper and more abundant metal, can enhance Pd electrode with electrocatalytic activity and stability when Ag and Pd or Pd/Carbon are combined[45-51]. Changchun Jin eta.[44] moficated Pd polycrystalline electrode with different loadings silver by potentiostatic deposition method, and found out Ag-modification will improve electrocatalytic activity and stability of Pd electrode for allyl alcohol oxidation. Yi Wang eta.[46] prepared Pd-Ag/C catalyst with varied Ag loadings by borohydride reduction, proving that the addition of Ag will both facilitates methanol oxidation and remove the adsorbed CO which will inactive catalyst. M.C. Oliveira eta.[41] alloyed Pd with three different loadings silver by sequential electroless deposition of Ag and Pd on a stainless steel substrate. The results showed that Pd-Ag with medium Ag content (21%) has highest catalytic activity. A. Safavi eta.[48] synthesis Pd-Ag alloy by microwave irradiation, which reveals high catalytic activity, stability, poisoning tolerance and capacity for electrooxidation of ethanol in alkaline medium. Although many methods have been developed to fabricate different Pd-Ag or Pd-Ag/Carbon catalyst, there are few

exhaustive works about electro-activities of Ag-decorated bulk Pd electrode in varied temperatures and EOR activation energy in alkaline media, especially comprehensive understanding on the mechanism at atomic level.

In this research, bulk Pd electrode was decorated with Ag of different coverage for the ethanol oxidation in alkaline media. Cyclic voltammetry and chronoamperometry with diverse temperatures were investigated to study the catalytic reactivity of Pd/Ag electrode towards ethanol oxidation reaction. It is proved that catalytic reactivity of bulk Pd can be activated by being decorated with Ag, and Ag/Pd electrode with appropriate coverage of 0.37 exhibits the best catalytic performance. More evidence to support the conclusion has been proposed by activation energy calculated based on Arrhenius Plots.

6.2 Experimental

6.2.1 Chemicals

$AgNO_3$ (99.99%), sulfuric acid (95-98%), absolute ethanol (≥99.9%), sodium hydroxide (semi-conduct degree) were purchased from Sigma-Aldrich. All chemicals were utilized without further purification. All the water used to clean the electrode and prepare aqueous solutions was purified by thermoscientific Barnstead water System (18 MΩ• cm at 298K). High purity nitrogen was used to deoxygenate the solution and to keep air-free atmosphere in the fuel cell during the measurements.

6.2.2 Electrode preparation

All the electrochemical measurements were carried out in a home developed three-electrode cell using an Autolab electrochemical workstation. A bulk Pd (ø = 6.5 mm) was employed as the working electrode. The bulk Pd electrode was mechanically polished to a mirror-finish to remove surface contaminants by using a range of alumina oxide powders of three different particle sizes in sequence, e.g. 1, 0.3 and 0.05 μm, then rinsed thoroughly with ultra pure water and followed up with ultrasonic washing in ultra pure water for several times. Further polish was performed by cyclic voltammetry (CV) in 0.1 M sulfuric acid, with a scan rate of 50 mV/s, a potential step of 0.00244 V and an initial potential range from 0.15 V to 1.35 V (*vs.* RHE). The reference electrode used in acidic media was Ag/AgCl while the counter electrode was a piece of Pt mesh.

6.2.3 Ag-decorated bulk Pd

To modify the bulk Pd electrode with Silver, a certain concentration of Silver Nitrate ($AgNO_3$) in 0.5 M H_2SO_4 solution was dropped onto the polished Pd electrode and stayed for a while, followed by being rinsed with ultra pure water before further test. Cyclic voltammetry with potential range of 0.15 V to 0.75 V (*vs.* RHE) in 0.1 M H_2SO_4 was performed until stable (about 10 cycles) for the potentiostatic decoration of Ag, using Ag/AgCl as the reference electrode and a piece of Pt mesh as the counter electrode. The upper potential limit of 0.75 V (*vs.* RHE) was set to prevent silver from oxidation. The coverage of decorated Ag was controlled by the concentration of $AgNO_3$ in 0.5 M H_2SO_4 from 0.5 mM to 1 mM and the dwell time from 30 s to 120 s.

6.2.4 Electrochemical characterization

The electrochemical surface areas (ECSA) of Pd electrode before and after Ag decoration were evaluated by counting total charge during hydrogen adsorption/desorption using CV in 0.1 M H_2SO_4 with a scan rate of 50 mV/s, a Ag/AgCl as the reference electrode.

In this work, all of the current densities are normalized to the electrochemical surface area (ESCA) of the respective bare bulk Pd since Ag has no distinct electrocatalytic activity for EOR.

Electrooxidation of ethanol on the bare and Ag-decorated Pd electrode were studied by Cyclic Voltammetry (CV) and chronoamperometry (CA) in a mixed solution of 0.1 M NaOH with 0.1 M Ethanol which was deaerated by bubbling ultrapure N_2 for 20 min to remove dissolved O_2 at different temperatures, a Hg/HgO electrode as the reference electrode and a Pt mesh as the counter electrode. The potential range of CV was employed between 0.11 and 1.11 V (*vs.* RHE) at a scan rate of 50 $mV \cdot s^{-1}$. The

potential of CA was kept at 1.01 V (*vs.* RHE) for 3 s to oxidize all the adsorbed intermediates, followed by the potential of 0.11V (*vs.* RHE) for 0.1 s to reduce the oxides as well as adsorbed ethanol, and finally stable at 0.71 V (*vs.* RHE) for 190 s for CA testing.

6.3 Results and discussion

6.3.1 Electrochemical study of bare and Ag-decorated Pd by cyclic voltammetry

(a).

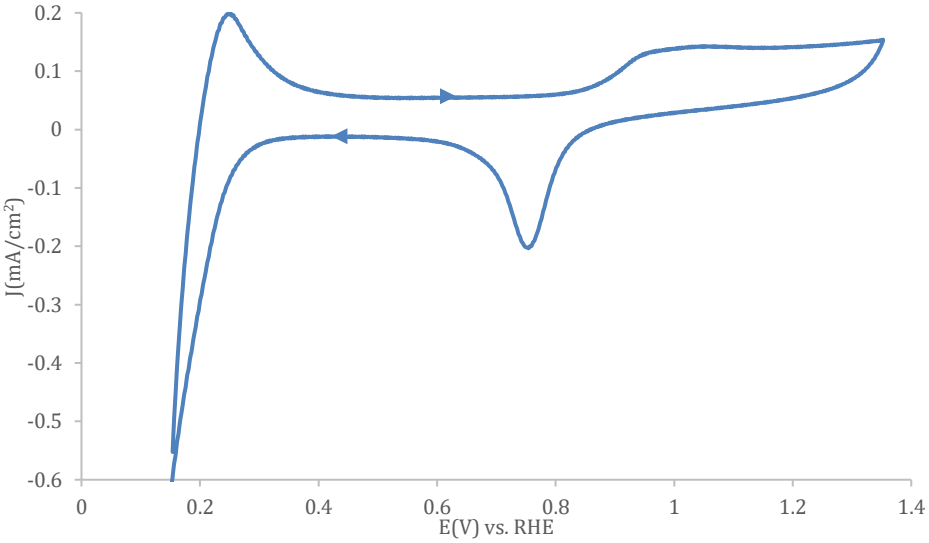

(b).

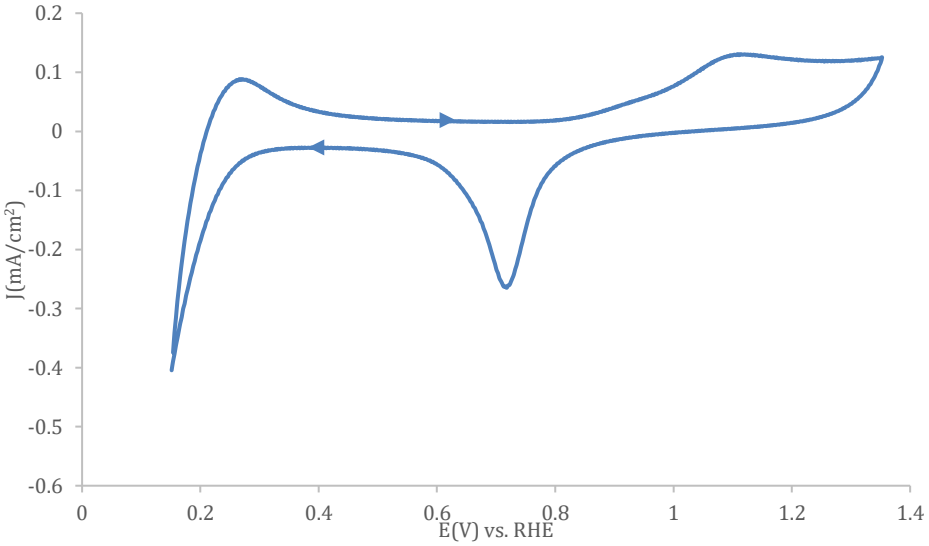

Figure 6.1 Cyclic voltammograms (CVs) of (a). bulk Pd in 0.1M H_2SO_4, (b). Ag-

decorated bulk Pd (θ_{Ag} = 0.23) in 0.1 M H_2SO_4 in 0.1 M H_2SO_4. Scan rate: 50 mV/s.

As represented in Figure 6.1.a and Figure 6.1.b, the typical cyclic voltammograms (CVs) of bare Pd electrode and a Ag-decorated Pd electrode in 0.1M H_2SO_4 with potential range from 0.15 V to 1.35 V (*vs.* RHE) at a scan rate of 50 mV•s^{-1} were studied to examine the affinity of hydrogen toward Pd catalyst[48]. A broaden peak in positive scan which can be observed from 0.15 V (*vs.* to 0.5 V (*vs.* RHE) is corresponding to the oxidation of the adsorbed hydrogen(H_{ad}) whilst a negative peak at 0.15 V(*vs.* RHE) is assigned to the oxidation of the absorbed of hydrogen (H_{ab}) on Pd surface[49-52]. A cathodic peak starts from 0.75 V (*vs.* RHE) in Figure 6.1.a. has been attributed to the reduction of Pd oxides produced during the forward scan[17.48.53].

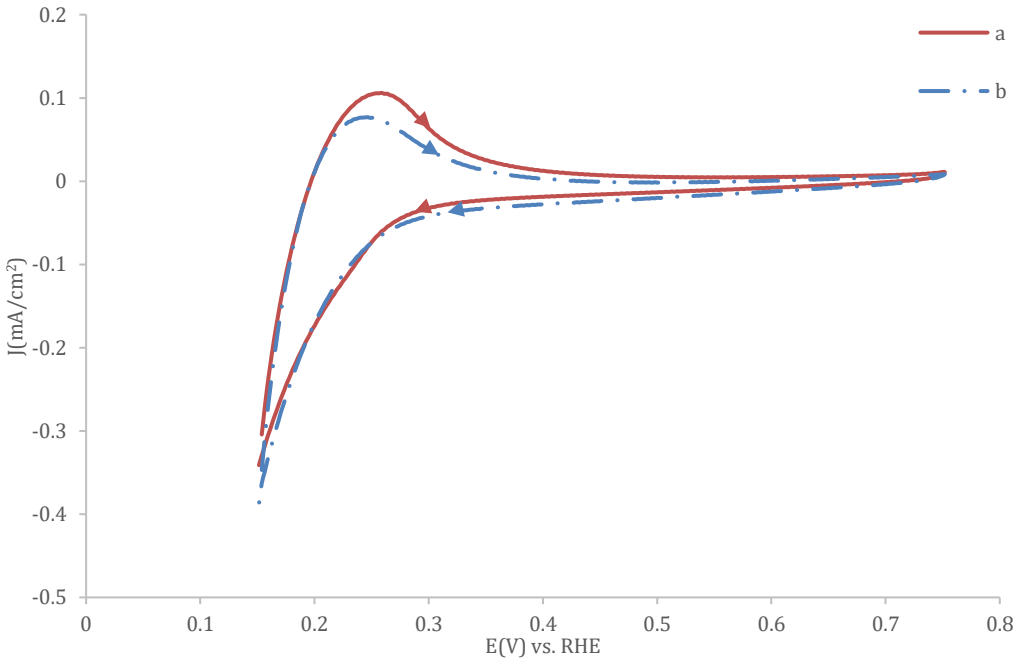

Figure 6.2 Cyclic voltammograms (CVs) of a. Bulk Pd and b. Ag-decorated Bulk Pd (θ_{Ag} = 0.26) in 0.1 M H_2SO_4. Scan rate: 50mV/s.

The effective catalytic surface area (ECSA) of Pd and Ag-Pd electrode were evaluated by CV in 0.1 M H_2SO_4, with potential range from 0.15 V to 0.75 V (*vs.* RHE). As shown in Figure 6.3, the hydrogen adsorption regions area of electrode between 0.2 V and 0.4 V (*vs.* RHE) decreases after Ag-decorated, which can be utilized to evaluate ECSA and coverage of Ag-Pd electrode, proving that Pd electrode is successfully decorated by Ag. Moreover, there is no peak of Ag and its oxide around 0.75V(*vs.* RHE) indicating that Ag is stable in the electrode. The assumption of 212 μC•cm^{-2} for Pd surface was adapted here to determine ECSA[17.54]. The evaluation of various Ag coverages (θ_{Ag}) can be equated with the blockage of hydrogen adsorption[17.53.55]. Therefore, θ_{Ag} can be defined as:

$$\theta_{Ag} = 1 - \theta_H = 1 - \frac{Q_H^{Ag}}{Q_H^{bare}} \qquad (1)$$

Where, Q_H^{Ag} is the total charge passed during hydrogen adsorption. Q_H^{Ag} is the charge associated with hydrogen adsorption on Ag-decorated Pd electrode, while Q_H^{bare} is the charge of hydrogen adsorption on Pd electrode. The integrations of hydrogen adsorption region between 0.2V and 0.4V (*vs.* RHE) are utilized to determine the coverage.

6.3.2 Ethanol electrooxidation on bare Pd and Ag-decorated Pd

(a).

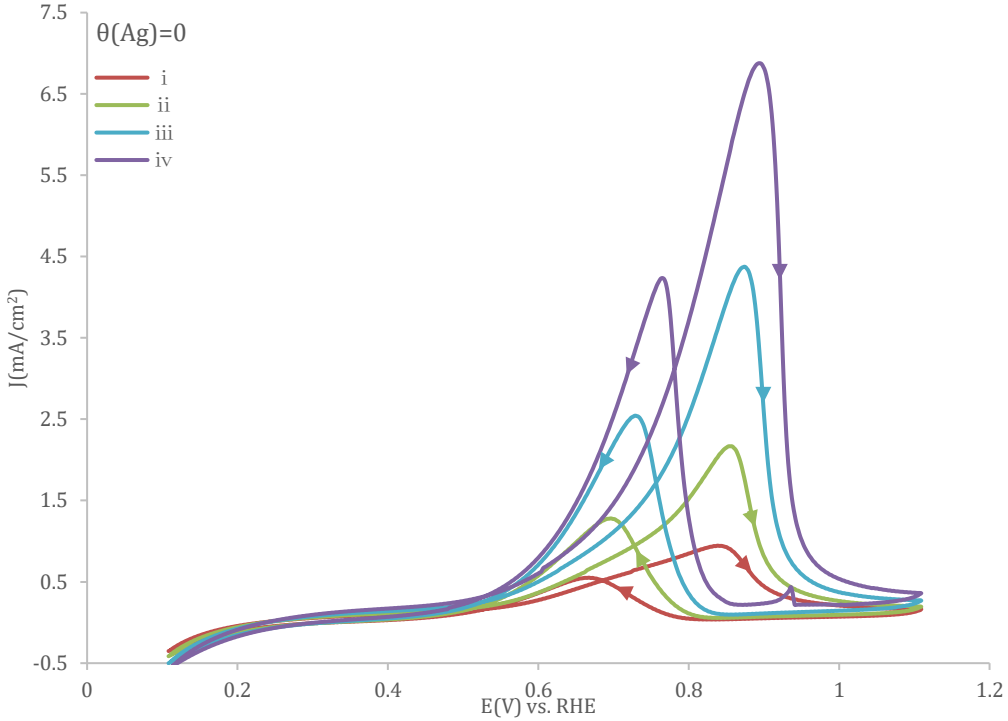

(b).

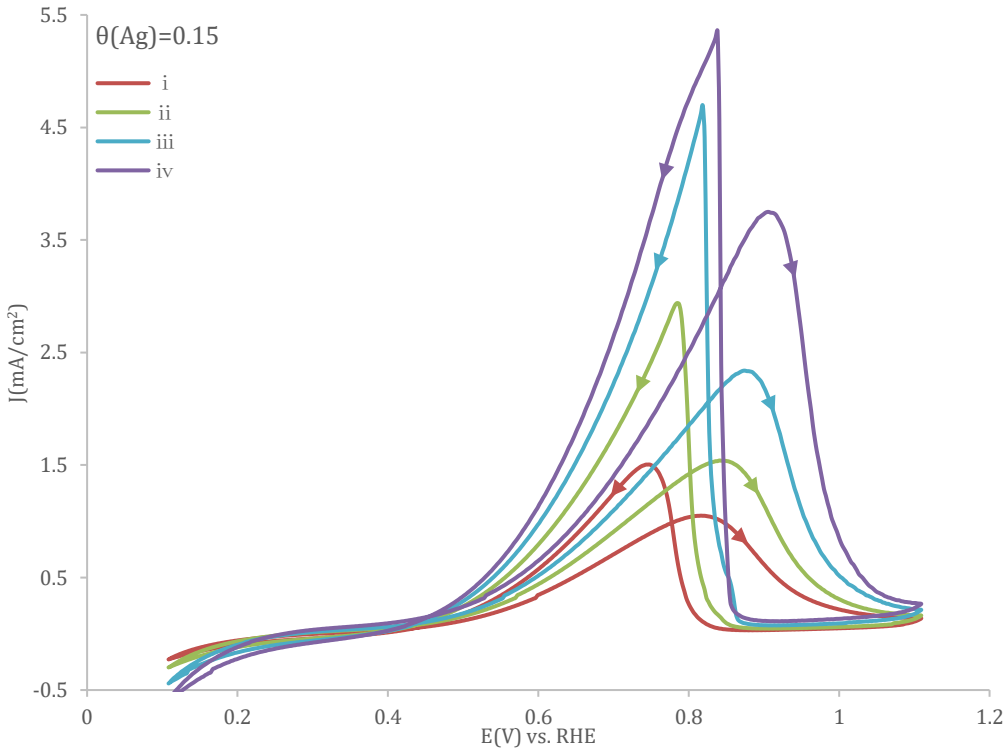

(c).

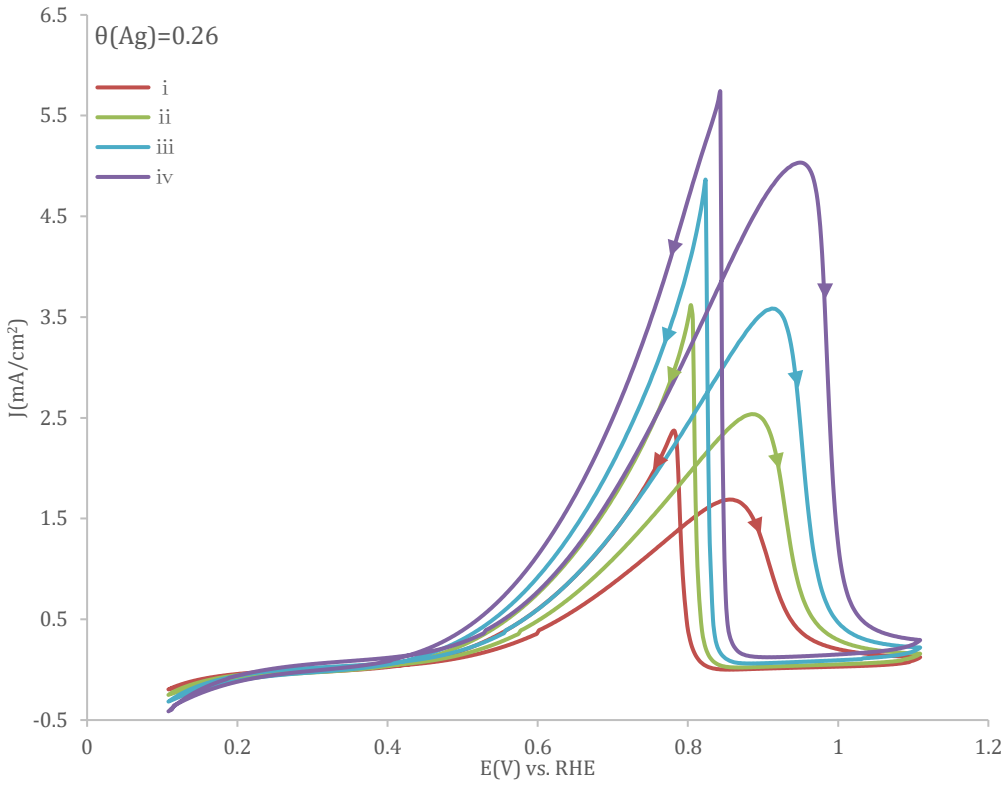
θ(Ag)=0.26
i
ii
iii
iv
J(mA/cm²)
E(V) vs. RHE
6.5
5.5
4.5
3.5
2.5
1.5
0.5
-0.5
0
0.2
0.4
0.6
0.8
1
1.2

(d).

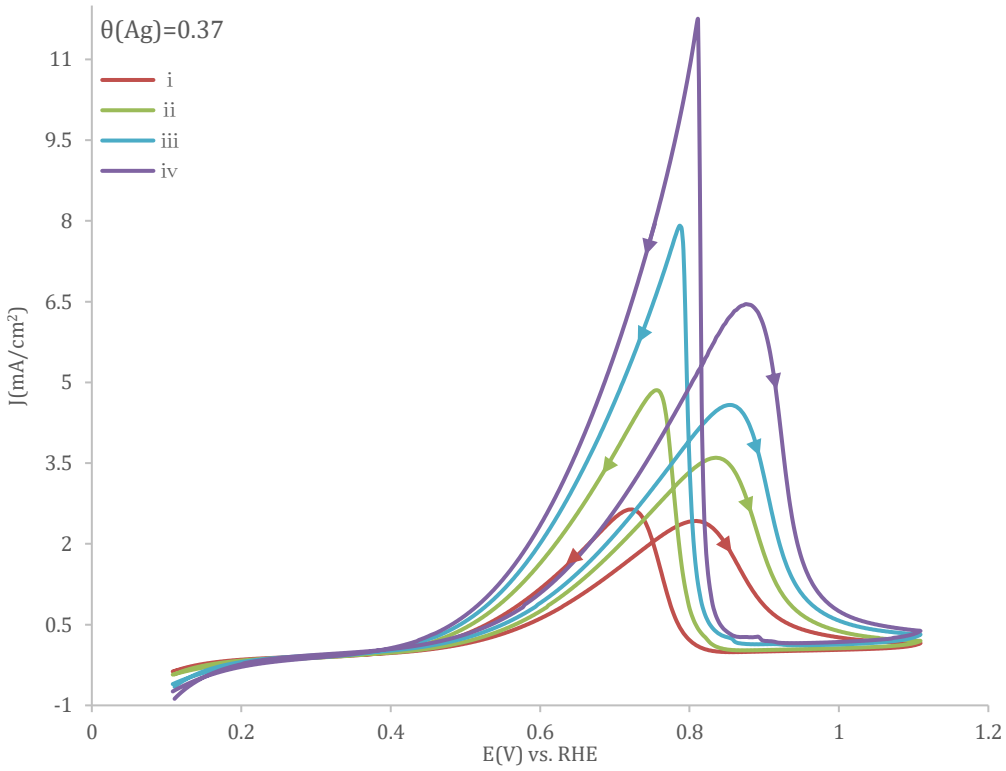
θ(Ag)=0.37
i
ii
iii
iv
J(mA/cm²)
E(V) vs. RHE
11
9.5
8
6.5
5
3.5
2
0.5
-1
0
0.2
0.4
0.6
0.8
1
1.2

(e).

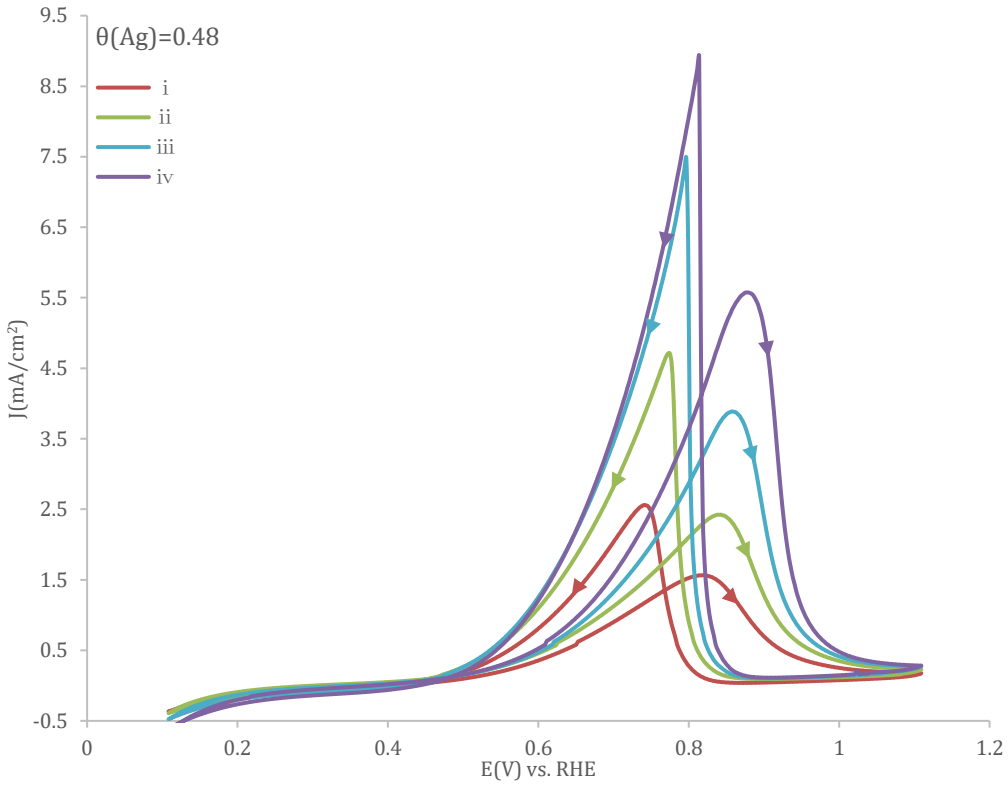

(f).

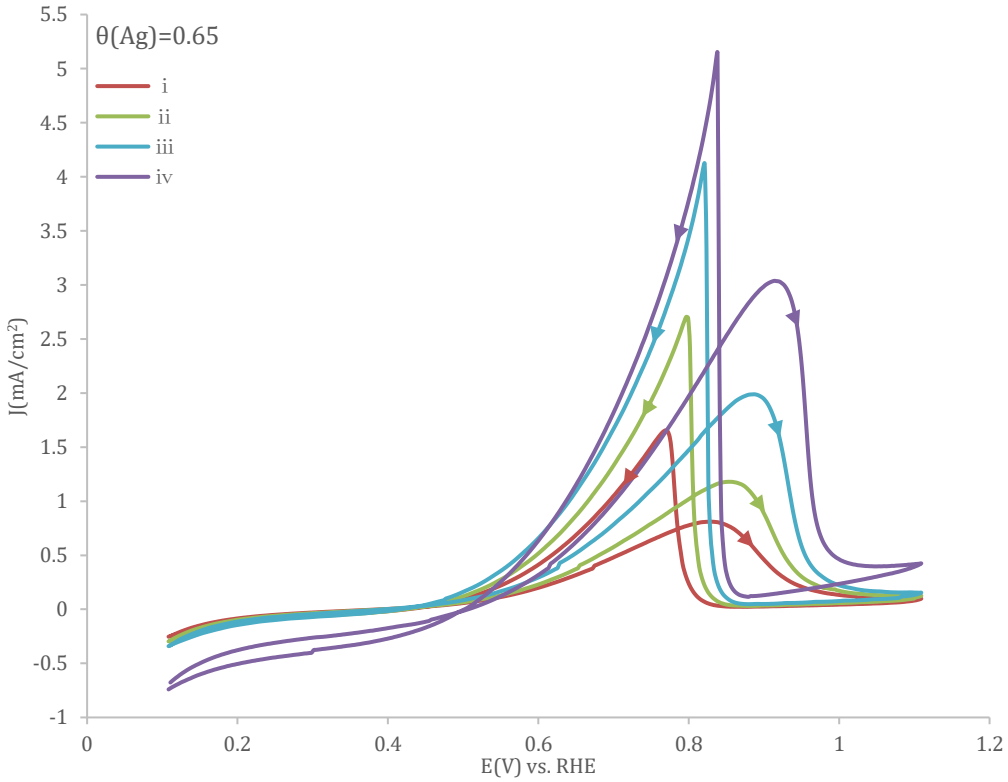

Figure 6.3. Cyclic voltammograms of bulk Pd with various Ag coverages: (a). $\boldsymbol{\theta_{Ag} = 0}$, ***(b).*** $\boldsymbol{\theta_{Ag} = 0.15}$, ***(c).*** $\boldsymbol{\theta_{Ag} = 0.26}$ ***(d).*** $\boldsymbol{\theta_{Ag} = 0.37}$, ***(e).*** $\boldsymbol{\theta_{Ag} = 0.48}$, ***(f).***

$\theta_{Ag} = 0.65$ towards ethanol electrooxidation from 0.15 V to 1.35 V (vs. RHE) in 0.1 M Ethanol + 0.1 M NaOH solution at different temperatures: i. T = 30 ˚C, ii. T = 40 ˚C, iii. T = 50 ˚C, iv. T = 60 ˚C. Scan rate: 50 mVs^{-1}.

Figure 6.3 displays the CVs of ethanol electrooxidation on bulk Pd with various Ag coverages ($\theta_{Ag} = 0, 0.15, 0.26, 0.36, 0.48, 0.65$) under different temperatures (30, 40, 50, 60 ˚C) in 0.1 M Ethanol+ 0.1 M NaOH solution with a scan rate of 50 mV/s.

The ethanol oxidation reaction (EOR) were studied to examine the electrocatalytic activities of as-prepared catalysts. The ethanol electrochemical oxidation occurs in both forward and backward scan. In the forward scan, the oxidation peak is always utilized for evaluating the catalytic activity as it is corresponding to the oxidation freshly chemisorbed species coming from ethanol adsorption. The negative scan peak is primarily associated with removal of carbonaceous species not completely oxidized in the forward scan than the oxidation of freshly chemisorbed species.

For all the electrochemical studies, remarkable enhancement in the EOR activities were observed with the increase of temperature from 30 ˚C to 60 ˚C. The onset potential shifted earlier/negatively and current density increased markedly at the elevated temperature, suggesting that formation of active surface oxidants and the kinetic of EOR were facilitated at higher temperatures[50].

Among all the CVs, the forward peak current densities gradually increased as the Ag coverage increased within a certain range, reaching a maximum value (2.42 mA/cm^2) at 30 ˚C for the AgPd (θ_{Ag}=0.37). Interestingly, the further increase in Ag content revealed an inhibiting effect toward the EOR. More details with respect to Ag coverage will be discussed later.

(a).

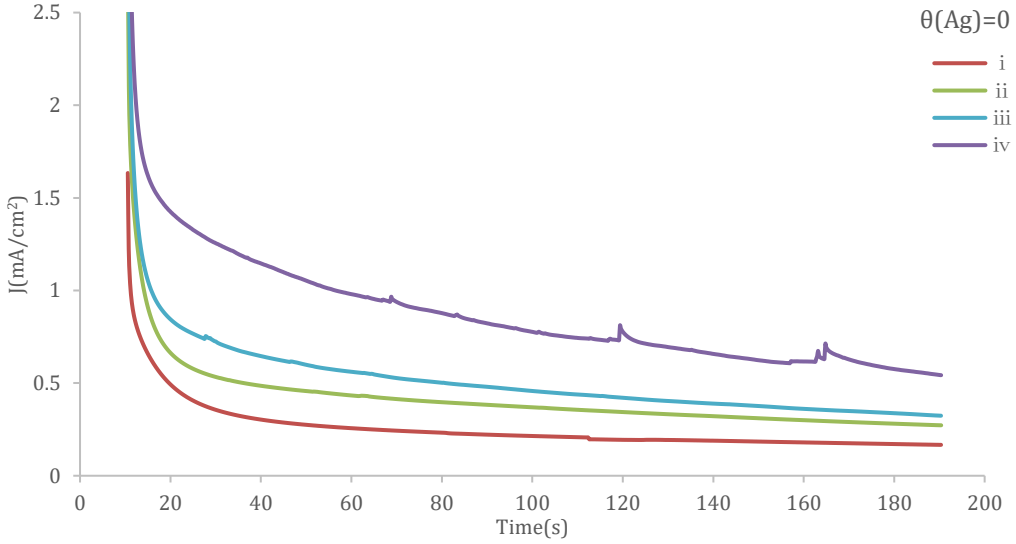
θ(Ag)=0
i
ii
iii
iv
J(mA/cm²)
Time(s)
0
0.5
1
1.5
2
2.5
0
20
40
60
80
100
120
140
160
180
200

(b).

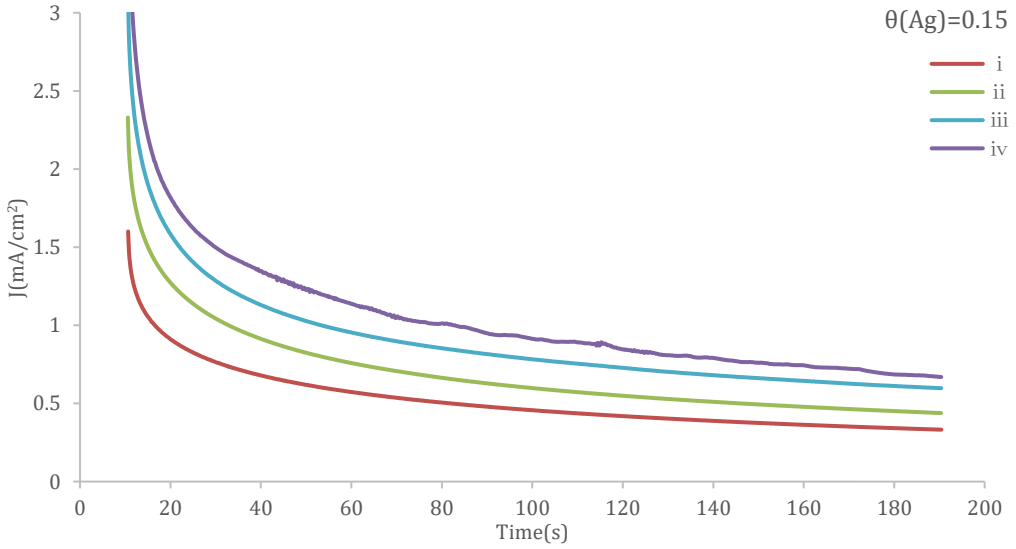
θ(Ag)=0.15
i
ii
iii
iv
J(mA/cm²)
Time(s)
0
0.5
1
1.5
2
2.5
3
0
20
40
60
80
100
120
140
160
180
200

(c).

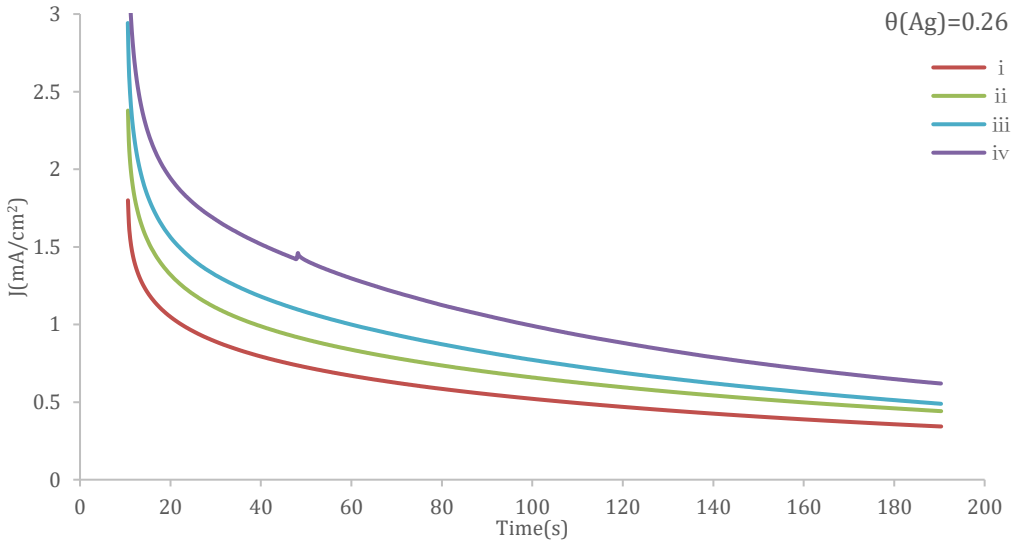
θ(Ag)=0.26
i
ii
iii
iv
J(mA/cm²)
Time(s)
0
0.5
1
1.5
2
2.5
3
0
20
40
60
80
100
120
140
160
180
200

(d).

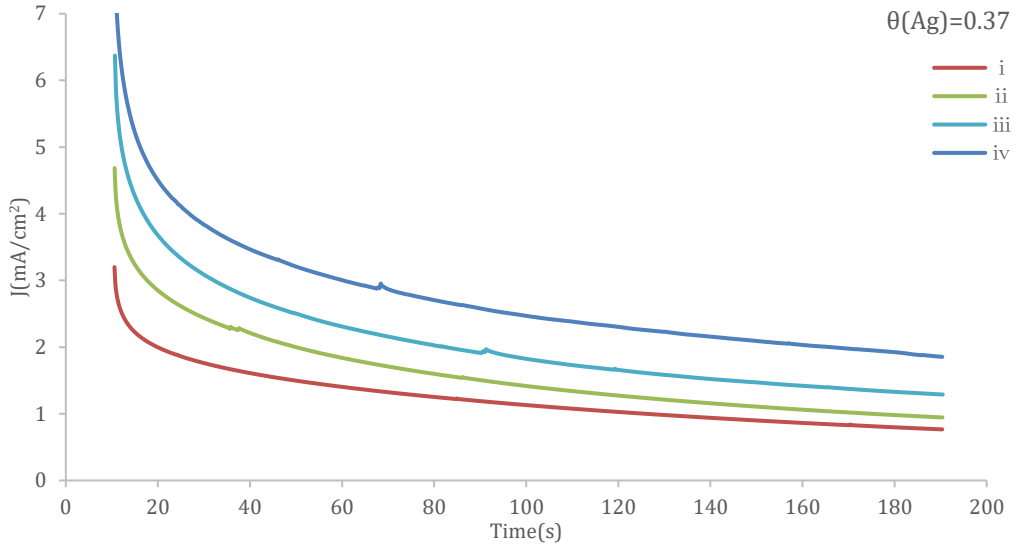
θ(Ag)=0.37
i
ii
iii
iv
J(mA/cm²)
Time(s)
0
1
2
3
4
5
6
7
0
20
40
60
80
100
120
140
160
180
200

(e).

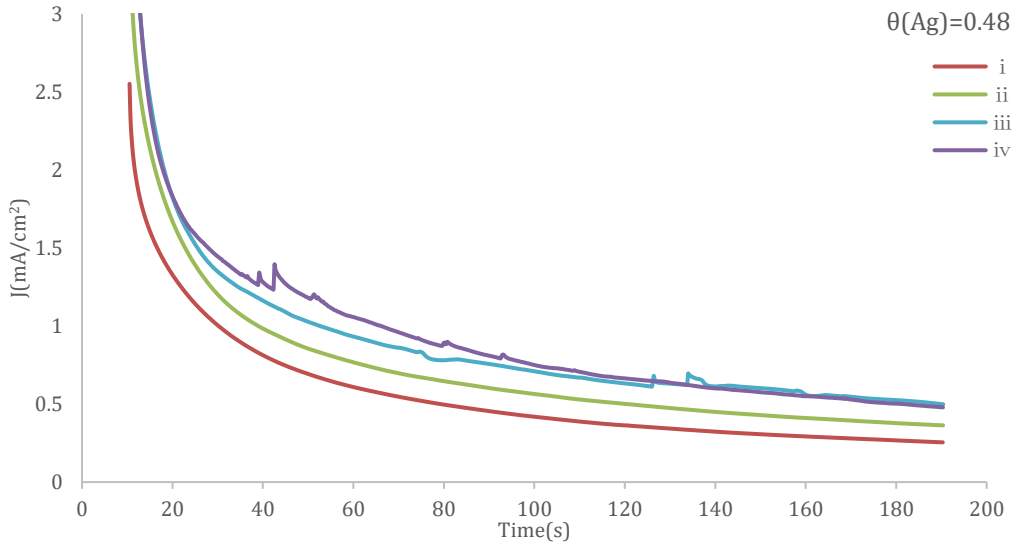
θ(Ag)=0.48
i
ii
iii
iv
J(mA/cm²)
Time(s)
0
0.5
1
1.5
2
2.5
3
0
20
40
60
80
100
120
140
160
180
200

(f).

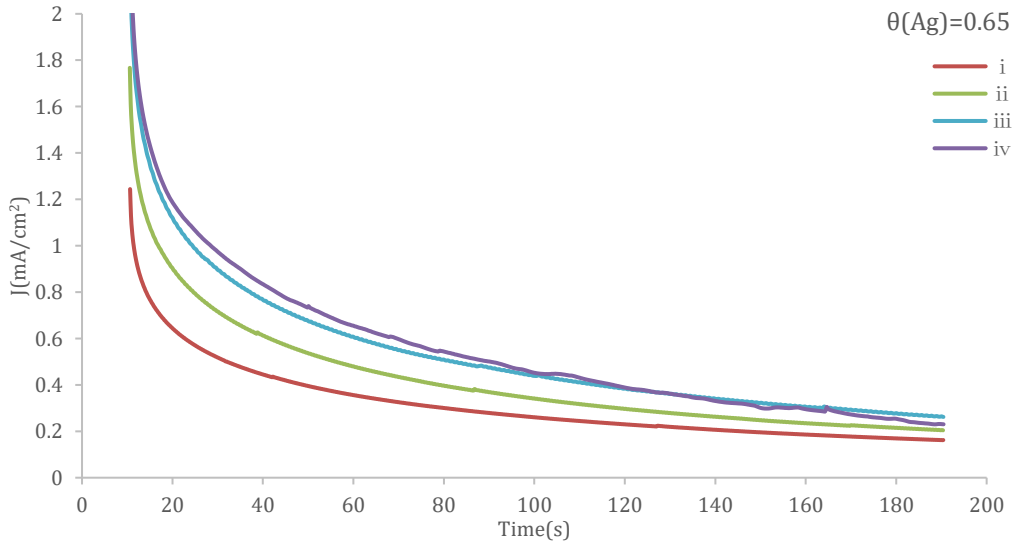
θ(Ag)=0.65
i
ii
iii
iv
J(mA/cm²)
Time(s)
0
0.2
0.4
0.6
0.8
1
1.2
1.4
1.6
1.8
2
0
20
40
60
80
100
120
140
160
180
200

Figure 6.4. Chronoamperometric curves of Ag-decorated Pd electrodes towards ethanol electrooxidation in 0.1 M Ethanol + 0.1 M NaOH solution at the potential of 0.071 V (vs. RHE) at different temperatures: i. T = 30 ˚C, ii. T = 40 ˚C, iii. T = 50 ˚C, iv. T = 60 ˚C. (a). $\boldsymbol{\theta_{Ag} = 0}$***, (b).*** $\boldsymbol{\theta_{Ag} = 0.15}$***, (c).*** $\boldsymbol{\theta_{Ag} = 0.26}$***, (d).*** $\boldsymbol{\theta_{Ag} = 0.37}$***, (e).*** $\boldsymbol{\theta_{Ag} = 0.48}$***, (f).*** $\boldsymbol{\theta_{Ag} = 0.65}$***, Scan rate: 50mVs^{-1}.***

In order to further investigate the steady-state performance of ethanol electrooxidation and the poisoning condition on both bulk Pd electrode and Ag-decorated Pd electrode, Figure 6.4.(a), (b), (c), (d), (e), (f) display the representative CAs of ethanol electrooxidation on bulk Pd with various Ag coverages ($\theta_{Ag} = 0, 0.15, 0.26, 0.37, 0.45, 0.48, 0.65$) under different temperatures(30, 40, 50, 60 ˚C) at a potential of 0.71 V (*vs.* RHE) for a period of 190 s in 0.1 M EtOH + 0.1 M NaOH solution presented.

Prior to the current transients recorded at the study potential, the electrodes were initially kept at 1.01 V (*vs.* RHE) for 5 s to oxidize all the adsorbed intermediated and get the surface cleaned. Subsequently, the electrodes were polarized at 0.11 V for 0.1 s to reduce the oxides and adsorbed ethanol. And finally, keep the voltage at 0.71 V (*vs.* RHE) for 190 s for CA testing.

In all the transient curves, the current densities drop quickly during the first few seconds which is ascribed to the double layer charging and the deactivation of Pd surface by chemisorbed carbonaceous species. Then it tends to be relatively steady. Initially, the active surface sites are free from any adsorbed species. Ethanol would then be adsorbed during the oxidation process and accumulate intermediates such as CH_3CHO and CO-like species, which poison the active sites of the catalyst. Meanwhile, the liberation of the adsorbed species provides the new active sites for ethanol[50].

In general, the data acquired shows that the electrocatalytic activity of both bulk Pd electrode and Ag-decorated Pd electrode improve progressively with increasing

temperature and are consistent with the cyclic voltammogram data, above all, Ag-decorated Pb shows a better activity and stability compared to the bulk Pd catalyst[51-52].

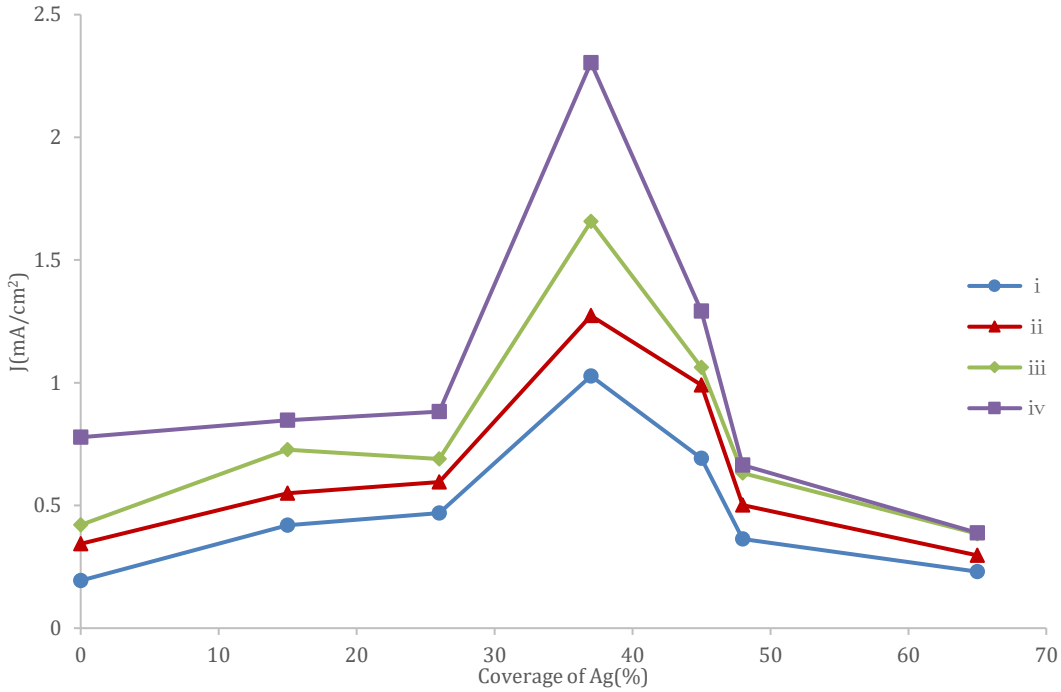

Figure 6.5. Comparison of the current density of Ag-Pd electrodes towards ethanol electrooxidation in 0.1 M Ethanol + 0.1 M NaOH solution at the potential of 0.71 V (vs. RHE) at 120 s as a function of Ag coverage at different temperatures of: i. 30 ˚C, ii. 40 ˚C, iii. 50 ˚C, iv. 60 ˚C. (Data taken from Figure 6.4).

In order to further evaluate the influence of coverage on the catalytic activities of the Ag-Pd in steady state conditions, CAs of Pd and Ag-Pd with different Ag coverages and different temperatures were studied, and the current densities of CAs at 120s were recorded in Figure 6.5. The current densities have huge jump to top level when the coverage change from 0.26 to 0.37 after a slightly increase when the coverage increase from 0 to 0.26. When the coverage increases to 0.47, the current densities drop to a

same level with that of coverage of 0.26. It is noteworthy that Ag-Pd with Ag coverage of 0.65 owns worse catalytic activity than that of bare Pd, suggesting that over coverage of Ag will damage the catalyst.

(a).

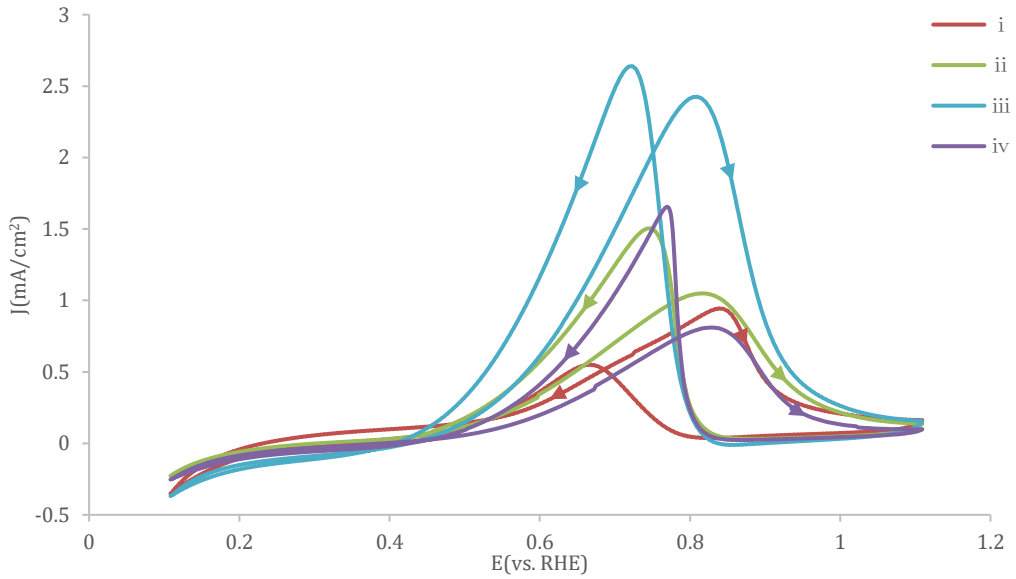

(b).

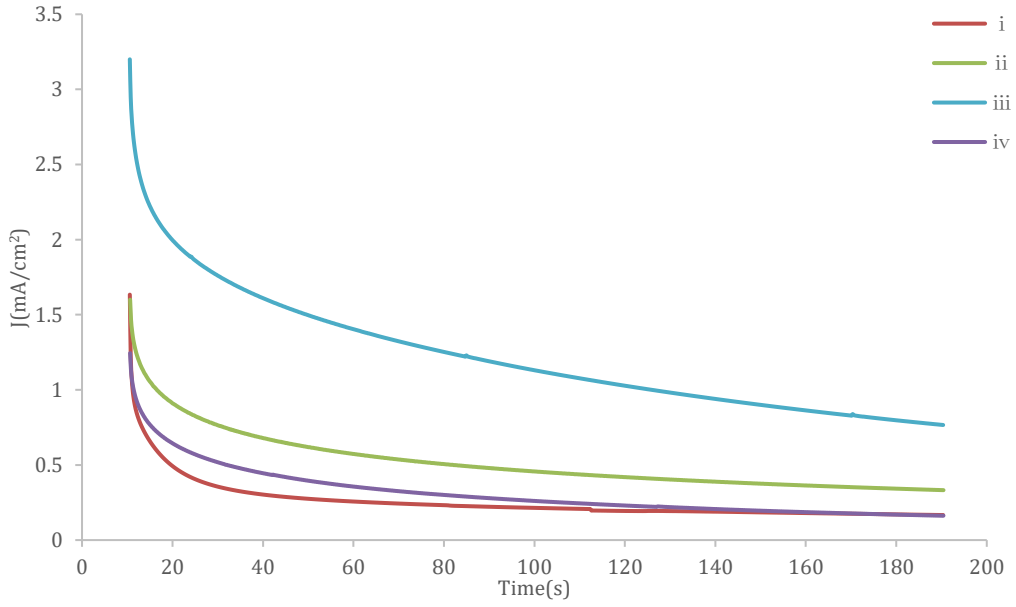

Figure 6.6. (a). Cyclic voltammograms (CVs) of the Bulk Pd with various Ag

coverages: i. $\theta_{Ag} = 0$, ii. $\theta_{Ag} = 0.15$, iii. $\theta_{Ag} = 0.37$, iv. $\theta_{Ag} = 0.65$ towards ethanol oxidation reaction (EOR) in 0.1 M Ethanol + 0.1 M NaOH solution at 30 ˚C, scan rate: 50 mVs^{-1}, (b). Chronoamperometric curves of bulk Pd with various Ag coveragse: i. $\theta_{Ag} = 0$, ii. $\theta_{Ag} = 0.15$, iii. $\theta_{Ag} = 0.37$, iv. $\theta_{Ag} = 0.65$, in 0.1 M ethanol + 0.1 M NaOH solution at the potential of 0.71 V (vs. RHE) at 30 ˚C. Scan rate: 50 mVs^{-1}.

Table 6.1. Electrochemical characterization observed from Figure 6.6.a.

Catalyst	Onset potential E_O/V(vs.RHE)	Positive-going peak current density J_p/mA·cm^{-2}	Negative-going peak current density J_n/mA·cm^{-2}
AgPd(θ_{Ag}=0)	0.521	0.945	0.552
AgPd(θ_{Ag}=0.15)	0.367	1.049	1.504
AgPd(θ_{Ag}=0.37)	0.350	2.426	2.639
AgPd(θ_{Ag}=0.65)	0.358	0.810	1.666

As shown in Figure 6.6.a., the CVs were measured in a mixed solution of 0.1 M NaOH and 0.1M Ethanol with a scan rate of 50 mV/s at 30 °C. Only four representative Ag coverage (θ_{Ag}=0, 0.15, 0.37, 0.65) are shown in this figure. All the catalysts exhibited two typical oxidation peaks in both forward and backward scan. The anodic peak occurs during the positive scan is always utilized for evaluating the catalytic activity as it is corresponding to the oxidation chemisorbed species coming from ethanol adsorption, as described by Eq. 2 and Eq. 3[60-63]. In addition, the current density drop sharply after reaching the acme, which maybe due to the formation of the Pd (II) oxide layer on the surface of the electrode at higher potentials that blocks the adsorption of the reaction species onto the Pd surface and lead to a decrease in the electrocatalytic

activity. For the negative-going scan of all CV curves, a sharp increase in the current density was exhibited. Another anodic peak can be observed, which is primarily associated with removal of carbonaceous intermediate species that are produced but not completely oxidized in the forward scan.

$$Pd + CH_3CH_2OH \leftrightarrow Pd - (CH_3CH_2OH)_{ads} \qquad (2)$$

$$Pd - (CH_3CH_2OH)_{ads} + 3OH^- \rightarrow Pd - (CH_3)_{ads} + 3H_2O + 3e^- \qquad (3)$$

It can be observed from the Figure 6.6.a., the positive-going peak current density on four catalysts can be ordered: $J_{Ag\ (\theta=0.37)/Pd} > J_{Ag\ (\theta=0.15)/Pd} > J_{Ag\ (\theta=0)/Pd} > J_{Ag\ (\theta=0.65)/Pd}$. The positive-going peak current density increased as the Ag composition increased, reaching a maximum value of 2.426 mA•cm^{-2} for the θ_{Ag}=0.37. After that, the further increase in Ag content revealed an inhibiting effect on the current density towards EOR since the excess surface occupation by the Ag would have decrease the available active sites of the Pd. Moreover, the onset potential listed at Table 6.1. also showed a similar tendency with that of the current density results, as evidenced by the order: $E_{O\ Ag\ (\theta=0.37)/Pd} < E_{O\ Ag\ (\theta=0.65)/Pd} < E_{O\ Ag\ (\theta=0.15)/Pd} < E_{O\ Ag\ (\theta=0)/Pd}$. The forward peak current density of Ag-Pd electrode with Ag coverage of 0.37 is almost 2.5 times higher than that of bare Pd electrode and almost 2.9 times higher than that of Ag-Pd electrode with Ag coverage of 0.65. A peak shift to negative for Ag-Pd electrode with Ag coverage of 0.37, indicating the electrode with coverage of 0.37 has a favorable effect on the ethanol oxidation reaction.

In accordance with the conclusion achieved by M.C. Oliveira eta[44], the result suggested that adding Ag with appropriate coverage could promote the Pd catalytic activity in ethanol oxidation. More specifically, Ag-Pd electrode with Ag coverage of 0.37 has best electrochemical catalytic activity. According to M.C. Oliveira eta[44], this might be attributed to the appropriate ability to promote the OH adsorption and consequently desorb intermediate products formed on the EOR.

Chronoamperometric curves (CAs) for EOR of AgPd with different Ag coverage (θ_{Ag}=0, 0.15, 0.37, 0.65) in 0.1 M NaOH + 0.1 M Ethanol at 0.71V (*vs.* RHE) is performed in Figure 6.6.b. to further investigate the activity and stability performance of Pd electrode decorated with Ag. In all the transient curves, the current density decay sharply at the first 30 s due to the ethanol molecules and hydroxyl adsorption and then, gradually tends to a flat end. It can be seen that the current densities of Ag-Pd electrode with coverage of 0.37 exceed over 2 times than bare Pd electrode, further confirmed that the Ag-Pd (θ_{Ag}=0.37) had the best steady state catalytic activity, indicating again the better tolerance poisonous species and catalytic durability of the catalyst towards EOR in an alkaline media. Thus, we focus on the electrochemical catalytic properties of Ag-Pd (θ_{Ag}=0.37) electrode to discuss the temperature influence on the EOR.

(a).

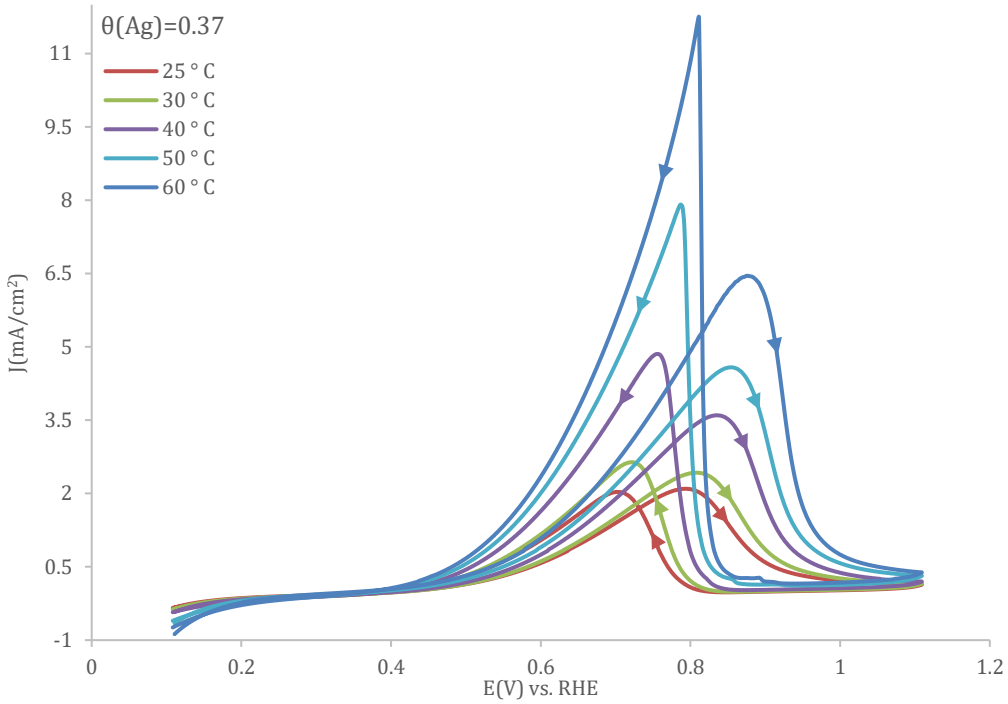

(b).

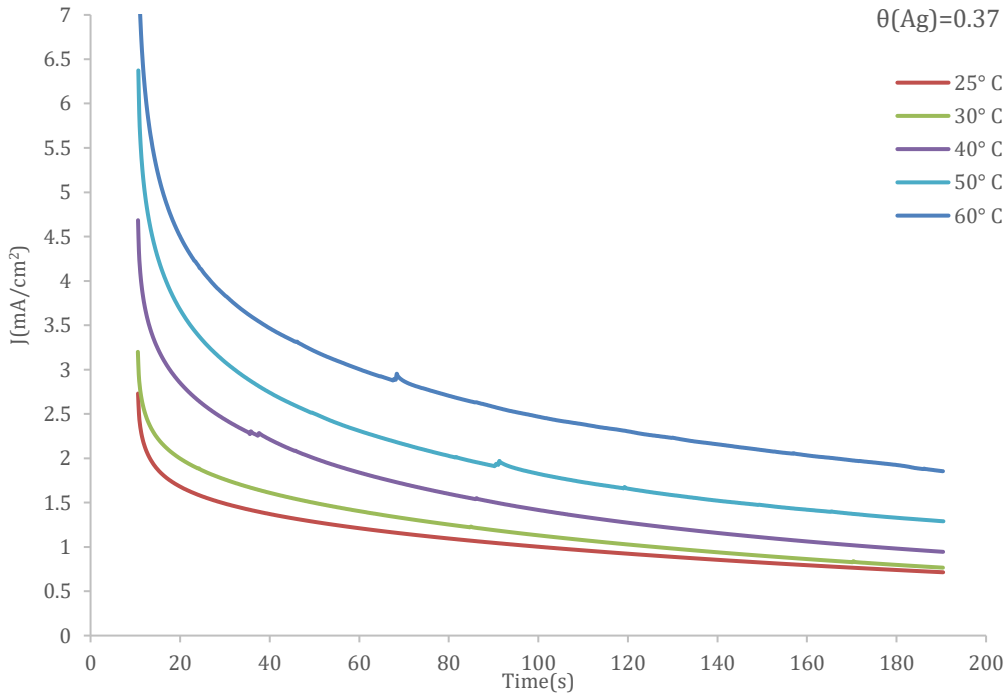

Figure 6.7. (a). CVs of Ag-decorated Pd ($\theta_{Ag} = 0.37$) in 0.1 M Ethanol + 0.1 M

NaOH solution at 30 ˚C, 40 ˚C, 50 ˚C, 60 ˚C. Scan rate: 50 mVs^{-1}. (b) Chronoamperometric curves of Ag-decorated Pd ($\theta_{Ag} = 0.37$)electrode in 0.1 M Ethanol + 0.1 M NaOH solution at the potential of 0.71 V (vs. RHE) under different temperatures. Scan rate: 50 mVs^{-1}.

Figure 6.7.a. displays the CVs of Ag-Pd electrode with Ag coverage of 0.37 at different temperature of 25 ˚C, 30 ˚C, 40 ˚C, 50 ˚C and 60 ˚C. The current density increased as the temperature increased. The peak current density at 60 ˚C is apparently over 3 times higher than that of 25°C and about 2 times higher than that of 40 ˚C. At the meantime, the onset potentials move towards negative during the increasing of temperature. It clarifies that higher temperatures benefit for the kinetic of EOR.

Chronoamperometric curves of Ag-decorated Pd ($\theta_{Ag} = 0.37$)electrode in 0.1M Ethanol + 0.1M NaOH solution at the potential of 0.71 V (*vs.* RHE) under different temperatures is shown in Figure 6.7.b. The order of current density in CA test accords with that in CV test: 60 ˚C > 50 ˚C > 40 ˚C > 30 ˚C > 25 ˚C.

Table 6.2.(a) List of onset potential, positive-going peak potential, positive-going peak current density, negative-going peak potential and negative-going peak current density obtained from Figure 6.3.a

Bulk Pd / Temp.	E_o / V (vs.RHE)	E_p / V (vs. RHE)	J_p /mA·cm^{-2}	E_n / V (vs. RHE)	J_n /mA·cm^{-2}
25 ˚C	0.521	0.811	0.596	0.655	0.320
30 ˚C	0.513	0.838	0.945	0.667	0.552
40 ˚C	0.501	0.853	2.167	0.696	1.280
50 ˚C	0.494	0.875	4.374	0.728	2.543
60 ˚C	0.486	0.894	6.877	0.765	4.236

Table 6.2.(b) List of onset potential, positive-going peak potential, positive-going peak current density, negative-going peak potential and negative-going peak current density obtained from Figure 6.3.d

θ_{Ag}=0.37 / Temp.	E_o / V (vs.RHE)	E_p / V (vs.RHE)	J_p /mA·cm^{-2}	E_n / V (vs.RHE)	J_n /mA·cm^{-2}
25 ˚C	0.35	0.794	2.097	0.701	2.033
30 ˚C	0.352	0.809	2.426	0.723	2.639
40 ˚C	0.355	0.836	3.600	0.755	4.854
50 ˚C	0.35	0.873	4.580	0.787	7.911
60 ˚C	0.358	0.875	6.453	0.811	11.740

In order to understand the electro-catalytic of bulk Pd electrode for ethanol electrooxidation reaction, the onset potential (E_o), positive-going peak potential (E_p), positive-going peak current density (J_p), negative-going peak potential (E_n) and negative-going current density (J_n) which obtained from Figure 6.3 are listed in Table

6.2. Here, the onset potential (E_o) and peak current density during the forward scan are the two important parameters to evaluate for a comparative account of the electrocatalytic performances. The E_o of ethanol electrooxidation obtained on AgPd (θ_{Ag}=0.37) at 25 ˚C is 0.35 V (vs. RHE) more negative than the bulk Pd of 0.521 V (vs. RHE) and this tends to apply for all temperatures. Basically, E_0 gets negative shifted whilst Ep gets positive shifted with the temperature ascending. The J_p of ethanol electrooxidation obtained on AgPd (θ_{Ag}=0.37) at 25 ˚C is 2.097 mA·cm^{-2} more than 3 times higher than the bulk Pd of 0.5967 mA·cm^{-2}. However, bulk Pd performed a higher value of positive peak current density at 60 ˚C than that of AgPd (θ_{Ag}=0.37) which might attribute to the instability of decorated Ag at higher temperature.

As the electroactive potential range for various alcohols are not identical, the peak current densities are obtained to plot profiles of the EOR activation energy can be evaluated by the Arrhenius equation seen below[54]:

$$Ln\, J = Ln\, A - \frac{E_a}{RT} \qquad (4)$$

Where, T presented for the tempreture (K), J presented for the forward peak current density (mA/cm^2), Ea presented for the EOR activation energy at peak potential on the anodic sweep (kJ/mol), R presented for universal gas constant (8.314 KJ/mol/K) and A presented for the prefactor.

6.3.3 Activation energies

(a).

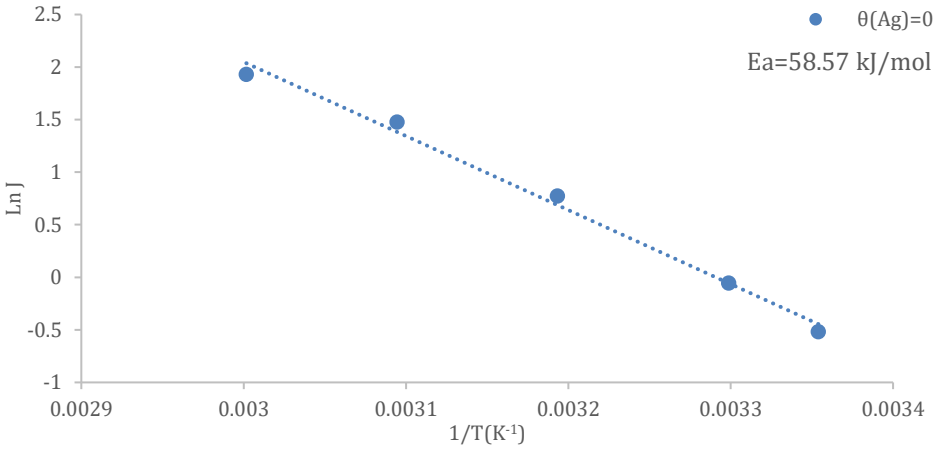

(b).

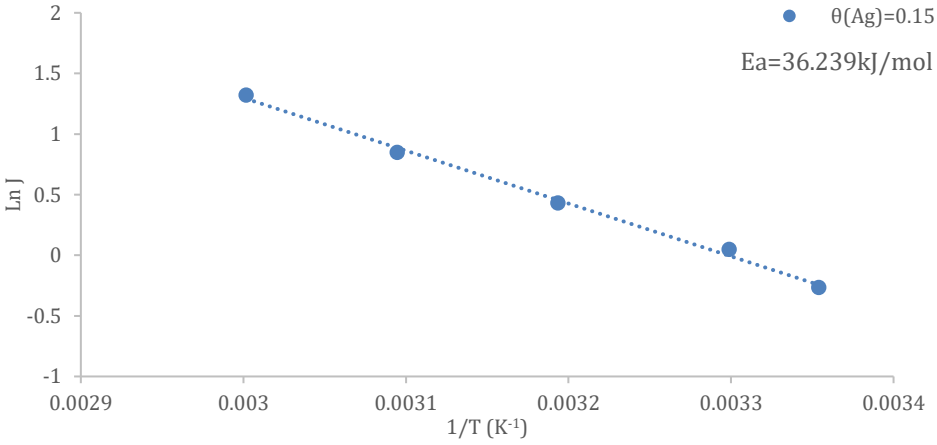

(c).

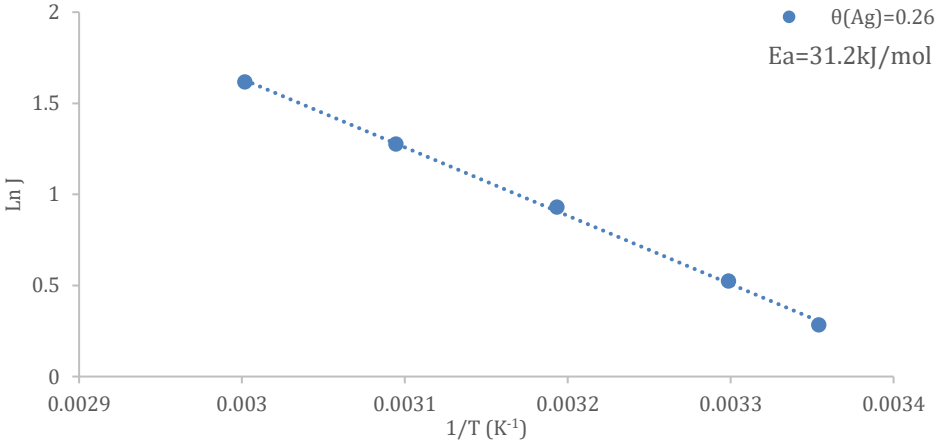

(d).

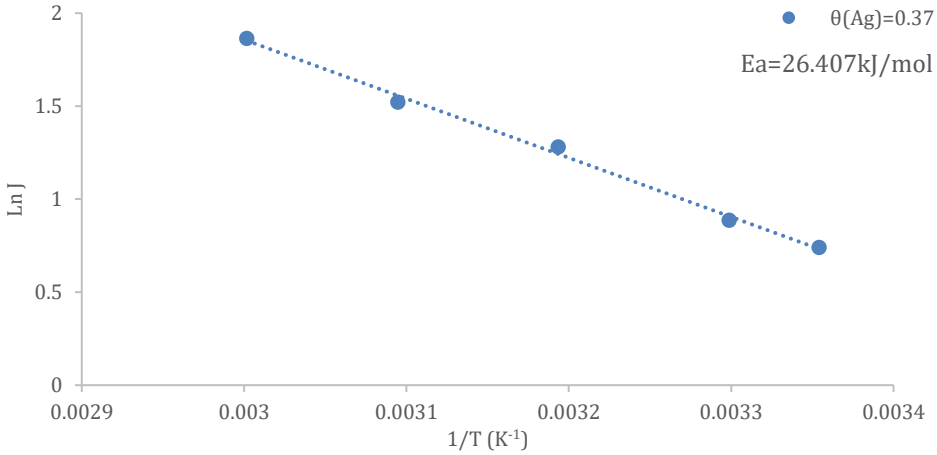

(e).

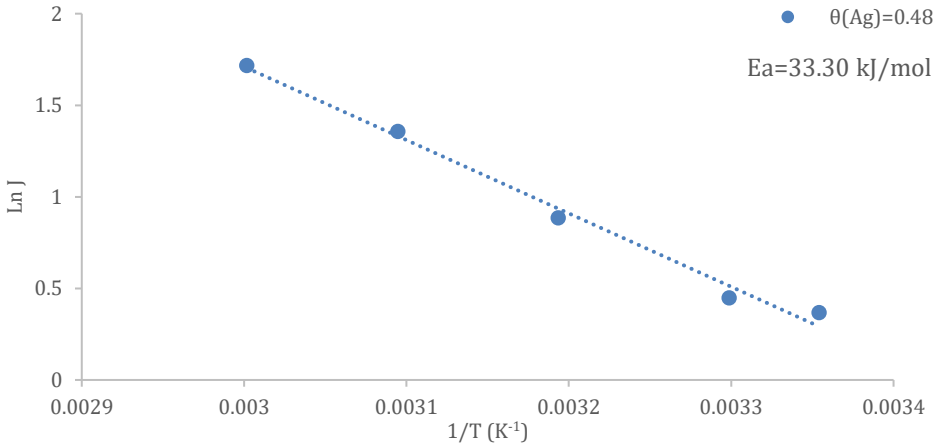

(f).

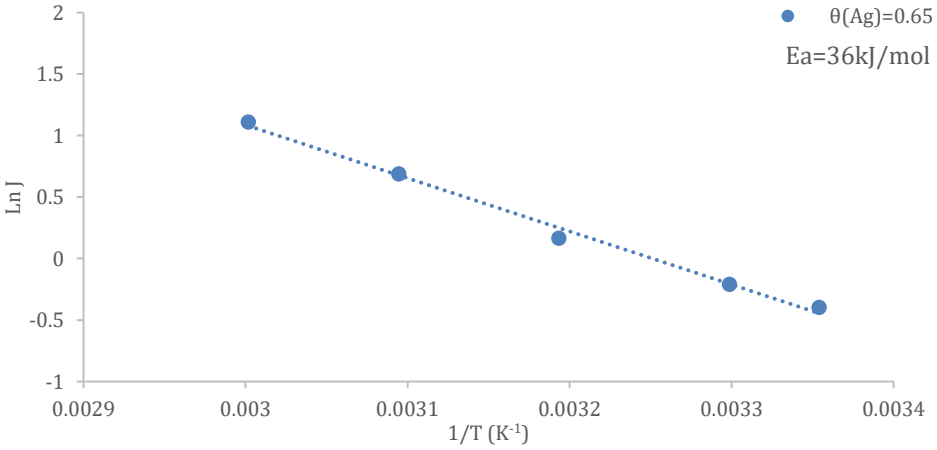

Figure 6.8. Arrhenius plots of EOR on Ag-Pd with different Ag-coverage of (a). 0, (b). 0.15, (c). 0.26, (d). 0.37, (e). 0.48, (f). 0.65, the data were achieved from peak current densities at forward potential scans for EOR at different temperatures in 0.1 M NaOH + 0.1 M Ethanol.

Figure 6.8 represent the Arrhenius plots for EOR on bare Pd and Ag-Pd electrode with different Ag coverage obtained from Figure 6.3. Peak current densities at peak potential of forward scan achieved by CVs of Pd with and without Ag-decorated in 0.1 M NaOH + 0.1 M ethanol with potential range from 0.11 V to 1.01 V (*vs.* RHE) at different temperatures. From these plots, the EOR activation energy value was calculated based on Arrhenius equation as appointed before. As is accepted widely, the electrooxidation of ethanol consists of a dual pathway mechanism[55], but generally speaking, lower E_a means a higher intrinsic activity.

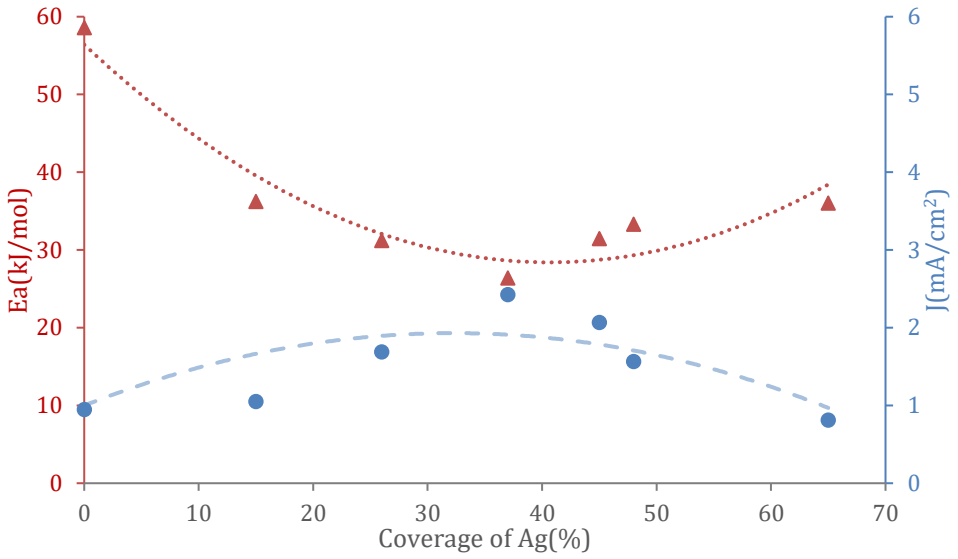

Figure 6.8. Plots of activation energy (black line) and peak current densities (red line) of EOR on Ag-Pd electrodes in 0.1 M NaOH + 0.1 M Ethanol as a function of Ag coverage. The peak current densities were recorded from CVs of EOR at 30 ˚C.

The influence of coverage on EOR activation energy and peak current density of CVs at 30 ˚C is represented in Figure 6.9. It is obvious that the EOR activation energy starts with a highest value with the Ag coverage of zero and keeps decreasing whilst the peak current density keeps increasing from a lowest station until the coverage increases to 0.37. A minimum value of Ea is exhibited with 26.4 kJ/mol at a Ag coverage of 0.37 while an optimum current density is achieved with over 2.42 $mA \bullet cm^{-2}$ at this Ag coverage. Then, Ea further increase to 36 kJ/mol while peak current density decreases to 1.38 $mA \bullet cm^{-2}$ with a higher Ag coverage of 0.65. Comparing the value of Ea and peak current density between bare Pd and Ag-Pd with coverage of 0.37, it comes to a conclusion that Ea of Ag-Pd with coverage of 0.37 (26.4kJ/mol) equals a half of Ea of bare Pd (58.5kJ/mol), and peak current density of Ag-Pd with Ag coverage of 0.37 (2.42mA/cm^2) is over 2 times than that of bare Pd (0.945mA/cm^2). The results show that optimal coverage will enhance the catalytic activity.

6.4 Conclusion

By combining cyclic voltammetry and chronoamperometry studies, an insight into the electrochemistry and the activity of Pd-Ag towards ethanol oxidation reaction (EOR) have been investigated. Our electrochemistry studies have shown that the addition of certain coverages of Ag into Pd catalyst contributes significantly to the efficient and stable catalyst activity for EOR in alkaline media. The optimum Ag-Pd (θ_{Ag}=0.37) expresses the highest current density, lowest activity energy and highest poison tolerance toward EOR in alkaline media among the series of Ag-Pd (θ_{Ag}=m). Meanwhile, the activity of Ag-Pd catalyst is greatly enhanced by the increasing temperature from 25 °C to 60°C applied for all EOR. The general kinetics data of EOR on Ag-decorated Pd were obtained from the activation energy calculated based on Arrhenius plots, and compared. An enhancement of almost 2 times in activity was achieved at the optimum Ag coverage, with corresponding activation energy being reduced significantly. In general, the addition of Ag adatom plays an efficient role in enhancing the performance of clean Pd surface which can remarkably accelerate the ethanol oxidation reaction and significantly lower the reaction energy as well as the OH* onset potential.

6.5 Reference

1. C. Bianchini, P. K. Shen. ***Palladium-Based Electrocatalysts for Alcohol Oxidation in Half Cells and in Direct Alcohol Fuel Cells***, Chem. Rev. 2009, 109, 4183–4206.

2. C. Lamy, E. M. Belgsir, J. M. Leger***. Electrocatalytic Oxidation of Aliphatic Alcohols: Application to the Direct Alcohol Fuel Cell (DAFC)***, J. Appl. Electrochem., 2001, 31, 799–809.

3. V. K. Puthiyapura, D. J. Brett, A. E. Russell, W. F. Lin, and C. Hardacre. ***Preliminary Investigation on the Electrochemical Activity of Butanol Isomers as Potential Fuel for Direct Alcohol Fuel Cell***, ECS Transactions, 2015, 69, 809-816.

4. V. K. Puthiyapura, D. J. L. Brett, A. E. Russell, W. F. Lin, C. Hardacre. ***Biobutanol as Fuel for Direct Alcohol Fuel Cells---Investigation of Sn-Modified Pt Catalyst for Butanol Electro-oxidation***, ACS Appl. Mater. Interfaces, 2016, 8, 12859-12870.

5. E. Antolini, ***Catalysts for Direct Ethanol Fuel Cells***, J. Power Sources, 2007, 170, 1-12.

6. S. Kabir, A. Serov, K. Artyushkova, P. Atanassov. ***Design of Novel Graphene Materials as a Support for Palladium Nanoparticles: Highly Active Catalysts towards Ethanol Electrooxidation***, Electrochim. Acta, 2016, 203, 144-153.

7. Umit B. Demirci, ***Theoretical Means for Searching Bimetallic Alloys as Anode Electrocatalysts for Direct Liquid-feed Fuel Cell***, J. Power Sources, 2007,173, 11–18.

8. M. A. F. Akhairi, S. K. Kamarudin, ***Catalysts in Direct Ethanol Fuel Cell (DEFC): An Overview***, Int. J. Hydrogen energy, 2016, 41, 4214-4228.

9. S. Q. Song, P. Tsiakaras, ***Recent Progress in Direct Ethanol Proton Exchange***

Membrane Fuel Cells (DE-PEMFCs), Appl. Catal., B, 2006, 63, 187-193.

10. Z. F. Xu, Y. X. Wang, ***Effects of Alloyed Metal on the Catalysis Activity of Pt for Ethanol Partial Oxidation: Adsorption and Dehydrogenation on Pt_3M (M = Pt, Ru, Sn, Re, Rh, and Pd)***, J. Phys. Chem., 2011, 115, 20565-20571.

11. L. D. Zhu, T. S. Zhao, J. B. Xu, Z. X. Liang, ***Preparation and Characterization of Carbon-Supported Sub-Monolayer Palladium Decorated Gold Nanoparticles for the Electro-Oxidation of Ethanol in Alkaline Media***, J. Power Sources, 2009, 187, 80-84.

12. S. Q. Song, P. Tsiakaras, ***Recent Progress in Direct Ethanol Proton Exchange Membrane Fuel Cells (DE-PEMFCs)***, Appl. Catal., B, 2006, 63, 187-193.

13. Y. X. Bai, J. J. Wu, X. P. Qiu, J. Y. Xi, J. S. Wang, J. F. Li, W. T. Zhu, L. Q. Chen, ***Electrochemical Characterization of Pt-CeO_2/C and Pt-$Ce_xZr_{1-x}O_2$/C Catalysts for Ethanol Electro-Oxidation***, *Appl. Catal.. B*, 2007, 73, 144-149.

14. G. C. Li, P. G. Pickup, ***Analysis of Performance Losses of Direct Ethanol Fuel Cells with the Aid of a Reference Electrode***, J. Power Sources, 2006, 161, 256-263.

15. E. Antolini, ***Catalysts for Direct Ethanol Fuel Cells***, J. Power Sources, 2007, 170, 1-12.

16. Y. Z. Su, C. W. Xu, J. P. Liu, ***Electrooxidation of 2-Propanol Compared Ethanol on Pd Electrode in Alkaline Medium,*** J. Power Sources, 2009, 194, 295-297.

17. P. Wang, X. Lin, B. Yang, J. M. Jin, C. Hardacre, N. F. Yu, S. G. Sun, W. F. Lin, ***Activity Enhancement of Tetrahexahedral Pd Nanocrystals by Bi Decoration towards Ethanol Electrooxidation in Alkaline Media***, Electrochim Acta., 2015, 162, 290-299.

18. W. X. Du, K. E. Mackenzie, D. F. Milano, N. A. Deskins, D. Su and X. W. *Teng,* ***Palladium-Tin Alloyed Catalysts for the Ethanol Oxidation Reaction in an Alkaline***

Medium, ACS Catal., 2012, 2, 287-297.

19. C. Bianchini, P. K. Shen, ***Palladium-Based Electrocatalysts for Alcohol Oxidation in Half Cells and in Direct Alcohol Fuel Cells***, Chem. Rev., 2009, 109, 4183–4206.

20. J. S. Spendelow, A. Wieckowski, ***Electrocatalysis of Oxygen Reduction and Small Alcohol Oxidation in Alkaline Media***, Chem. Chem. Phys., 2007, 9, 2654–2675.

21. G. K. Surya Prakash, F. C. Krause, F. A. Viva, S. R. Narayanan, G. A. Olah, ***Study of Operating Conditions and Cell Design on the Performance of Alkaline Anion Exchange Membrane Based Direct Methanol Fuel Cells***, G. A.J. Power Sources, 196, 7967-7972.

22. J. R. Varcoe, R. C. T. Slade, E. L. H. Yee, ***An Alkaline Polymer Electrochemical Interface: A Breakthrough in Application of Alkaline Anion-exchange Membranes in Fuel Cells***, E.Chem. Commun., 2006, 0, 1428–1429.

23. S. A. Grigoriev, P. Millet and V. N. Fateev, ***Evaluation of Carbon-Supported Pt and Pd Nanoparticles for the Hydrogen Evolution Reaction in PEM Water Electrolysers***, J. Power Sources, 2008, 177, 281-285.

24. X. Teng, ***Anodic Catalyst Design for Ethanol Oxidation Fuel Cell***. Available online: http://www.formatex.info/energymaterialsbook/book/473-484.pdf

25. E. Antolini, ***Palladium in Fuel Cell Catalysis***, Energy and Environmental Science, 2009, 2, 915-931.

26. E. Antolini, E. R. Gonzalez, ***Alkaline Direct Alcohol Fuel Cells***, J. Power Sources, 2010, 195, 3431–3450.

27. M. Z. F. Kamarudin, S. K. Kamarudin, M. S. Masdar, W. R. W. Daud, ***Review: Direct Ethanol Fuel Cells***, Int. J. Hydrog Energy, 2013, 38, 9438–9453.

28. B. Braunchweig, D. Hibbitts, M. Neurock, A. Wieckowski, ***Electrocatalysis: A Direct Alcohol Fuel Cell and Surface Science Perspective***. Catal. Today, 2013, 202:197–201.

29. Q. Yi, F. J. Niu, L. Z. Sun, ***Fabrication of Novel Porous Pd Particles and their Electroactivity Towards Ethanol Oxidation in Alkaline Media***. Fuel, 2011, 90, 2617–2623.

30. S. MH, L. EJ, C. SM, N. SH, K. HJ, K. WB, ***Synthesis, Characterization, and Electrocatalytic Properties of a Polypyrrole-Composited Pd/C Catalyst***, Int. J. Hydrogen Energy, 2011, 36, 11545-11553.

31. J. D. Cai, Y. Y. Huang, Y. L. Guo, ***Bi-Modified Pd/C Catalyst via Irreversible Adsorption and its Catalytic Activity for Ethanol Oxidation in Alkaline Medium***, Electrochim. Acta, 2013, 99, 22–29.

32. K. Kakaei, H. Gharibi, S. Abbaspour, ***One–step Synthesis of Pd_3Co Alloy Nanoparticles Deposited on Reduced Grapheme Oxide as an Electro-Catalyst for the Oxygen Reduction Reaction in Passive Direct Methanol Fuel Cells***, Iranian Journal of Hydrogen and Fuel Cell, 2015, 1, 27-33.

33. R. Jana, U. Subbarao, S. C. Peter, ***Ultrafast Synthesis of Flower-Like Ordered Pd_3Pb Nanocrystals with Superior Electrocatalytic Activities Towards Oxidation of Formic Aid and Ethanol***, J. Power Sources, 2016, 301, 160-169.

34. C. H. Liu, X. L. Cai, J. S. Wang, J. Liu, A. Riese, Z. D. Chen, X. L. Sun, S. D. Wang, ***One-step Synthesis of AuPd Alloy Nanoparticles on Grapheme as a Stable Catalyst for Ethanol Electro-Oxidation***, Int. J. Hydrogen Energy, 2016, 41, 13476-13484.

35. Z. F. Guo, T. F. Liu, W. P. Li, C. Zhang, D. Zhang, Z. J. Pang, ***Carbon Supported Oxide-Rich Pd-Cu Bimetallic Electrocatalysts for Ethanol***

Electrooxidation in Alkaline Media Enhanced by Cu/CuOx. Catal., 2016, 6, 62-76.

36. M. D. Obradovia, Z. M. Stančić, U. Č. Lacnjevac, V. V. Radmilović, A. Gavrilović-Wohlmuther, V. R. Radmilović, S. Lj. Gojković, ***Electrochemical Oxidation of Ethanol on Palladium-Nickel Nanocatalyst in Alkaline Media***, Appl. Catal., B, 2016, 189, 110–118.

37. E. J. Lim, Y. Kim, S. M. Choi, S. Lee, Y. Nohab, W. B. Kim, ***Binary PdM Catalysts (M = Ru, Sn, or Ir) over a Reduced Grapheme Oxide Support for Electrooxidation of Primary Alcohols (Methanol, Ethanol, 1-Propanol) under Alkaline Conditions***, J. Mater. Chem. A, 2015, 3, 5491–5500.

38. S. Carrión-Satorre, M. Montiel, R. Escudero-Cid, J. L. G. Fierro, E. Fatás, P. Ocón, ***Performance of Carbon-Supported Palladium and Palladium-Ruthenium Catalysts for Alkaline Membrane Direct Ethanol Fuel Cells***, Int. J. Hydrogen Energy, 2016, 41, 8954-8962.

39. Y. H. Li, Y. J. Wang, H. M. Mao, Q. X. Li. ***Synthesis of Carbon Supported Pd-Sn Catalysts by Ethylene Glycol Method for Ethanol Electrooxidation***, Int. J. Electrochem. Sci., 2016, 11, 7011 – 7019.

40. R. Carrera-Cerritos, C. Ponce de León, J. Ledesma-García, R. Fuentes-Ramíreza, L. G. Arriaga, ***Full Factorial Design Applied to the Synthesis of Pd-Ag Nanobars by the Polyol Method and the Perspective for Ethanol Oxidation***, RSC Adv., 2014, 4, 16632–16640.

41. M. C. Oliveira, R. Rego, L. S. Fernandes, P. B. Tavares, ***Evaluation of the Catalytic Activity of Pd–Ag Alloys on Ethanol Oxidation and Oxygen Reduction Reactions in Alkaline Medium***, J. Power Sources, 2011, 196, 6092–6098.

42. J. Greeley, J. K. Nørskov, and M. Mavrikakis***. Electronic Structure and Catalysis on Metal Surefaces***, Annu. Rev. Phys. Chem., 2002, 53, 319–48.

43. K. Lee, O. Savadogo, A. Ishihara, S. Mitsushima, N. Kamiya and Ken-ichiro Ota, ***Methanol-Tolerant Oxygen Reduction Electrocatalysts Based on Pd-3D Transition Metal Alloys for Direct Methanol Fuel Cells***, J. Electrochem. Soc., 2006, 153, A20-A24.

44. A. Ruban, B. Hammer, P. Stoltze, H. L. Skriver, J. K. Nørskov, ***Surface Electronic Structure and Reactivity of Transition and Noble Metals***, J. Mol. Catal. A: Chem., 1997, 115, 421-429.

45. C. C. Jin, Z. Zhang, Z. D. Chen, Q. Chen, ***Effect of Ag Modification on Catalytic Activity of Pd Electrode for Allyl Alcohol Oxidation in Alkaline Solution***. Appl. Catal., B, 2016, 199, 494–503.

46. Y. Wang, Z. M. Sheng, H. B. Yang, S. P. Jiang, C. M. Li, ***Electrocatalysis of carbon black- or activated carbon nanotubes-supported Pd-Ag towards methanol oxidation in alkaline media***, Int. J. Hydrogen Energy, 2010, 35, 10087-10093.

47. M. C. Oliveira, R. Rego, L. S. Fernandes, P. B. Tavares, ***Evaluation of the Catalytic Activity of Pd–Ag Alloys on Ethanol Oxidation and Oxygen Reduction Reactions in Alkaline Medium***, J. Power Sources, 2011, 196, 6092–6098.

48. A. Safavi, H. Kazemi, S. Momeni, M. Tohidi, P. K. Mehrin, ***Facile Electrocatalytic Oxidation of Ethanol Using Ag/Pd Nanoalloys Modified Carbon Ionic Liquid Electrode***, Int. J. Hydrogen Energy, 2013, 38, 3380-3386.

49. S. T. Nguyen, H. M. Law, H. T. Nguyen, N. Kristian, S. Y. Wang, S. H. Chan, X. Wang, ***Enhancement Effect of Ag for Pd/C towards the Ethanol Electro-Oxidation in Alkaline Media***, Appl. Catal., B, 2009, 91, 507–515.

50. J. S. Wang, C. H. Liu, A. Lushington, N. C. Cheng, M. N. Banis, A. Riese, X. L. Sun, ***Pd on carbon nanotubes-supported Ag for formate oxidation: The effect of Ag on anti-poisoning performance***, Electrochim. Acta, 2016, 210, 285–292.

51. G. L. Li, L. H. Jiang, Q. Jiang, S. L. Wang, G. Q. Sun, ***Preparation and Characterization of PdxAgy/C Electrocatalysts for Ethanol Electrooxidation Reaction in Alkaline Media***, Electrochim. Acta, 2011, 56, 7703–7711.

52. R. K. Pandey, V. Lakshminarayanan, ***Electro-Oxidation of Formic Acid, Methanol, and Ethanol on Electrodeposited Pd-Polyaniline Nanofiber Films in Acidic and Alkaline Medium***, J. Phys. Chem., 2009, 113, 21596-21603.

53. H. P. Liang, N. S. Lawerence, T. G. J. Jones, C. E. Banks, C. Ducati, ***Nanoscale Tunable Proton/Hydrogen Sensing: Evidence for Surface-Adsorbed Hydrogen Atom on Architectured Palladium Nanoparticles***, J. Am. Chem. Soc. 2007, 129, 6068-6069.

54. W. Pan, X. K. Zhang, H. Y. Ma, J. T. Zhang, ***Electrochemical Synthesis, Voltammetric Behavior, and Electrocatalytic Activity of Pd Nanoparticles***, J. Phys. Chem. C, 2008, 112, 2456-2461.

55. Y. Gimeno, A. Hernandez Creus, S. Gonzalez, R. C. Salvarezza, A. J. Arvia, ***Preparation of 100-160-nm-Sized Branched Palladium Islands with Enhanced Electrocatalytic Properties on HOPG***, Chem. Mater., 2001, 13, 1857-1864.

56. C. Batchelor-McAuley, C. E. Banks, A. O. Simm, T. G. J. Jones, R. G. Compton, ***Nano-Electrochemical Detection of Hydrogen or Protons Using Palladium Nanopartocles: Distinguishing Surface and Bulk Hydrogen***, ChemPhysChem, 2006, 7, 1081-1085.

57. A. J. Armenta-González, R. Carrera-Cerritos, M. Guerra-Balcázar, L. G. Arriaga, J. Ledesma-García, ***Comparative study of carbon-supported Pd and PdAg catalysts synthesised by the polyol process and reverse micelles methods***, J. Appl. Electrochem, 2015, 45, 33–41.

58. N. Tian, Z. Y. Zhou, N. F. Yu, L. Y. Wang, S. G. Sun, ***Direct Electrodeposition of Tetrahexahedral Pd Nanocrystals with High-Index Facets and High Catalytic Activity for Ethanol Electrooxidation***, J. Am. Chem. Soc. 2010, 132, 7580-7581.

59. G. L. Caneppele, T. S. Almeida, C. Z. Zanata, E. Teixeira-Neto, P. S. Fernandez, G. A. Camara, C. A. ***Martins, Exponential Improving in the Activity of Pt/C Nanoparticles Towards Glycerol Electrooxidation by Sb ad-atoms Deposition***, Appl. Catal., B, 2017, 200, 114-120.

60. A. Roy, T. Pal, ***Silver-Induced Electronic Drift in AgPd Bimetallics: Rationale for Enhanced Electrocatalytic Activity of Ethanol Oxidation Reaction***, New J. Chem., 2017, 41, 12278-12287.

61. Y. G. Jo, S. M. Kim, J. W. Kim, S. Y. Lee, Composition-tuned Porous Pd-Ag ***Bimetallic Dendrites for the enhancement of Ethanol Oxidation Reactions,*** J. Alloys. Compd., 2016, 688, 477-453.

62. H. C. Zhang, Y. Y. Shang, J. Zhao, J. J. Wang, ***Enhanced Electrocatalytic Activity of Ethanol Oxidation Reaction on Palladium-Silver Nanoparticles via Removable Surface Ligands***, ACS Appl. Mater. Interfaces, 2017, 0, 16635-16643.

63. F. F. Yuan, Z. H. Liu, W. Q. Kong, Q. Y. Yin, L. X. Du, ***Promotion of Palladiun Catalysis by Silver for Ethanol Electro-Oxidation in Alkaline Electrolyte***, Int. J. Hydrog. Energy, 2014, 39, 2497-2504.

Chapter Seven

Activity Enhancement of Bulk Pd with Sb Decorated towards Ethanol Electrooxidation in Alkaline Media

7.1 Introduction

Due to the growing global energy demand, electrochemical research in recent years has focused on the exploitation of different metals as anode electrocatalysts for the direct alcohol fuel cell (DAFC) applications[1]. Compared to other fuel sources, the utilization of ethanol has the potential to be a sustainable and renewable fuel source due to its' production from a fermentation process[2] and possessing a superior mass energy density of 8 kWh kg^{-1}[3]. It is also environmental-friendly in comparison with other liquid fuels such as methanol and formic acid[4]. According to previous research, Platinum has been observed to be an excellent candidate for ethanol oxidation, however its' scalability is limited due to its' scarcity and high costs[5]. Alternatively, Palladium has been identified as a superior substitute to Platinum for its' higher activity and higher tolerance to poisoning during the oxidation of ethanol in alkaline conditions[5-7]. Alkaline conditions also have shown to yield favorable improvements for ethanol oxidation, compared to acidic conditions, due to the enhancement of electrochemical kinetics at low anode overpotentials. However, the Pd catalyst has some drawbacks. Especially, Pd is easily oxidized compared with Pt. Thus, one of the disadvantages of Pd as an anodic catalyst is its instability[8]. As a result, a number of different metals have been utilized in conjunction with Palladium as bimetallic electrocatalysts, in an effort to not only improve electrocatalytic activity by improving the tolerance the carbonaceous intermediate poisoning, but to also reduce the loading of Pd to reduce costs. Previous research reported some efforts to improve the performance of Pd by combining Pd with other metals, such as Pd-Pt, Pd-Au[9], Pd-Ag[10], Pd-Sn[11]. PdNi[12], PdCu[13]. Obviously, the right combination of metals is important for producing the desirable effect[8]. Of the limited available literature sources pertaining to the utilization of these metals for this application, the addition of Sb to Pd appears to yield superior electrocatalytic activity for the oxidation of ethanol in nano-catalytic form, explained by the electronic and bi-functional effect[14]. The presence of Sb appears to facilitate the formation of oxygenated species resulting in the oxidation of accumulated carbonaceous residues remaining on the electrocatalyst surface after the anodic sweep

scan, thus improving tolerance to poisoning and providing sufficient catalytic surface area to propagate superior reaction kinetics, current density and lower EOR activation energy[11,14]. However, to the best of our knowledge, investigation into utilizing coverages of Sb on a bulk Pd electrode has not yet been investigated.

Therefore, we have managed to organize and compose Sb-decorated Pd and analyzed their electrocatalysts activity and durability in the direction of ethanol oxidation reaction(EOR) in alkaline circumstances by using Cyclic Voltammetry (CV) and Chronoamperometry (CA) respectively at diversified temperatures and under half-cell conditions. It has showed, compared with conventional Pd, Sb-Pd catalyst displays considerably greater catalytic activity with a certain Pb coverage range. Moreover, Arrhenius data was plotted to obtain the activation energy (Ea) for the ethanol oxidation reaction (EOR) with bulk Pd.

7.2 Experimental

7.2.1 Chemicals

Sulphuric acid (95%~98%, puriss grade), absolute ethanol, sodium hydroxide (semiconductor grade, 99.99%), Sb_2O_3 (≥99%). All chemicals were purchased from Sigma-Aldrich and used as received without further purification steps. Water was purified in a thermoscientific Barnstead water System (18.2 MΩ•cm resistivity) and was used for the preparation of all aqueous solutions.

7.2.2 Electrochemical preparation and characterization

A water-jacketed variable temperature three-electrode setup was used to evaluate the efficiency of the PbPd catalyst towards the oxidation of ethanol in a alkaline media under a N_2 atmosphere. The electrochemical setup includes a piece of Pd mesh as the counter electrode, an Ag/AgCl (in saturated KCl) reference electrode for acidic media or a Hg/HgO (in 1 M NaOH) reference electrode for alkaline media, a bulk Pd / PbPd as working electrode. The cell was thoroughly cleaned by a solution of hydrogen peroxide and sulphuric acid followed by rinsed with boiling water before use. Prior to the electrochemical measurements, all solutions were deoxygenated by bubbling through high purity nitrogen gas for 30 minutes. Bulk Pd, working electrode, was mechanically polished successively using a range of alumina powders of different particle sized, e.g., 1,0.3 and 0.05 μm. It was then sonicated thoroughly with water in a bath-type ultrasonicator several times.

An Autolab electrochemical work station (Potentiostat, Eco Chemie, Netherlands) was employed for the electro-deposition and electrochemical measurements. Electrochemical data were recorded using Autolab NOVA software and further analysed using Excel.

7.2.3 Sb-decorated on bulk Pd

Deposition of varying coverages of Sb onto the bulk Pd electrode were achieved by dropping a 0.5mM solution of Sb_2O_3 in 0.5M H_2SO_4 directly onto the electrode surface for a given amount of time. Clearly a longer doping time was utilized to achieve a higher coverage. The electrode was then gently cleaned with ultra-pure water. CV with 0.1M H_2SO_4 was then employed with a lower and upper vertex potential of 0.15 and 0.75V (*vs.* RHE) at a scan rate of 50 mV s^{-1}. The peak current density at the Hydrogen desorption peak was then obtained and the coverage was calculated by Equ. 1 which shows the peak current for Hydrogen desorption with bulk Pd which will be discussed later.

7.2.4 Ethanol electrooxidation on bare and Sb –decorated bulk Pd

The solution of 0.1 M (EtOH and NaOH) was bubbled with N_2 for 30 minutes before testing and a N_2 atmosphere in the test cell was maintained throughout CV testing. The reference and counter electrodes utilized were Hg/HgO and Pt mesh. A temperature-controlled water jacket was used to vary the cell temperature. Once the desired water temperature was reached, both CV and CA tests were conducted at operating temperatures of 25, 30, 40, 50 and 60 ˚C. The potential range between 0.11 and 1.11 V (*vs.* RHE) at a scan rate of 50 mV s^{-1} was used in the CV, whilst a fixed potential of 0.71 V (*vs.* RHE) was chosen for the CA as it is relevant to alkaline ethanol fuel cell. The current density of ethanol electrooxidation was normalized with the electrochemical surface area (ECSA) of bare bulk Pd. All scan parameters are utilised to ensure that the removal of the deposited Sb is minimised.

7.3 Results and discussion

7.3.1 Electrochemical study of bulk Pd by cyclic voltammetry

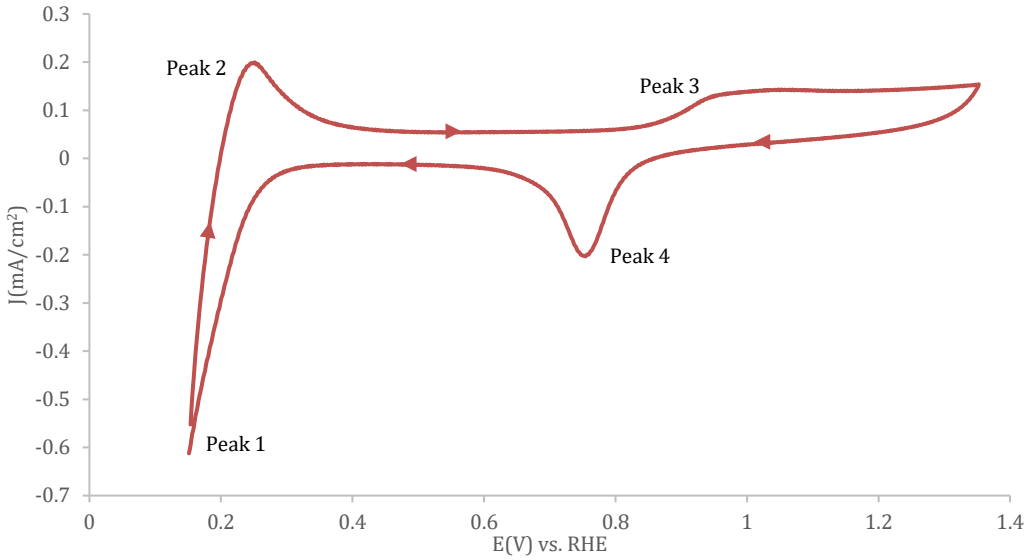

Figure 7.1 Cyclic voltammograms (CVs) obtained for bulk Pd in 0.1 M H_2SO_4 solution at room temperature. Scan rate: 50 mVs^{-1}.

The cyclic voltammetric measurement of bulk Pd electrode was examined in 0.1 M H_2SO_4 solution with a scan rate of 50 mVs^{-1} from 0.15V to 1.35V(*vs.* RHE) as shown in Figure 7.1. It can be seen that, on bulk Pd electrode, not only the adsorption and desorption of hydrogen, but also the hydrogen absorption can be noted, which follows the results reported formerly[15-16]. More specifically, the initial cathodic and anodic current peak (peak 2) between 0.20V and 0.45 V (*vs.* RHE) were associated with the hydrogen adsorption-desorption processes which characterises the ability of the ethanol to adsorb to the electrode. Therefore a higher magnitude of peak 2 implies a greater ECSA[17] The low potentials observed between 0.24 to 0.18V (*vs.* RHE) indicate the efficient adsorption of Hydrogen from the Pd surface (Peak 1)[18], thus confirming that the surface is free of Pd oxide and that the electrode is sufficiently polished. Then, a

peak (peak 3) of hydroxyl and oxygen species adsorption begins with 0.80 V (*vs*. RHE) shows the oxidation peak of the Pd surface[19], also confirming the high electrocatalytic activity of the bulk Pd electrode due to its' capacity for the adsorption of oxygen containing species to the electrode. Lastly, a Pd oxide reduction peak (peak 4) shows up between 0.95 V to 0.6 V (*vs*. RHE) with the corresponding cathodic peak at around 0.75V (*vs*. RHE)[20], therefore showing that the test conditions are free of dissolved oxygen. Additionally, the electrochemical active surface area (ECSA) of bulk Pd was determined by the integrated charge of hydrogen adsorption/ desorption region by adjusting the assumption of 212 μC cm^{-2}. In order to contrast the electrooxidation performance of bulk Pd, the current is stabilized to electrochemical surface area (ECSA) current density (*J*).

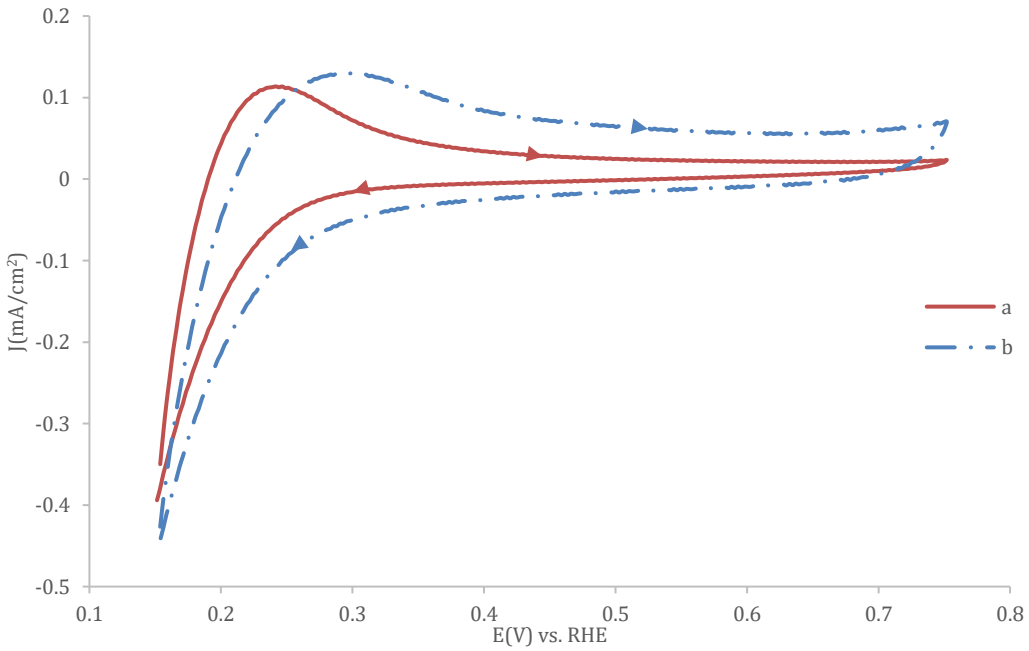

Figure 7.2 Cyclic voltammograms (CVs) obtained for a. bulk Pd and b. Sb-Pd (θ_{Sb} = 0.16) in 0.1 M H_2SO_4 solution at room temperature. Scan rate: 50 mVs^{-1}.

Presented in Figure 7.2 are the cyclic voltammograms of the bulk Pd electrode and Sb-Pd electrode in 0.1 M H_2SO_4 operated from 0.15 V to 1.35 V (*vs*. RHE) at a scan rate of 50 mVs^{-1}. It can be observed that the hydrogen adsorption and desorption peaks of bulk Pd electrodes between 0.2 V to 0.45 V (*vs.* RHE) at a peak of 0.13 $mA \cdot cm^{-2}$ while it's between 0.2 V to 0.33 V (*vs.* RHE) at a peak of 0.075 $mA \cdot cm^{-2}$ of Sb-Pd electrode, these observation clearly suggest that the deposition of Sb onto the bulk Pd electrode reduces the ECSA, thus reducing the available surface sites of the bulk Pd electrode for EOR, thus the electrochemical surface area (ECSA) as well as the coverage of Sb can be evaluated. Furthermore, the formation waves and stripping peaks for Sb-Pd oxide on Sb-Pd electrode are much more distinct than those on bulk Pd, indicating the presence of hydroxide adsorption as well as he high index facets on Sb-Pd electrode.

The total charge passed during hydrogen adsorption (Q_H)/desorption region between 0.2 V to 0.45 V (*vs.* RHE), after accounting for the double layer capacity, is used to determine the ECSA, dividing the proven assumption of 212 μC cm^{-2} for Pd surface[20].

The evaluation of Sb coverage (θ_{Sb}) can be equated with the blockage of hydrogen adsorption. Therefore, θ_{Sb} can be defined as:

$$\theta_{Sb} = 1 - \theta_H = 1 - \frac{Q_H^{Sb}}{Q_H^{bare}} \qquad (1)$$

Here Q_H^{Sb} is the charge for hydrogen adsorption on the Sb-Pd electrode while Q_H^{bare} is the charge for hydrogen adsorption on bare Pd.

It can be seen that the presence of Sb results in inhibited hydrogen adsorption and desorption processes on bulk Pd. The hydrogen adsorption/desorption peak at around 0.21 V (*vs.* RHE) disappears while that at 0.29 V (*vs.* RHE) remains noticeable, indicating Sb adatom being present preferentially on the stepped sites of the bulk Pd surface.

Therefore, any improvements in electrocatalytic activity may not be attributed to the addition of a greater density of surface sites through the deposition of Sb[21], and

therefore could initially be attributed to the electronic interaction between the two metals yielding a favourable environment for the adsorption of ethanol to the electrode surface along with other activity promoting species to potentially aid in EOR. This proposed interaction between the two metals is known as the electronic effect[22], which has been found for various other metal additions with Pd[23-25]. Once the desired coverages of Sb had been attained, the electrode was then tested in 0.1M EtOH and NaOH to evaluate EOR activity.

7.3.2 Ethanol electrooxidation reaction (EOR)

(a).

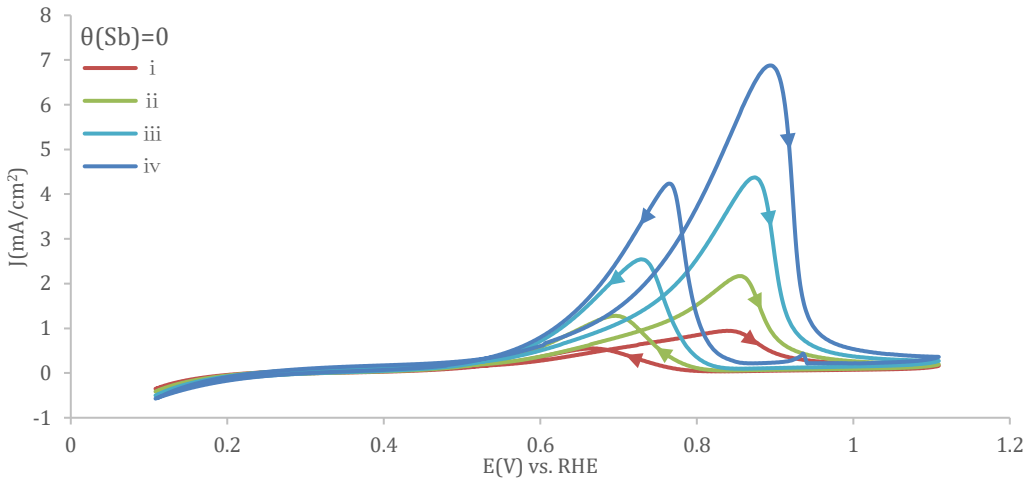

(b).

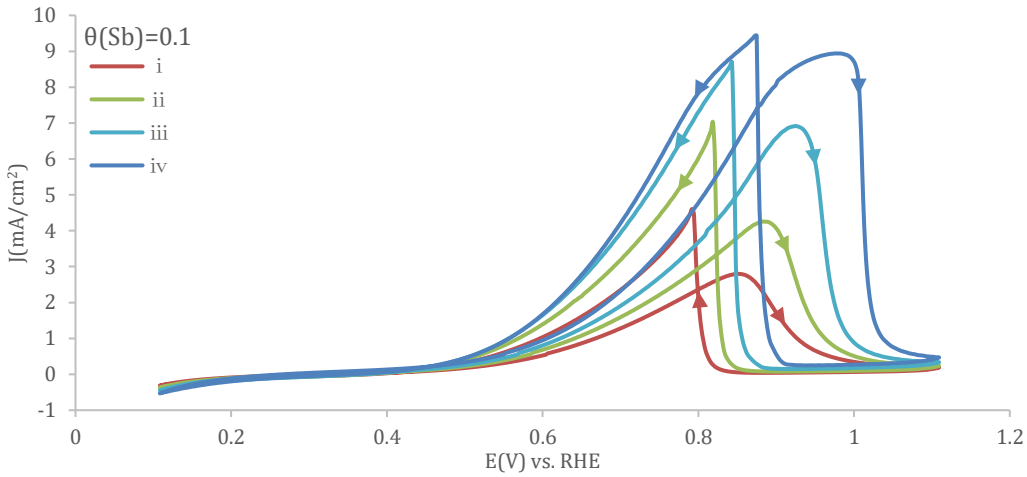

(c).

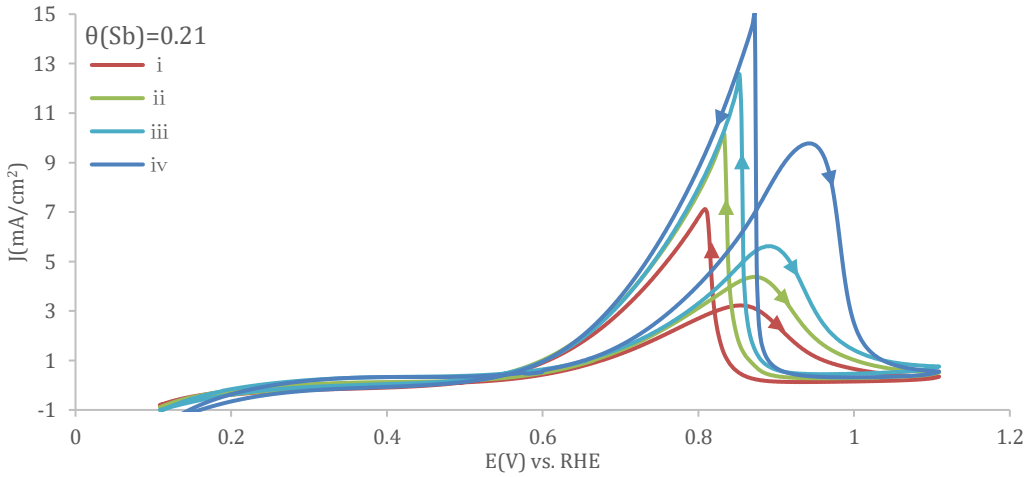

(d).

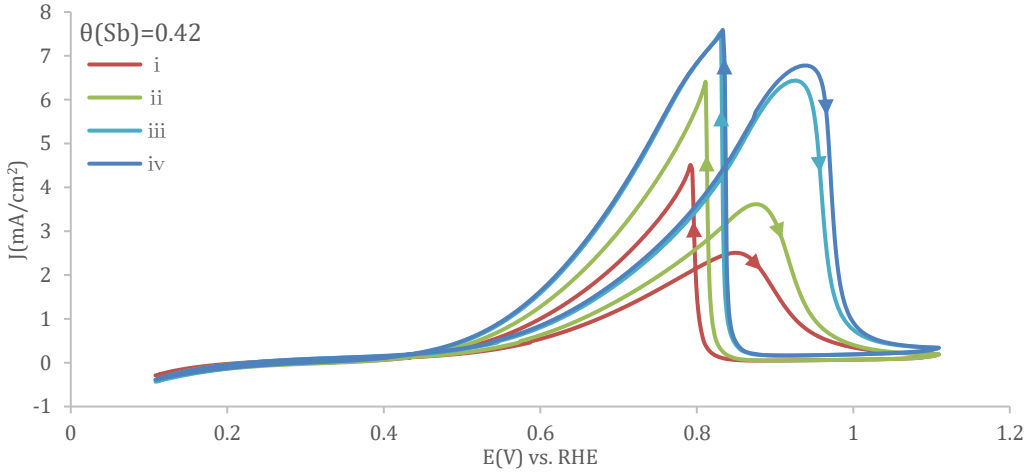

(e).

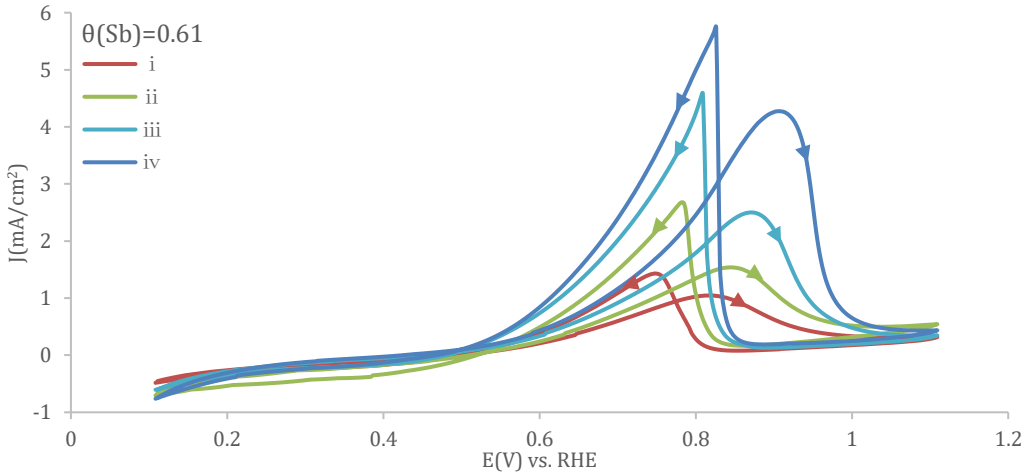

Figure 7.3 Cyclic voltammograms (CVs) of bulk Pd with various Sb coverages: (a). $\theta_{Sb} = 0$, (b). $\theta_{Pb} = 0.1$, (c). $\theta_{Pb} = 0.21$, (d). $\theta_{Pb} = 0.42$, (e). $\theta_{Pb} = 0.61$, toward ethanol electrooxidation at different temperatures: i. 30 ˚C, ii. 40 ˚C, iii. 50 ˚C, iv. 60 ˚C in 0.1 M Ethanol + 0.1 M NaOH solution. Scan rate: 50 mVs^{-1}.

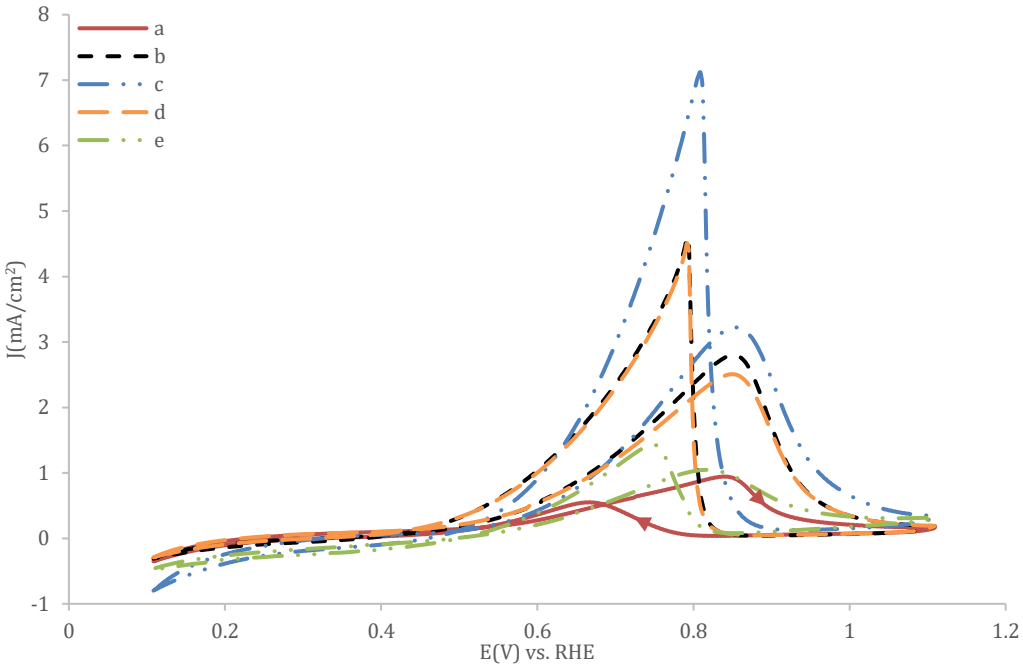

Figure 7.4 CVs of ethanol electrooxidation on bulk Pd with various Pb coverage, (a). $\boldsymbol{\theta_{Sb} = 0}$***, (b).*** $\boldsymbol{\theta_{Sb} = 0.1}$***, (c).*** $\boldsymbol{\theta_{Sb} = 0.21}$***, (d).*** $\boldsymbol{\theta_{Sb} = 0.42}$***, (e).*** $\boldsymbol{\theta_{Sb} = 0.61}$ ***under 30 ˚C in 0.1 M Ethanol + 0.1 M NaOH solution. Scan rate: 50 mVs$**$^{-1}$**$*.***

Figure 7.3 displays the CVs of ethanol electrooxidation on bulk Pd with various Sb coverage ($\theta_{Sb} = 0, 0.1, 0.21, 042, 0.61$) under different temperatures (30, 40, 50, 60 ˚C) in 0.1M Ethanol+ 0.1M NaOH solution. For all the catalysts studies, remarkable enhancement in the EOR activities were observed with the increase of temperature from 30 ˚C to 60 ˚C. The onset potential shifted earlier/negatively and current density increased markedly at the elevated temperature, suggesting that formation of active surface oxidants and the kinetic of EOR were facilitated at higher temperatures[9]. Figures 7.3.b, 7.3.c, 7.3.d, 7.3.e, when compared to figure 7.3.a, show distinctly sharper anodic and cathodic sweep peaks as a result of the deposition of Sb. These characteristic peaks could be attributed to a more pronounced influence of surface adsorbed oxygen-containing species. These observations could suggest that the addition of Sb improves the adsorption capacity of oxygen-containing species which directly oxidises reaction intermediates, such as CO, that are responsible for poisoning

the anode electrocatalyst, resulting in a reduction in activity. This is further confirmed by the reduction in difference between the anodic and cathodic sweep peak current density, which implies that there is a lower magnitude of carbonaceous intermediate species and subsequent poisoning after the anodic sweep scan due to the improved oxidation of CO intermediates. Cai et al. supported this by suggesting that the specific enhancement in activity is attributed to the formation of hydroxyl species through the dissociation of water and lower onset potentials. It was also suggested that the bifunctional effect was also a factor in improving electrocatalytic activity along with the electronic effect[14], thus implying that Sb may play a similar role as observed with Sn, Bi and Ni[21,26-27]. The improved poisoning tolerance therefore suggests that a lower cell temperature for commercial application could be utilised as the influence of cell temperature to improve poisoning tolerance is not as significant[28]. It is also shown that peak anodic current density is improved independent of coverage of Sb compared to bulk Pd alone. These improvements support the characteristic peaks shown in Figures 7.3 in which that the bi-functional mechanism and the electronic effect are responsible for these improvements in electrocatalytic performance. Therefore, the transfer of electrons between Pd and Sb, as a result of the electronic effect, could result in the increase in electron density, therefore attracting a higher concentration of water molecules which are then disassociated at lower onset potentials due to the presence of Sb[14]. Carbonaceous poisons, such as CO, that are formed due to the oxidation of ethanol through bulk Pd are then oxidised by the hydroxyl species formed through the presence of Sb, thus implying that the bi-functional mechanism is responsible for the improvements in EOR[14,29]. As a result of this, the poisoning tolerance is drastically improved, allowing for the optimal availability of surface active sites on the bulk Pd electrode for EOR.

For greater contrast, Figure 7.4 exhibits the cyclic voltammograms of different Sb-Pd coverages in 0.1 M Ethanol + 0.1 M NaOH solution at 30 ˚C and it is obviously showing that Sb contributes a lot in the whole process. Sb-Pd (θ_{Sb} =0.21) catalyst exhibits a maximum positive peak current density of 1.655 mA/cm^2. Moreover, the onset

potential on the Sb-Pd (θ_{Sb} =0.54) catalyst and Pb-Pd (θ_{Pb} =0.36) catalyst at 30 ˚C are 0.408 V (*vs.* RHE) and 0.425 V (*vs.* RHE) respectively, more negative than that of bulk Pd. As is well known, the negative shift of onset potential indicates the significant enhancement in kinetics of the EOR[30]. Considering of owing a higher current density as well as a superior kinetics, the optimal Sb coverage is achieved at approximately 21%.

(a).

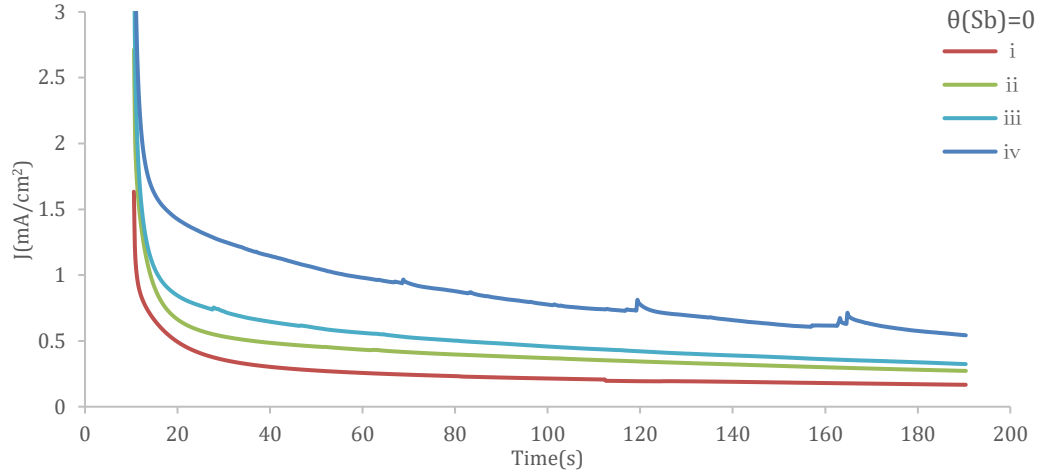
θ(Sb)=0
i
ii
iii
iv
J(mA/cm²)
Time(s)
0
0.5
1
1.5
2
2.5
3
0
20
40
60
80
100
120
140
160
180
200

(b).

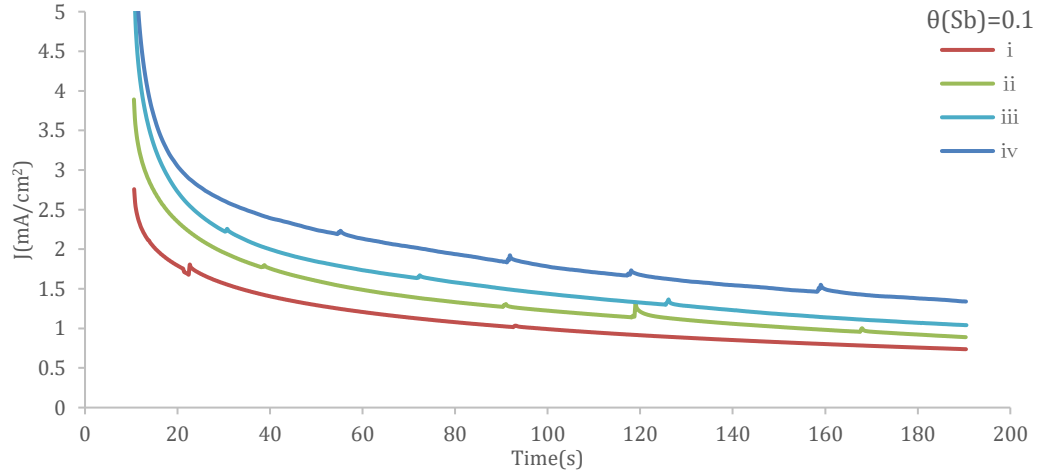
θ(Sb)=0.1
i
ii
iii
iv
J(mA/cm²)
Time(s)
0
0.5
1
1.5
2
2.5
3
3.5
4
4.5
5
0
20
40
60
80
100
120
140
160
180
200

(c).

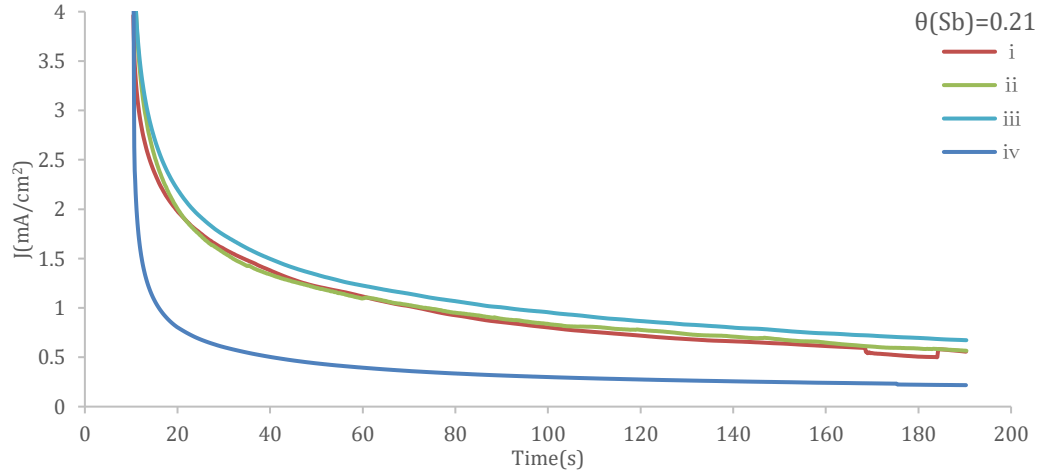
θ(Sb)=0.21
i
ii
iii
iv
J(mA/cm²)
Time(s)
0
0.5
1
1.5
2
2.5
3
3.5
4
0
20
40
60
80
100
120
140
160
180
200

(d).

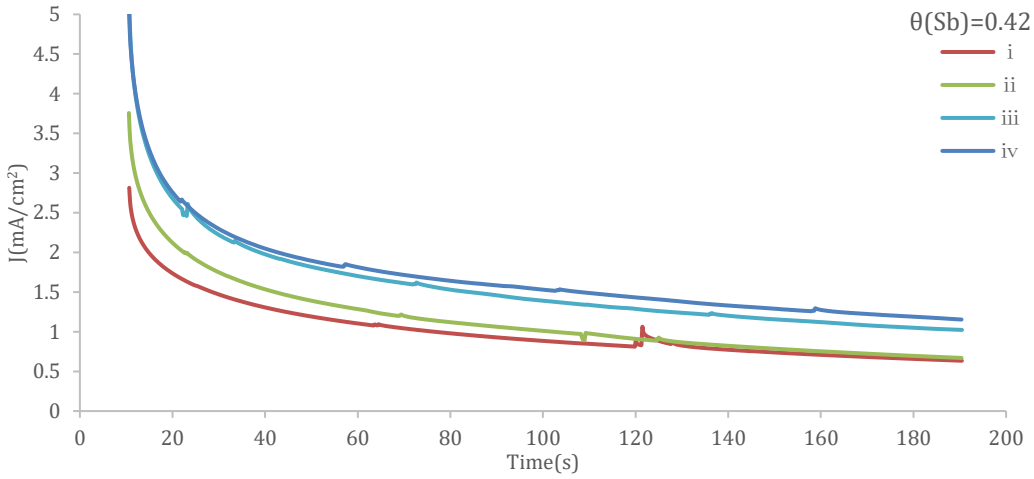

(e).

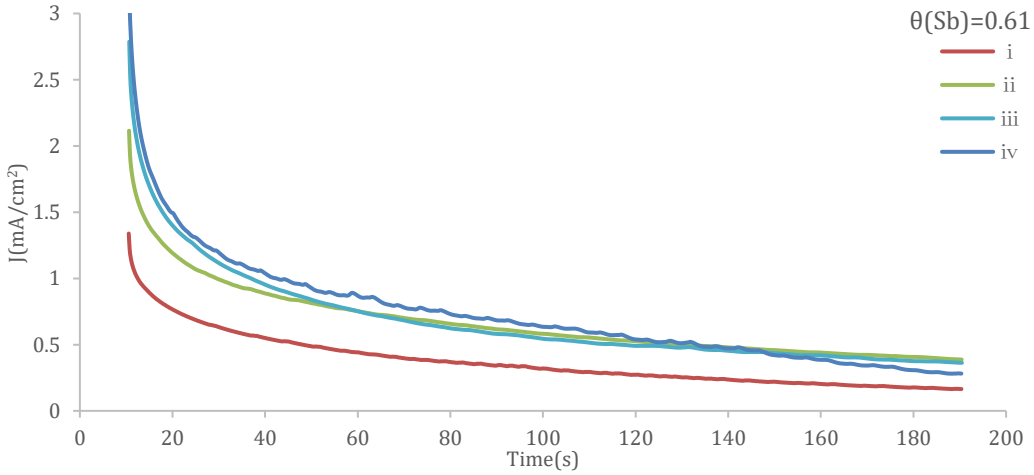

Figure 7.5 Chronoamperometric curves (CAs) of bulk Pd with various Sb coverages: (a). $\theta_{Sb} = 0$, (b). $\theta_{Pb} = 0.1$, (c). $\theta_{Pb} = 0.21$, (d). $\theta_{Pb} = 0.42$, (e). $\theta_{Pb} = 0.61$ in 0.1 M Ethanol + 0.1 M NaOH solution at the potential of 0.71 V (vs. RHE) under different temperatures: i. 30 ˚C, ii. 40 ˚C, iii. 50 ˚C, iv. 60 ˚C in 0.1 M Ethanol + 0.1 M NaOH solution. Scan rate: 50 mVs^{-1}.

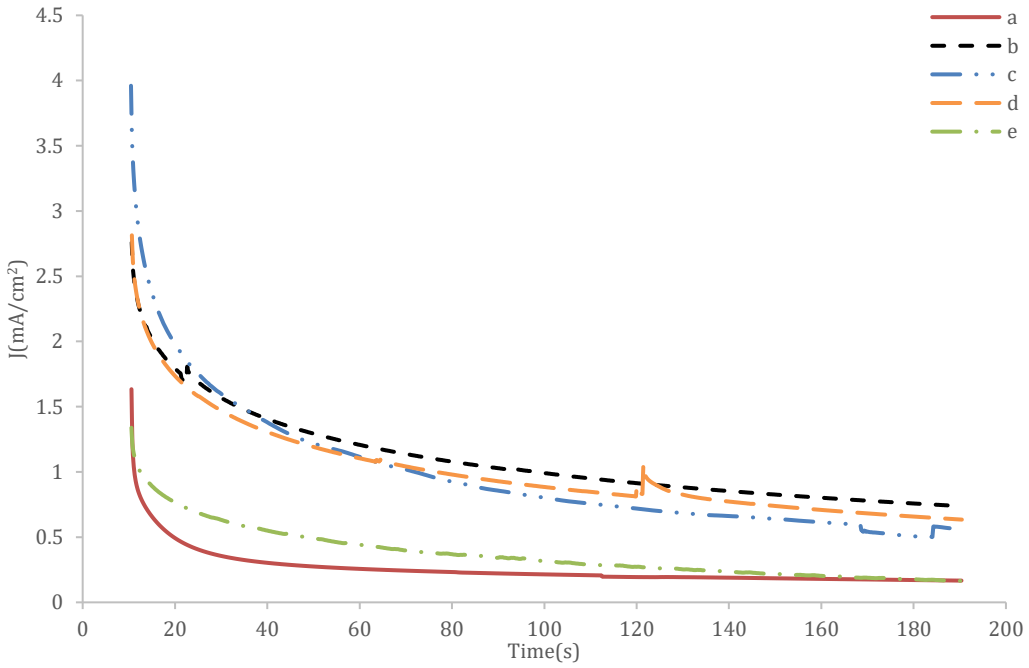

Figure 7.6 Chronoamperometric curves (CAs) of bulk Pd with various Sb coverage, a. $\theta_{Sb} = 0$, b. $\theta_{Sb} = 0.1$, c. $\theta_{Sb} = 0.21$, d. $\theta_{Sb} = 0.42$, e. $\theta_{Sb} = 0.61$ at the potential of 0.71 V (vs. RHE) under 30 ˚C in 0.1 M ethanol + 0.1 M NaOH solution. Scan rate: 50 mVs^{-1}.

Table 7.1: Comparison for current density after 190 seconds with varying coverages of Sb

θ_{Sb}/(%)	Current density after 190s during CA at 30 ˚C/(mA·cm^{-2})
0	0.17
0.10	1.49
0.21	1.61
0.42	0.56
0.61	0.38

In order to further investigate the steady-state performance of ethanol electrooxidation and the poisoning condition on SbPd electrode, Figure 7.5 displays the representative CAs of ethanol electrooxidation on bulk Pd with various Pb coverages ($\theta_{Sb} = 0, 0.1, 0.21, 0.42, 0.61$) under different temperatures (30, 40, 50, 60 ˚C) at a potential of 0.71 V (*vs.* RHE) for a period of 190 s in 0.1 M EtOH + 0.1 M NaOH solution presented. Prior to the current transients recorded at the study potential, the electrodes were initially kept at 1.01 V (*vs.* RHE) for 3 s to oxidize all the adsorbed intermediated and get the surface cleaned. Then, the electrodes were polarized at 0.11 V (*vs.* RHE) for 0.1 s to reduce the oxides and adsorbed ethanol. Subsequently, constant potential tests were kept at 0.71 V (*vs.* RHE) for 190 s.

In all the transient curves, the current densities of all catalysts fall quickly at the stage of 0-20s, which are ascribed to the deactivation of Pd surface by chemisorbed carbonaceous species, and then decrease slowly after that stage, finally tend to be relatively steady. Initially, the active surface sites are free from any adsorbed species. Ethanol would then be adsorbed during the oxidation process and accumulate intermediates such as CH_3CHO and CO-like species, which poison the active sites of the catalyst. Meanwhile, the liberation of the adsorbed species provides the new active sites for ethanol to continue EOR[31]. The data acquired shows that the electrocatalytic activity of both bulk Pd electrode and Sb-Pd electrodes improve progressively with increasing temperature.

Figure 7.6 shows chomoamperometric curves of as-prepared Sb-Pd electro-catalysts with different Sb coverage in 0.1M Ethanol + 0.1M NaOH solution at the potential of 0.71 V (vs. RHE) at 30 ˚C. According to the current transient curves, the current densities decay dramatically at the initial stage and decay gradually achieving a pseudo steady state. It can be seen that current densities of Sb-Pd ($\theta_{Sb} = 0.21$) keeps highest in the first 100s among all catalysts with that of bulk Pd has the bottommost activity indicating the better tolerance towards poisonous species and catalytic durability of the catalyst. Analyst of Table 7.1 shows that Sb is sufficiently stable in conjunction with

Pd and there weren’t any significant signs of the removal of Sb from the bulk Pd electrode.

In general, the chronoamperometry data are consistent with the cyclic voltammogram data and Sb-Pb catalyst particularly with Sb coverage of 21% shows better activities and stabilities compared to the bulk Pd catalyst.

Table 7.2.(a) List of onset potential, positive-going peak potential, positive-going peak current density, negative-going peak potential and negative-going peak current density obtained from Figure 7.3.a

Bulk Pd / Temp.	E_o / V (*vs.*RHE)	E_p / V (*vs.*RHE)	j_p /mA·cm^{-2}	E_n / V (*vs.*RHE)
30 ˚C	0.513	0.838	0.945	0.667
40 ˚C	0.501	0.853	2.167	0.696
50 ˚C	0.494	0.875	4.374	0.728
60 ˚C	0.486	0.894	6.877	0.765

Table 7.2.b List of onset potential, positive-going peak potential, positive-going peak current density, negative-going peak potential and negative-going peak current density obtained from Figure 7.3.c

θ_{Sb}=0.21 / Temp.	E_o / V (*vs.*RHE)	E_p / V (*vs.*RHE)	j_p /mA·cm^{-2}	E_n / V (*vs.*RHE)
30 ˚C	0.425	0.838	1.617	0.769
40 ˚C	0.425	0.862	2.194	0.794
50 ˚C	0.422	0.886	3.167	0.813
60 ˚C	0.421	0.901	4.700	0.828

In order to understand the electro-catalytic of Sb-Pd electrode for ethanol electrooxidation reaction, the onset potential (E_o), positive-going peak potential (E_p), positive-going peak current density (j_p), negative-going peak potential (E_n) and negative-going current density (j_n) which obtained from Figure 7.3 are listed in Table

4.2. As observed from Figure 7.3 and 7.4, E_o gets negative shifted whilst E_p gets positive shifted with the temperature ascending. The E_o of ethanol electrooxidation obtained on bulk Pd at 30 ˚C is 0.513V (*vs.* RHE) while E_o of ethanol electrooxidation obtained on Sb-Pd (θ_{Pb} =0.21) at 30 ˚C is 0.437V (*vs.* RHE), more negative than that of the bulk Pd and this tends to apply for all temperatures.

As the electroactive potential range for various alcohols are not identical, the peak current densities are obtained to plot profiles of the activation energy values calculated that are based on the Arrhenius equation seen below[32]:

$$\ln j = lnA - \frac{E_a}{RT} \qquad (2)$$

Where, j is the corresponding peak current densities. R is the gas constant, assuming 8.314 J K^{-1} mol^{-1}. T is the thermodynamic temperature (K) and E_a is the apparent activation energy at relevant peak potential.

7.3.3 Activation energies

To evaluate the activation energy for EOR utilizing bulk Pd with varying coverages of Sb, the anodic peak current density at 30, 40, 50 and 60 ˚C at each coverage of Sb was utilized in Arrhenius plots to find the gradient in anodic sweep peak current density with varying cell temperature to calculate the activation energy in accordance with Equ.2.

(a).

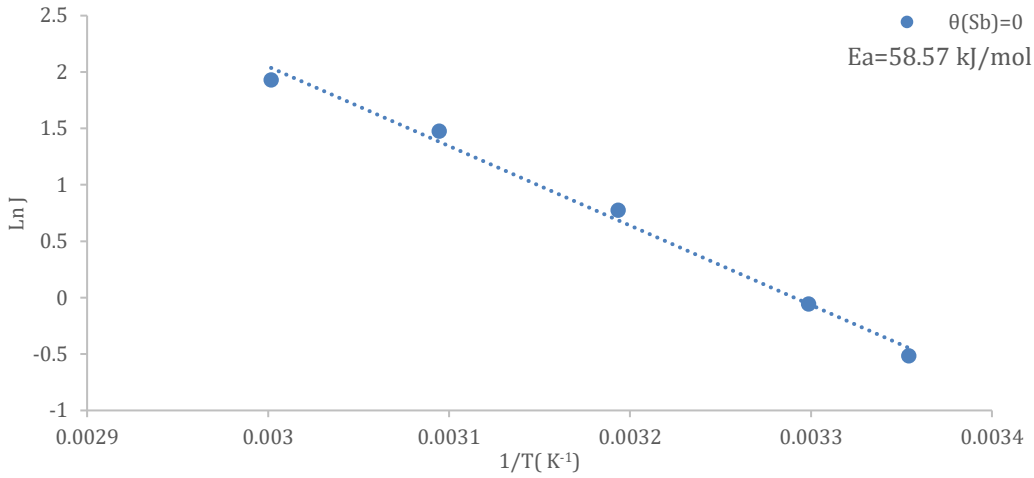

(b).

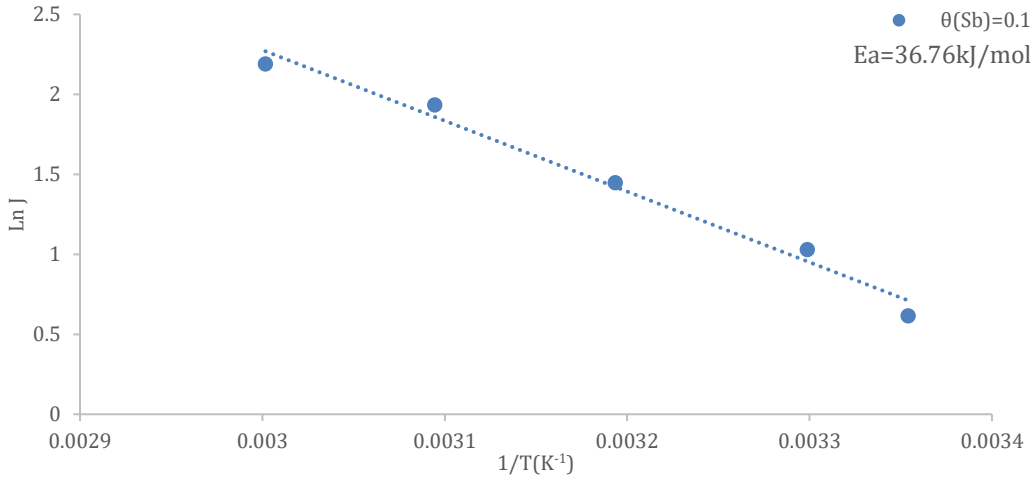

(c).

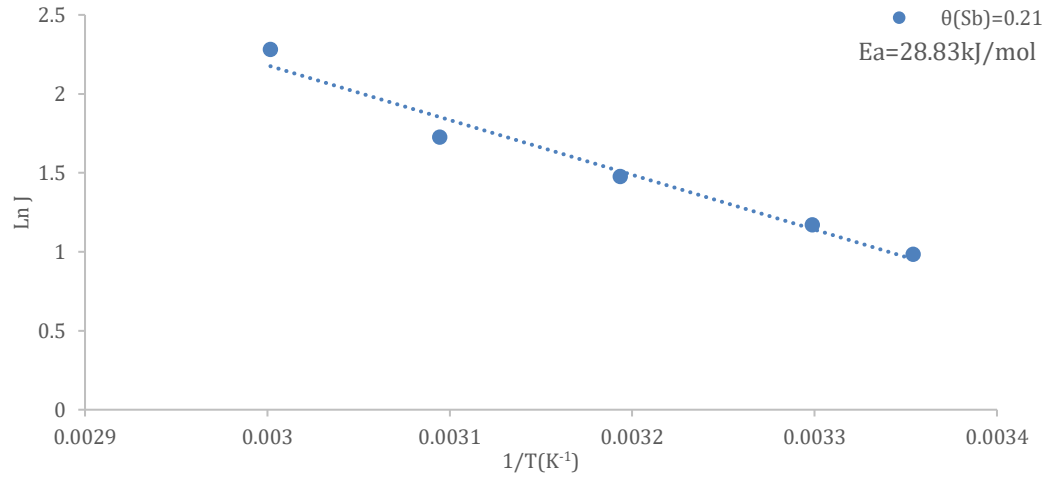

(d).

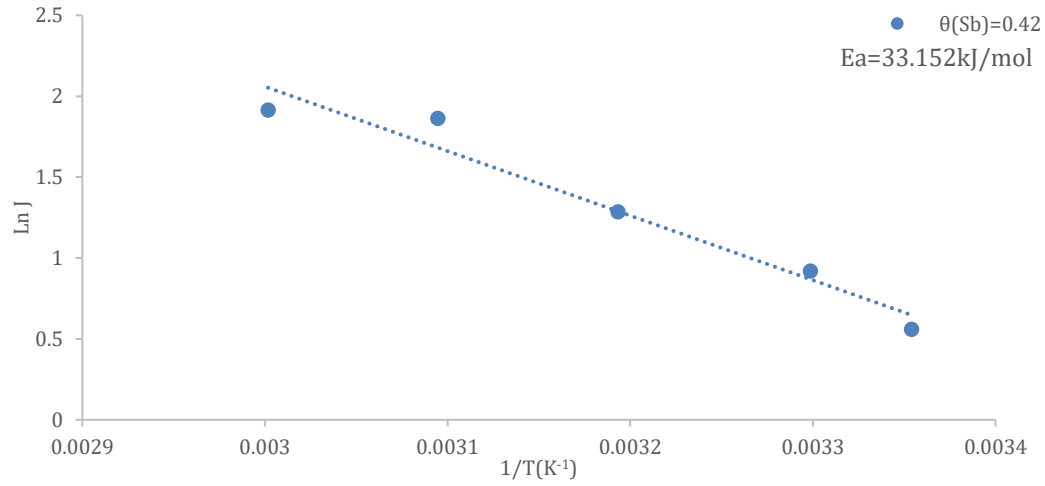

(e).

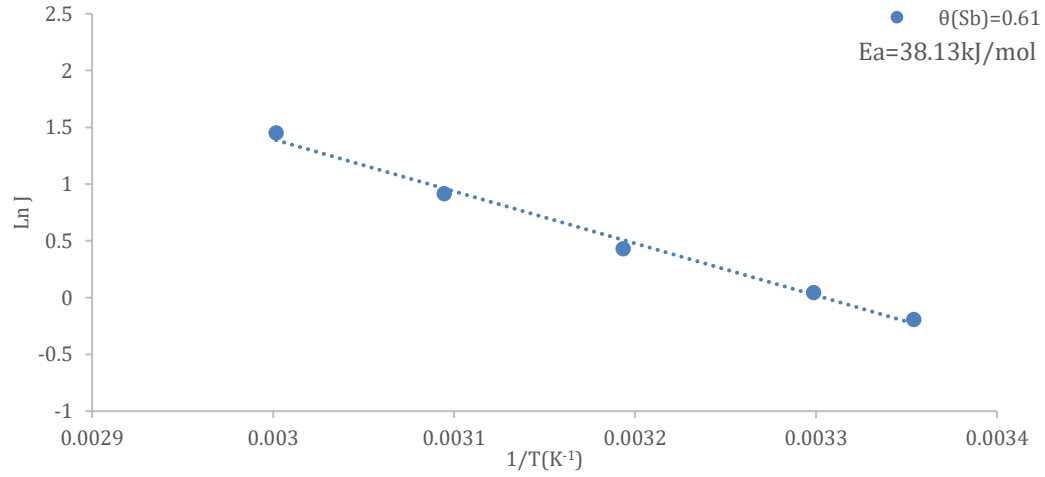

Figure 7.7 Arrhenius plots of the ethanol electrooxidation reaction (EOR) on the Pd with various Sb coverages: (a). $\theta_{Sb} = 0$, (b). $\theta_{Pb} = 0.1$, (c). $\theta_{Pb} = 0.21$, (d). $\theta_{Pb} = 0.42$, (e). $\theta_{Pb} = 0.61$, the data were obtained from current densities at peak

potential on the anodic sweep for EOR at different temperatures: i. 30 °C, ii. 40 °C, iii. 50 °C, iv. 60 °C in 0.1 M Ethanol + 0.1 M NaOH solution.

Figure 7.7 shows that there is an excellent linear relationship between thr logarithmic values of cell temperature and anodic sweep peak current density evidenced by the high values for the coefficient of proportionality. This therefore confirms the validity of the results obtained from this investigation and that the activation energy obtained from these Arrhenius plots are highly accurate. The lowest value of 28.83 kJ/mol for the EOR on Sb-Pd (θ_{Pb} = 0.21) is obtained as against the highest value of 58.57 kJ/mol on Sb-Pd (θ_{Sb} = 0). The activation energy values for Sb-Pd (θ_{Sb} = 0), Sb-Pd (θ_{Sb} = 0.10), Sb-Pd (θ_{Sb} = 0.21), Sb-Pd (θ_{Sb} = 0.42), Sb-Pd (θ_{Pb} = 0.61) are 58.57, 36.76, 28.83,33.15, 38.13 kJ/mol, respectively. This therefore implies that with the addition of Sb, the reliance on cell temperature to sustain sufficient reaction kinetics to oxidise carbonaceous intermediates responsible for electrocatalytic poisoning and to therefore overcome the EOR activation energy is lowered[33]. This therefore further validates the improvements in poisoning tolerance as a result of the addition of Sb and could address the current limitation with scalability where high electrocatalytic activity at low operating temperatures is required.

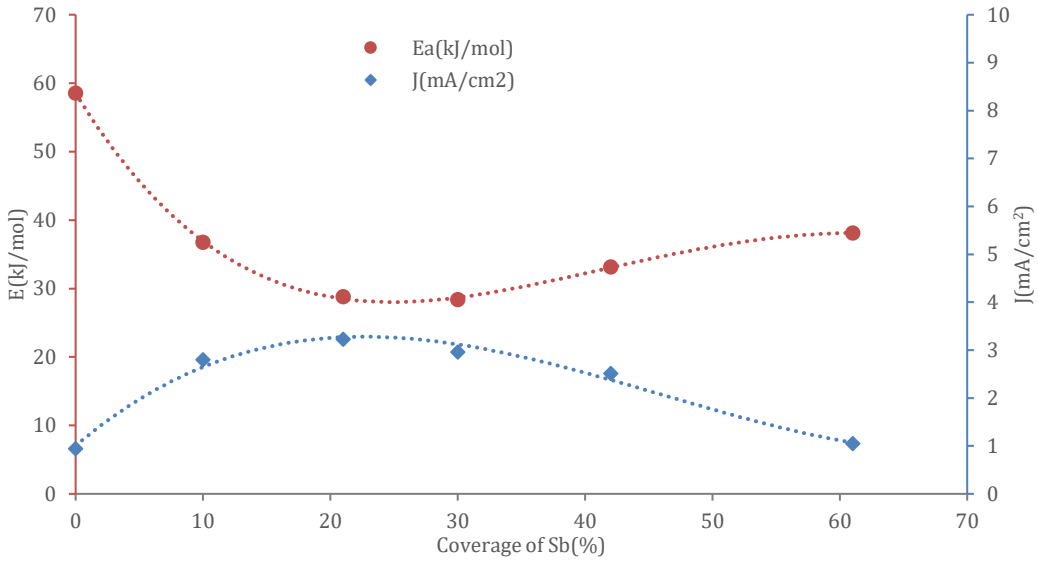

Figure 7.8 Plots of the peak current densities and activation energies obtained for EOR on Sb-Pd as a function of typical Sb-coverages. Activation energies were calculated from the Arrhenius plots in Figure 7.7 and the Arrhenius equation whilst peak current densities were only referred to CVs of EOR at 30 ˚C.

To quantify the optimal coverage of Sb, the activation energy and peak current density at 30 ˚C were plotted as a function of Sb coverage, shown in Figure 7.8. It can be obtained that E_a starts with a highest value of 58.57 kJ/mol with the Sd coverage of zero whilst the current density is in a lower station. Followed by a decreasing tendency, the optimal coverage of Sb to yield the greatest improvement in electrocatalytic properties is 21% with an EOR activation energy of 28.83 kJ/mol and an anodic sweep peak current density of 1.617 mA/cm^2. This is a remarkable improvement compared to when a bare bulk Pd is utilised, with an activation energy of 58.57 kJ/mol and anodic sweep peak current density of 0.945m A/cm^2. Therefore, the deposition of 20% Sb onto the bulk Pd electrode resulted in a reduction in activation energy by a factor of 2.03 and the improvement in anodic sweep peak current density by a factor of 1.71. The increased reaction kinetics as a result of this coverage of Sb is attributed to sufficient available surface sites of the bulk Pd electrode with a sufficient coverage of

Sb to facilitate water activation to yield the optimal concentration of hydroxyl species to oxidise the CO that poison the available surface active sites[14]. This therefore also validates that the bi-functional mechanism and electronic effect are responsible for the improvements in poisoning tolerance and electrocatalyic activity. However, further deposition of Sb results in the increase activation energy for EOR and reduction in anodic sweep peak current density. There is ambiguity as to the exact reasoning for this observation, but the main reasoning is attributed to the addition of excess Sb resulting in the reduction in electronic conductivity and deposition resulting in the occupation of the surface active sites of bulk Pd[27]. Wang et al. stated that through DFT calculations, water activation may be the rate limiting step with a bare Pd electrode and low coverages of Sb. Due to the optimal coverage of Sb, sufficient activation of water is achieved to facilitate EOR. However, with higher Sb coverages, the reduction in available surface active sites may result in ethanol adsorption and dehydrogenation steps becoming the rate limiting step[14]. Both explanations yield justifiable reasons for these observations shown in Figure7.8, however it is clear that the availability of surface active sites of bulk Pd and thus optimal Sb coverage is critical to ensure sufficient activity for EOR.

7.4 Conclusions

This investigation has shown that the addition of Sb to the bulk Pd electrode yielded remarkable improvements in electrocatalytic activity for the electro-oxidation of ethanol, as evidenced by Cyclic Voltammetry and Chronoamperometry techniques. The reactivity of the catalysts towards ethanol electrooxidation reaction (EOR) was studied at various temperatures and under other conditions that practical fuel cells operate. For all catalysts, increasing temperature from 25 ˚C to 60 ˚C enhance the reactivity commendable. This investigation has shown that the optimal coverage of 21% Sb on the bulk Pd electrode revealed remarkable improvements in electrocatalytic activity, where the EOR activation energy is reduced by 2.47 times from 58.57 kJ/mol with a bare bulk Pd electrode to 28.83 kJ/mol. The anodic sweep peak current density also improved by 1.71 times from 0.945 mA/cm^2 at 30 ˚C to 1.617 mA/cm^2.

7.5 Reference

1. F. A. Zakil, S. K. Kamarudin, S. Basri, ***Modified Nafion Membranes for Direct Alcohol Fuel Cells: An Overview***, Renewable and Sustainable Energy Reviews, 2016, 65, 841-852.

2. F. P. Hu, C. L. Chen, Z. Y. Wang, G. Y. Wei, p.k. Shen, ***Mechanistic study of ethanol oxidation on Pd-NiO/C electrocatalyst,*** Electrochim. Acta, 2006, 52, 1087-1091.

3. S. Abdullah, S. K. Kamarudin, U. A. Hasran, M. S. Masdar, W. R. W. Daud, ***Modeling and Simulation of a Direct Ethanol Fuel Cell : An Overview***, J. Power Sources, 2014, 262, 401-406.

4. C. Lamy, E. M. Belgsir, J. M. Leger, ***Electrocatalytic Oxidation of Aliphatic Alcohols: Application to the Direct Alcohol Fuel Cell (DAFC)***, J. Appl. Electrochem., 2001, 31, 799–809.

5. C. W. Xu, L. Q. Cheng, P. K. Shen, Y. L. Liu, ***Methanol and Ethanol Electrooxidation on Pt and Pd Supported on Carbon Microspheres in Alkaline Media***, Electrochem. commun. 2007, 9, 997-1001.

6. L. Ma, D. Chu, R. R. Chen, ***Comparison of Ethanol Electro-Oxidation on Pt/C and Pd/C Catalysts in Alkaline Media***, Int J Hydrogen Energy, 2012, 37, 11185-11194.

7. V. Bambagioni, C. Bianchini, A. Marchionni, et al., ***Pd and Pt–Ru Anode Electrocatalysts Supported on Multi-Walled Carbon Nanotubes and their use in Passive and Active Direct Alcohol Fuel Cells with an Anion-Exchange Membrane (Alcohol=Methanol, Ethanol, Glycerol)***, J. Power Sources, 2009, 190, 241-251.

8. K. Persson, A. Ersson, K. Jansson, N. Iverlund, S. Jaras, ***Influence of co-metals on Bimetallic Palladium Catalysts for Methane Combustion***. J. Catal., 2005, 231, 139.

9. S. S. Mahapatra, A. Dutta, J. Datta, ***Temperature Effect on the Electrode Kinetics of Ethanol Oxidation on Pd Modified Pt Electrodes and the Estimation of Intermediates Formed in Alkali Medium***, Electrochim, Acta, 2010, 55, 9097-9104.

10. S. T. Nguyen, H. M. Law, A. T. Nguyen, N. Kristian, S. Wang, S. H. Chan, X. Wang, ***Enhancement Effect of Ag for Pd/C Towards the Ethanol Electro-oxidation in Alkaline Media***, Appl. Catal., B: Environmental, 2009, 91, 507-515.

11. A. Sadiki, P. Vo, S. Z. Hu, T. S. Copenhaver, L. Scudiero, S. Ha, J. L. Haan, ***Increase Electrochemical Oxidation Rate of Alcohols in Alkaline Media on Palladium Surfaces Electrochemically Modified by Antimony, Lead, and Tin,*** Electrochim, Acta, 2014, 139, 302-307.

12. Y. Feng, D. Bin, B. Yan, Y. Du, T. Majima, W. Zhou. ***Porous Bimetallic PdNi Catalyst with High Electrocatalytic Activity for Ethanol Electrooxidation***, J Colloid Interface Sci., 2017, 493, 190-197.

13. Z. P. Xiong, B. Yan, K. Zhang, et al., ***A Facile Synthesis of 3D Network PdCu Nanostructure with Enhanced Electrocatalytic Activity Towards Ethanol Oxidation***, Journal of the Taiwan Institute of Chemical Engineers, 2017, 75, 12-17.

14. J. D. Cai, Y. Y. Huang, Y. L. Guo. ***Facile Synthesis of PdSbx/C Nanocatalyst with High Performance for Ethanol Electro-Oxidation in Alkaline Medium***. Int J Hydrogen Energy, 2014, 39, 18256-18263.

15. P. M. Rigano, C. Mayer, T. Chierchie, ***Structural Investigation of the Initial Stages of Copper Electrodeposition on Polycrystalline and Single Crystal Palladium Electrodes***, Electrochim. Acta, 1990, 45, 1189-1194.

16. A. N. Correia, L. H. Mascaro, S. A. S. Machado, L. A. Avaca, ***Active Surface Area Determination of Pd- Si Alloys by H-adsorption***, Electrochim. Acta, 1997, 42, 493-495.

17. C. Y. Hu, X. Wang. ***Highly Dispersed Palladium Nanoparticles on Commercial Carbon Black with Significantly High Electro-Catalytic Activity for Methanol and Ethanol Oxidation***, Int J Hydrogen Energy, 2015, 40, 12382-12391.

18. Y. T. Zhang, H. H. Shu, G. Chang, Y. B. He, ***Facile Synthesis of Palladium – Graphene Nanocomposites and their Catalysis for Electro-Oxidation of Methanol and Ethanol***, Electrochim Acta, 2013, 109, 570-576.

19. X. G. Wang, W. M. Wang, Z. Qi, C. C. Zhao, H. Ji, Z. H. Zhang, ***High Catalytic Activity of Ultrafine Nnanoporous Palladium for Electro-Oxidation of Methanol , Ethanol , and Formic Acid***, Electrochem commun., 2009, 11, 1896-1899.

20. N. Tian, Z. Y. Zhou, N. F. Yu, L. Y. Wang, S. G. Sun, ***Direct Electrodeposition of Tetrahexahedral Pd Nanocrystals eith High-Index Facets and High Catalytic Activity for Ethanol Electrooxidation***, J. Am. Chem. Soc., 2010, 132, 7580-7581.

21. W. X. Du, K. E. Mackenzie, D. F. Milano, N. A. Deskins, D. Su, X. W. Teng, ***Palladium−Tin Alloyed Catalysts for the Ethanol Oxidation Reaction in an Alkaline Medium***, ACS Catalysis, 2012, 2, 287-297.

22. G. M. Alvarenga, I. B. C. Gallo, H. M. Villullas. ***Enhancement of Ethanol Oxidation on Pd Nanoparticles Supported on Carbon-Antimony Tin Oxide Hybrids Unveils the Relevance of Electronic Effects***, J Catal., 2017, 348, 1-8.

23. Y. G. Jo, S. M. Kim, J. W. Kim, S. Y. Lee, ***Composition-Tuned Porous Pd-Ag Bimetallic Dendrites for the Enhancement of Ethanol Oxidation Reactions***, J Alloys Compd., 2016, 688, 447-453.

24. P. Mukherjee, P. Sarathi, K. Mandal, D. Bhattacharjee, S. Dasgupta, S. Kumar, ***Improved Catalysis of Room Temperature Synthesized Pd-Cu Alloy Nanoparticles for Anodic Oxidation of Ethanol in Alkaline Media***, Electrochim. Acta, 2015, 154, 447-455.

25. R. M. Modibedi, T. Masombuka, M. K Mathe, ***Carbon Supported Pd-Sn and Pd-Ru-Sn Nanocatalysts for Ethanol Electro-Oxidation in Alkaline Medium***, Int. J. Hydrogen Energy, 2011, 36, 4664-4672.

26. D. Soundararajan, J. H. Park, K. H. Kim, J. M. Ko, ***Pt-Ni Alloy Nanoparticles Supported on CNF as Catalyst for Direct Ethanol Fuel Cells***, Curr. Appl. Phys., 2012, 12, 854-859.

27. Y. Y. Huang, J. D. Cai, Y. L. Guo, ***A High-Efficiency Microwave Approach to Synthesis of Bi-modified Pt Nanoparticle Catalysts for Ethanol Electro-Oxidation in Alkaline Medium***, Appl. Catal., B, Environ. 2013, 129, 549-555.

28. Z. X. Liang, T. S. Zhao, J. B. Xu, L. D. Zhu, ***Mechanism Study of the Ethanol Oxidation Reaction on Palladium in Alkaline Media***, Electrochim. Acta, 2009, 54, 2203-2208.

29. Y. Wang, F. Shi, Y. Yang, W. Cai, ***Carbon Supported Pd-Ni-P Nanoalloy as an Efficient Catalyst for Ethanol Electro-Oxidation in Alkaline Media***, J. Power Sources, 2013, 243, 369-373.

30. Y. Y. Feng, Z. H. Liu, W. Q. Kong, Q. Y. Yin, L. X. Du, ***Promotion of Palladium Catalysis by Silver for Ethanol Electro-Oxidation in Alkaline Electrolyte***, Int. J. Hydrogen Energy, 2013, 39, 2497-2504.

31. Y. Ma, H. Li, H. Wang, X. Mao, V. Linkov, S. Ji, O. U. Gcilitshana, R. Wang, ***Evolution of the Electrocatalytic Activity of Carbon-supported Amorphous Platinum-ruthenium-nickel-phosphorous nanoparticles for Methanol Oxidation***, J. Power Sources, 2014, 268, 498-507.

32. J. L. Cohen, D. J. Volpe, H. D. Abruna, ***Electrochemical Determination of Activation Energies for Methanol Oxidation on Polycrystalline Platinum in Acidic and Alkaline Electrolytes***, Phys. Chem. Chem. Phys., 2007, 9, 49-77.

33. M. Grdeń, A. Czerwiński. ***EQCM Studies on Pd-Ni Alloy Oxidation in Basic Solution***, J. Solid State Electrochem., 2008, 12, 375-385.

Chapter Eight

Conclusions and Future Work

8.1 Conclusions

In this thesis work, firstly the temperature effects on Pd electrocatalyst towards alcohol (methanol, ethanol butanol and glycerol) electrooxidation reaction in alkaline media were studied for the direct alcohol fuel cells applications, then a series of Pd-based bimetallic electrocatalysts were developed to improve the activity and stability for ethanol electrooxidation reaction (EOR) in alkaline media under various conditions that a practical fuel cell would operate. Moreover, the kinetics of alcohol oxidation reaction on Pd-based electrocatalysts were explored from the activation energy calculated by Arrhenius plots using the data obtained from cyclic voltammetry (CV) and chronoamperometry (CA) studies at various temperatures and compared.

8.1.1 Mechanistic study of bulk Pd for alcohol electrooxidation in alkaline media

For all the alcohols (methanol, ethanol butanol and glycerol) studied, the electrooxidation reaction on the Pd electrode was facilitated at higher temperatures. The improvements in catalytic reactions with increasing temperature were attributed to higher concentrations of surface oxidants and faster reaction kinetics at higher temperatures thus reducing the concentration of alcohol residues poisoning the surface of the electrode.

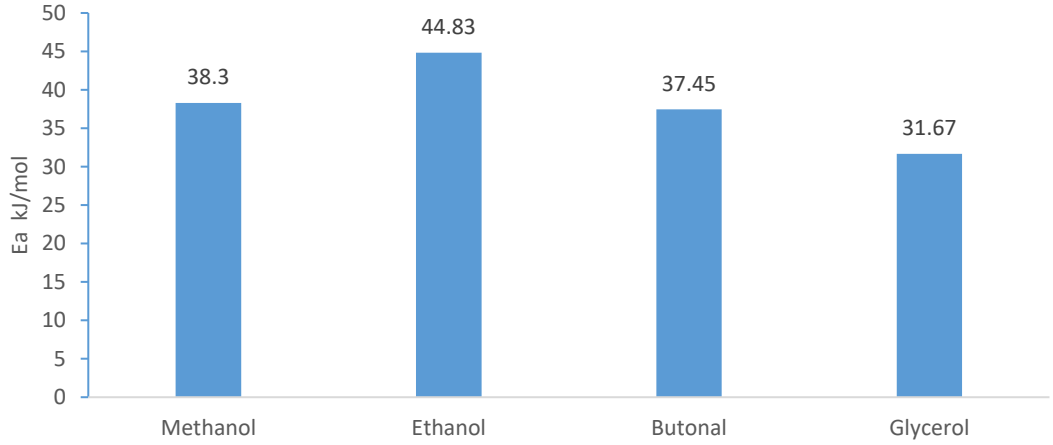

***Figure 8.1** Comparison of reaction energies of different alcohols electrooxidation reactions on bulk Pd electrode.*

In comparison of the different alcohols electrooxidation reactions, the positive peak current densities (J_p) at 30 ˚C follow such order: $J_{Glycerol} > J_{Butanol} > J_{Ethanol} > J_{Methanol}$, while the activation energies (Ea) follow the order of: $Ea_{Glycerol} < Ea_{Butanol} < Ea_{Methanol} < Ea_{Ethanol}$. These results implied that the reaction activities increased while the activation energy decreased with respect to increases in the length of the carbon chain of the primary alcohols. As shown in Figure 8.1, reaction energy of MOR defies the order, predictably ascribed to a different reaction mechanism or poisoning mechanism of electrocatalyst which will need further research employing FTIR and DFT.

8.1.2 Activity enhancement of bulk Pd with Pb decorated towards ethanol electrooxidation in alkaline media

Based on comparison of the electrooxidation of ethanol on bulk Pd electrode and various coverages of Pb-decorated Pd electrodes in alkaline media, Pb-Pd catalyst displays considerably greater catalytic activity with a certain Pb coverage range. Addition of Pb can promote catalyst tolerance towards CO-like specie poisoning by weakening the bond energy of Pd-CO or enhancing electrooxidation of CO-like species.

For all catalysts, increasing temperature from 25 ˚C to 60 ˚C enhances the reactivity commendable. The optimum Pb-Pd (θ_{Pb} =0.36) catalyst displayed almost the highest peak current density of 1.617 mA·cm^{-2} at 30 ˚C, which is roughly 3 times higher than that of bulk Pd (0.609 mA·cm^{-2}). Moreover, relevant activity enhancements up to 3 times, was observed for the Pb-Pd (θ_{Pb} = 0.36) with corresponding activation energy being reduced significantly.

8.1.3 Preparation and structure and reactivity studies of Au-Pd nanoparticles-polymer nanocomposites towards ethanol electrooxidation in alkaline media

In this work, a benign one-step synthesis process for AuNPs-PEDOT:PSS nanocomposites and their applications in alkaline type direct ethanol fuel cells has been successfully demonstrated. Results show that by controlling the precursor/polymer concentration ratio and the plasma processing conditions, nanocomposites with wide range of structures/properties can be obtained.

When characterizing selected nanocomposite films as direct ethanol fuel cell electrocatalysts under alkaline conditions, significant enhancement in EOR activity have been achieved hence suggesting the AuNP/PEDOT:PSS nanocomposite can serve as a promising candidate for a new class of Pt-free fuel cell catalysts. More importantly, this simple, rapid and environmentally friendly approach may be expanded to the synthesis of a much greater range of metal NPs/polymer nanocomposites with controlled structure/properties, providing enhanced functionality in various applications.

8.1.4 High electrochemical performance of Ag-Pd bimetallic catalyst for the ethanol electrooxidation in alkaline media

By combining cyclic voltammetry and chronoamperometry, an insight into the electrochemistry and electrocatalytic activity of Pd-Ag towards ethanol oxidation reaction (EOR) has been investigated. Our electrochemistry data have shown that the addition of certain coverages of Ag onto Pd catalyst contributes significantly to the efficient and stable catalyst activity for EOR in alkaline media. Ag-Pd ($\theta_{Ag} = 0.37$) expresses the highest current density, lowest activity energy and highest poison tolerance toward EOR in alkaline media among the series of Ag-Pd (θ_{Ag}=m). Meanwhile, the activity of Ag-Pd catalyst is greatly enhanced by increasing temperature from 25 ˚C to 60 ˚C applied for all EOR. The general kinetics data of EOR on Ag-decorated Pd were obtained from the activation energy calculated based on Arrhenius plots, and compared. An enhancement of almost 2 times in activity was achieved at the optimum Ag coverage, with corresponding activation energy being reduced significantly. In general, the addition of Ag adatom plays an efficient role in enhancing the performance of clean Pd surface which can remarkably accelerate the ethanol oxidation reaction and significantly lower the reaction energy as well as the OH* onset potential.

8.1.5 Activity enhancement of Bulk Pd with Sb secorated towards ethanol electrooxidation in alkaline media

The addition of Sb to the bulk Pd electrode yielded remarkable improvements in electrocatalytic activity for the electro-oxidation of ethanol, as evidenced by Cyclic Voltammetry and Chronoamperometry techniques. For all catalysts, increasing temperature from 25 ˚C to 60 ˚C enhance the reactivity commendable. This investigation has shown that the optimal coverage of 21% Sb on the bulk Pd electrode

revealed remarkable improvements in electrocatalytic activity, where the EOR activation energy is reduced by 2.47 times from 58.57 kJ/mol with a bare bulk Pd electrode to 28.83 kJ/mol. The anodic sweep peak current density also improved by 1.71 times from 0.945 mA/cm^2 at 30 ˚C to 1.617 mA/cm^2. The presence of Sb appears to facilitate the formation of oxygenated species resulting in the oxidation of accumulated carbonaceous residues remaining on the electrocatalyst surface after the anodic sweep scan, thus improving tolerance to poisoning and providing sufficient catalytic surface area to propagate superior reaction kinetics, current density and lower EOR activation energy. This investigation has shown that the utilization of Sb with a bulk Pd yields remarkable improvements in electrocatalytic activity towards EOR, which could potentially aid in the effort to resolve the current limitations that inhibit the scalability of a DEFC for commercial applications.

(a).

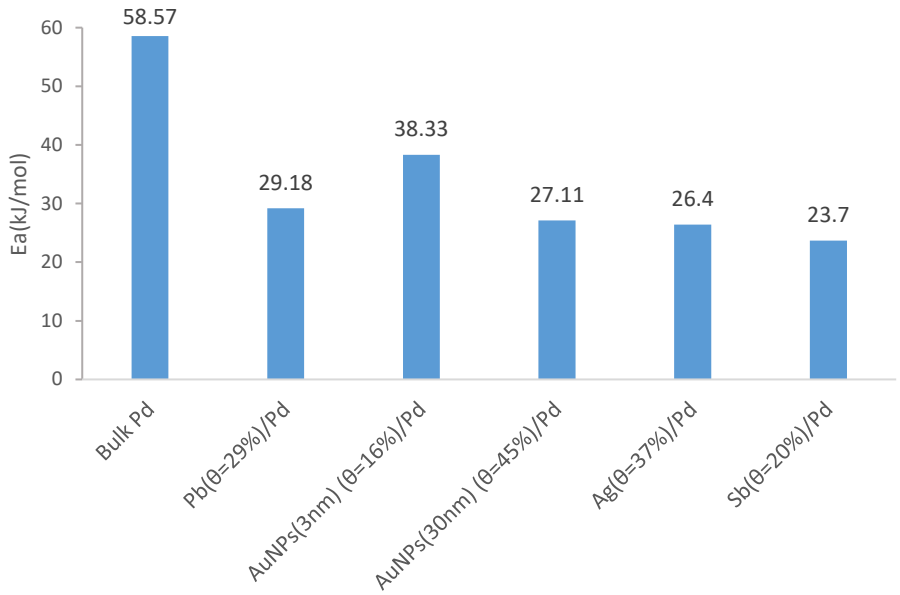

(b).

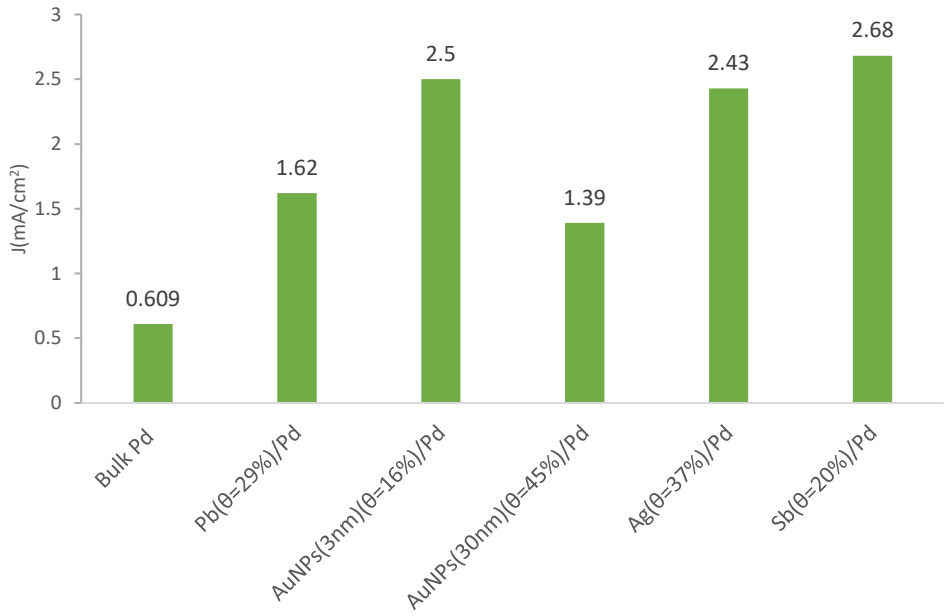

Figure 8.2 (a). Actitation energies of ethanol oxidation reaction with various X/Pd catalysts, (b). Peak current densities of ethanol oxidation reaction with various X/Pd catalysts

For ethanol electrooxidation reaction (EOR) in alkaline media, the catalytic reactivity

of Pd is significantly enhanced by being decorated with a second metal (Pb, Ag, AuNPs, Sb). Activation energy (Ea) of X/Pd (X= Pb, Ag, AuNPs, Sb) at an optimal coverage of X is following the order: $Ea_{Sb(\theta=20\%)/Pd} < Ea_{Ag(\theta=37\%)/Pd} < Ea_{AuNPs(30nm)\ (\theta=45\%)/Pd} < Ea_{Pb(\theta=29\%)/Pd} < Ea_{AuNPs(3nm)\ (\theta=16\%)/Pd} < Ea_{bulk\ Pd}$, while oxidation peak current density at 30 ºC is following such order: $J_{Sb(\theta=20\%)/Pd} > J_{AuNPs(3nm)\ (\theta=16\%)/Pd} \approx J_{Ag(\theta=37\%)/Pd} > J_{Pb(\theta=29\%)/Pd} > J_{AuNPs(30nm)\ (\theta=45\%)/Pd} > Ja_{bulk\ Pd}$. Among all these catalysts studied, $Sb_{(\theta=20\%)}/Pd$ and $Ag_{(\theta=37\%)}/Pd$ exhibit the highest reactivity, having the lowest Activation energy and highest peak current density.

8.2 Future work

To further understand the specific electrocatalytic mechanisms of the bimetallic electrocatalysts so developed, it is very desirable to employ in-situ FTIR (Fourier-Transform Infrared spectroscopy) to investigate the reaction intermediates and products distributions on molecular level, Density Function Theory (DFT) atomistic modelling to study and predict the C-C bond cleavage pathways and X-ray adsorption spectroscopy to understand electronic effects to improve the understanding of the fundamental reaction mechanisms and electronic effects involved in the reactions. The further research from these three methods will provide an understanding of the electronic interaction between the Pd and the second metal to provide clarity as to what is specifically responsible for the improvement in electrocatalytic improvements and the main reaction products and how these are formed so that certain reaction pathways can be proposed.

Finally, to further explor and design new electrocatalysts with high efficacy, Pd-based ternary metallic electrocatalysts such as AgSb/Pd is recommended to be investigated.

Appendices

Chapter 4

(a).

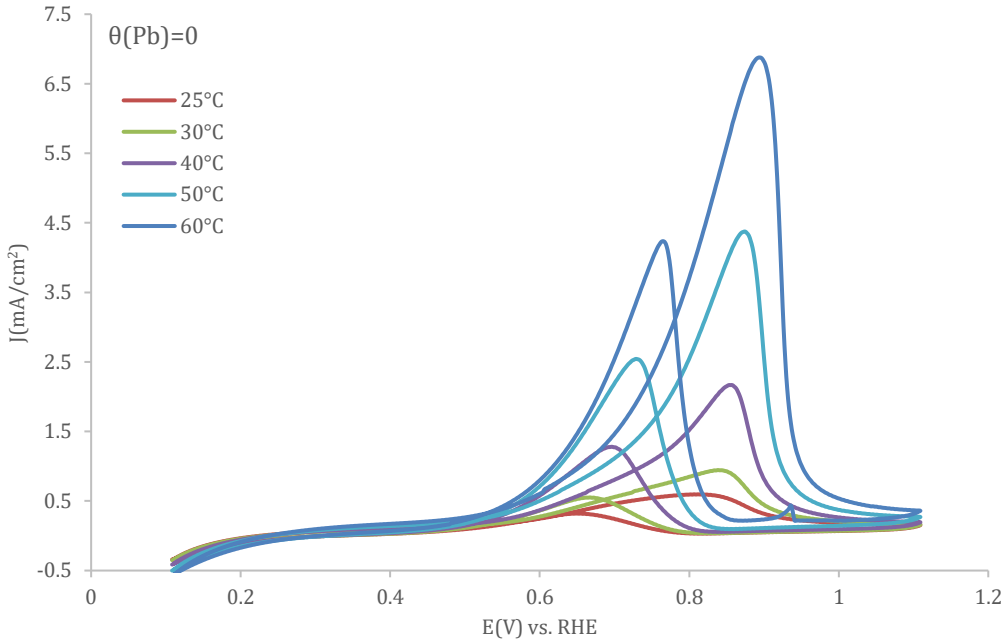

(b).

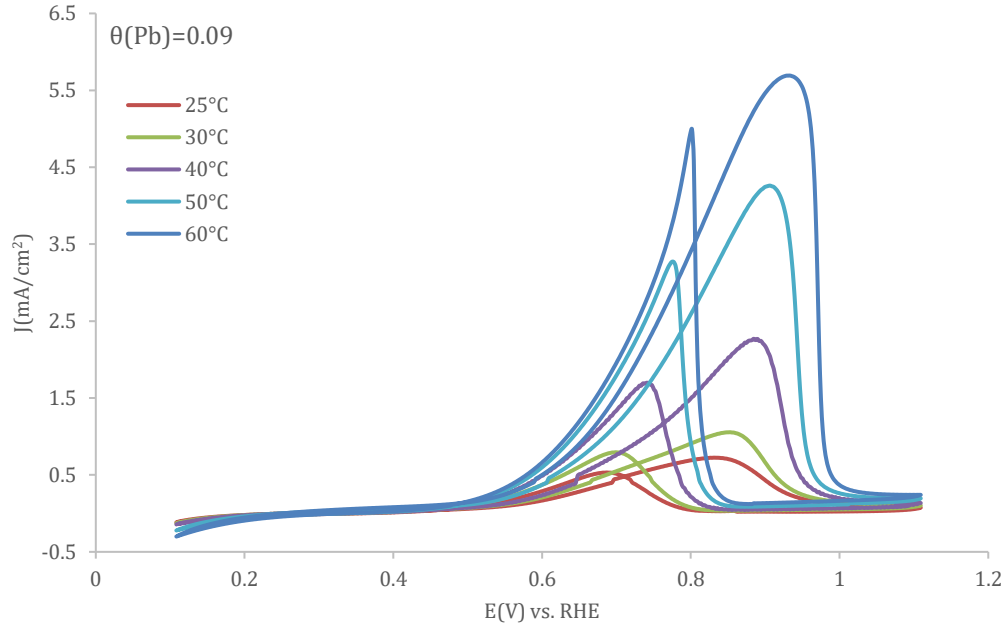

(c).

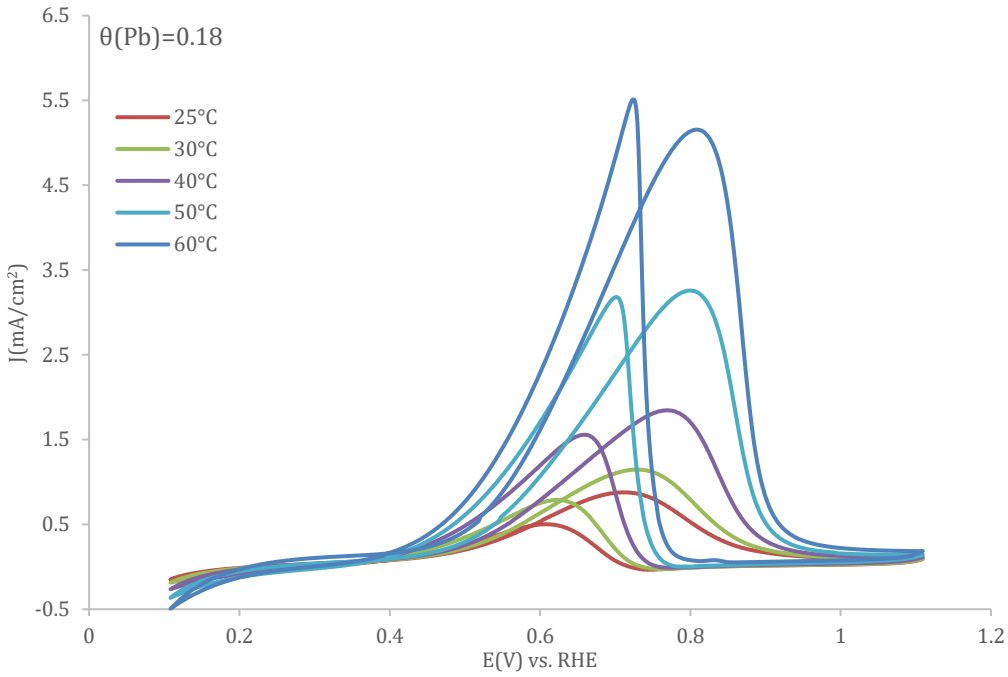
θ(Pb)=0.18
25°C
30°C
40°C
50°C
60°C
J(mA/cm²)
E(V) vs. RHE
6.5
5.5
4.5
3.5
2.5
1.5
0.5
-0.5
0
0.2
0.4
0.6
0.8
1
1.2

(d).

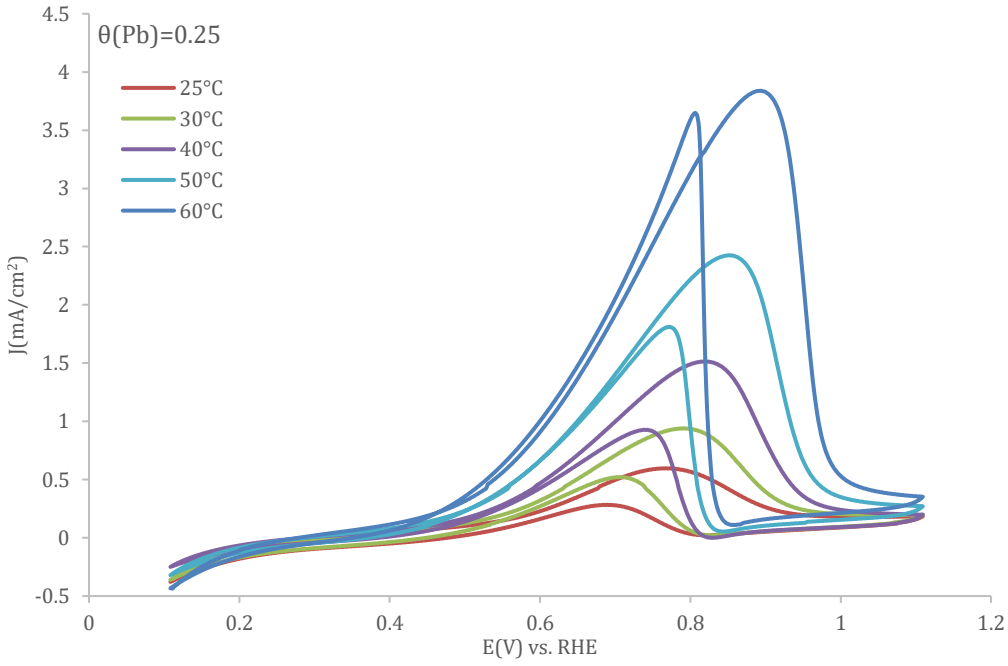
θ(Pb)=0.25
25°C
30°C
40°C
50°C
60°C
J(mA/cm²)
E(V) vs. RHE
4.5
4
3.5
3
2.5
2
1.5
1
0.5
0
-0.5
0
0.2
0.4
0.6
0.8
1
1.2

(e).

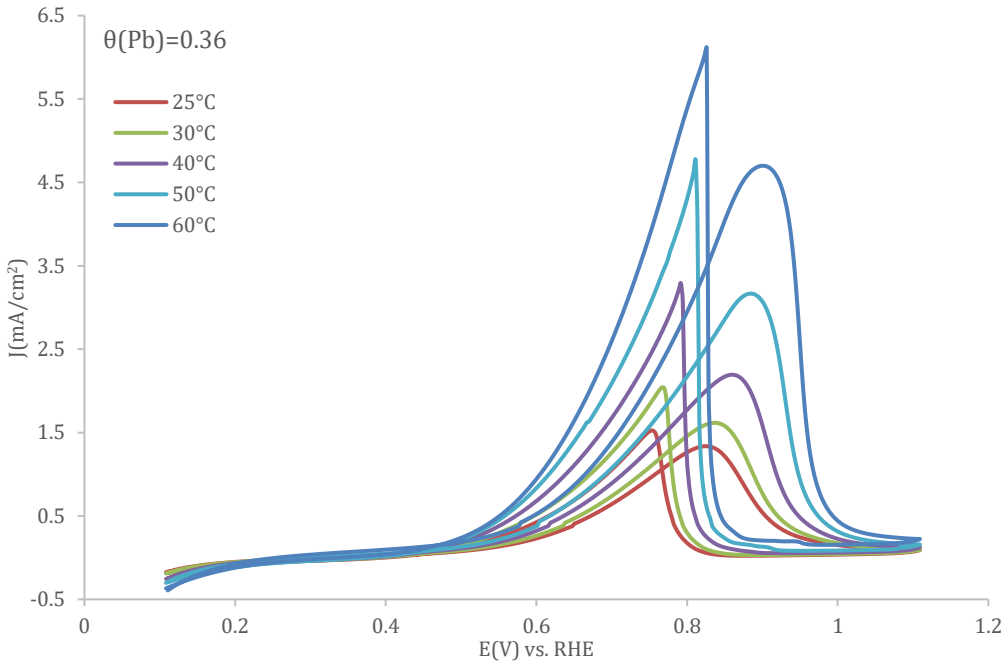
θ(Pb)=0.36
25°C
30°C
40°C
50°C
60°C
J(mA/cm²)
E(V) vs. RHE
6.5
5.5
4.5
3.5
2.5
1.5
0.5
-0.5
0
0.2
0.4
0.6
0.8
1
1.2

(f).

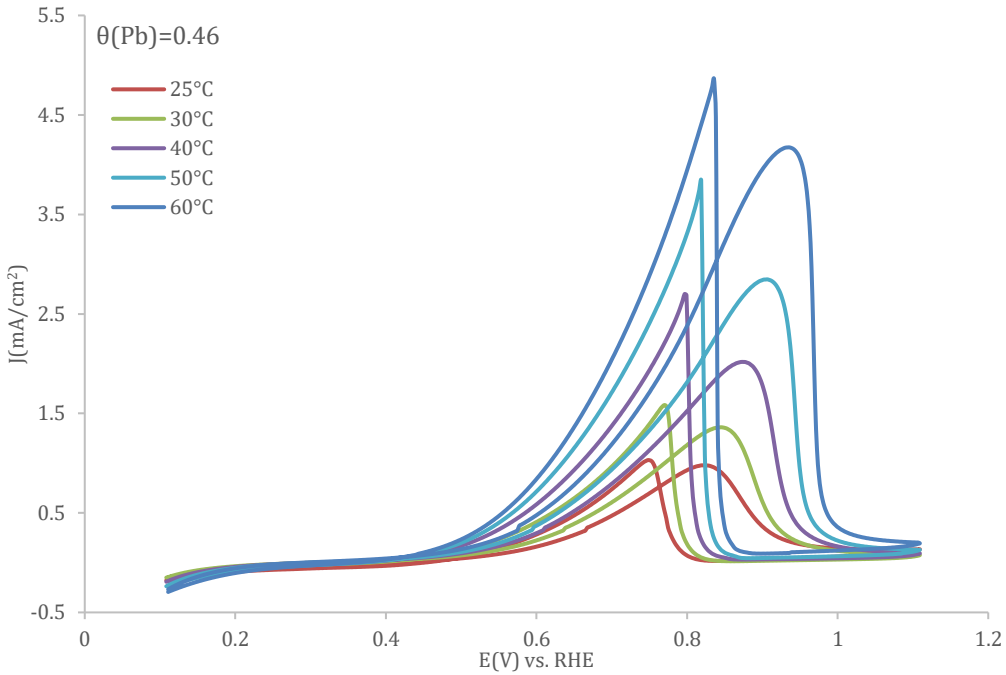
θ(Pb)=0.46
25°C
30°C
40°C
50°C
60°C
J(mA/cm²)
E(V) vs. RHE
5.5
4.5
3.5
2.5
1.5
0.5
-0.5
0
0.2
0.4
0.6
0.8
1
1.2

(g).

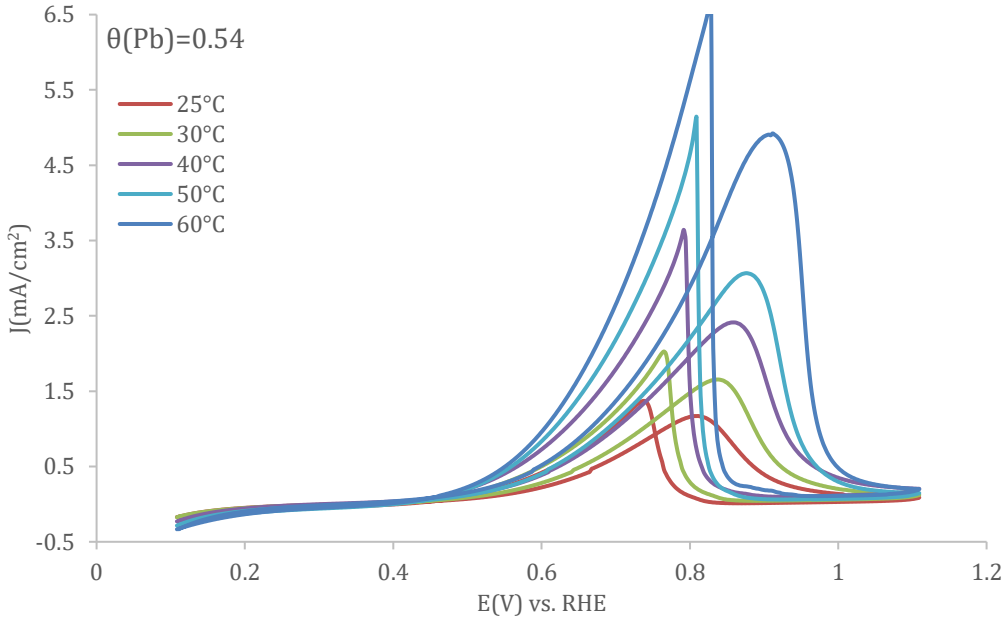

(h).

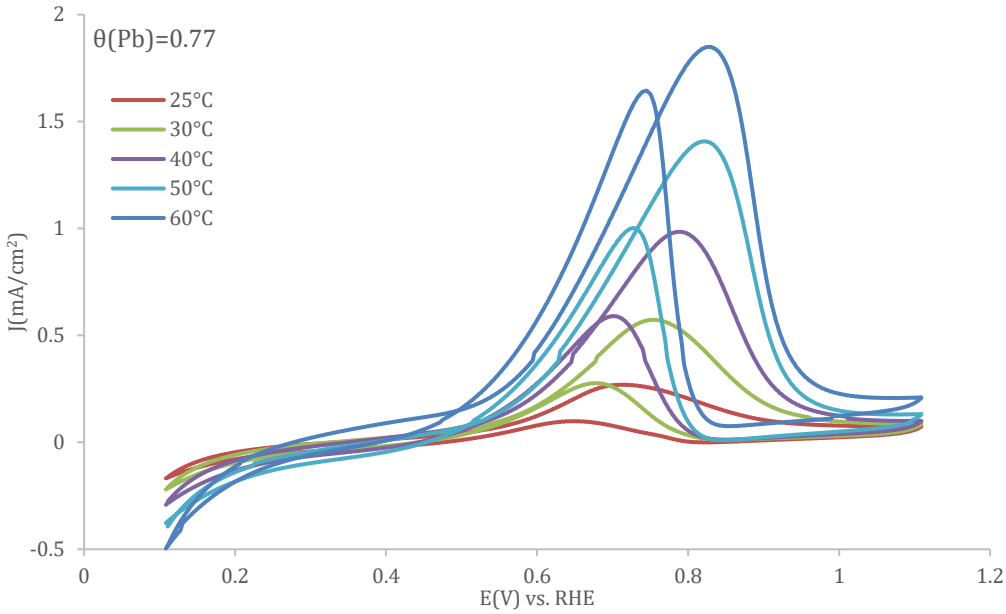

Figure A.4.1. Cyclic voltammograms of bulk Pd with various Pb coverages: (a). $\theta_{Pb} = 0$, (b). $\theta_{Pb} = 0.09$, (c). $\theta_{Pb} = 0.18$, (d). $\theta_{Pb} = 0.25$, (e). $\theta_{Pb} = 0.36$, (f). $\theta_{Pb} = 0.46$, (g). $\theta_{Pb} = 0.54$, (h). $\theta_{Pb} = 0.77$ towards ethanol electrooxidation from 25 to 60 ˚C in 0.1 M Ethanol + 0.1 M NaOH solution. Scan rate: 50 mVs^{-1}.

(a).

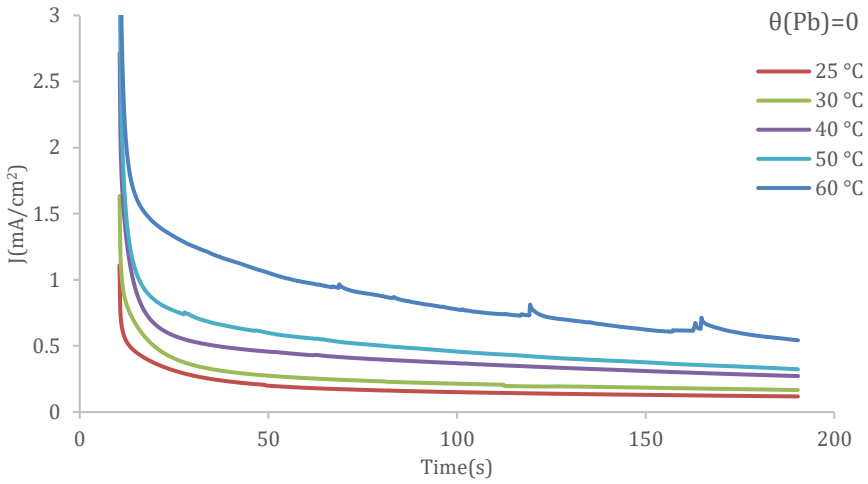
θ(Pb)=0
25 °C
30 °C
40 °C
50 °C
60 °C
J(mA/cm²)
Time(s)
0
0.5
1
1.5
2
2.5
3
0
50
100
150
200

(b).

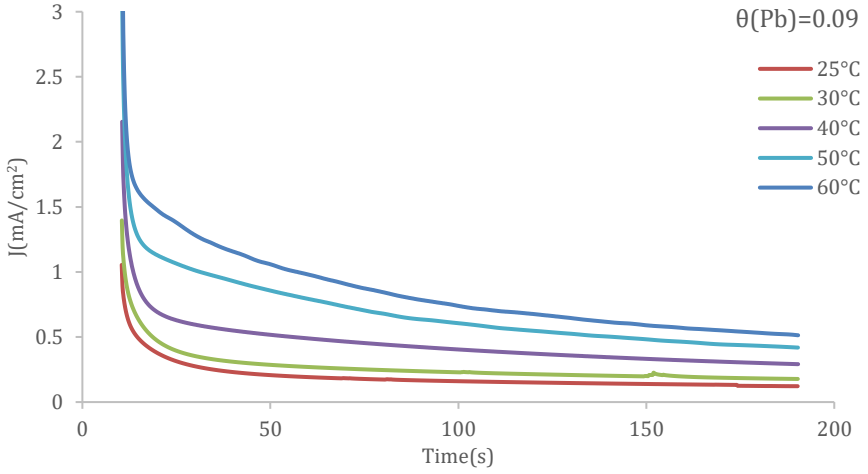
θ(Pb)=0.09
25°C
30°C
40°C
50°C
60°C
J(mA/cm²)
Time(s)
0
0.5
1
1.5
2
2.5
3
0
50
100
150
200

(c).

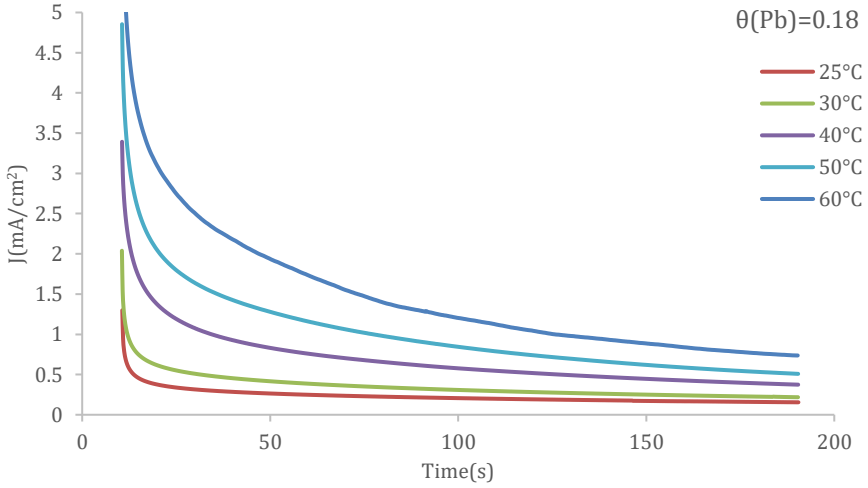
θ(Pb)=0.18
25°C
30°C
40°C
50°C
60°C
J(mA/cm²)
Time(s)
0
0.5
1
1.5
2
2.5
3
3.5
4
4.5
5
0
50
100
150
200

(d).

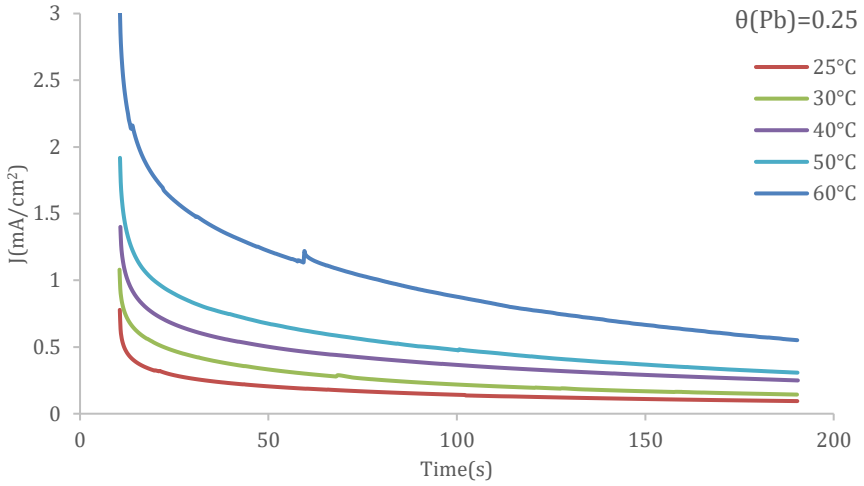
θ(Pb)=0.25
25°C
30°C
40°C
50°C
60°C
J(mA/cm²)
Time(s)
0
0.5
1
1.5
2
2.5
3
0
50
100
150
200

(e).

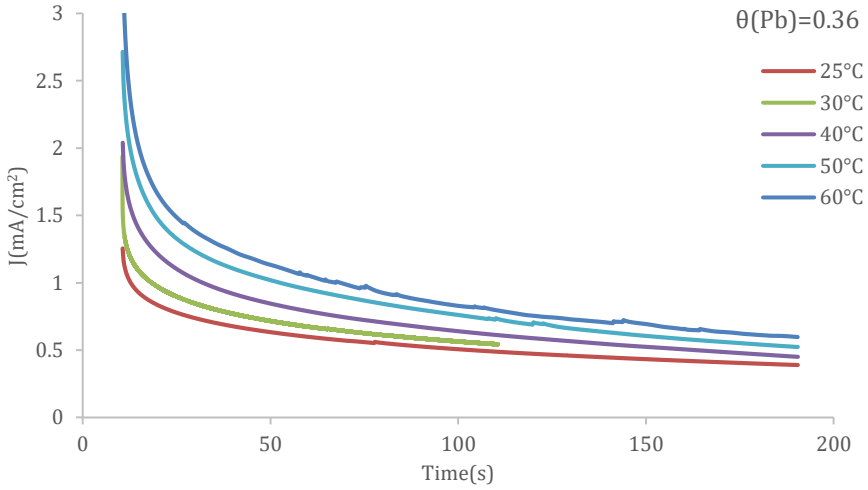
θ(Pb)=0.36
25°C
30°C
40°C
50°C
60°C
J(mA/cm²)
Time(s)
0
0.5
1
1.5
2
2.5
3
0
50
100
150
200

(f).

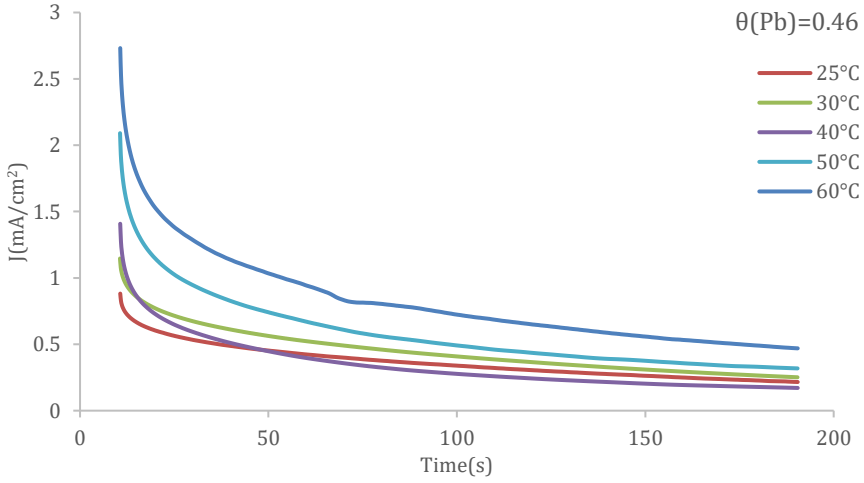
θ(Pb)=0.46
25°C
30°C
40°C
50°C
60°C
J(mA/cm²)
Time(s)
0
0.5
1
1.5
2
2.5
3
0
50
100
150
200

(g).

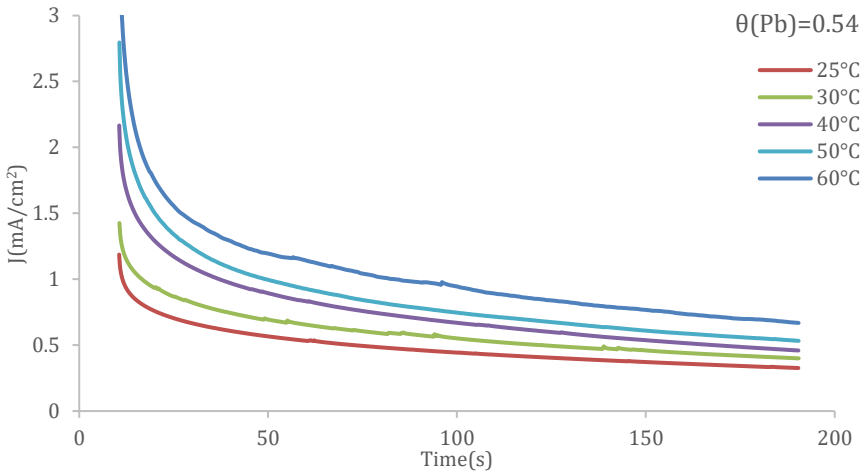

(h).

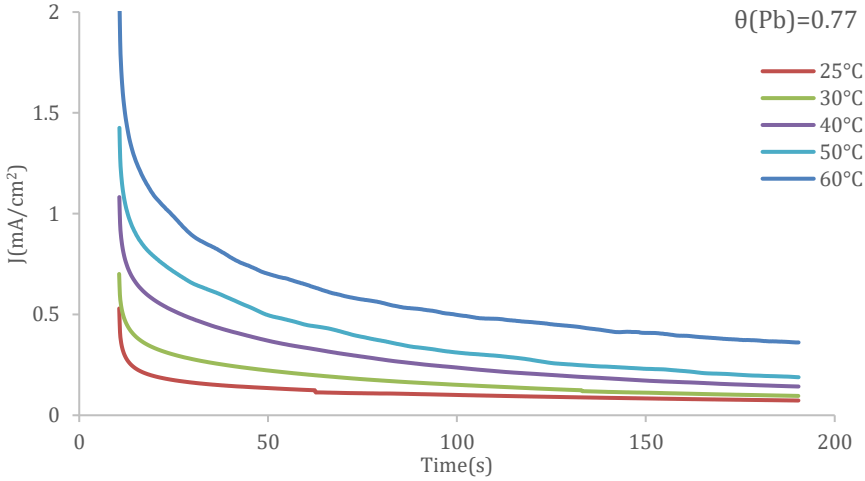

Figure A.4.2. Chronoamperometric curves of bulk Pd with various Pb coverages: (a). $\theta_{Pb} = 0$, (b). $\theta_{Pb} = 0.09$, (c). $\theta_{Pb} = 0.18$, (d). $\theta_{Pb} = 0.25$, (e). $\theta_{Pb} = 0.36$, (f). $\theta_{Pb} = 0.46$, (g). $\theta_{Pb} = 0.54$, (h). $\theta_{Pb} = 0.77$ in 0.1 M Ethanol + 0.1 M NaOH solution at the potential of 0.71 V (vs. RHE) from 25 to 60 ˚C. Scan rate: 50 mVs^{-1}.

(a).

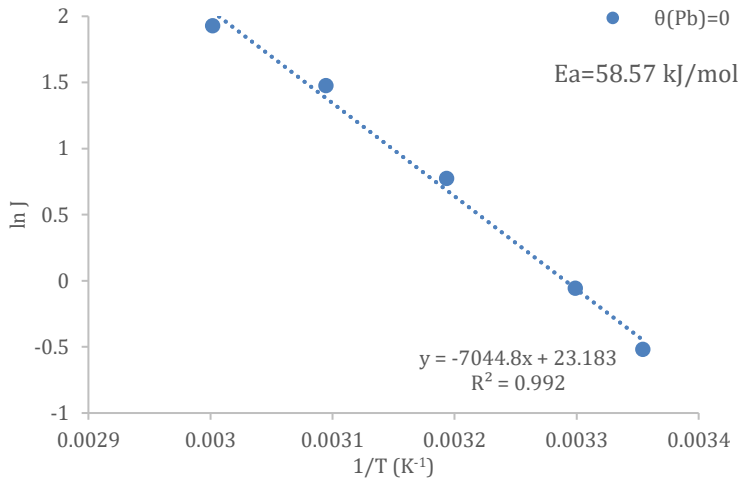
θ(Pb)=0
Ea=58.57 kJ/mol
ln J
y = -7044.8x + 23.183
R² = 0.992
1/T (K⁻¹)

(b).

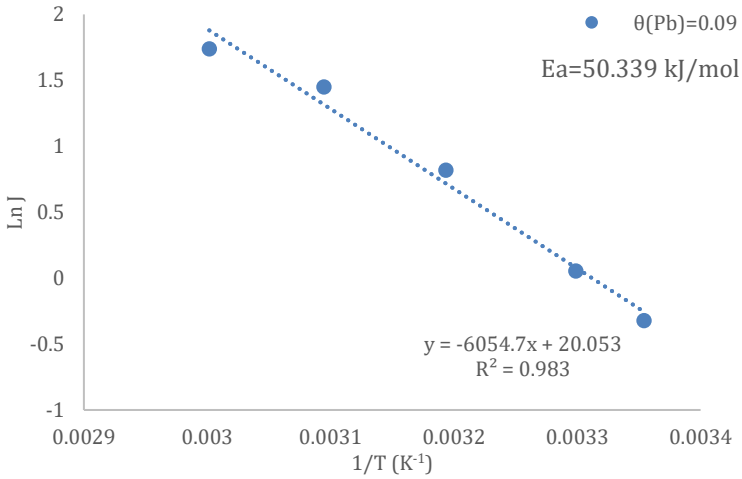
θ(Pb)=0.09
Ea=50.339 kJ/mol
Ln J
y = -6054.7x + 20.053
R² = 0.983
1/T (K⁻¹)

(c).

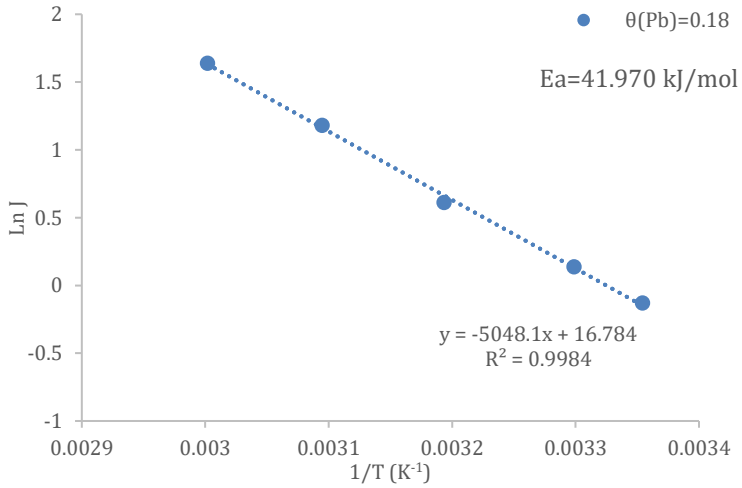
θ(Pb)=0.18
Ea=41.970 kJ/mol
Ln J
y = -5048.1x + 16.784
R² = 0.9984
1/T (K⁻¹)

(d).

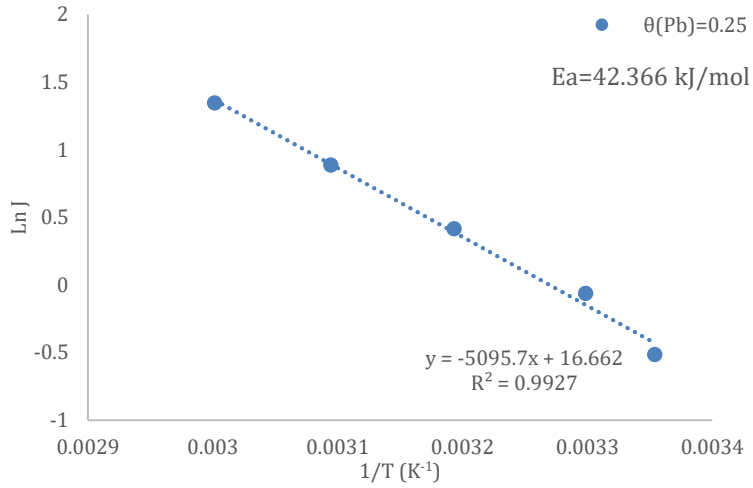
θ(Pb)=0.25
Ea=42.366 kJ/mol
y = -5095.7x + 16.662
R² = 0.9927
Ln J
1/T (K⁻¹)
2
1.5
1
0.5
0
-0.5
-1
0.0029
0.003
0.0031
0.0032
0.0033
0.0034

(e).

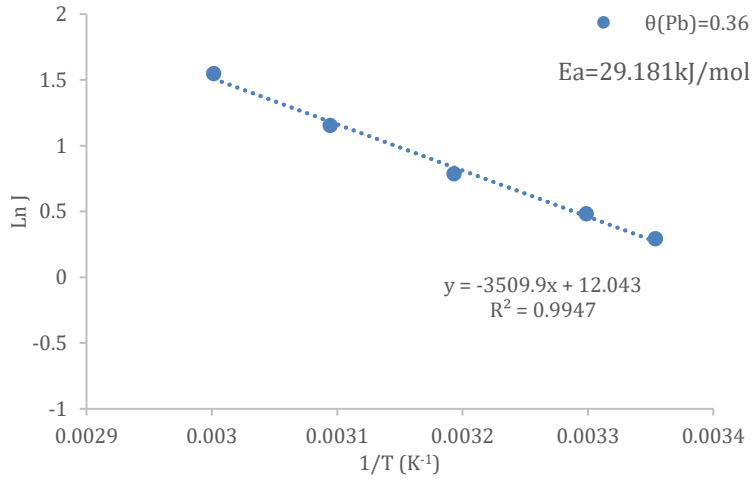
θ(Pb)=0.36
Ea=29.181kJ/mol
y = -3509.9x + 12.043
R² = 0.9947
Ln J
1/T (K⁻¹)
2
1.5
1
0.5
0
-0.5
-1
0.0029
0.003
0.0031
0.0032
0.0033
0.0034

(f).

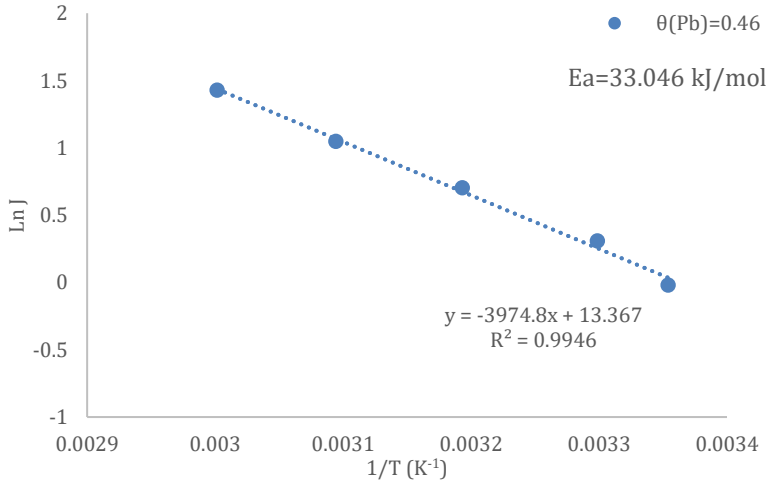
θ(Pb)=0.46
Ea=33.046 kJ/mol
y = -3974.8x + 13.367
R² = 0.9946
Ln J
1/T (K⁻¹)
2
1.5
1
0.5
0
-0.5
-1
0.0029
0.003
0.0031
0.0032
0.0033
0.0034

(g).

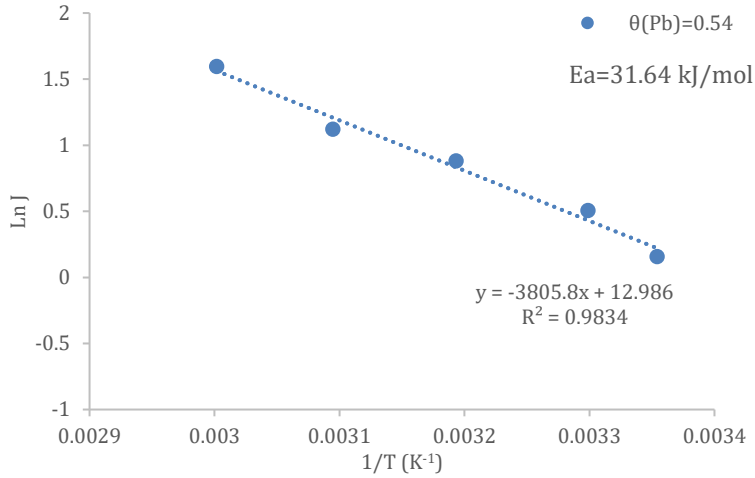

(h).

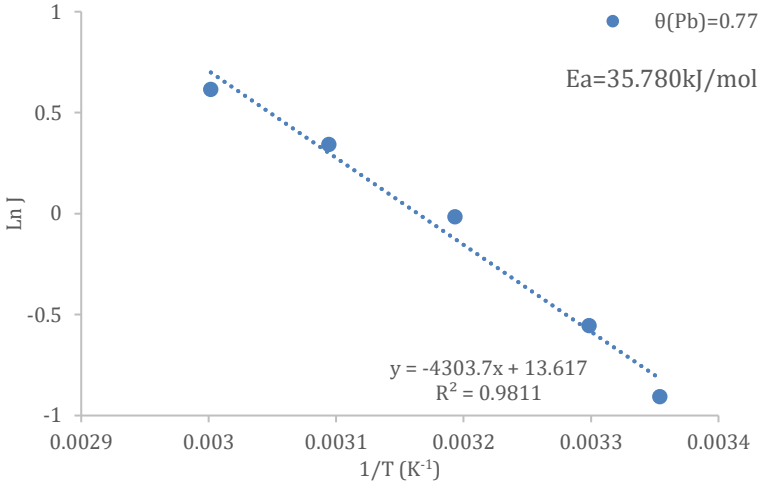

Figure A.4. 3. Arrhenius plots of the ethanol electrooxidation reaction (EOR) on the Pd with various Pb coverages: (a).$\theta_{Pb} = 0$, (b). $\theta_{Pb} = 0.09$, (c). $\theta_{Pb} = 0.18$, (d). $\theta_{Pb} = 0.25$, (e). $\theta_{Pb} = 0.36$, (f). $\theta_{Pb} = 0.46$, (g). $\theta_{Pb} = 0.54$, (h). $\theta_{Pb} = 0.77$, the data were obtained from current densities at peak potential on the anodic sweep for EOR at different temperatures in 0.1 M Ethanol + 0.1 M NaOH solution.

Chapter 5

(a).

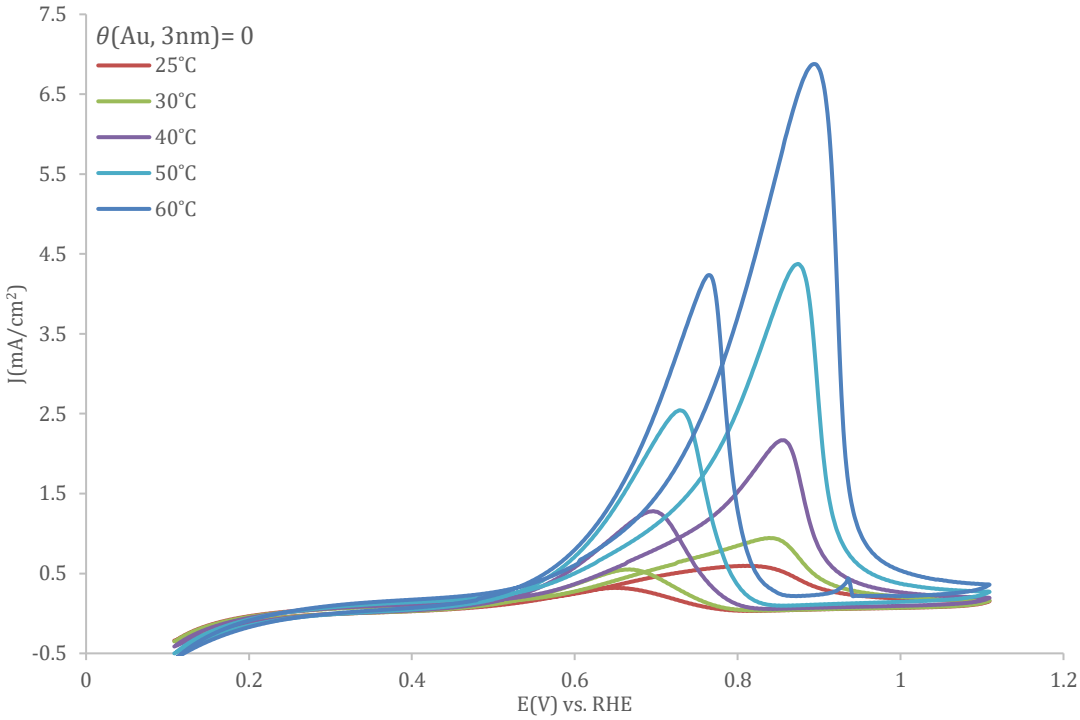
θ(Au, 3nm)= 0
25°C
30°C
40°C
50°C
60°C
J(mA/cm²)
E(V) vs. RHE
7.5
6.5
5.5
4.5
3.5
2.5
1.5
0.5
-0.5
0
0.2
0.4
0.6
0.8
1
1.2

(b).

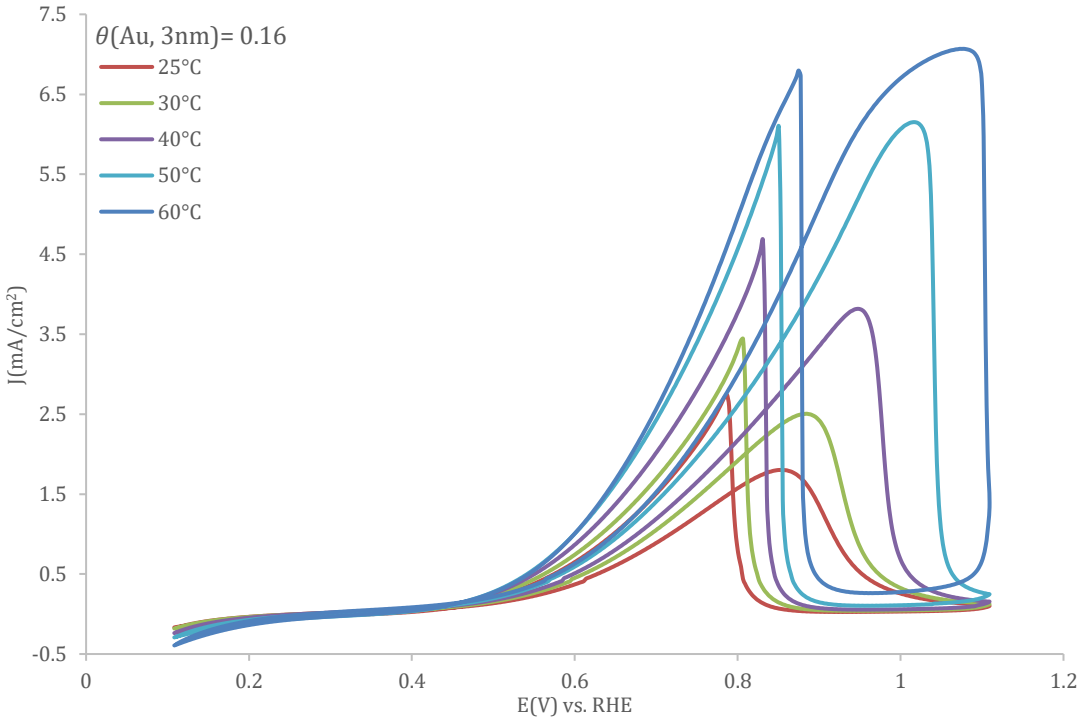
θ(Au, 3nm)= 0.16
25°C
30°C
40°C
50°C
60°C
J(mA/cm²)
E(V) vs. RHE
7.5
6.5
5.5
4.5
3.5
2.5
1.5
0.5
-0.5
0
0.2
0.4
0.6
0.8
1
1.2

(c).

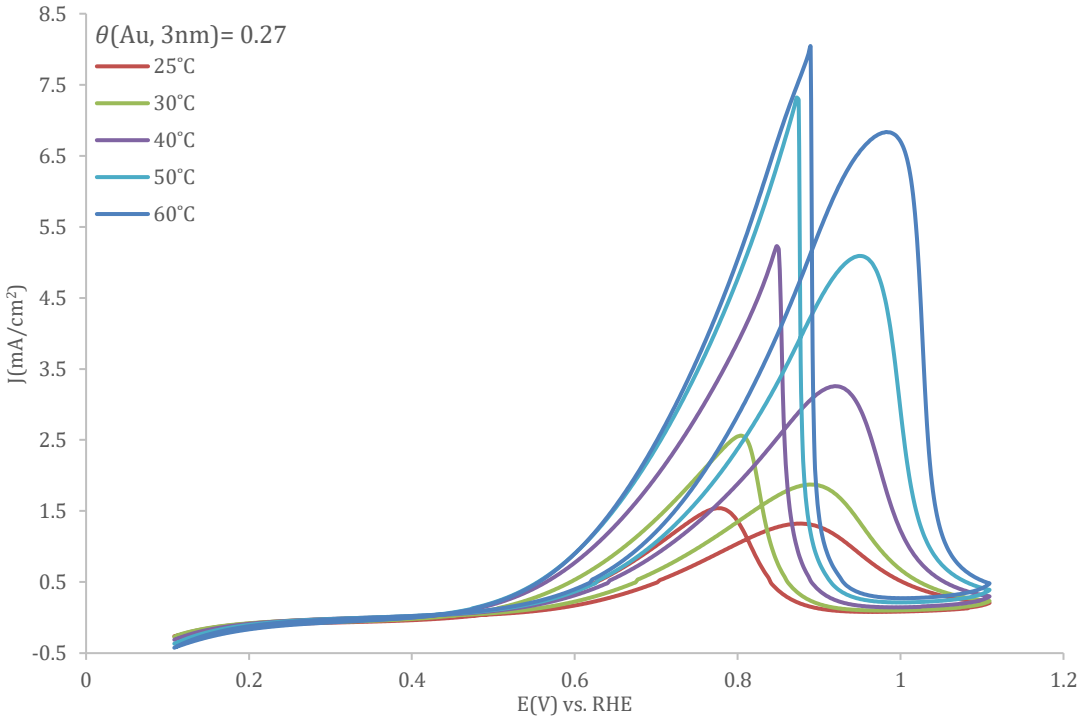
θ(Au, 3nm)= 0.27
25°C
30°C
40°C
50°C
60°C
J(mA/cm²)
E(V) vs. RHE
8.5
7.5
6.5
5.5
4.5
3.5
2.5
1.5
0.5
-0.5
0
0.2
0.4
0.6
0.8
1
1.2

(d).

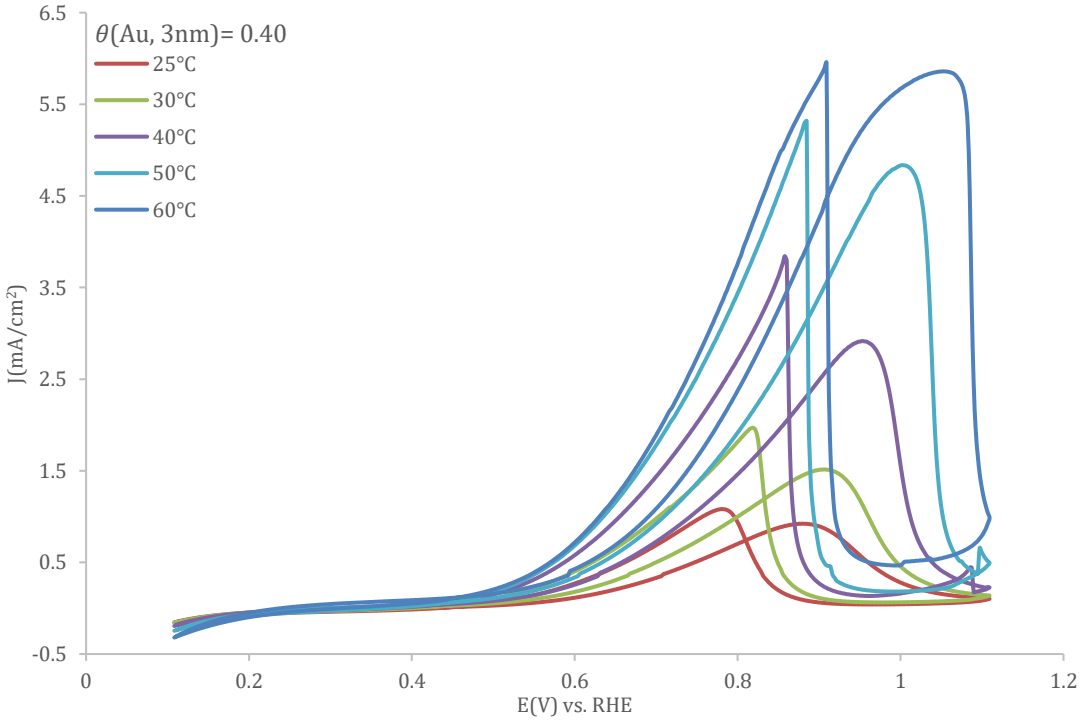
θ(Au, 3nm)= 0.40
25°C
30°C
40°C
50°C
60°C
J(mA/cm²)
E(V) vs. RHE
6.5
5.5
4.5
3.5
2.5
1.5
0.5
-0.5
0
0.2
0.4
0.6
0.8
1
1.2

(e).

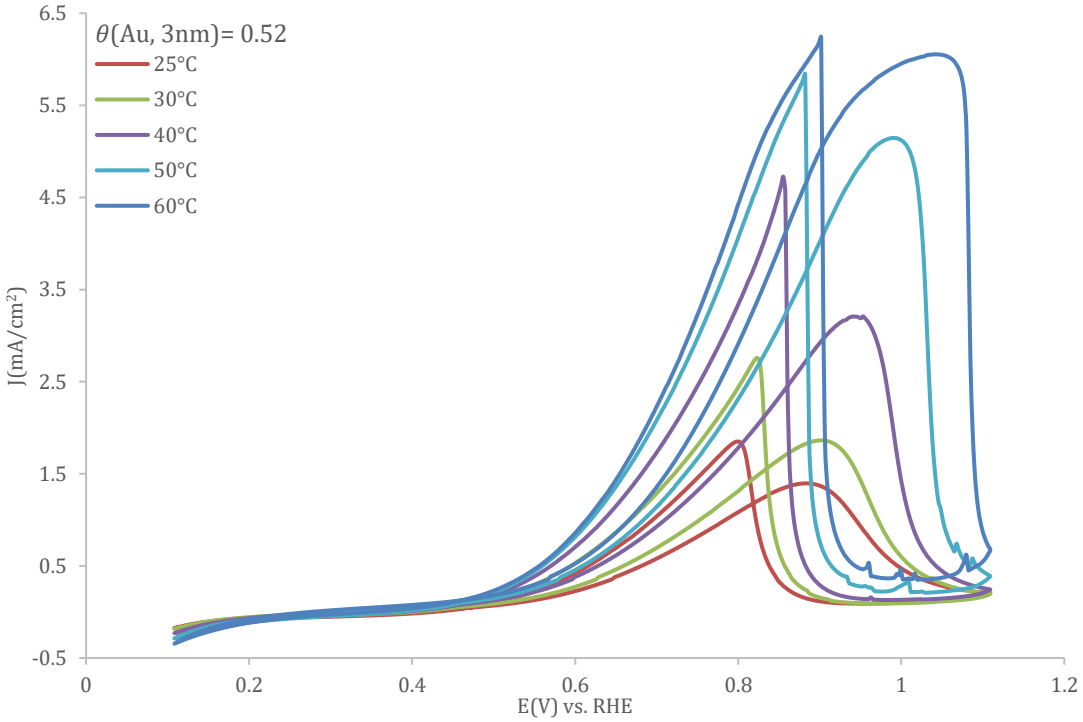
θ(Au, 3nm)= 0.52
25°C
30°C
40°C
50°C
60°C
J(mA/cm²)
E(V) vs. RHE
6.5
5.5
4.5
3.5
2.5
1.5
0.5
-0.5
0
0.2
0.4
0.6
0.8
1
1.2

(f).

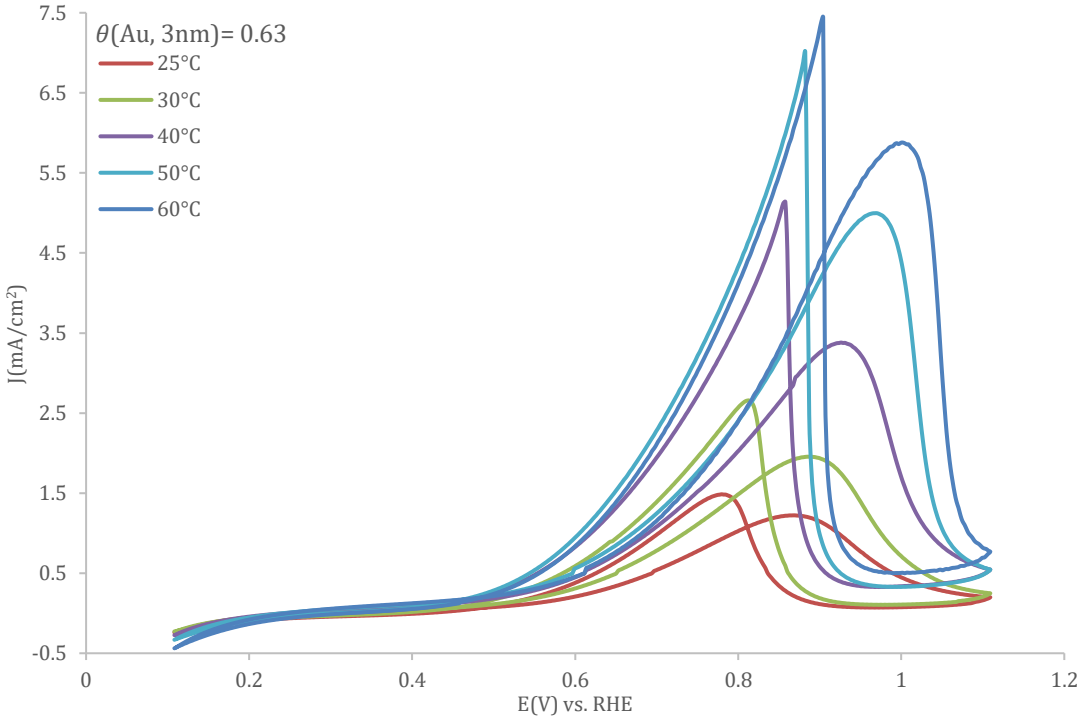
θ(Au, 3nm)= 0.63
25°C
30°C
40°C
50°C
60°C
J(mA/cm²)
E(V) vs. RHE
7.5
6.5
5.5
4.5
3.5
2.5
1.5
0.5
-0.5
0
0.2
0.4
0.6
0.8
1
1.2

A.5.1. Cyclic voltammograms of Au_{3nm}/PEDOT:PSS-decorated Pd electrodes with different Au_{3nm} coverage: (a). $\theta_{Au,3nm} = 0$, (b). $\theta_{Au,3nm} = 0.16$, (c). $\theta_{Au,3nm} = 0.27$, (d). $\theta_{Au,3nm} = 0.40$, (e). $\theta_{Au,3nm} = 0.52$, (f). $\theta_{Au,3nm} = 0.63$ toward ethanol electrooxidation at different temperatures from 0.11 V to 1.11 V (vs. RHE) in 0.1 M Ethanol + 0.1 M NaOH solution. Scan rate: 50 mVs^{-1}

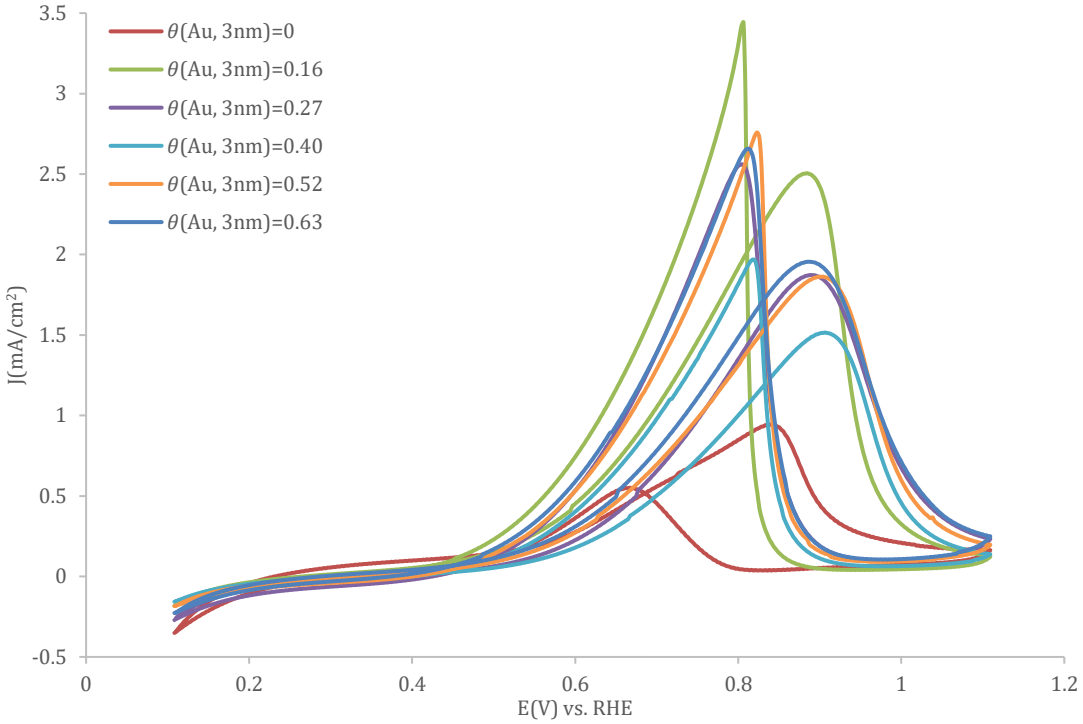

A.5.2. Cyclic voltammograms of Au_{3nm}/PEDOT:PSS-decorated Pd electrodes with different Au_{3nm} coverages towards ethanol electrooxidation from 0.11 V to 1.11 V (vs. RHE) at 30 ˚C in 0.1 M Ethanol + 0.1 M NaOH solution. Scan rate: 50 mVS^{-1}.

(a).

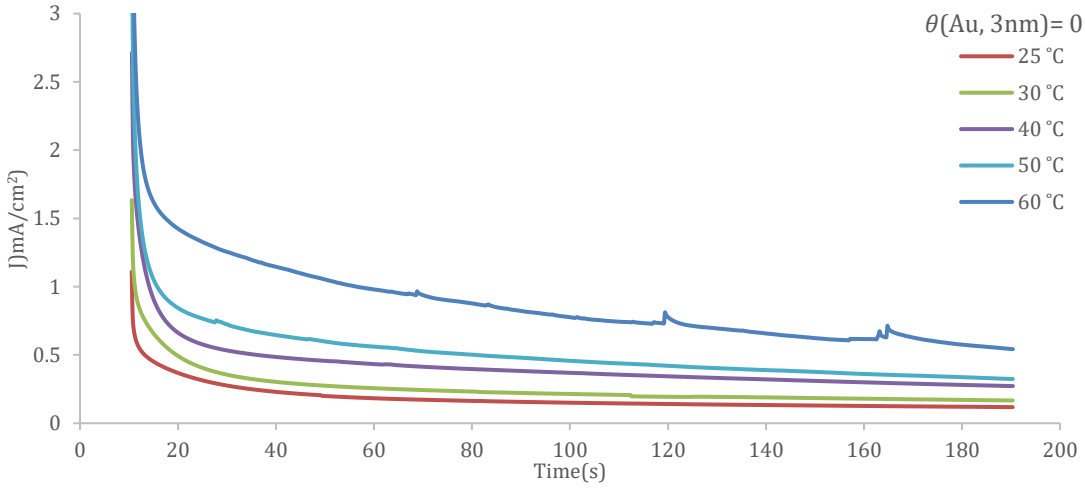
θ(Au, 3nm)= 0
25 ℃
30 ℃
40 ℃
50 ℃
60 ℃
JmA/cm²)
Time(s)

(b).

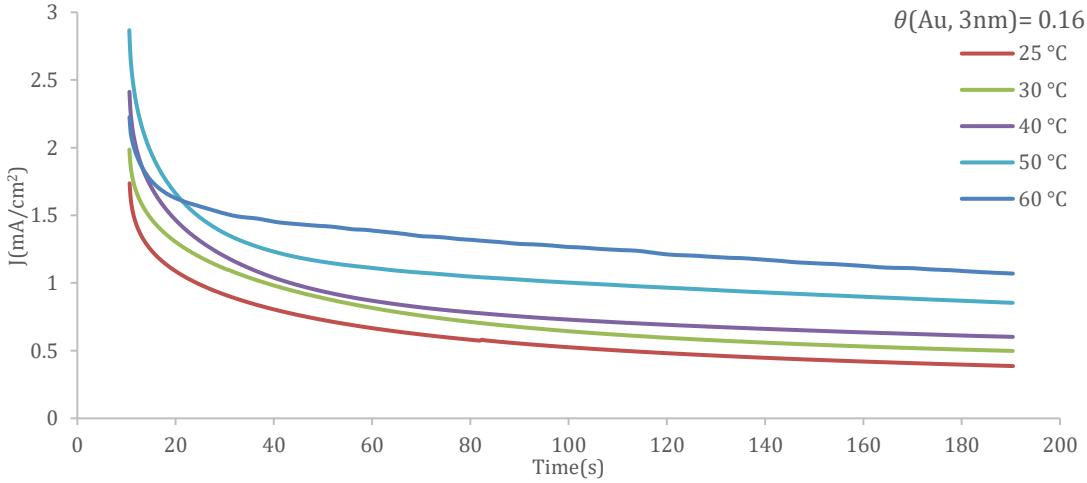
θ(Au, 3nm)= 0.16
25 ℃
30 ℃
40 ℃
50 ℃
60 ℃
J(mA/cm²)
Time(s)

(c).

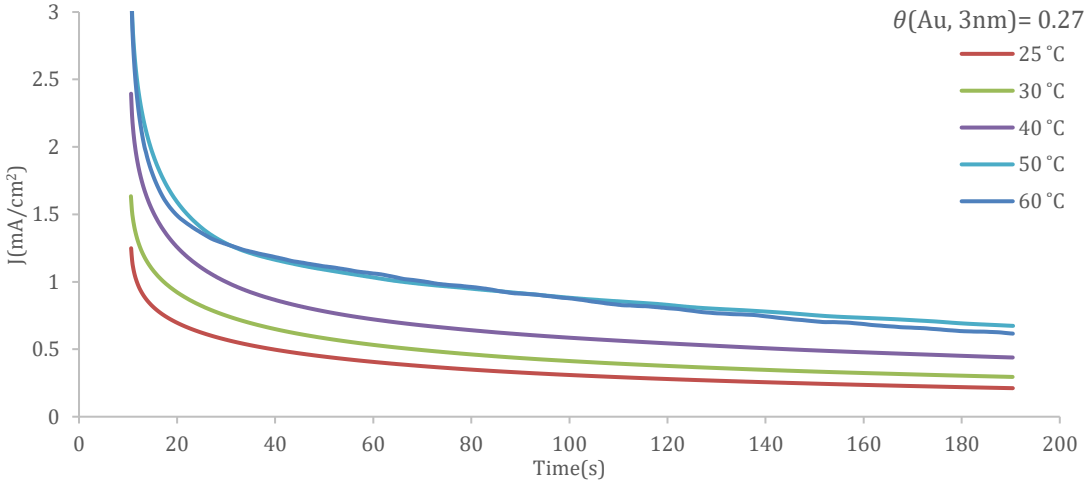
θ(Au, 3nm)= 0.27
25 ℃
30 ℃
40 ℃
50 ℃
60 ℃
J(mA/cm²)
Time(s)

(d).

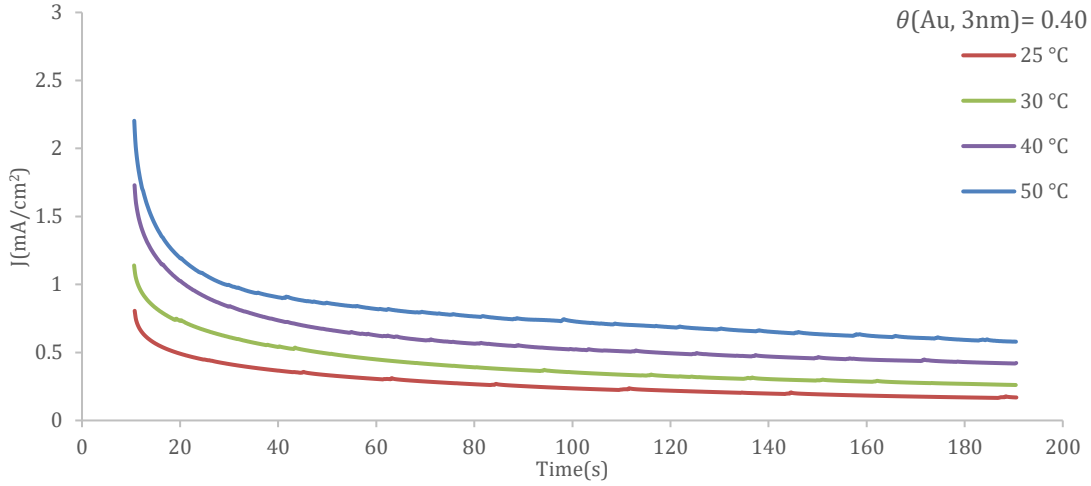

(e).

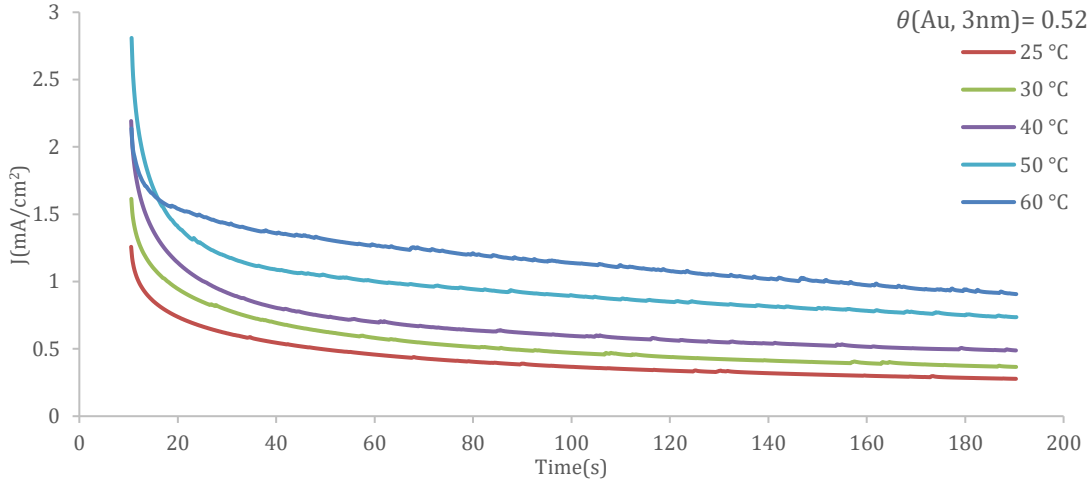

(f).

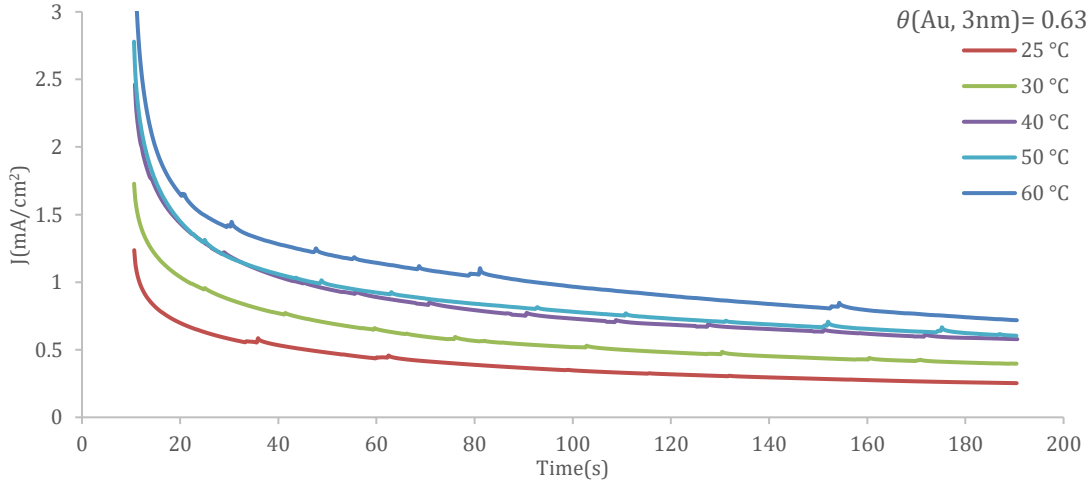

A.5.3. Chronoamperometric curves of Au_{3nm}/PEDOT:PSS-decorated Pd electrodes with different Au_{3nm} coverages: (a). $\theta_{Au,3nm} = 0$, (b). $\theta_{Au,3nm} = 0.16$, (c).

$\theta_{Au,3nm} = 0.27$, (d). $\theta_{Au,3nm} = 0.40$, (e). $\theta_{Au,3nm} = 0.52$, (f). $\theta_{Au,3nm} = 0.63$ toward ethanol electrooxidation at the potential of 0.71 V (vs. RHE) from 25 to 60 ˚C in 0.1 M Ethanol + 0.1 M NaOH solution. Scan rate: 50 mVs^{-1}.

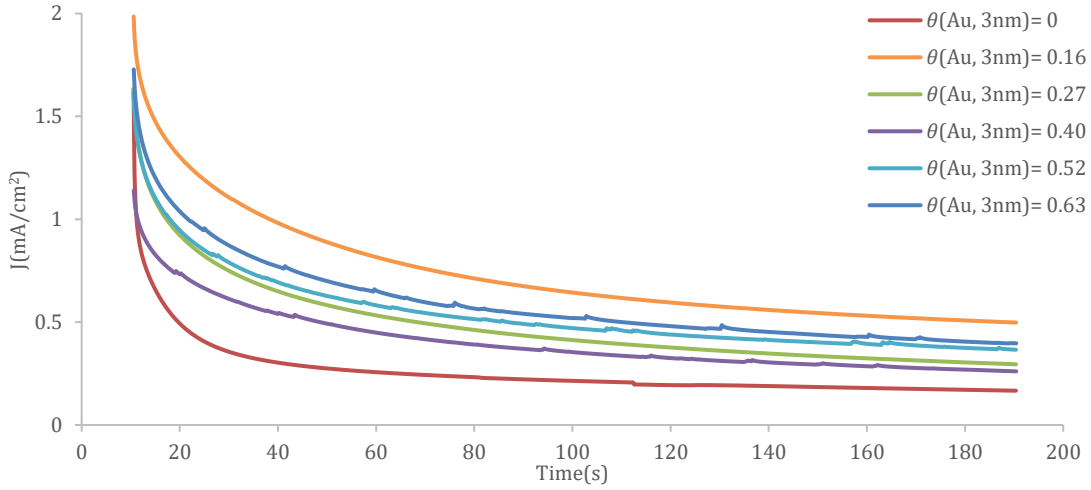

A.5.4. Chronoamperometric curves of Au_{3nm}-decorated Pd electrodes with different Au_{3nm} coverages towards ethanol electrooxidation at the potential of 0.71 V (vs. RHE) at 30˚C in 0.1 M Ethanol + 0.1 M NaOH solution. Scan rate: 50 mVs^{-1}.

(a).

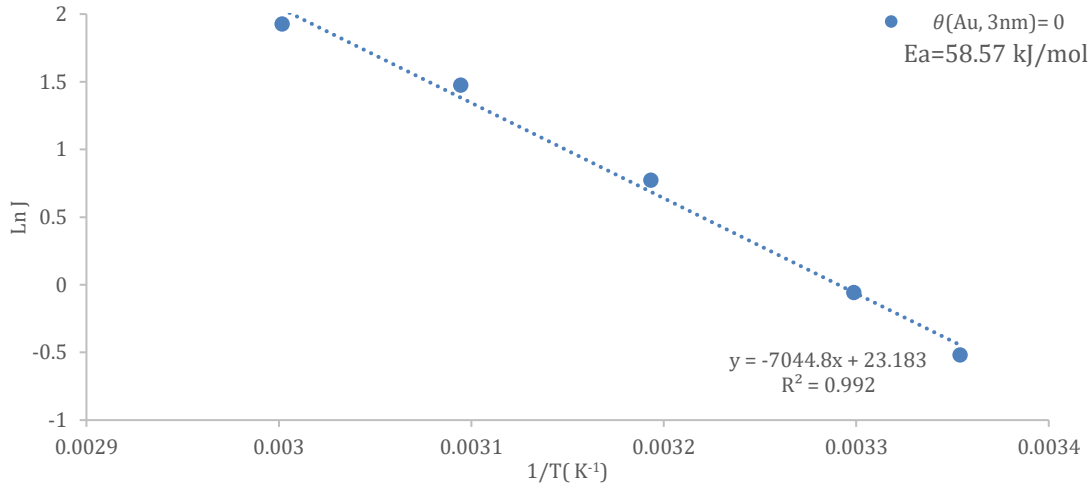
θ(Au, 3nm)= 0
Ea=58.57 kJ/mol
y = -7044.8x + 23.183
R² = 0.992
Ln J
1/T(K⁻¹)
2
1.5
1
0.5
0
-0.5
-1
0.0029
0.003
0.0031
0.0032
0.0033
0.0034

(b).

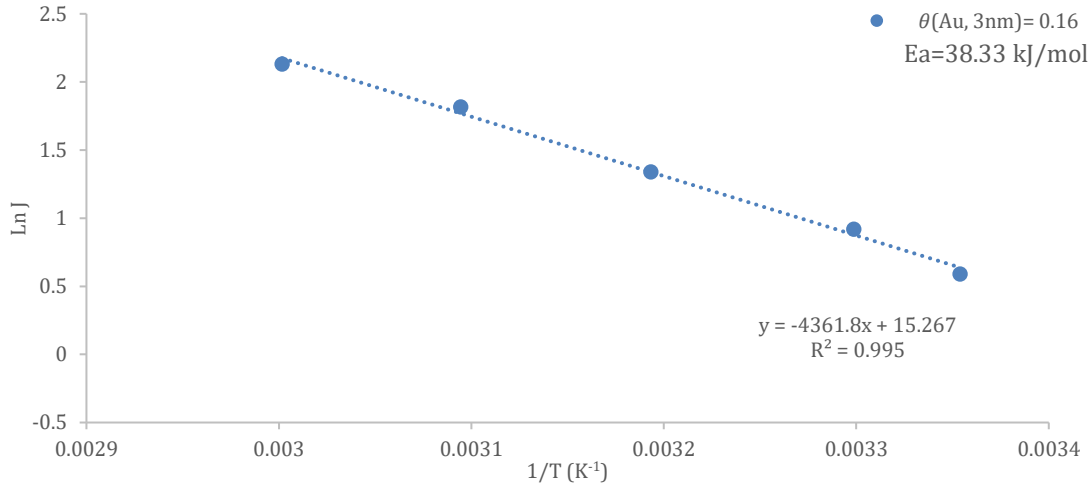
θ(Au, 3nm)= 0.16
Ea=38.33 kJ/mol
y = -4361.8x + 15.267
R² = 0.995
Ln J
1/T (K⁻¹)
2.5
2
1.5
1
0.5
0
-0.5
0.0029
0.003
0.0031
0.0032
0.0033
0.0034

(c).

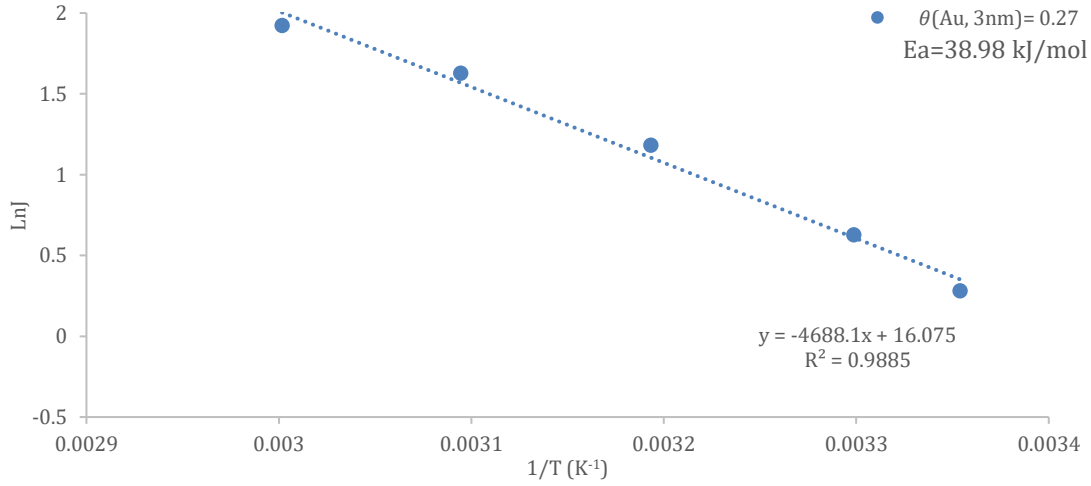
θ(Au, 3nm)= 0.27
Ea=38.98 kJ/mol
y = -4688.1x + 16.075
R² = 0.9885
LnJ
1/T (K⁻¹)
2
1.5
1
0.5
0
-0.5
0.0029
0.003
0.0031
0.0032
0.0033
0.0034

(d).

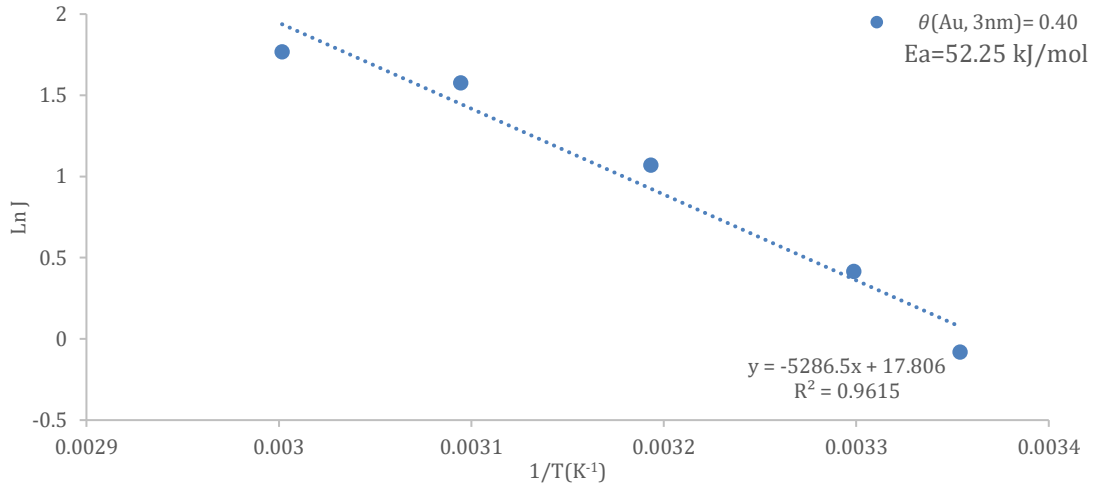

(e).

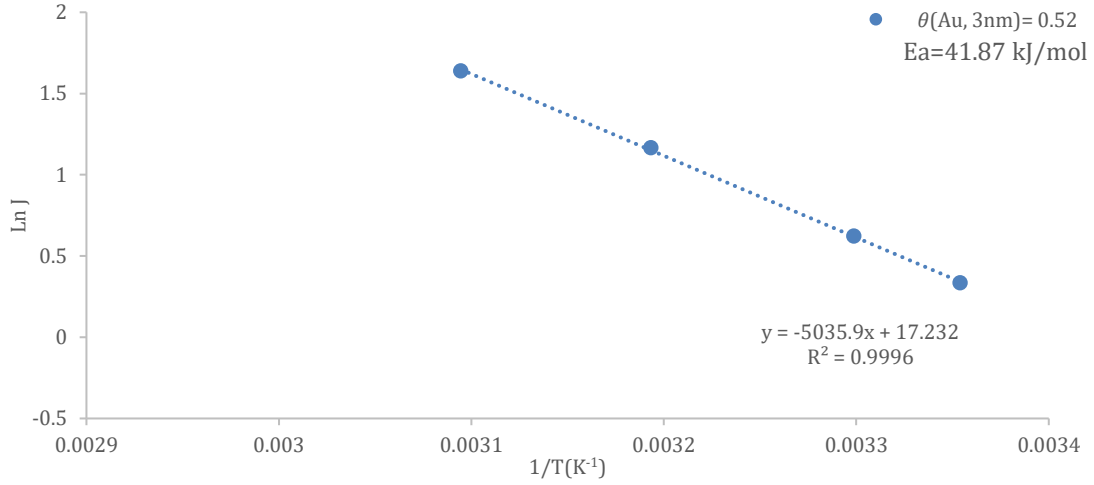

(f).

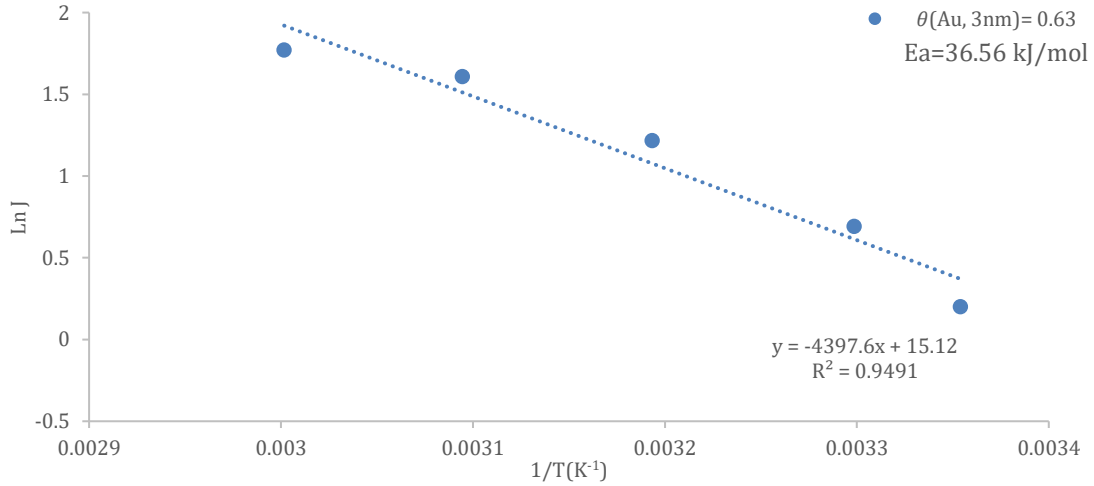

A.5. 5. Arrhenius plots of the ethanol electrooxidation reaction (EOR) on the Pd with various Au_{3nm}/PEDOT:PSS coverages: (a). $\theta_{Au,3nm} = 0$, (b). $\theta_{Au,3nm} = 0.16$, (c).

$\boldsymbol{\theta_{Au,3nm} = 0.27}$, ***(d).*** $\boldsymbol{\theta_{Au,3nm} = 0.40}$, ***(e).*** $\boldsymbol{\theta_{Au,3nm} = 0.52}$, ***(f).*** $\boldsymbol{\theta_{Au,3nm} = 0.63}$, ***the data were obtained from current densities at peak potential on the anodic sweep for EOR at different temperatures in 0.1 M Ethanol + 0.1 M NaOH solution.***

(a).

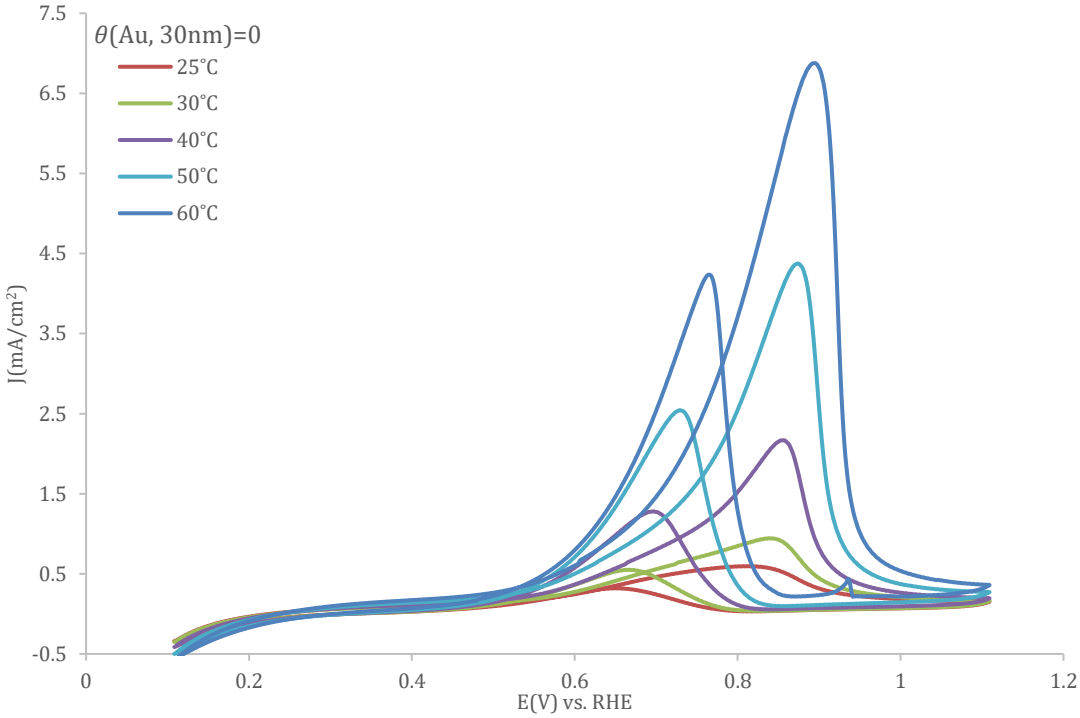
θ(Au, 30nm)=0
25°C
30°C
40°C
50°C
60°C
J(mA/cm²)
E(V) vs. RHE
7.5
6.5
5.5
4.5
3.5
2.5
1.5
0.5
-0.5
0
0.2
0.4
0.6
0.8
1
1.2

(b).

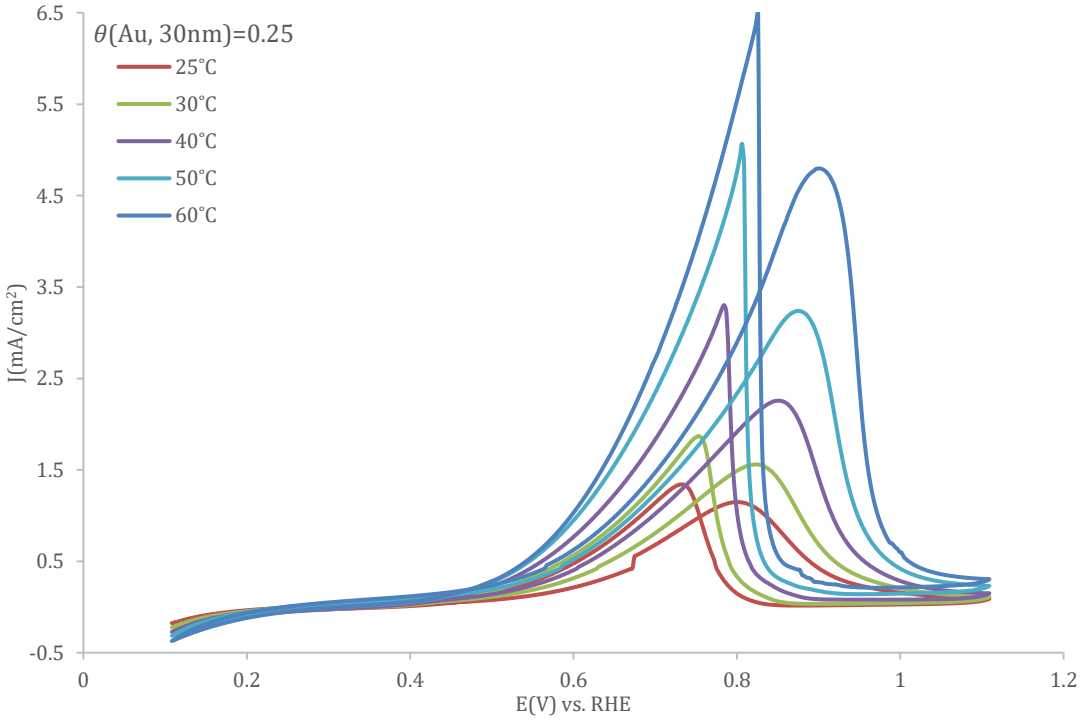
θ(Au, 30nm)=0.25
25°C
30°C
40°C
50°C
60°C
J(mA/cm²)
E(V) vs. RHE
6.5
5.5
4.5
3.5
2.5
1.5
0.5
-0.5
0
0.2
0.4
0.6
0.8
1
1.2

(c).

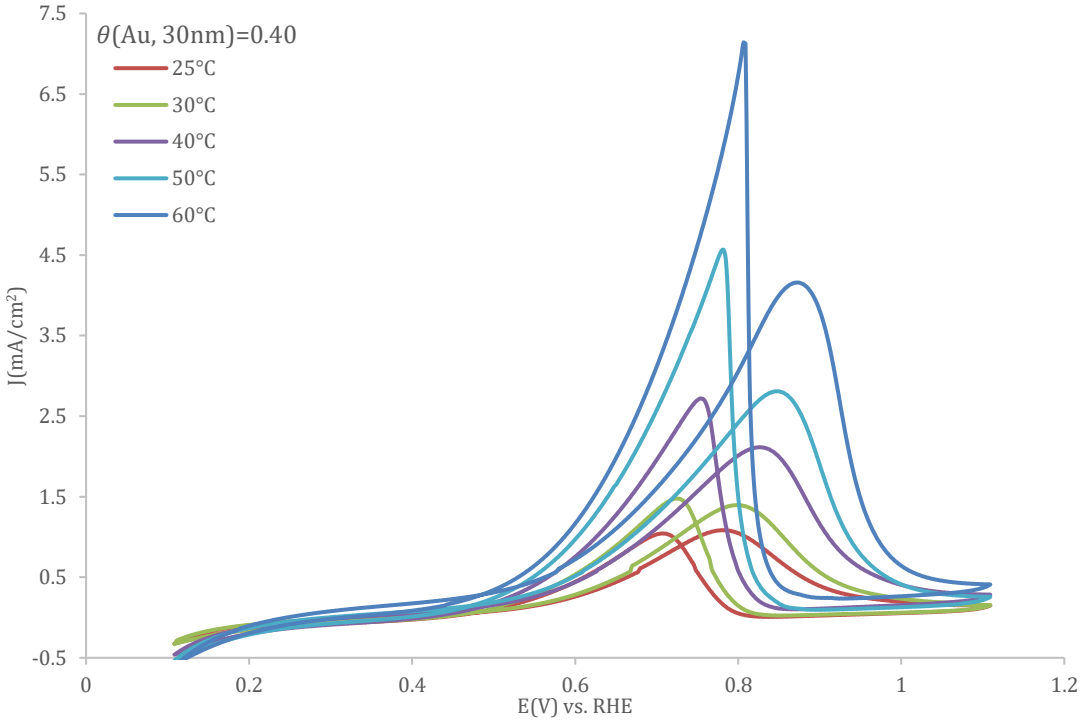
θ(Au, 30nm)=0.40
25°C
30°C
40°C
50°C
60°C
J(mA/cm²)
E(V) vs. RHE
7.5
6.5
5.5
4.5
3.5
2.5
1.5
0.5
-0.5
0
0.2
0.4
0.6
0.8
1
1.2

(d).

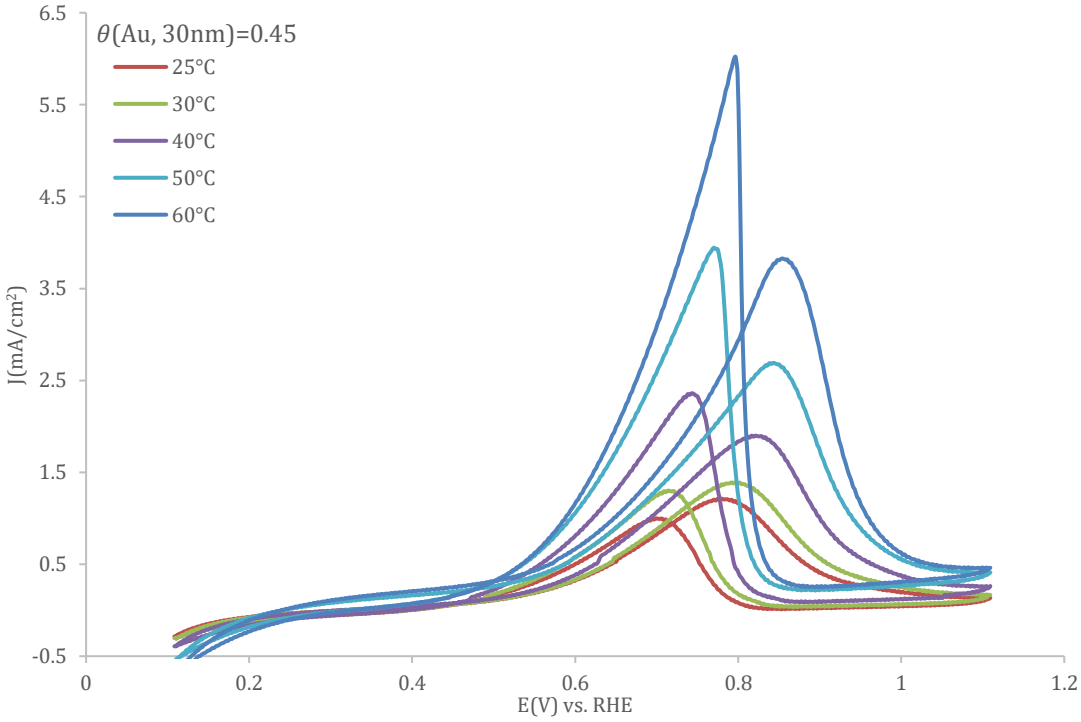
θ(Au, 30nm)=0.45
25°C
30°C
40°C
50°C
60°C
J(mA/cm²)
E(V) vs. RHE
6.5
5.5
4.5
3.5
2.5
1.5
0.5
-0.5
0
0.2
0.4
0.6
0.8
1
1.2

(e).

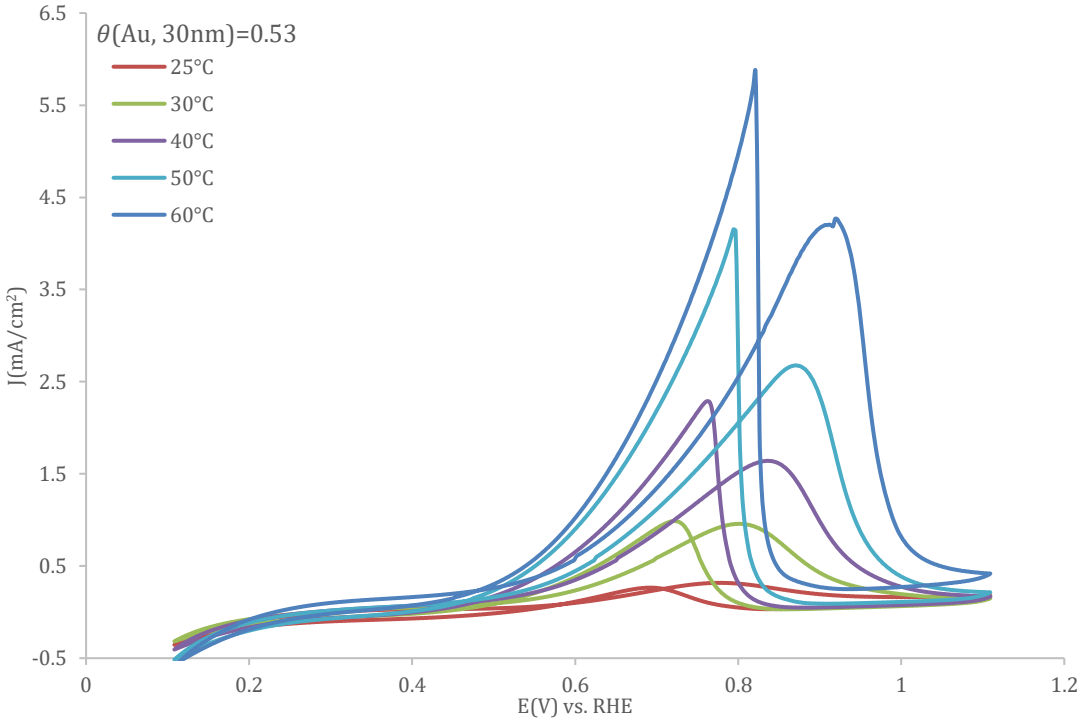

A.5. 6. Cyclic voltammograms of Au_{30nm}/PEDOT:PSS-decorated Pd electrodes with different Au_{30nm} coverages: (a). $\theta_{Au,30nm} = 0$, (b). $\theta_{Au,30nm} = 0.25$, (c). $\theta_{Au,30nm} = 0.40$, (d). $\theta_{Au,30nm} = 0.45$, (e). $\theta_{Au,30nm} = 0.53$ toward ethanol electrooxidation at different temperatures from 0.11 V to 1.11 V (vs. RHE) in 0.1 M Ethanol + 0.1 M NaOH solution. Scan rate: 50 mVs^{-1}.

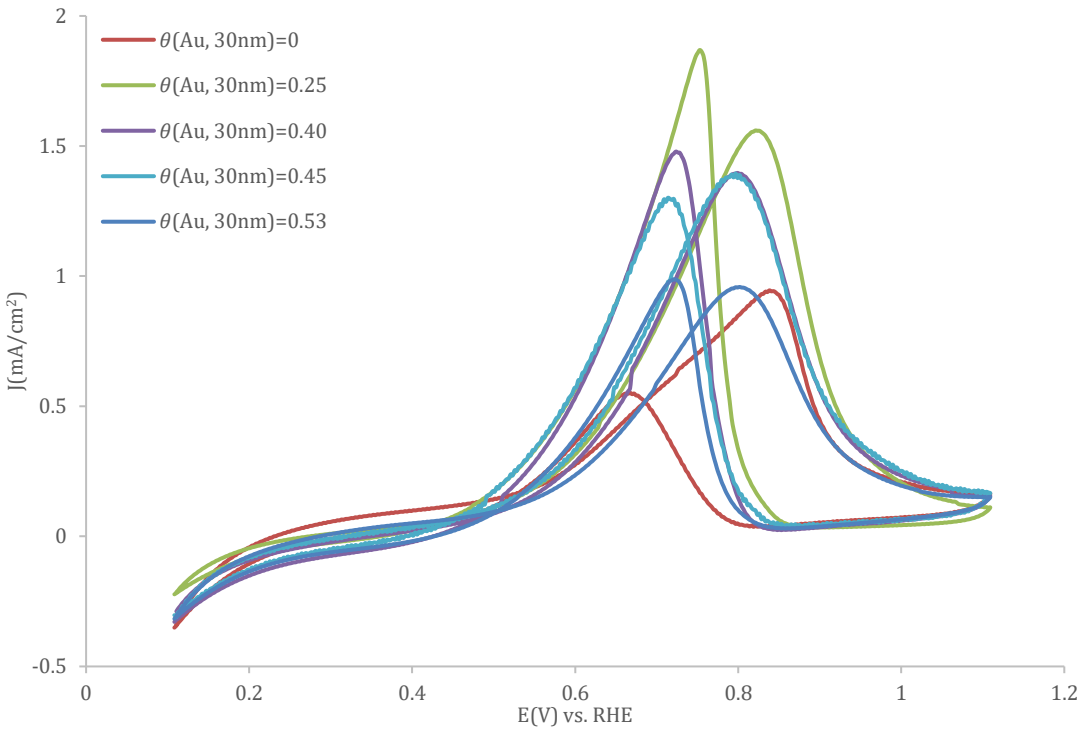

A.5. 7. Cyclic voltammograms of Au_{30nm}/PEDOT:PSS-decorated Pd electrodes with different Au_{30nm}/PEDOT:PSS coverages towards ethanol electrooxidation from 0.11 V to 1.11 V (vs. RHE) at 30 ˚C in 0.1 M Ethanol + 0.1 M NaOH solution. Scan rate: 50 mVs^{-1}.

(a).

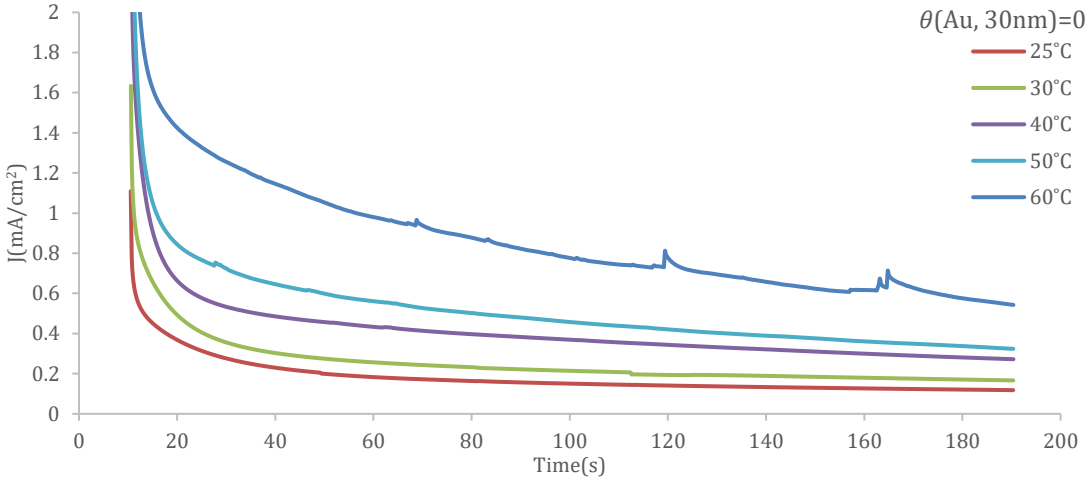
θ(Au, 30nm)=0
25°C
30°C
40°C
50°C
60°C
J(mA/cm²)
Time(s)

(b).

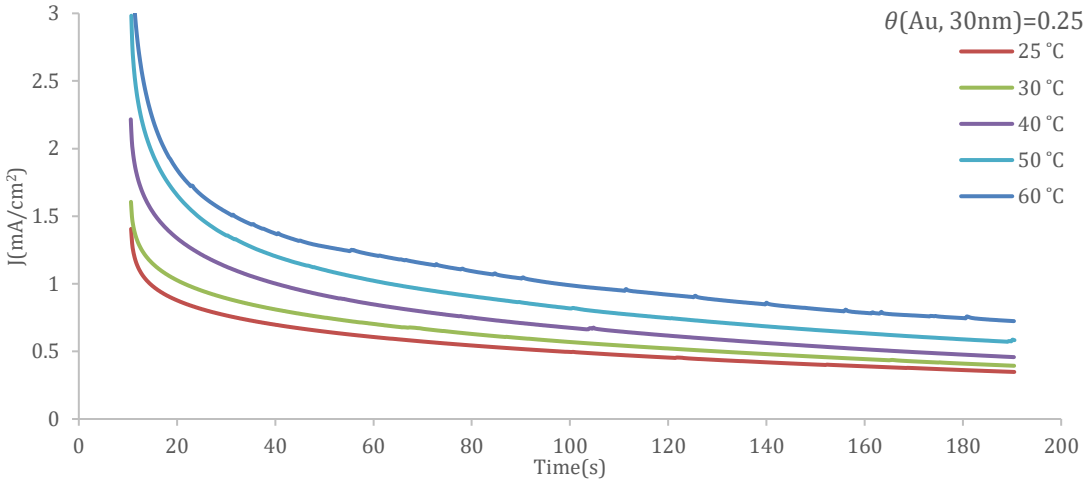
θ(Au, 30nm)=0.25
25 °C
30 °C
40 °C
50 °C
60 °C
J(mA/cm²)
Time(s)

(c).

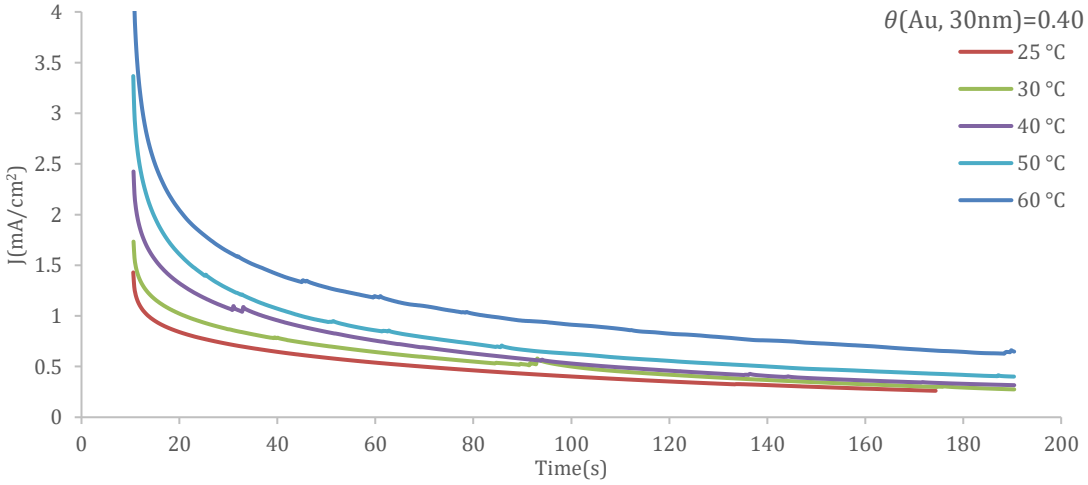
θ(Au, 30nm)=0.40
25 °C
30 °C
40 °C
50 °C
60 °C
J(mA/cm²)
Time(s)

(d).

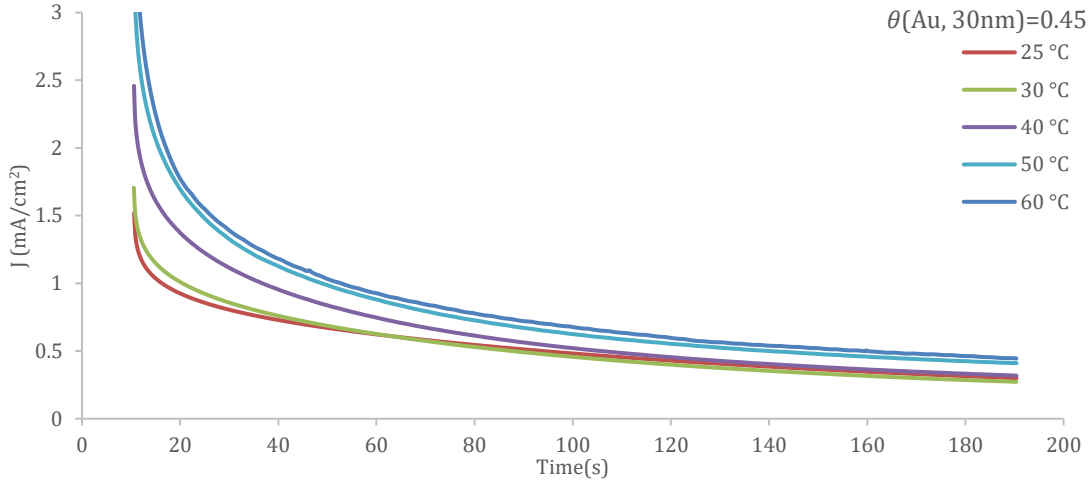

(e).

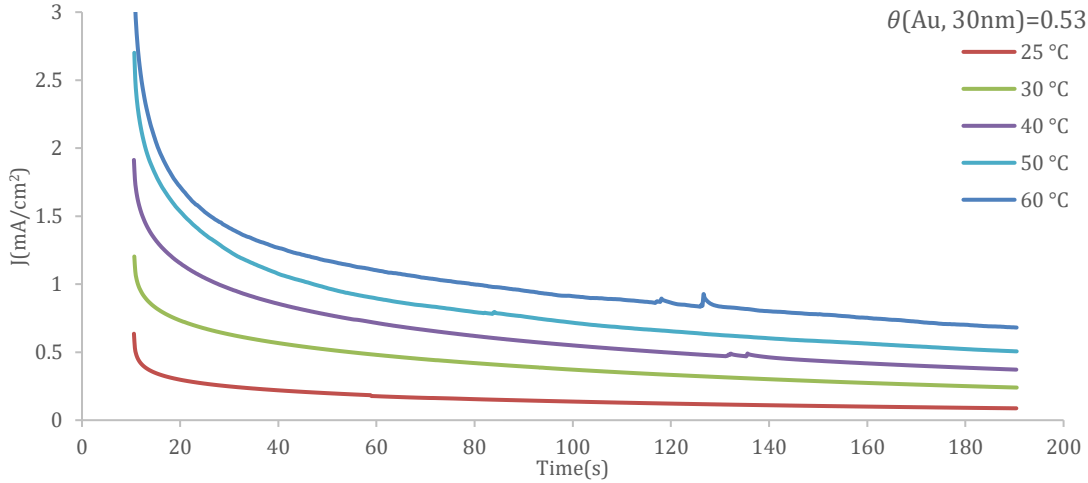

A.5. 8. Chronoamperometric curves of Au_{30nm}/PEDOT:PSS-decorated Pd electrodes with different Au_{30nm} coverages: (a). $\theta_{Au,30nm} = 0$, (b). $\theta_{Au,30nm} = 0.25$, (c). $\theta_{Au,30nm} = 0.40$, (d). $\theta_{Au,30nm} = 0.45$, (e). $\theta_{Au,30nm} = 0.53$ toward ethanol electrooxidation at the potential of 0.71 V (vs. RHE) from 25 to 60 ℃ in 0.1 M Ethanol + 0.1 M NaOH solution. Scan rate: 50 mVs^{-1}.

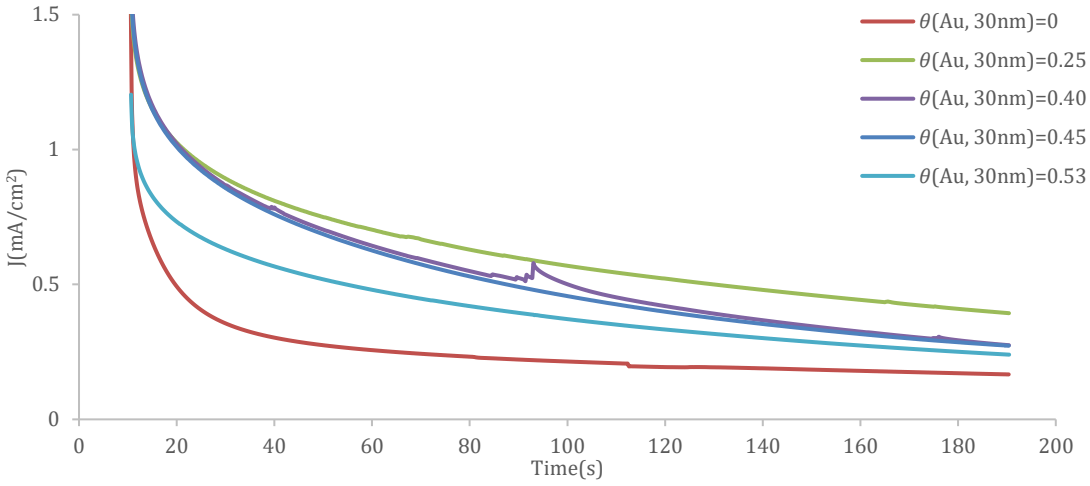

A.5. 9. Chronoamperometric curves of Au_{30nm}/PEDOT:PSS-decorated Pd electrodes with different Au_{30nm} coverages toward ethanol electrooxidation at the potential of 0.71 V (vs. RHE) at 30 ˚C in 0.1 M Ethanol + 0.1 M NaOH solution. Scan rate: 50 mVs^{-1}.

(a).

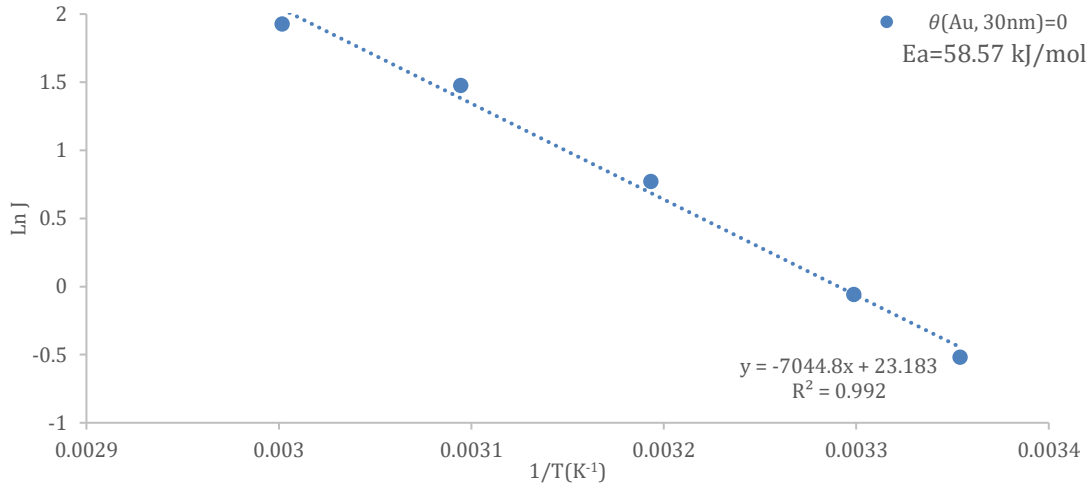
θ(Au, 30nm)=0
Ea=58.57 kJ/mol
y = -7044.8x + 23.183
R² = 0.992
Ln J
1/T(K⁻¹)
2
1.5
1
0.5
0
-0.5
-1
0.0029
0.003
0.0031
0.0032
0.0033
0.0034

(b).

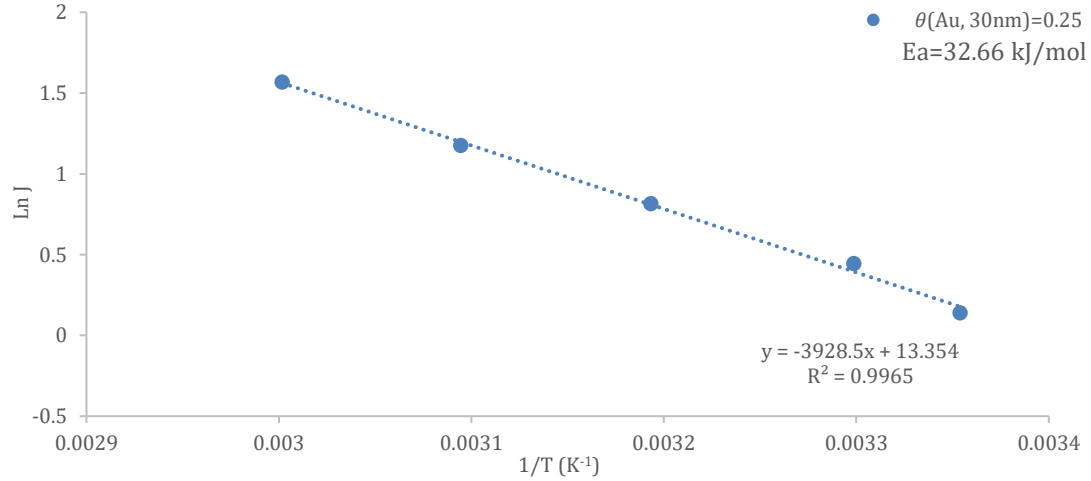
θ(Au, 30nm)=0.25
Ea=32.66 kJ/mol
y = -3928.5x + 13.354
R² = 0.9965
Ln J
1/T (K⁻¹)
2
1.5
1
0.5
0
-0.5
0.0029
0.003
0.0031
0.0032
0.0033
0.0034

(c).

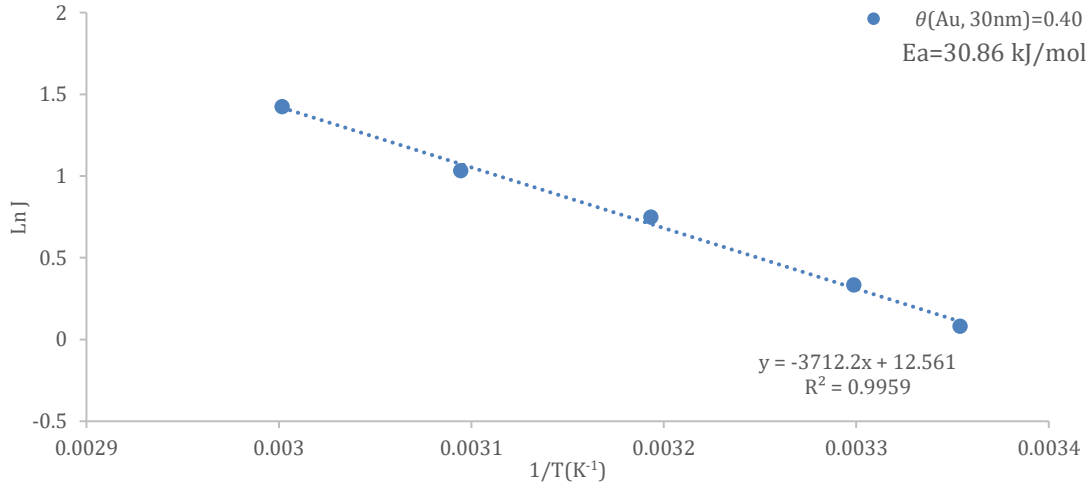
θ(Au, 30nm)=0.40
Ea=30.86 kJ/mol
y = -3712.2x + 12.561
R² = 0.9959
Ln J
1/T(K⁻¹)
2
1.5
1
0.5
0
-0.5
0.0029
0.003
0.0031
0.0032
0.0033
0.0034

(d).

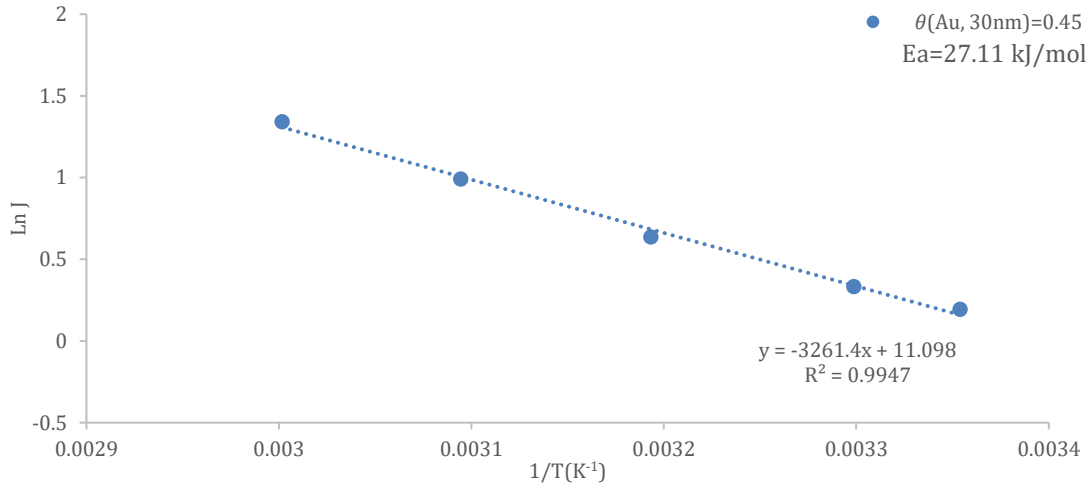

(e).

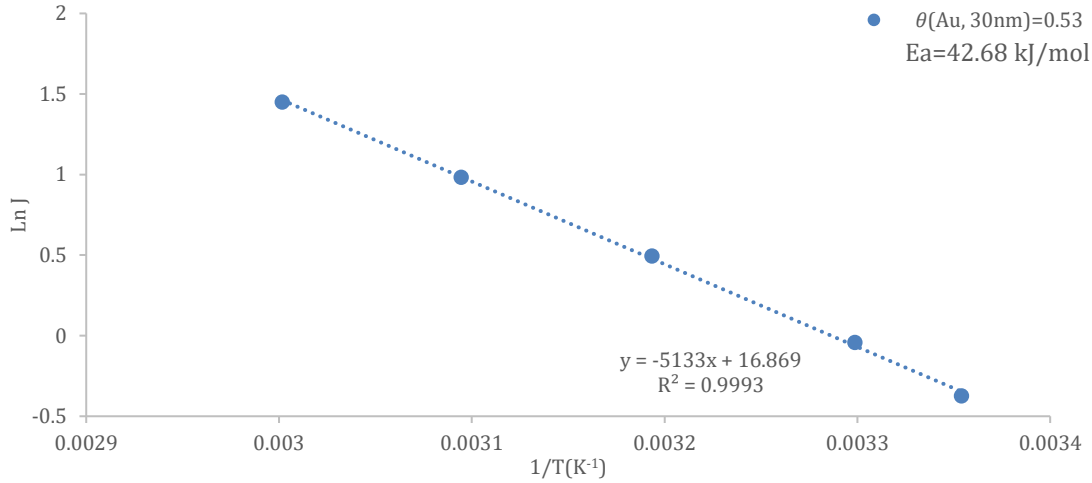

A.5.10. Arrhenius plots of the ethanol electrooxidation reaction (EOR) on the Pd with various Au_{30nm}/PEDOT:PSS coverages: (a). $\theta_{Au,30nm} = 0$, (b). $\theta_{Au,30nm} = 0.25$, (c). $\theta_{Au,30nm} = 0.40$, (d). $\theta_{Au,30nm} = 0.45$, (e). $\theta_{Au,30nm} = 0.53$, the data were obtained from current densities at peak potential on the anodic sweep for EOR at different temperatures in 0.1 M Ethanol+0.1 M NaOH solution.

Chapter 6

(a).

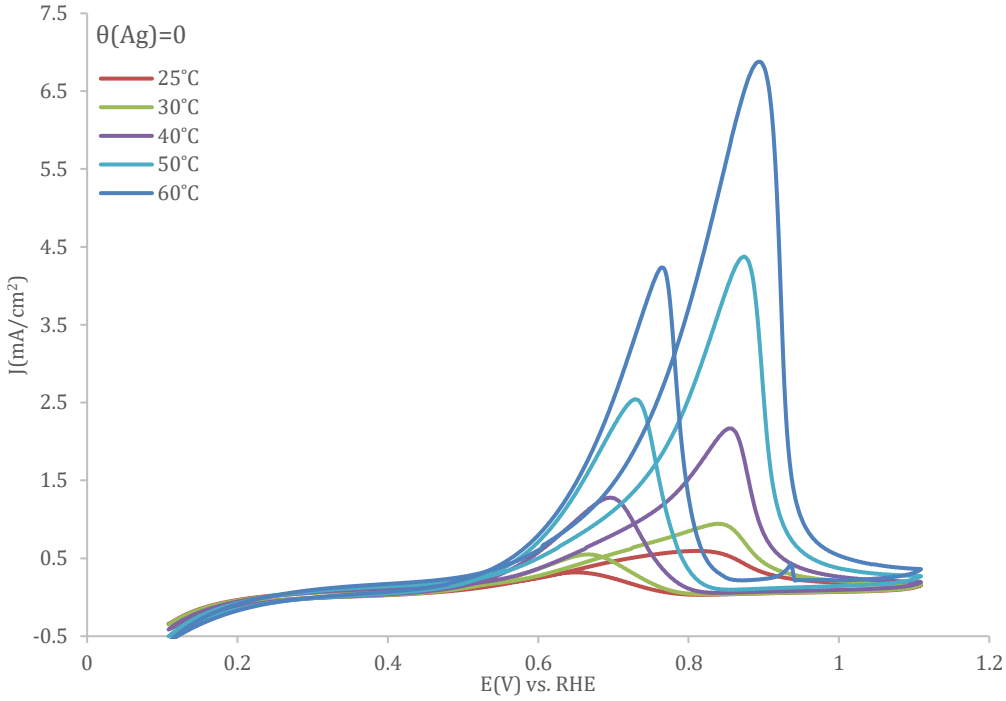
θ(Ag)=0
25°C
30°C
40°C
50°C
60°C
J(mA/cm²)
E(V) vs. RHE
7.5
6.5
5.5
4.5
3.5
2.5
1.5
0.5
-0.5
0
0.2
0.4
0.6
0.8
1
1.2

(b).

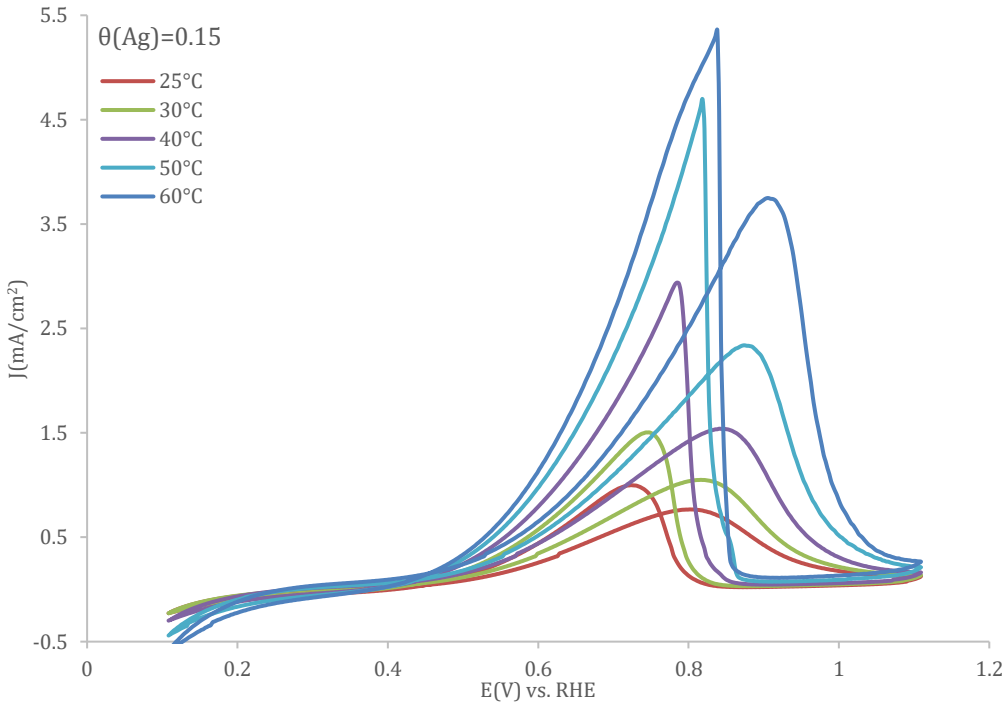
θ(Ag)=0.15
25°C
30°C
40°C
50°C
60°C
J(mA/cm²)
E(V) vs. RHE
5.5
4.5
3.5
2.5
1.5
0.5
-0.5
0
0.2
0.4
0.6
0.8
1
1.2

(c).

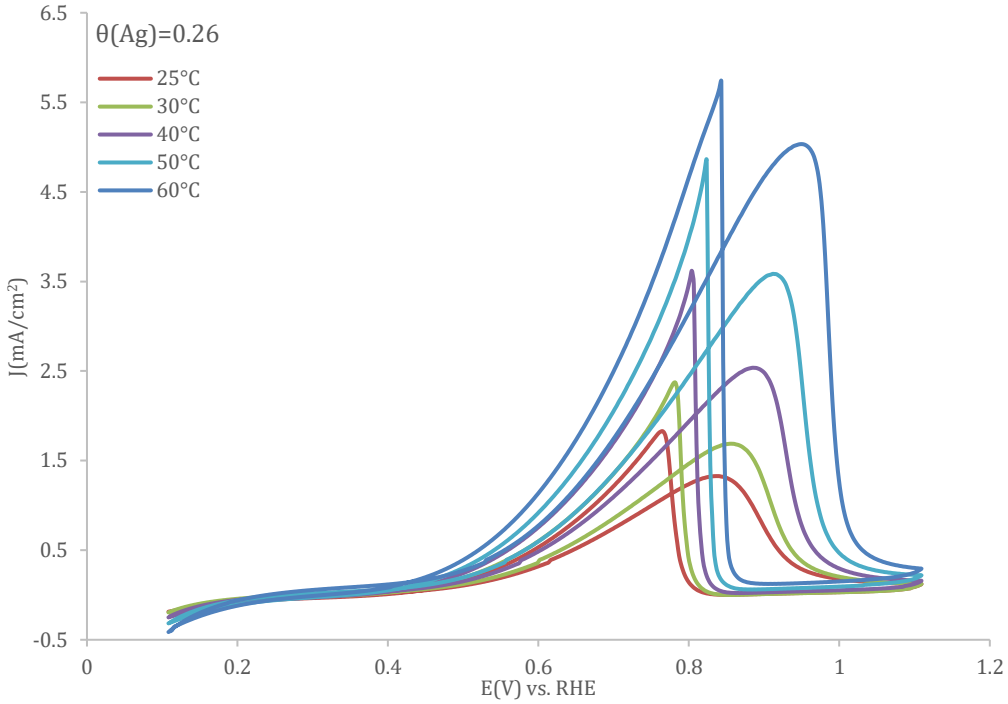
θ(Ag)=0.26
25°C
30°C
40°C
50°C
60°C
J(mA/cm²)
E(V) vs. RHE
6.5
5.5
4.5
3.5
2.5
1.5
0.5
-0.5
0
0.2
0.4
0.6
0.8
1
1.2

(d).

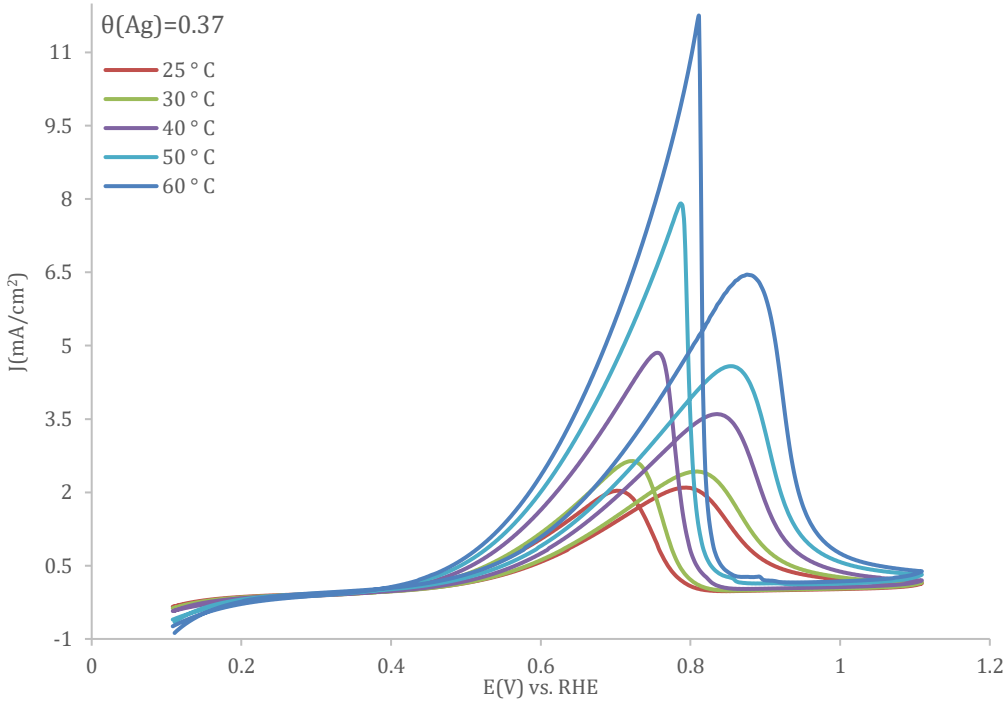
θ(Ag)=0.37
25 ° C
30 ° C
40 ° C
50 ° C
60 ° C
J(mA/cm²)
E(V) vs. RHE
11
9.5
8
6.5
5
3.5
2
0.5
-1
0
0.2
0.4
0.6
0.8
1
1.2

(e).

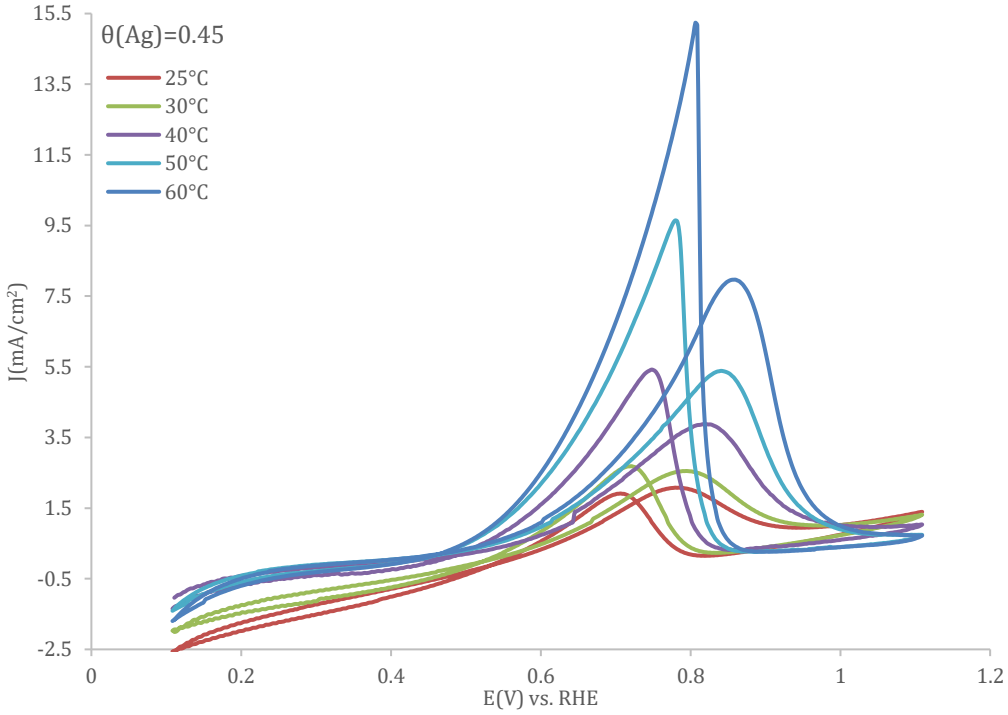
θ(Ag)=0.45
25°C
30°C
40°C
50°C
60°C
J(mA/cm²)
E(V) vs. RHE
15.5
13.5
11.5
9.5
7.5
5.5
3.5
1.5
-0.5
-2.5
0
0.2
0.4
0.6
0.8
1
1.2

(f).

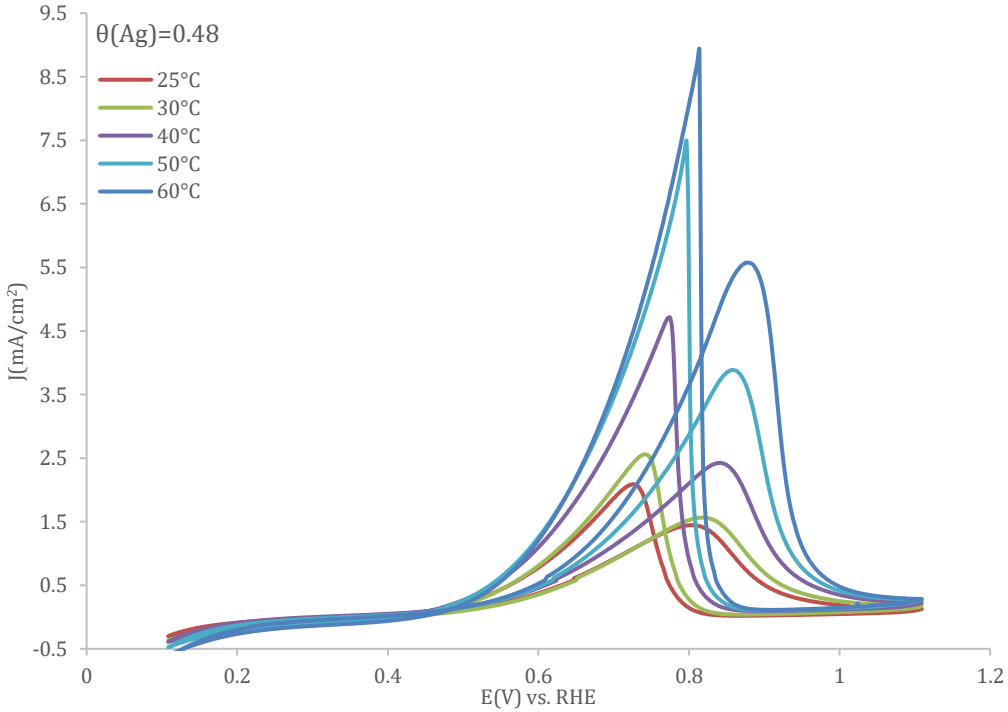
θ(Ag)=0.48
25°C
30°C
40°C
50°C
60°C
J(mA/cm²)
E(V) vs. RHE
9.5
8.5
7.5
6.5
5.5
4.5
3.5
2.5
1.5
0.5
-0.5
0
0.2
0.4
0.6
0.8
1
1.2

(g).

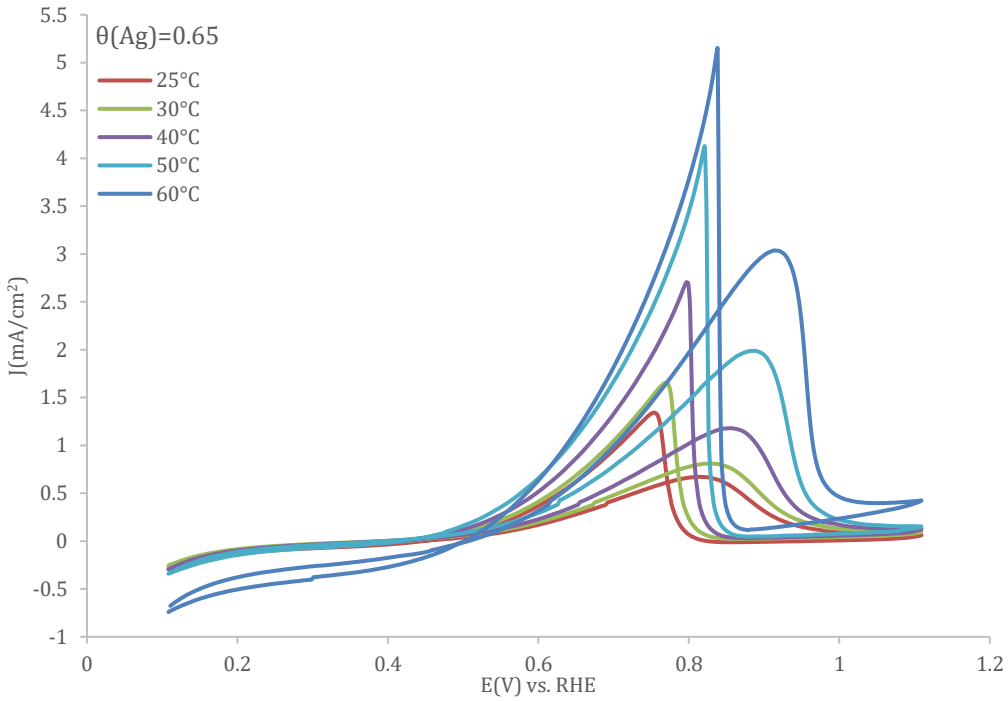

A.6.1. Cyclic voltammograms of bulk Pd with various Ag coverages: (a). $\theta_{Ag} = 0$, (b). $\theta_{Ag} = 0.15$, (c). $\theta_{Ag} = 0.26$ (d). $\theta_{Ag} = 0.37$, (e). $\theta_{Ag} = 0.45$, (f). $\theta_{Ag} = 0.48$, (g). $\theta_{Ag} = 0.65$ toward ethanol electrooxidation from 0.15V to 1.35V(vs. RHE) in 0.1 M Ethanol + 0.1 M NaOH solution at different temperatures: i. T = 30 °C, ii. T = 40 °C, iii. T = 50 °C, iv. T = 60 °C. Scan rate: 50 mVs^{-1}.

(a).

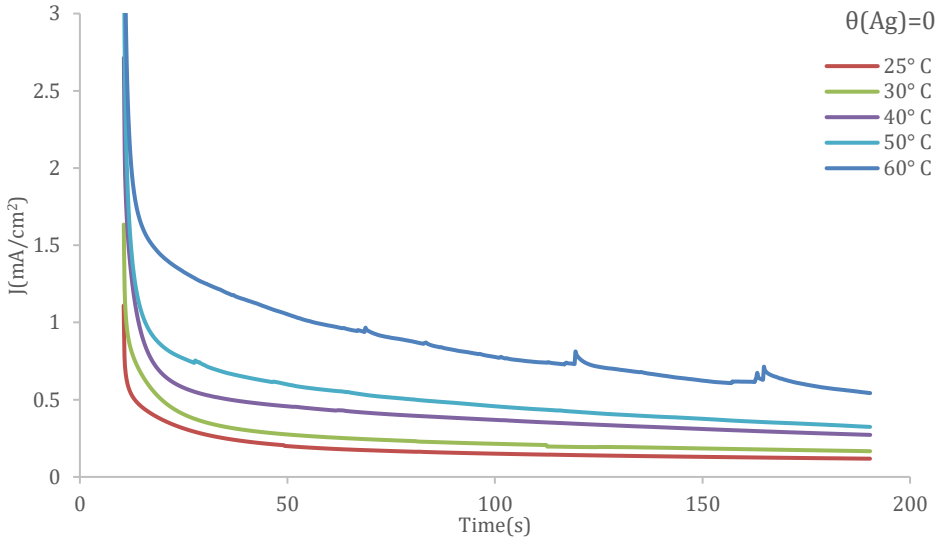
θ(Ag)=0
25° C
30° C
40° C
50° C
60° C
J(mA/cm²)
Time(s)
0
0.5
1
1.5
2
2.5
3
0
50
100
150
200

(b).

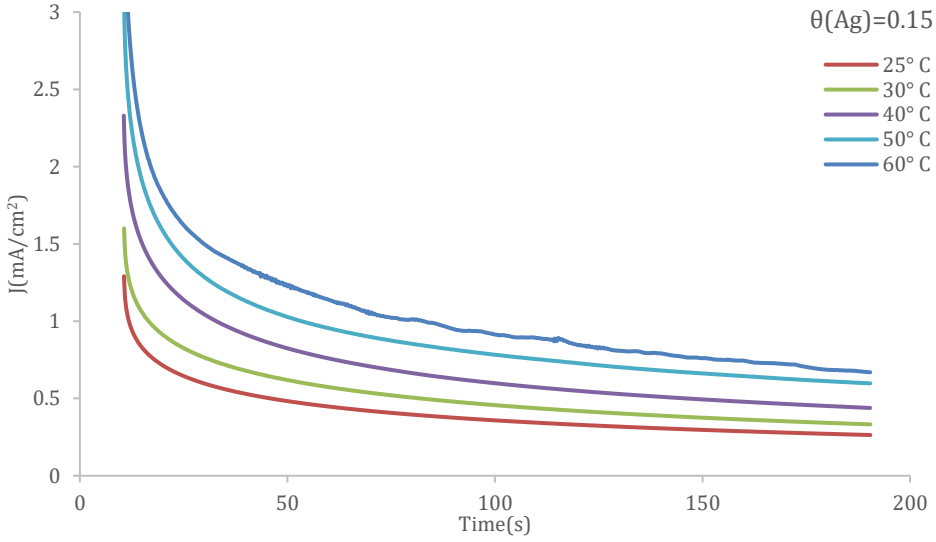
θ(Ag)=0.15
25° C
30° C
40° C
50° C
60° C
J(mA/cm²)
Time(s)
0
0.5
1
1.5
2
2.5
3
0
50
100
150
200

(c).

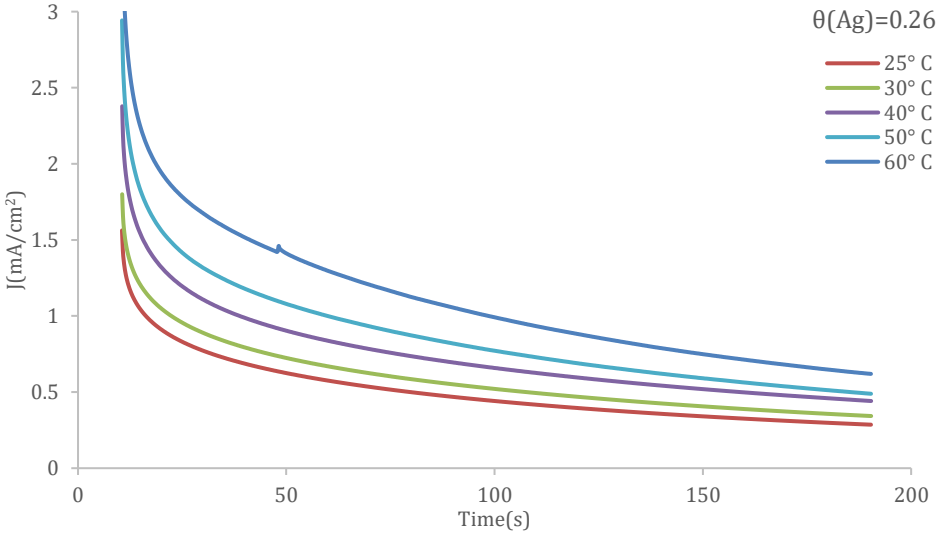
θ(Ag)=0.26
25° C
30° C
40° C
50° C
60° C
J(mA/cm²)
Time(s)
0
0.5
1
1.5
2
2.5
3
0
50
100
150
200

(d).

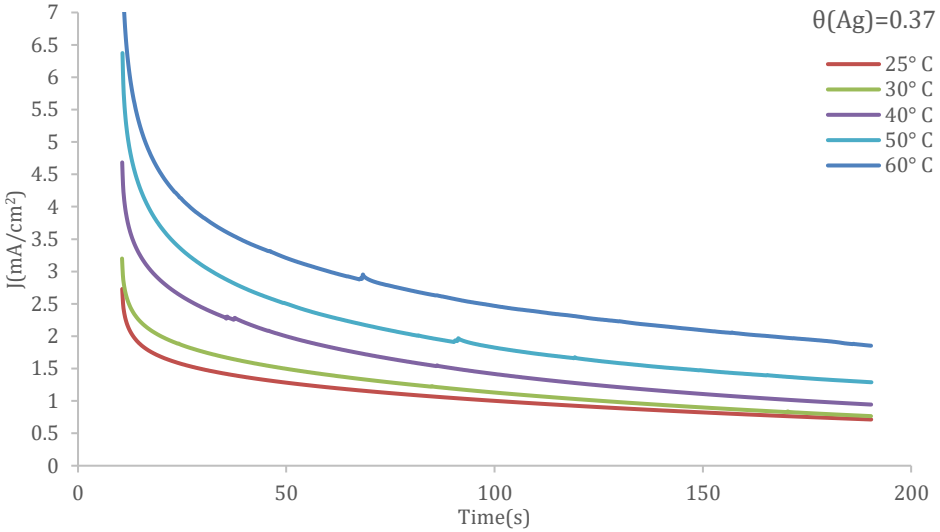
θ(Ag)=0.37
25° C
30° C
40° C
50° C
60° C
J(mA/cm²)
Time(s)
0
0.5
1
1.5
2
2.5
3
3.5
4
4.5
5
5.5
6
6.5
7
0
50
100
150
200

(e).

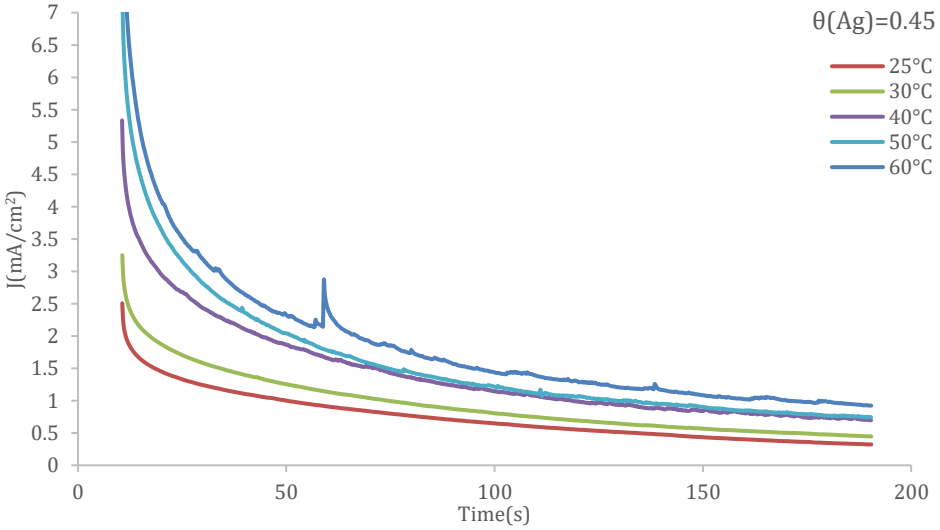
θ(Ag)=0.45
25°C
30°C
40°C
50°C
60°C
J(mA/cm²)
Time(s)
0
0.5
1
1.5
2
2.5
3
3.5
4
4.5
5
5.5
6
6.5
7
0
50
100
150
200

(f).

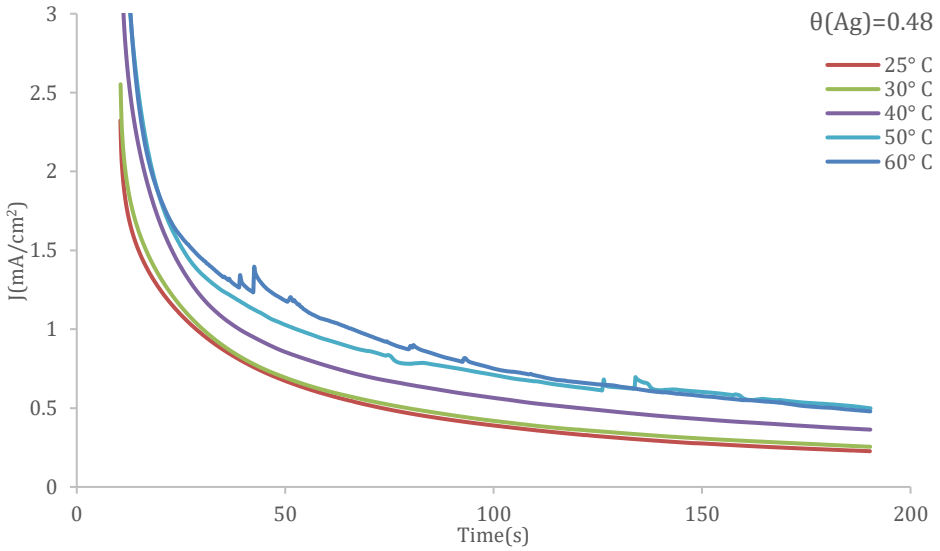
θ(Ag)=0.48
25° C
30° C
40° C
50° C
60° C
J(mA/cm²)
Time(s)
0
0.5
1
1.5
2
2.5
3
0
50
100
150
200

(g).

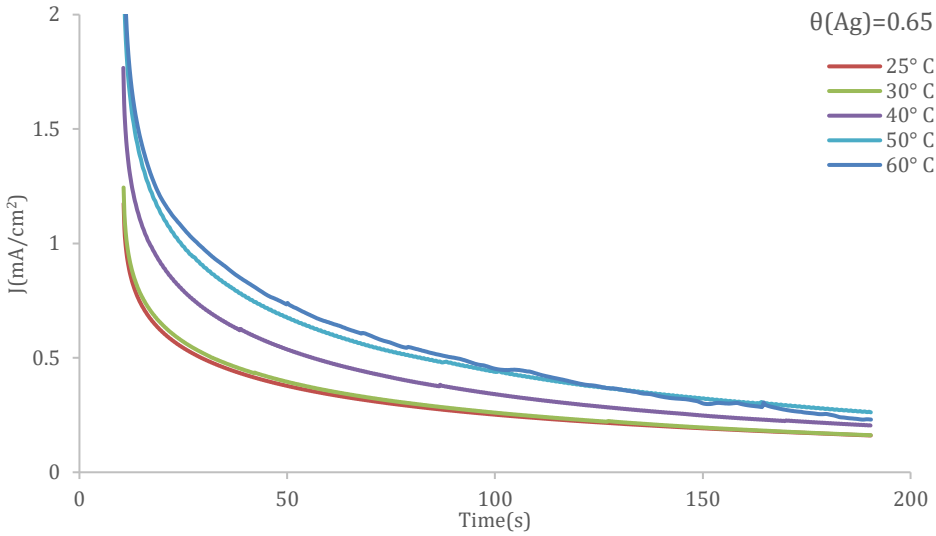

A.6.2. Chronoamperometric curves of Ag-decorated Pd electrodes with different Ag coverages:(a). $\theta_{Ag} = 0$, **(b).** $\theta_{Ag} = 0.15$, ***(c).*** $\theta_{Ag} = 0.26$, ***(d).*** $\theta_{Ag} = 0.37$, ***(e).*** $\theta_{Ag} = 0.45$, ***(f).*** $\theta_{Ag} = 0.48$, ***(g).*** $\theta_{Ag} = 0.65$ ***toward ethanol electrooxidation in 0.1 M Ethanol + 0.1 M NaOH solution at the potential of 0.71 V (vs. RHE) at different temperatures. Scan rate: 50 mVs$**$-1$**$.***

(a).

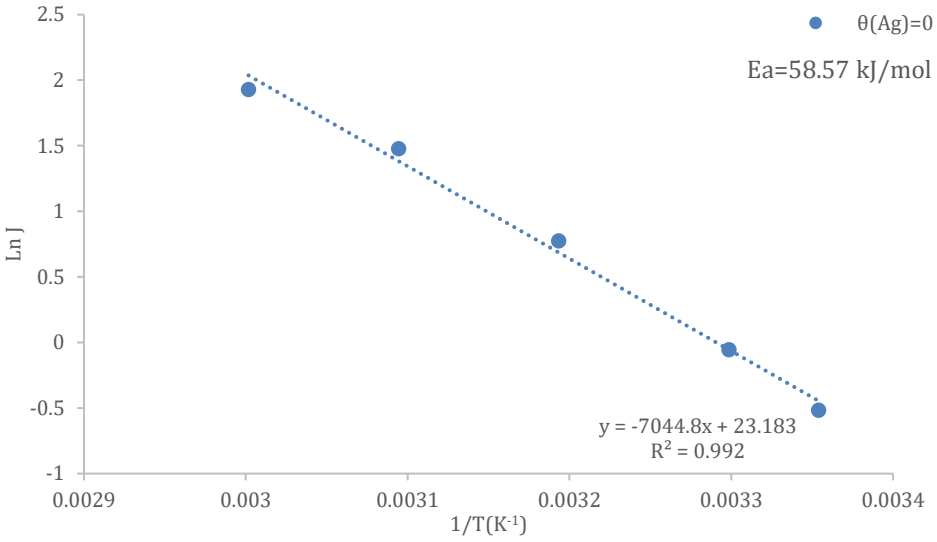
θ(Ag)=0
Ea=58.57 kJ/mol
Ln J
1/T(K-1)
y = -7044.8x + 23.183
R2 = 0.992
2.5
2
1.5
1
0.5
0
-0.5
-1
0.0029
0.003
0.0031
0.0032
0.0033
0.0034

(b).

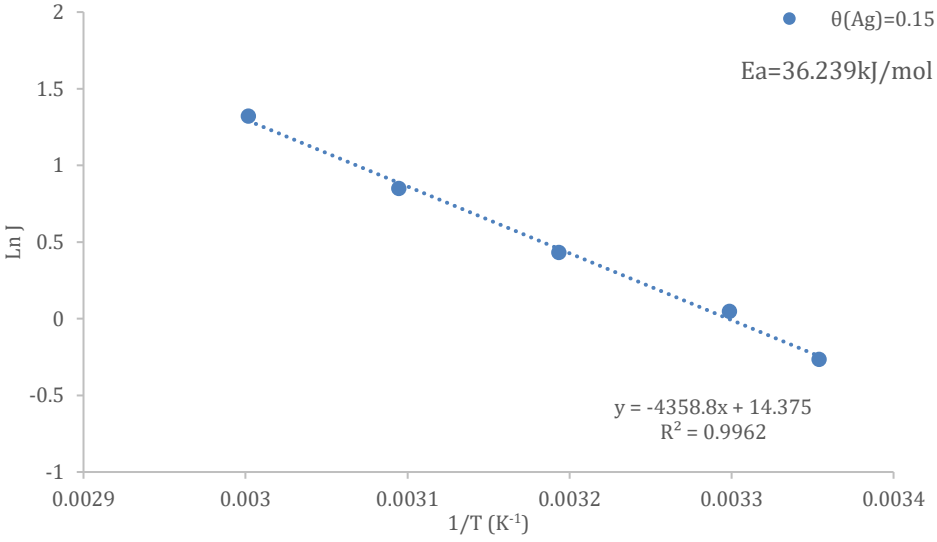
θ(Ag)=0.15
Ea=36.239kJ/mol
Ln J
1/T (K-1)
y = -4358.8x + 14.375
R2 = 0.9962
2
1.5
1
0.5
0
-0.5
-1
0.0029
0.003
0.0031
0.0032
0.0033
0.0034

(c).

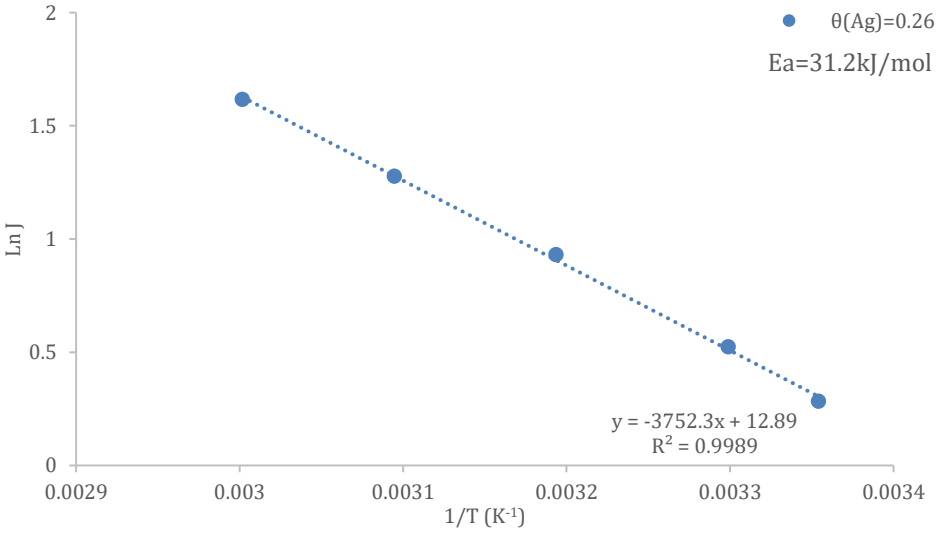
θ(Ag)=0.26
Ea=31.2kJ/mol
Ln J
1/T (K-1)
y = -3752.3x + 12.89
R2 = 0.9989
2
1.5
1
0.5
0
0.0029
0.003
0.0031
0.0032
0.0033
0.0034

(d).

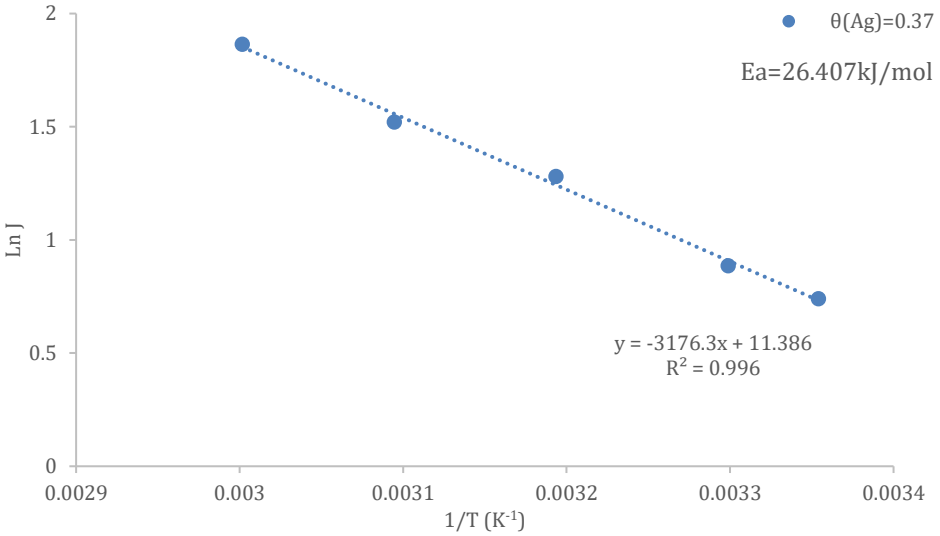
θ(Ag)=0.37
Ea=26.407kJ/mol
y = -3176.3x + 11.386
R² = 0.996
Ln J
1/T (K⁻¹)
2
1.5
1
0.5
0
0.0029
0.003
0.0031
0.0032
0.0033
0.0034

(e).

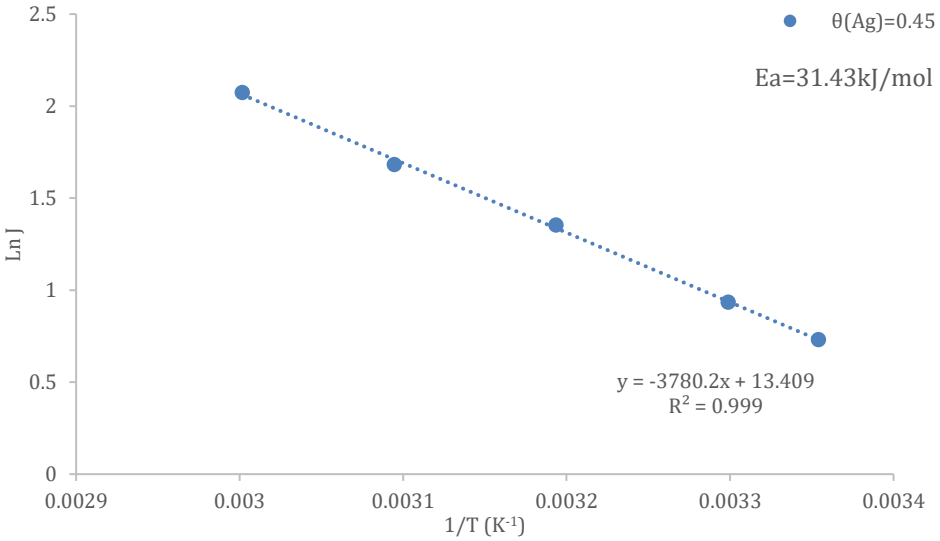
θ(Ag)=0.45
Ea=31.43kJ/mol
y = -3780.2x + 13.409
R² = 0.999
Ln J
1/T (K⁻¹)
2.5
2
1.5
1
0.5
0
0.0029
0.003
0.0031
0.0032
0.0033
0.0034

(f).

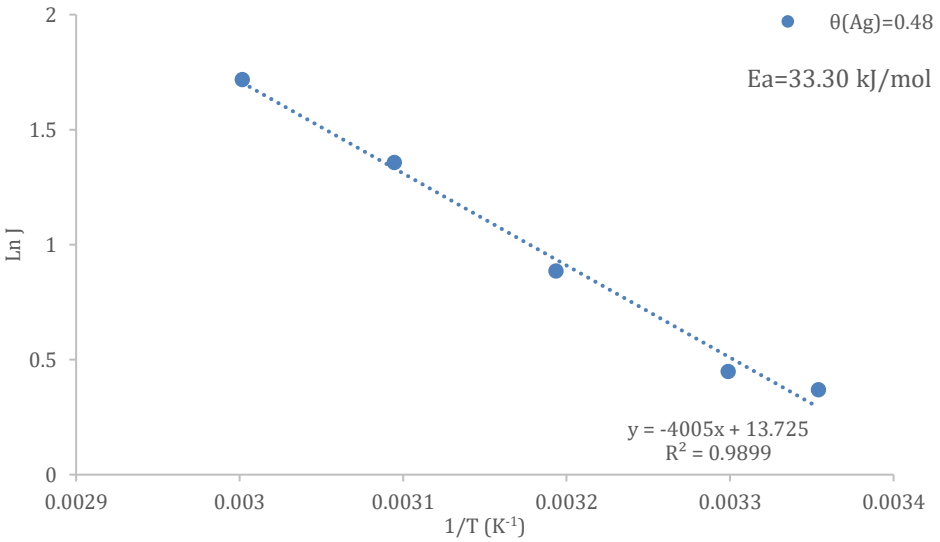
θ(Ag)=0.48
Ea=33.30 kJ/mol
y = -4005x + 13.725
R² = 0.9899
Ln J
1/T (K⁻¹)
2
1.5
1
0.5
0
0.0029
0.003
0.0031
0.0032
0.0033
0.0034

(g).

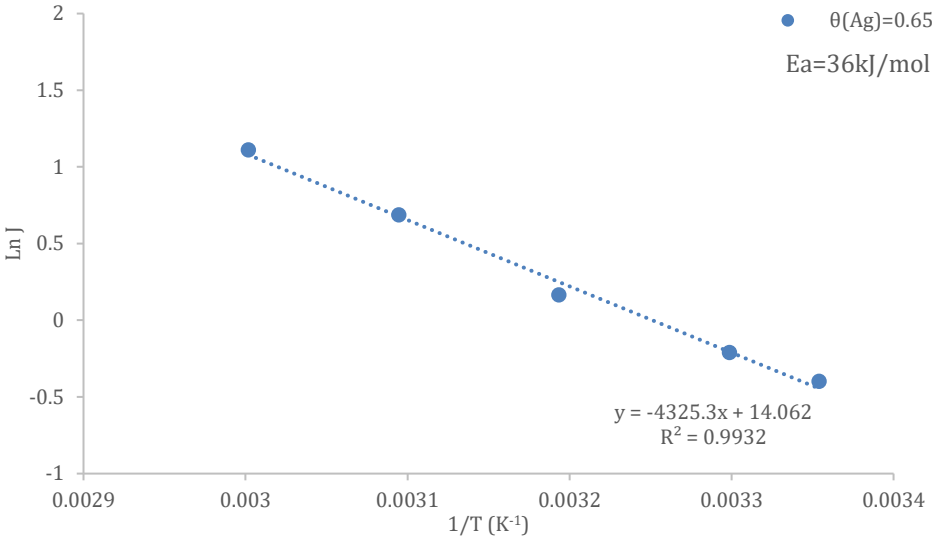

A.6.3. Arrhenius plots of EOR on Ag-Pd with different Ag-coverage of (a). 0, (b). 0.15, (c). 0.26, (d). 0.37, (e). 0.45, (f). 0.48, (g). 0.65. The data were achieved from peak current densities at forward potential scans for EOR at different temperatures in 0.1 M NaOH + 0.1 M Ethanol.

Chapter 7

(a).

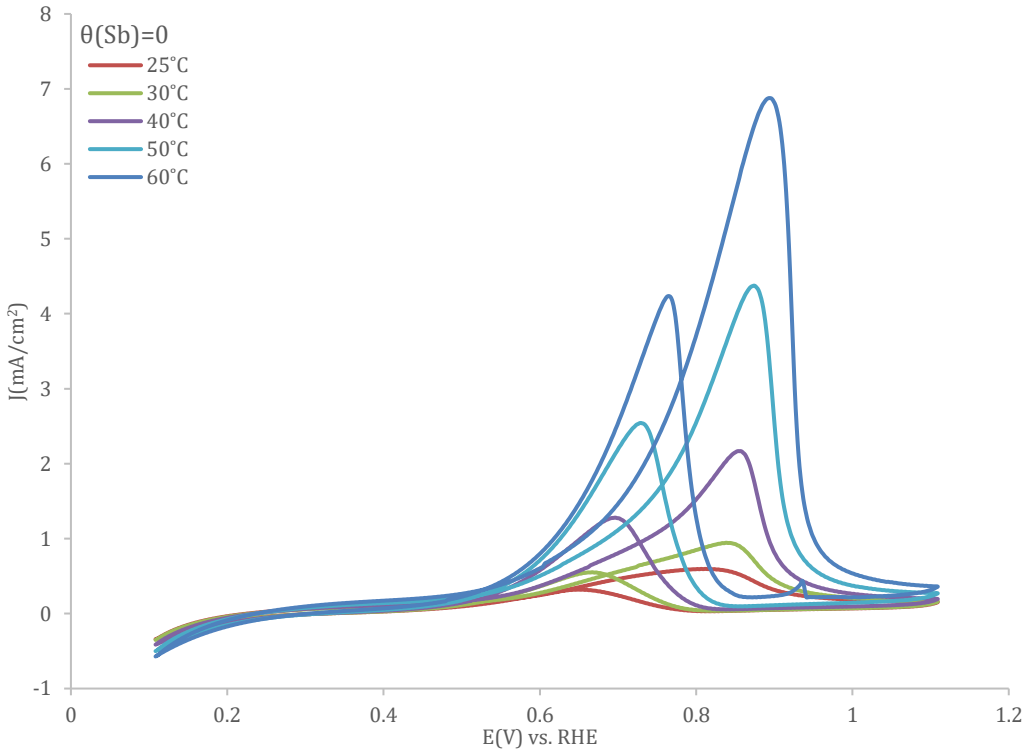
θ(Sb)=0
25°C
30°C
40°C
50°C
60°C
J(mA/cm²)
E(V) vs. RHE
8
7
6
5
4
3
2
1
0
-1
0
0.2
0.4
0.6
0.8
1
1.2

(b).

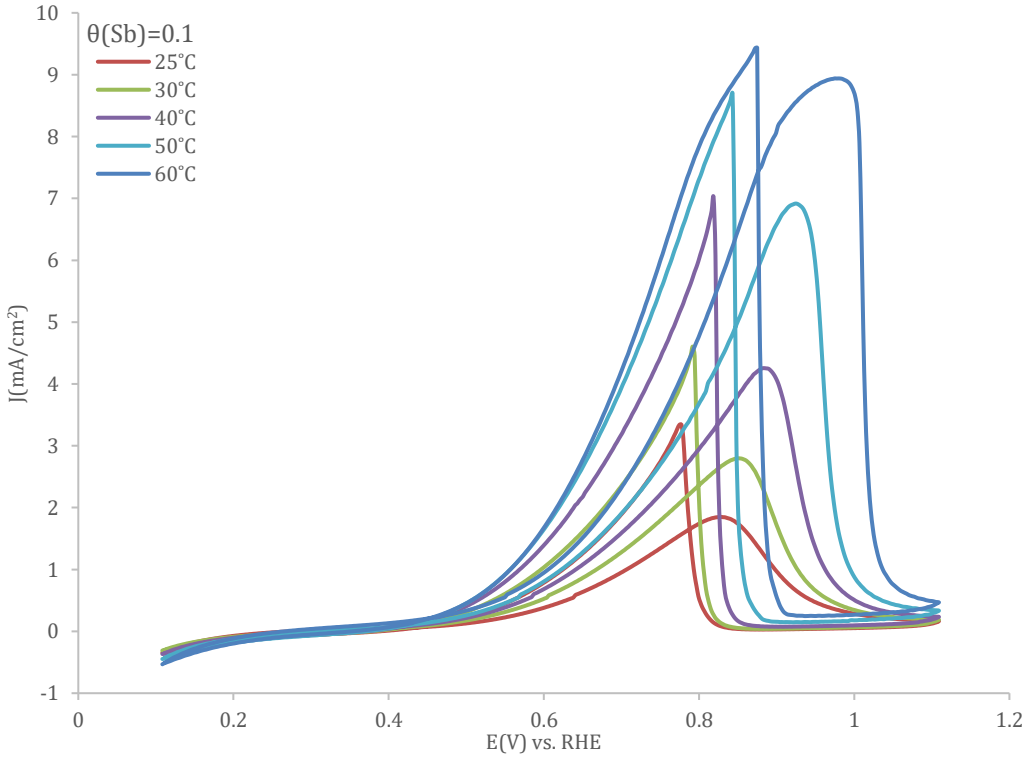
θ(Sb)=0.1
25°C
30°C
40°C
50°C
60°C
J(mA/cm²)
E(V) vs. RHE
10
9
8
7
6
5
4
3
2
1
0
-1
0
0.2
0.4
0.6
0.8
1
1.2

(c).

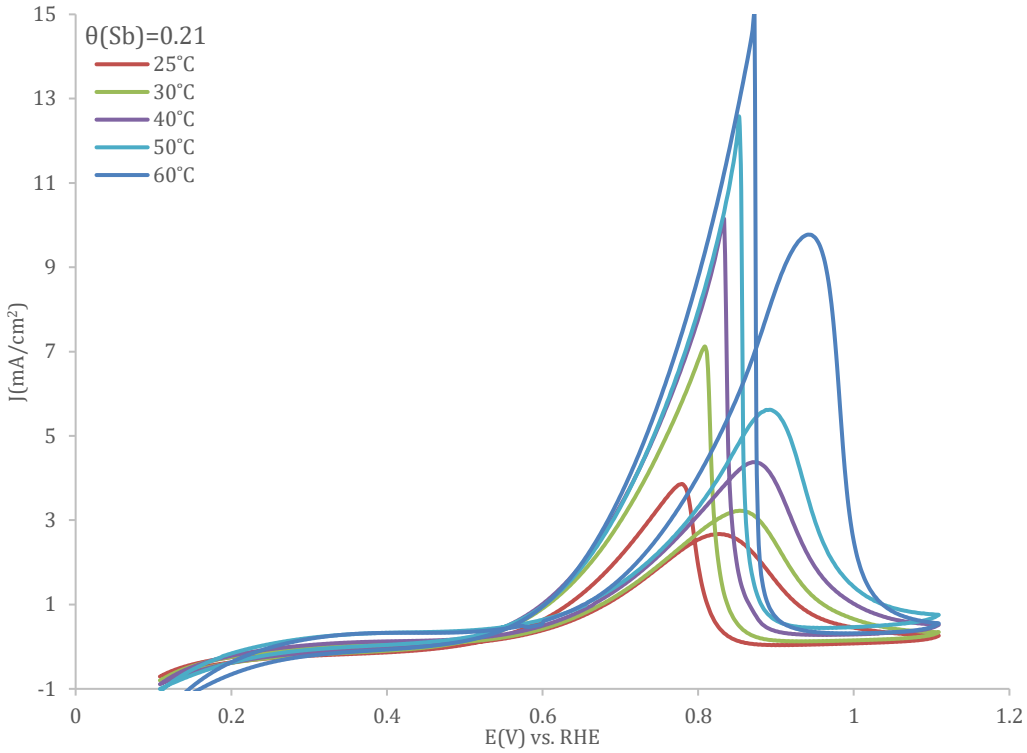
θ(Sb)=0.21
25°C
30°C
40°C
50°C
60°C
J(mA/cm²)
E(V) vs. RHE
15
13
11
9
7
5
3
1
-1
0
0.2
0.4
0.6
0.8
1
1.2

(d).

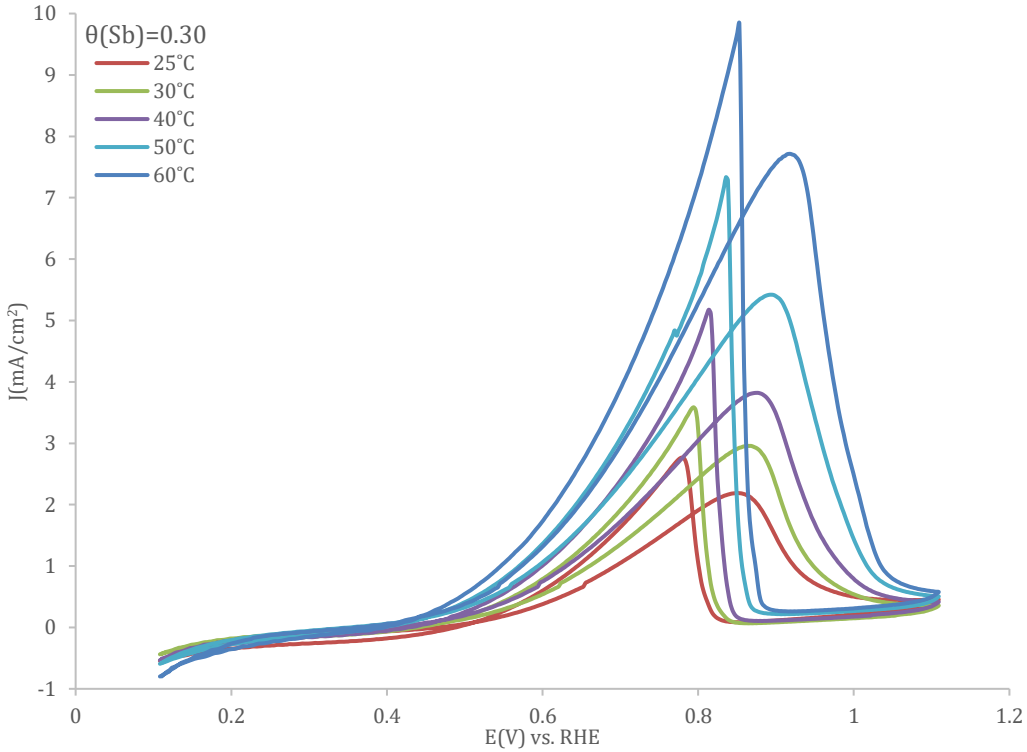
θ(Sb)=0.30
25°C
30°C
40°C
50°C
60°C
J(mA/cm²)
E(V) vs. RHE
10
9
8
7
6
5
4
3
2
1
0
-1
0
0.2
0.4
0.6
0.8
1
1.2

(e).

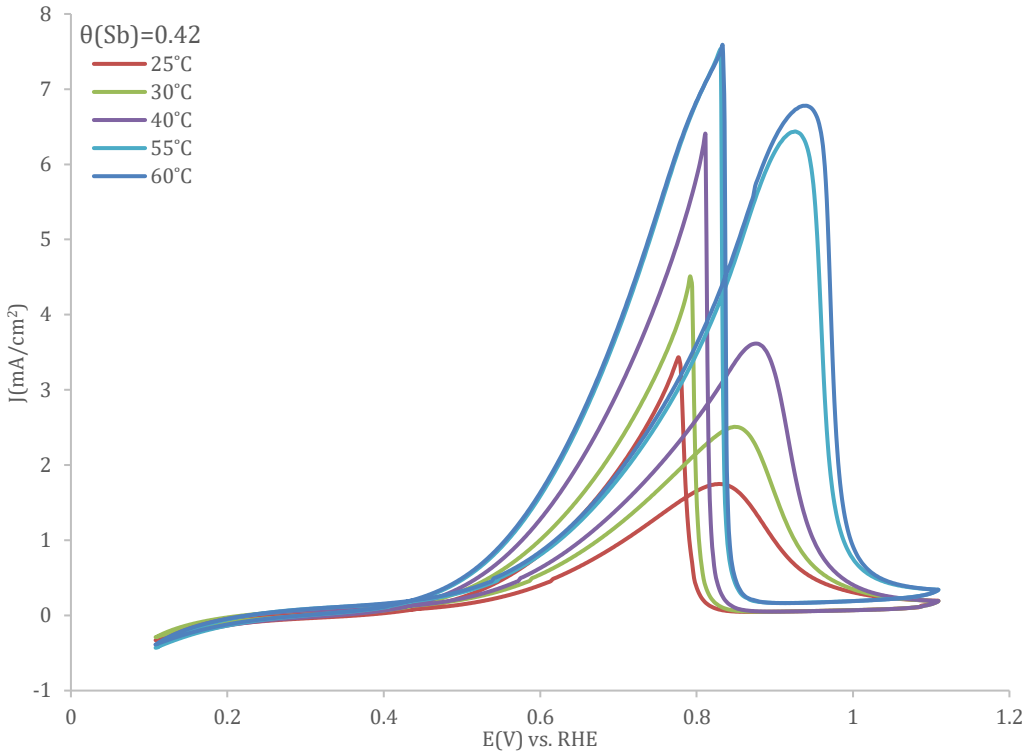

(f).

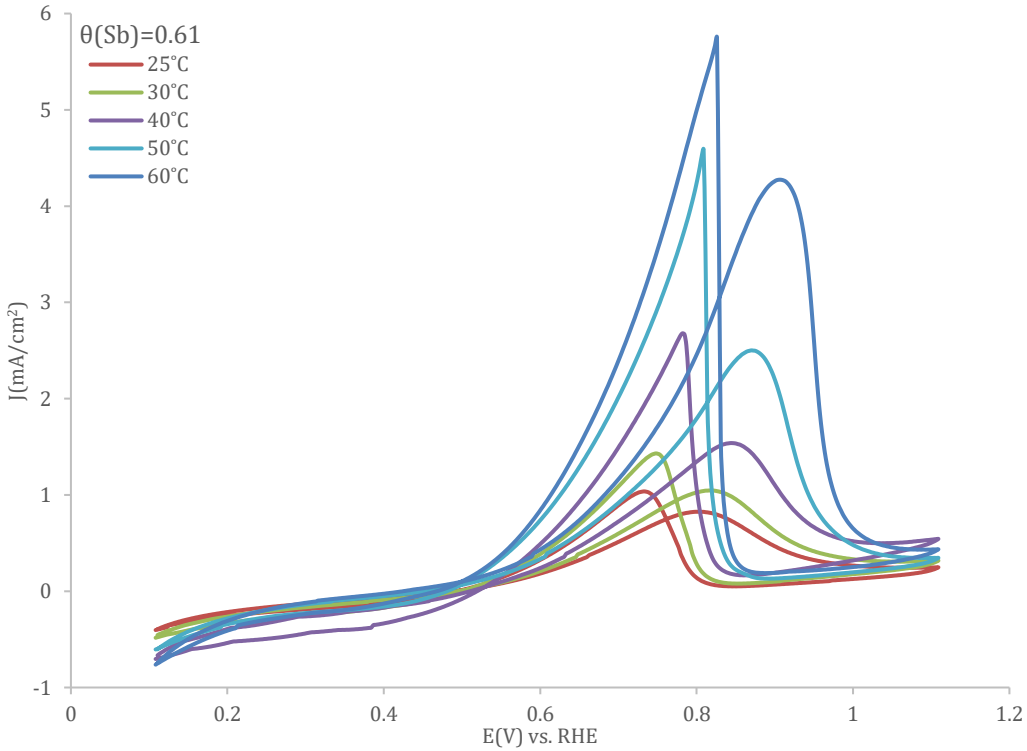

A.7.1. Cyclic voltammograms of bulk Pd with various Ag coverages: (a). $\theta_{Sb} = 0$, (b). $\theta_{Sb} = 0.1$, (c). $\theta_{Sb} = 0.21$ (d). $\theta_{Sb} = 0.30$, (e). $\theta_{Sb} = 0.43$, (f). $\theta_{Sb} = 0.61$ toward ethanol electrooxidation from 0.15V to 1.35 V (vs. RHE) in 0.1 M

Ethanol + 0.1 M NaOH solution at different temperatures: i. T = 30 °C, ii. T = 40 °C, iii. T = 50 °C, iv. T = 60 °C. Scan rate: 50 mVs^{-1}.

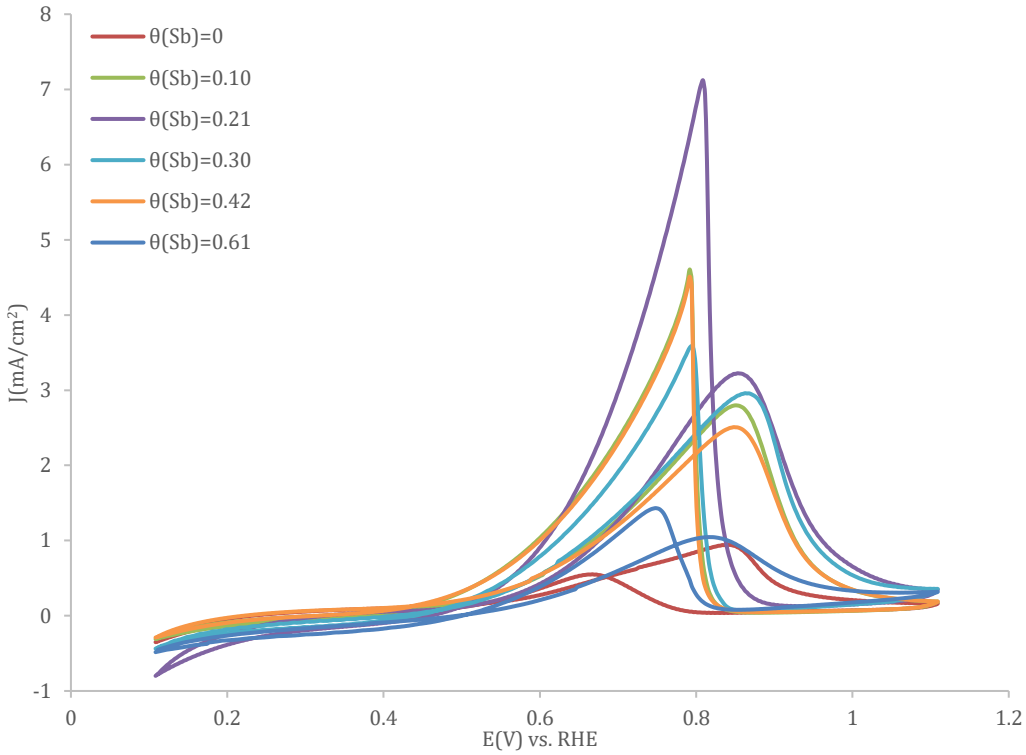

A.7.2. Cyclic voltammograms of Sb-decorated Pd electrodes with different Sb coverages towards ethanol electrooxidation from 0.11 V to 1.11 V (vs. RHE) at 30 °C in 0.1 M Ethanol + 0.1 M NaOH solution. Scan rate: 50 mVs^{-1}.

(a).

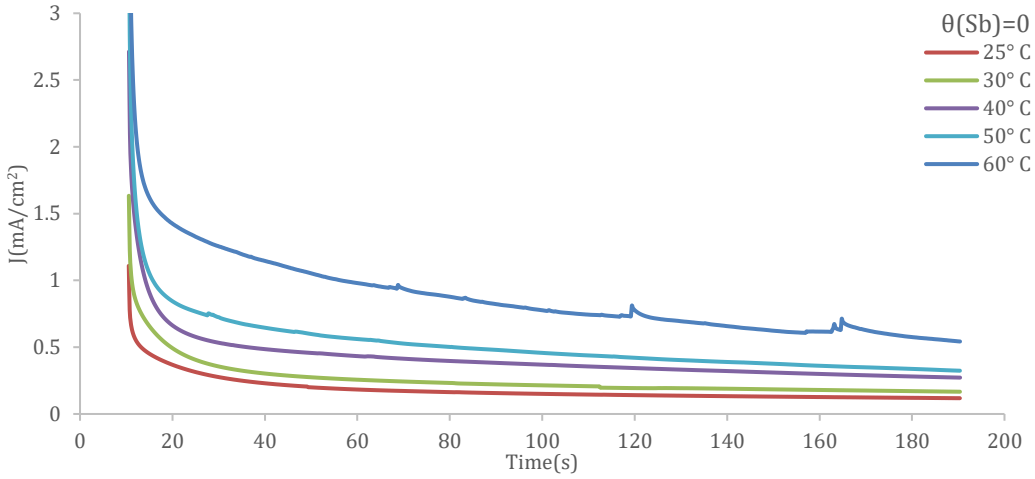
θ(Sb)=0
25° C
30° C
40° C
50° C
60° C
J(mA/cm²)
Time(s)

(b).

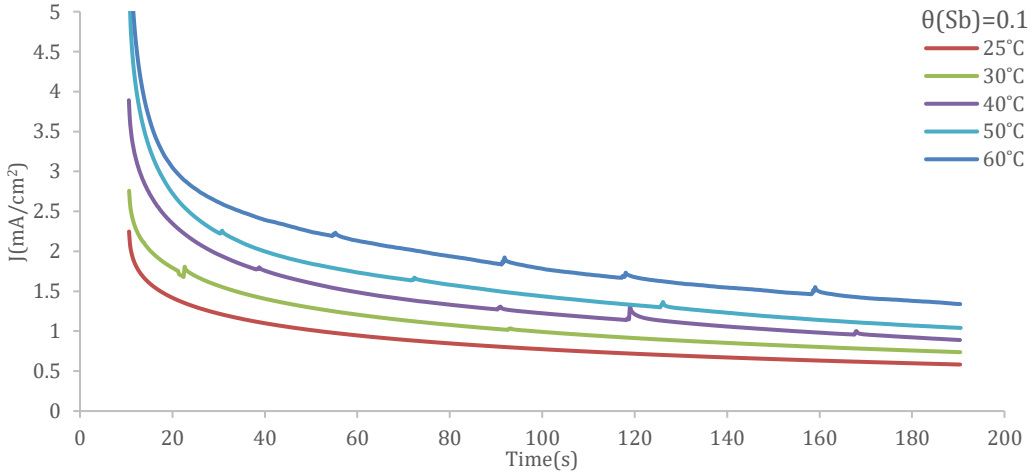
θ(Sb)=0.1
25°C
30°C
40°C
50°C
60°C
J(mA/cm²)
Time(s)

(c).

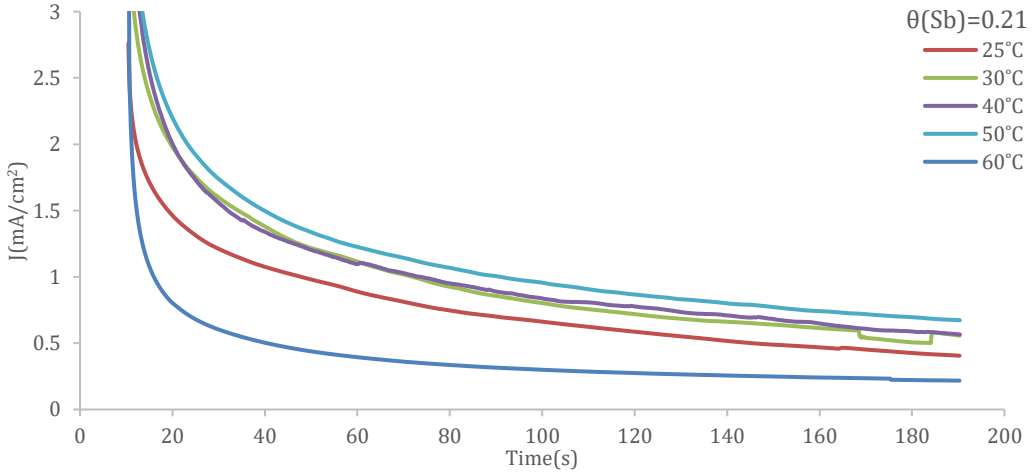
θ(Sb)=0.21
25°C
30°C
40°C
50°C
60°C
J(mA/cm²)
Time(s)

(d)

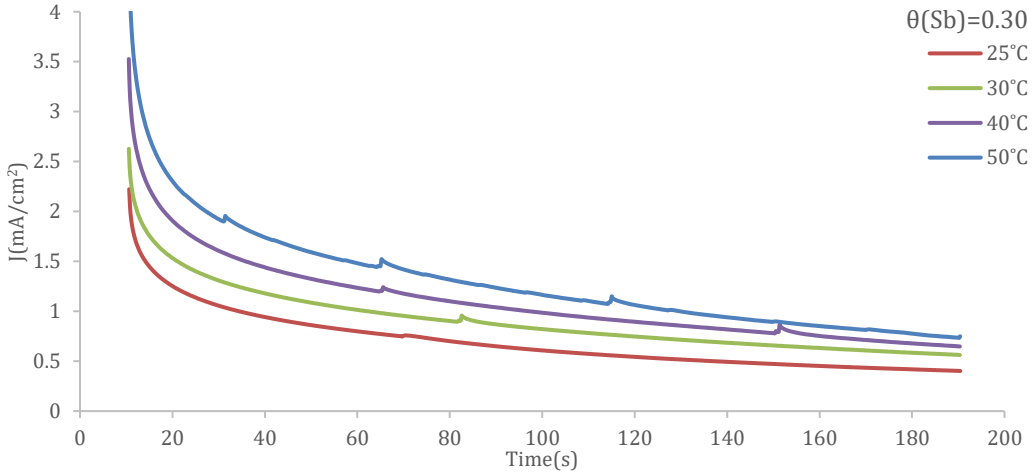

(e).

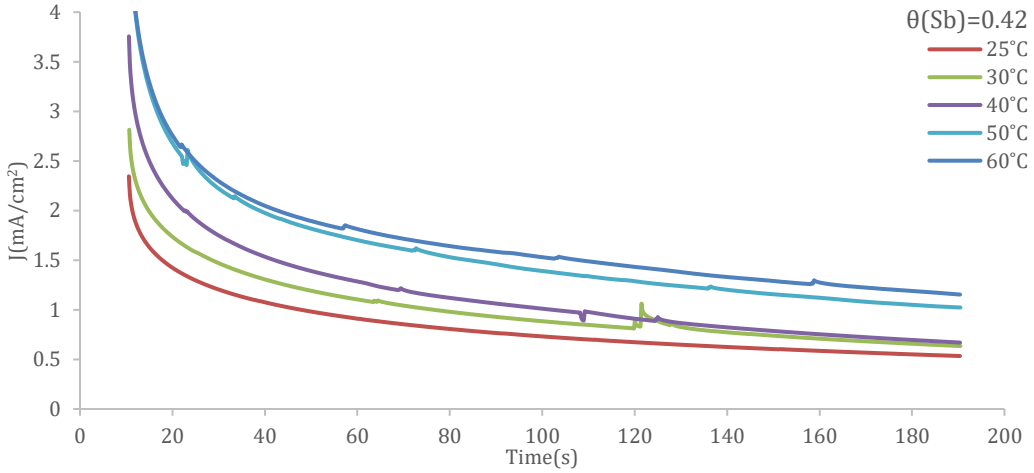

(f).

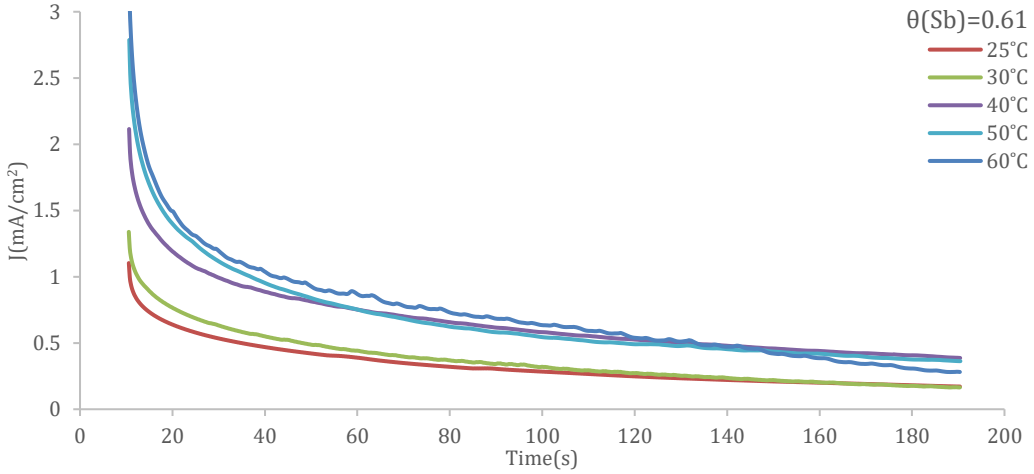

A.7.3. Chronoamperometric curves of Ag-decorated Pd electrodes with different Ag coverages: (a). $\theta_{Sb} = 0$, (b). $\theta_{Sb} = 0.1$, (c). $\theta_{Sb} = 0.21$ (d). $\theta_{Sb} = 0.30$, (e). $\theta_{Sb} = 0.43$, (f). $\theta_{Sb} = 0.61$ toward ethanol electrooxidation in 0.1 M Ethanol +

0.1 M NaOH solution at the potential of 0.71 V (vs. RHE) at different temperatures. Scan rate: 50 mVs^{-1}.

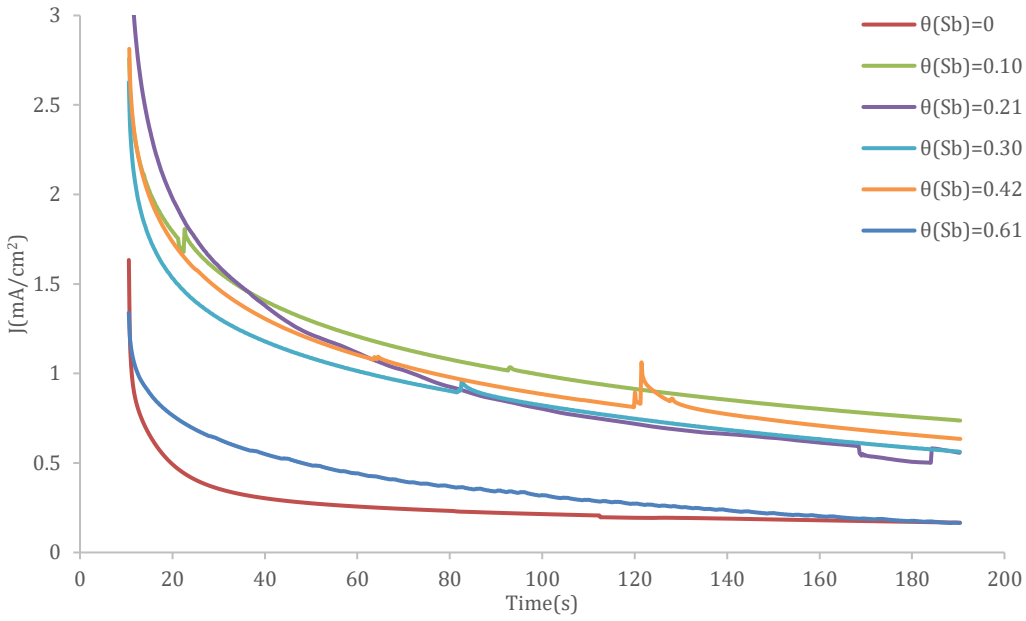

A.7.4 Chronoamperometric curves of Sb Pd electrodes with different Sb coverages toward ethanol electrooxidation at the potential of 0.71 V (vs. RHE) at 30 ˚C in 0.1 M Ethanol + 0.1 M NaOH solution. Scan rate: 50 mVs^{-1}.

(a).

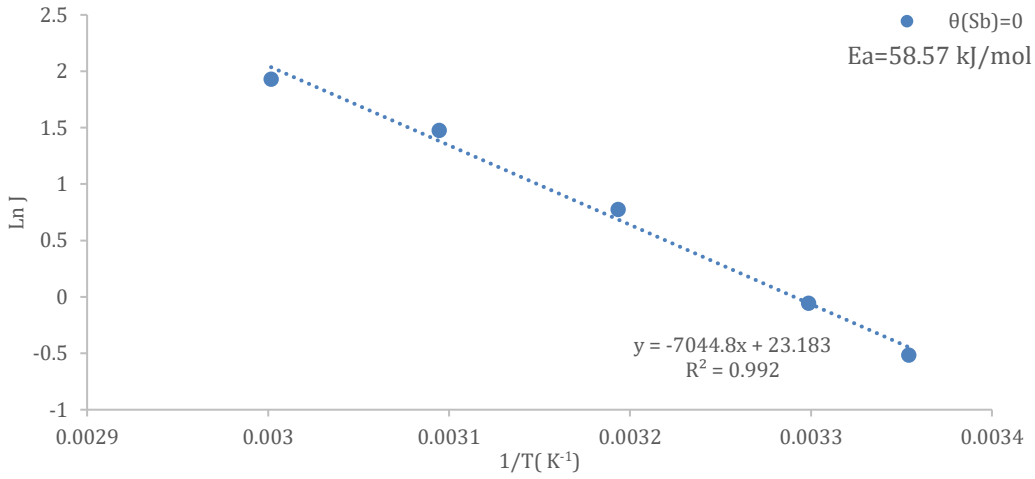
θ(Sb)=0
Ea=58.57 kJ/mol
Ln J
y = -7044.8x + 23.183
R² = 0.992
1/T(K-1)
2.5
2
1.5
1
0.5
0
-0.5
-1
0.0029
0.003
0.0031
0.0032
0.0033
0.0034

(b).

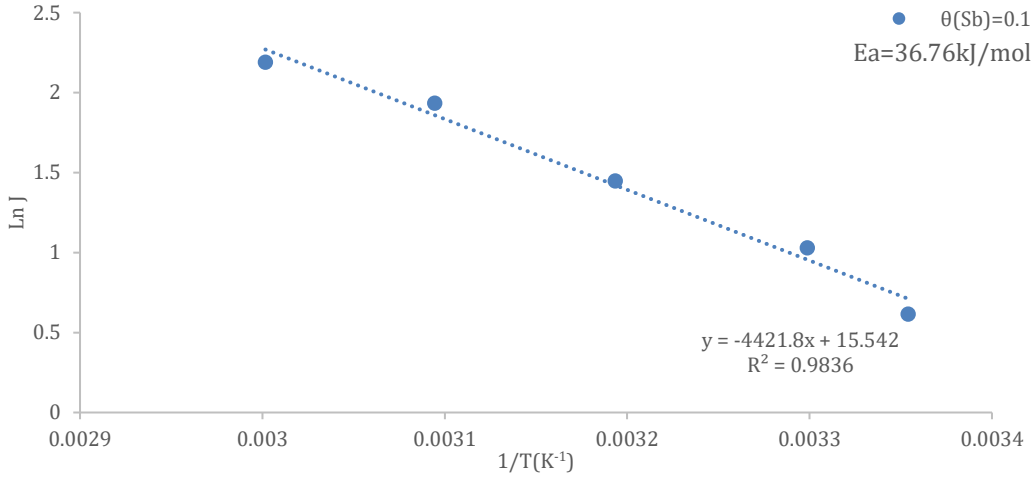
θ(Sb)=0.1
Ea=36.76kJ/mol
Ln J
y = -4421.8x + 15.542
R² = 0.9836
1/T(K-1)
2.5
2
1.5
1
0.5
0
0.0029
0.003
0.0031
0.0032
0.0033
0.0034

(c).

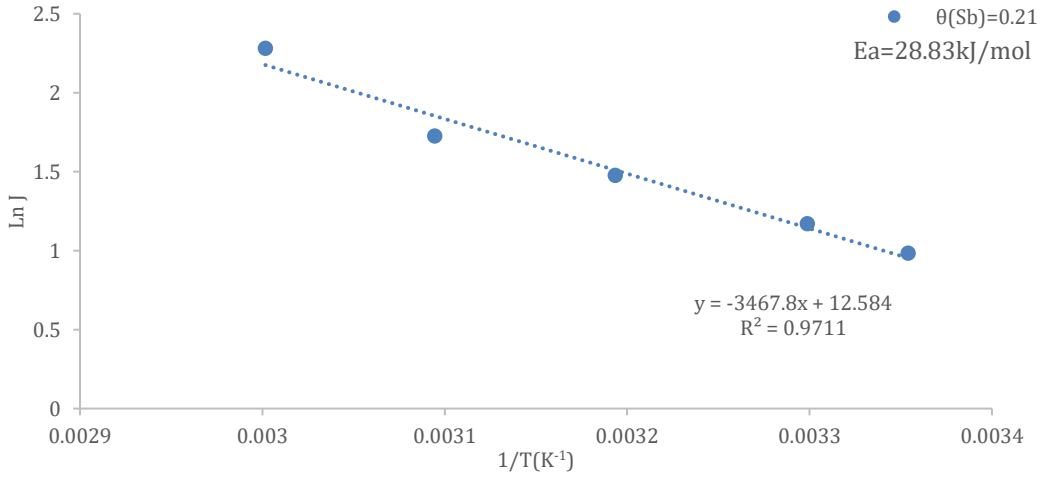
θ(Sb)=0.21
Ea=28.83kJ/mol
Ln J
y = -3467.8x + 12.584
R² = 0.9711
1/T(K-1)
2.5
2
1.5
1
0.5
0
0.0029
0.003
0.0031
0.0032
0.0033
0.0034

(d).

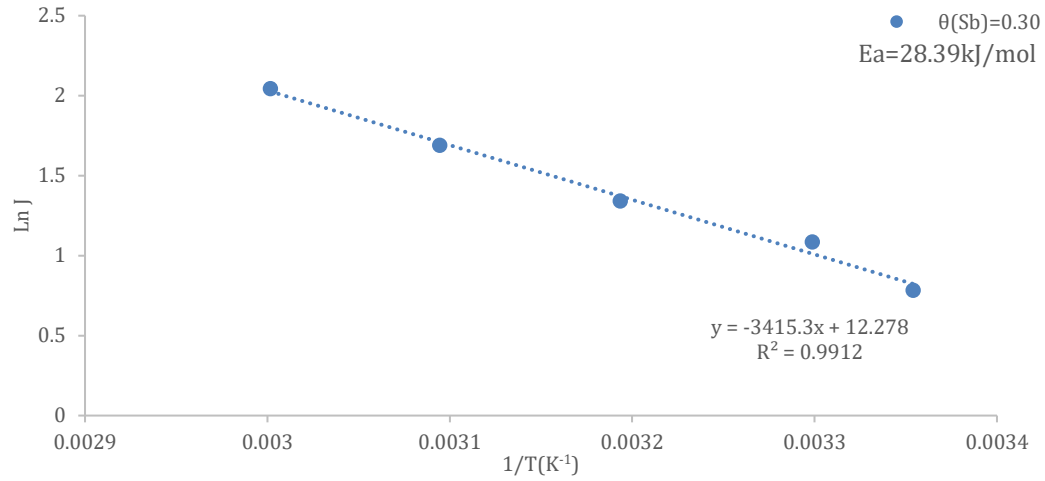

(e).

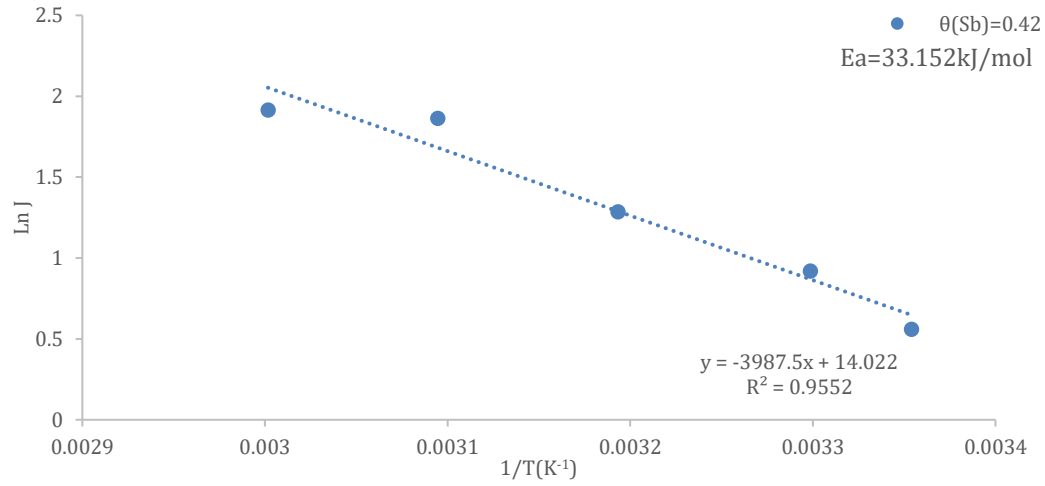

(f).

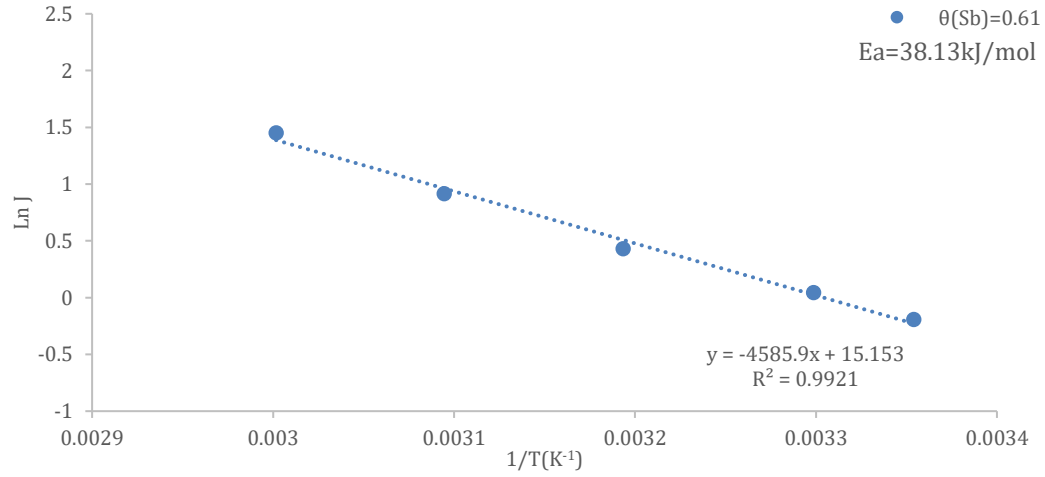

A.7.5. Arrhenius plots of EOR on Ag-Pd with different Sb-coverage of (a). 0, (b). 0.1, (c). 0.21, (d). 0.30, (e). 0.42, (f). 0.61. The data were achieved from peak current densities at forward potential scans for EOR at different temperatures in 0.1 M

NaOH + 0.1 M Ethanol.